Accelerating, Characterising and Controlling Nucleation Processes

Peter Lloyd Kaskiewicz

Submitted in accordance with the requirements for the degree of

Doctor of Philosophy

(Chemical Engineering)

The University of Leeds

Centre for Doctoral Training in Complex Particulate Products and Processes

School of Chemical and Process Engineering

July 2021

This work is submitted as an alternative style of doctoral thesis, which includes published material, due to the number of peer-reviewed publications that have already been published in internationally recognised research journals, resulting from this work. These publications are presented to demonstrate the research outputs that have resulted from this doctoral research study. An overarching commentary is also presented that provides context and rationale of the research undertaken, critical discussion that supports and links the published material and a conclusion that ties the work together and indicates directions for future work.

The candidate confirms that the work submitted is their own, except where work which has formed part of jointly authored publications has been included. The contribution of the candidate and the other authors to this work has been explicitly indicated below. The candidate confirms that appropriate credit has been given within the thesis where reference has been made to the work of others.

Chapter 2 – Presents published material resulting from this doctoral study, which is detailed as follows:

Isothermal by design: An accelerated approach to the prediction of the crystallisability of slowly nucleating systems. P. L. Kaskiewicz, G. Xu, X. Lai, N. Warren, K. J. Roberts, C. Morton, P. Dowding, N. George. *Org. Process Res. Dev.* 2019, 23, 1948−1959. Available: https://pubs.acs.org/doi/10.1021/acs.oprd.9b00242

Reprinted (adapted) with permission from Org. Process Res. Dev. 2019, 23, 1948−1959. Copyright 2021 American Chemical Society. Further permissions related to the material excerpted should be directed to the ACS. I was the lead author of this paper. Kevin J. Roberts helped towards the conceptualisation of this work and, alongside Neil George, participated in active discussions during the study. All author's inputted ideas and offered guidance and corrections during the writing process. All research outputs are my own, except: Guangyi Xu, a fellow PhD researcher at the time of this work, provided solubility data and subsequent analysis, relating to Section 3.1, Figures 2 and 3 and Table 1 of the paper.

Chapter 3 – Presents published material resulting from this doctoral study, which is detailed as follows:

Isothermal by Design: Comparison with an Established Isothermal Nucleation Kinetics Analysis Method. P. L. Kaskiewicz, T. D. Turner, N. Warren, C. Morton, P. J. Dowding, N. George, K. J. Roberts. *Chem. Eng. Technol.* 2020, 43, No. 10, 1971–1980. DOI: 10.1002/ceat.202000113.

I was the lead author of this paper. Kevin J. Roberts and Thomas D. Turner helped towards the conceptualisation of this work and participated in active discussions during the study. All author's inputted ideas and offered guidance and corrections during the writing process. All research outputs are my own, except: Thomas D. Turner, a research fellow at the time of this study, provided the induction time data for p-aminobenzoic acid crystallising from pure ethanol and water solutions using a standard induction time crystallisation method and aided in the analysis of results.

Chapter 4 – Presents published material resulting from this doctoral study, which is detailed as follows:

Influence of Solution Chemistry on the Solubility, Crystallisability and Nucleation Behaviour of Eicosane in Toluene : Acetone Mixed-Solvents. P. L. Kaskiewicz, I. Rosbottom, D. M. Camacho Corzo, R. B. Hammond, R. Downie, P. J. Dowding, N. George, K. J. Roberts. *Cryst. Eng. Comm*. Available: https://pubs.rsc.org/en/content/articlelanding/2021/ce/d1ce00322d.

I was the lead author of this paper. Kevin J. Roberts and Neil George participated in active discussions during the study. All author's inputted ideas and offered guidance and corrections during the writing process. All research outputs are my own, except: Ian Rosbottom, a research fellow at the time of this study, provided the atomic fractional charges used for the grid-based modelling studies and Diana M. Camacho Corzo provided the data for the ideal solubility of eicosane from Differential Scanning Calorimetry data.

Chapter 5 – Presents published material resulting from this doctoral study, which is detailed as follows:

Understanding and Designing Tailor-Made Additives for Controlling Nucleation: Case Study of p-Aminobenzoic Acid Crystallising from Ethanolic Solutions. P. L. Kaskiewicz, I. Rosbottom, R. B. Hammond, N. Warren, C. Morton, P. J. Dowding, N. George, K. J. Roberts. *Cryst. Growth Des.* 2021, 21, 1946−1958. Available: https://pubs.acs.org/doi/abs/10.1021/acs.cgd.0c01209.

Reprinted (adapted) with permission from Cryst. Growth Des. 2021, 21, 1946−1958. Copyright 2021 American Chemical Society. "I was the lead author of this paper. Kevin J. Roberts helped towards the conceptualisation of this work and, alongside Ian Rosbottom and Neil George, participated in active discussions during the study. All author's inputted ideas and offered guidance and corrections during the writing process. All research outputs are my own, except: Ian

Rosbottom provided the atomic fractional charges used for the grid-based modelling studies and aided in the analysis of molecular modelling results.

Further permissions related to the material excerpted should be directed to the ACS.

Chapter 6 – Presents work submitted for publication to a research journal, resulting from this doctoral study, which is detailed as follows:

Influence of a Polymeric Additive on the Characterisation, Solubility, Crystallisability and Nucleation of Eicosane in Toluene Solution. P. L. Kaskiewicz, R. Downie, P. J. Dowding, N. George, K. J. Roberts. *J. Cryst. Growth*. Submitted. Manuscript ID: CRYS-D-21-00437.

I was the lead author of this paper. All author's inputted ideas and offered guidance and corrections during the writing process. All research outputs are my own.

This copy has been supplied on the understanding that it is copyright material and that no quotation from the thesis may be published without proper acknowledgement © 2021 The University of Leeds and Peter Lloyd Kaskiewicz.

The right of Peter Lloyd Kaskiewicz to be identified as Author of this work has been asserted by him in accordance with the Copyright, Designs and Patents Act 1988.

Abstract

Unwanted nucleation poses a technological problem in a number of particle processing industries, encompassing fuels, agrochemicals, pharmaceuticals, foods, etc. In this, formulated products can undergo unwanted nucleation events over a vast range of time scales, from seconds to years, however, there is currently an inability to predict when these events might occur and a lack of fundamental understanding of how to prevent these events from taking place, either entirely or by suppressing nucleation outside of storage/operational conditions. Therefore, it is necessary to develop a route to predicting when these events might take place over long time scales and also develop better understanding of how formulation conditions and nucleation inhibition additives can affect the complex processes involved in crystal nucleation from solution environments. These developments are the focus of the research presented within this thesis, which utilises both aqueous and non-aqueous crystallising systems to advance the understanding of how to accelerate, control and characterise nucleation process within solutions with a view to predicting and inhibiting unwanted nucleation events.

An accelerated nucleation method, termed Isothermal by Design (IbD), is developed, which enables the rate of nucleation within solutions to be accelerated by rapidly generating high levels of solution supersaturation. Through this, induction times to nucleation are reduced by 5 orders of magnitude for p-aminobenzoic acid crystallising from mixed ethanol/water solutions and key nucleation kinetic parameters are derived over a wide range of supersaturations. A comparison of IbD with a conventional nucleation kinetic analysis route demonstrates the effectiveness of IbD for generating nucleation kinetic data both at low and high supersaturations and provides insight into the behaviour of nucleation in mixed-solvent systems.

An investigation focussing on the influence of solution chemistry on the nucleation process in mixed-solvent systems builds upon these insights and is presented for the system of eicosane crystallising from mixed toluene/acetone solutions. In this, mixed-solvent solution composition is found to be responsible for concurrent trends in the crystallisability, solution thermodynamics and nucleation mechanism over the full range of compositions studied. Grid-based molecular modelling provides molecular-scale insight into the solution structure, suggestive that the high solubility solvent, toluene, dominates the local solvation environment but, as the proportion of acetone increases, a ‘cage’ structure constituting a secondary solvation shell forms, drawing away solvation power towards eicosane, until a critical acetone composition is reached that overcomes this behaviour.

Two types of nucleation inhibition additives are investigated to provide insight into the ability of tailor-made additives and polymeric based additives to disrupt nucleation within solution environments. A workflow is developed to aid in both the understanding and designing of tailor-made additives for nucleation inhibition through a combination of grid-based molecular modelling and experimental techniques. Knowledge of the key intermolecular interactions (synthons) of the crystallising compound is key and is utilised as a foundation in the determination of three effective tailor-made additives from a screen of seven potentially effective ones, corroborated by experimental results.

The impact of a commercially available polymeric based cold-flow improver additive on the nucleation of eicosane from toluene solutions is presented, introducing a developed characterisation procedure for assessing nucleation kinetics from additive systems undergoing phase separations. Insight is gained into the nucleation mechanism and kinetic effects of different additive concentrations (treat rates) as well as fundamental understanding of the inhibition effect.

Conclusions are drawn from these studies and an assessment as to the success of meeting aims and objectives set out as part of this doctoral research is made, with suggested future work that could continue from the foundations built by this research study described.

Acknowledgements

I would like to express my gratitude towards:

Both my academic and industrial supervisors, without whom I would not be able to complete this project. With regards to my academic supervisors, Professor Kevin J. Roberts and Dr Nicholas J. Warren, I am grateful for both their supervision and guidance. I am especially grateful to Kevin who not only acted as a supervisor but also a mentor and a friend, making this project more enjoyable, engaging in regular intense intellectual discussions focussed towards and away from this work and also providing me with an environment in which to actively drive my project forward independently from the start. With regards to my industrial supervisors from Infineum UK, Dr Ruth Downie and Professor Pete Dowding, I am grateful for their support with this project, helping me progress and aiding in discussions of where the project should focus. I am also grateful to my industrial supervisor from Syngenta UK, Dr Neil George, who was very active in this project and regularly took the time to engage in meaningful and insightful discussions about my work.

The outputs of this project would also not have been possible without help from a number of my colleagues. To Tom Turner, Ian Rosbottom, Hien Nguyen and Diana Camacho Corzo I am tremendously thankful, not just for your friendship, but also for helping me to become a more knowledgeable and better crystal engineer and for contributing to my research. In this latter respect I would also like to acknowledge Guangyi Xu for providing me with research data to use in my project.

I would also like to acknowledge the contribution of the Engineering and Physical Sciences Research Council (EPSRC) for providing funding that enabled me to be a part of the Centre for Doctoral Training in Complex Particulate Products and Processes (CDT CP^3) and to undertake my project. Further to this, I am very grateful for the financial contributions of both Infineum UK and Syngenta UK.

Away from this research I would like to thank my close friends within the CDT CP^3, especially David Austin, Dewi Ballard, Jonathan White and Lewis Scott, who made the time during this project very enjoyable and created a working atmosphere in which I could relax, have fun and still work intensely on this project.

Perhaps most importantly, I would like to acknowledge my family and my partner. I would like to thank my family for pushing me in both academic and non-academic pursuits, providing me

with an environment in which to excel myself and giving me the balanced mind-set to not focus too heavily and stress over certain things, which has been invaluable to me during this project. You are a major contributor to everything I have achieved and will achieve in the future. To my partner, I am eternally grateful for so many things, but perhaps, with respect to this project, I am most grateful that you helped me to switch off and relax when I came home each day, you do not know how much this has helped me to achieve what I have in my PhD project.

Table of Contents

Abstract V

Acknowledgements VII

Contents IX

List of Figures XIII

List of Tables XVIII

Nomenclature XX

List Of Abbreviations XXIII

Chapter 1 Introduction 24

1.1 Research Context 25

1.2 Aims & Objectives 30

1.3 Delivery Plan 33

1.4 Project Management 35

1.5 Structure of Report 36

1.6 References 38

Chapter 2 Isothermal by design: An accelerated approach to the prediction of the crystallisability of slowly nucleating systems 39

2.1 Abstract 40

2.2 Introduction 40

2.3 Materials and Methods 43

2.3.1 Materials 45

2.3.2 Experimental procedure 45

2.3.3 Analysis of Nucleation Kinetics and Mechanism 47

2.4 Results and Discussion 48

2.4.1 Solubility analysis 48

2.4.2 Calorimetry - effect of antisolvent temperature 51

2.4.3 Compositions, Concentrations and Supersaturations 53

2.4.4 Nucleation Kinetics Analysis 57

2.5 Conclusions 61

2.5.1 Conclusions of this study....61
2.5.2 Future Work and Current Limitations....62
2.5.3 Potential for Transferring IbD Methodology to Industrial Scales....63
2.6 References....64
Chapter 3 Isothermal by Design: Comparison with an Established Isothermal Nucleation Kinetics Analysis Method....69
3.1 Abstract....70
3.2 Introduction....70
3.3 Materials and Methods....71
3.3.1 Materials....71
3.3.2 Experimental Procedure....71
3.3.3 Nucleation Kinetics Analysis....73
3.4 Results and Discussion....75
3.4.1 IbD Calorimetry Calibrations....75
3.4.2 Induction Time Measurements....76
3.4.3 Nucleation Kinetic Parameters....79
3.4.4 Advantages and Disadvantages of TJM and IbD....84
3.5 Conclusions....85
3.6 References....87
Chapter 4 Influence of Solution Chemistry on the Solubility, Crystallisability and Nucleation Behaviour of Eicosane in Toluene/Acetone Mixed-Solvents....89
4.1 Abstract....90
4.2 Introduction....90
4.3 Materials & Methods....92
4.3.1 Workflow....92
4.3.2 Materials....94
4.3.3 Experimental Procedure....94
4.3.4 Molecular Modelling....97
4.4 Results....100
4.4.1 Assessment of Solubility and Crystallisability....100

4.4.2 Analysis of the Solution Thermodynamics 106
4.4.3 Analysis of the Nucleation Kinetics 108
4.4.4 Compositional Trends 109
4.4.5 Intermolecular Grid-Search Modelling 110
4.5 Discussion 115
4.6 Conclusions 117
4.6.1 Future Work and Current Limitations 118
4.7 References 119
Chapter 5 Understanding and Designing Tailor-Made Additives for Controlling Nucleation: Case Study of p-Aminobenzoic Acid Crystallising from Ethanolic Solutions 123
5.1 Abstract 124
5.2 Introduction 124
5.3 Workflow, Materials & Methods 126
5.3.1 Material Properties & Bulk Synthon Characterisation 128
5.3.2 Additive Selection 128
5.3.3 In Silico Screening 128
5.3.4 Experimental Screening 130
5.4 Results & Discussion 132
5.4.1 Material Properties 132
5.4.2 Bulk Synthon Characterisation 132
5.4.3 Additive Selection 133
5.4.4 In Silico Screening 134
5.4.5 Experimental Screening 141
5.4.6 Mechanistic Understanding 143
5.5 Conclusions 146
5.6 References 149
Chapter 6 Influence of a Polymeric Additive on the Crystallisability and Nucleation Mechanism for the Model Fuel System of Eicosane Crystallising from Supersaturated Toluene Solutions 155
6.1 Abstract 156

6.2 Introduction 156
6.3 Materials & Methods 158
6.3.1 Materials 158
6.3.2 Experimental Procedure 158
6.4 Results & Discussion 161
6.4.1 Transmission Profiles 161
6.4.2 Characterisation of Crystallisability and Solubility 163
6.4.3 Analysis of Solution Thermodynamics 166
6.4.4 Analysis of Nucleation Mechanism 167
6.4.5 Assessment of the Nucleation Kinetics 170
6.5 Conclusions 171
6.6 References 172
Chapter 7 Conclusions & Future Work 175
7.1 Conclusions of this Work 176
7.1.1 Accelerated Nucleation Testing 176
7.1.2 Influence of Solution Structure on Nucleation from Solution 178
7.1.3 Effect of Tailor-Made Additives on Nucleation 179
7.1.4 Effect of a Polymeric Additive on Nucleation 180
7.2 Review of the Aims & Objectives 181
7.3 Suggested Future Work 184
7.3.1 IbD Non-aqueous System 184
7.3.2 Extrapolation of Induction Time Data 185
7.3.3 IbD Variable Flow 187
7.3.4 Numerical Solution of Crystallisation Kinetics Approach 188
7.4 Closing Remarks 190
7.5 References 190
Appendices 191

List of Figures

Figure 1.1 - Flat plate-like wax crystals formed in fuel and a blocked vehicle fuel filter as a result of wax crystal agglomeration[1].....28

Figure 2.1. Workflow detailing the steps required in order to perform the IbD approach for any system of study.....44

Figure 2.2. Solubility of pABA in EtOH/H_2O mixtures at different temperatures collected by dissolution studies. 50 °C (▼), 40 °C (▲), 30 °C (●) and 20 °C (■).....49

Figure 2.3. van't Hoff plot for pABA in EtOH/H_2O mixed solvent solutions. Dashed black line represents ideal solubility and solid lines represent experimental solubilities for different solvent compositions: 100 wt% EtOH (X), 90 wt% EtOH (|), 80 wt% EtOH (⬟), 70 wt% EtOH (★), 60 wt% EtOH (+), 50 wt% EtOH (►), 40 wt% EtOH (◄), 30 wt% EtOH (⧫), 20 wt% EtOH (▼), 10 wt% EtOH (▲), 100 wt% H_2O (●). a) plots for all compositions studied. b) Plot over a smaller range of molar solubility, showing more clearly the variation observed with EtOH solubility as a function of temperature. 50

Figure 2.4. Effect antisolvent temperature had on solutions of pABA in EtOH/H_2O mixed solvent held at constant temperature (24 °C). Effect of antisolvent temperature on 0.2 ml initial solution (⧫), 0.3 ml initial solution (▼), 0.5 ml initial solution (▲), 0.65 ml initial solution (●) and 0.8 ml initial solution (■) shown by the gradients of the linear relationships.51

Figure 2.5. Antisolvent temperature calibration for addition of water to pABA in 70:30 wt% EtOH/H_2O solution held at set temperatures [28 °C (⧫), 26 °C (▼), 24 °C (▲), 22 °C (●) and 20 °C (■)], in order to maintain solution temperatures. Temperature of the antisolvent is plotted against the initial amount of solution used. 52

Figure 2.6. Difference in induction time measurements for uncontrolled (■) and controlled (●) antisolvent temperature addition for a solution temperature of 22 °C. Error bars show standard deviation of repeats. Trend lines fitted for both data sets to highlight deviation. 53

Figure 2.7. Induction time vs. supersaturation for pABA in EtOH/H_2O mixture solutions, with error bars showing standard deviation of 16 repeats for each data point. a) Data obtained at a final solution concentration of 67.2 g pABA kg^{-1} solvent mixture at all temperatures, b) All concentrations and compositions at all temperatures (log scale used for y-axis). 55

Figure 2.8. Change in standard deviation of induction time measurements, over 16 repeats, as a function of supersaturation. 56

Figure 2.9. Induction time vs. supersaturation for single temperature and multiple composition solutions of pABA in EtOH/H_2O mixtures for solutions at 26 °C.....59

Figure 2.10. $\boldsymbol{r}*$ (solid objects) and $\boldsymbol{i}*$ (hollow objects) vs. supersaturation from data obtained at a final solution concentration of 34.4 g pABA kg^{-1} solvent mixture (■/□) and a final solution concentration of 67.2 g pABA kg^{-1} solvent mixture (●/○). Break applied to graph between 1.9 to 2.4.....60

Figure 3.1. Effect of antisolvent temperature upon solutions of pABA in EtOH/H_2O mixed solvent system held at constant temperature (24 °C). Effect of antisolvent temperature on 0.3 ml initial solution (green diamond), 0.5 ml initial solution (pink down-pointing triangle), 0.65 ml initial solution (blue up-pointing triangle) and 0.8 ml initial solution (red circle), shown by the gradients of the linear relationships. Dotted line shows solution temperature prior to antisolvent addition[1]. 75

Figure 3.2. Supersaturation vs. induction time data collected from pABA in EtOH solutions at concentration of 180 and 200 g kg^{-1} (red circles), pABA in water solutions at 6 and 180 g kg^{-1} (blue triangles) and IbD experiments over the full range of concentrations, compositions and supersaturations[1] (black squares). Standard deviations of repeats are displayed. $\boldsymbol{\tau}$ axis in log format. Inset shows data collected for 100 s $< \boldsymbol{\tau} <$ 16000, from 1.0 $< \boldsymbol{S} <$ 1.15. 78

Figure 3.3. Coefficient of variation calculated for the IbD experiments, as a function of induction time. Dashed line shows linear regression fitted to data. 78

Figure 3.4. Induction time data to determine linear slope values for calculation of effective interfacial tension from data obtained for pABA in water solution at 6 g kg^{-1} concentration. 79

Figure 3.5. Calculated values of effective interfacial tension from pABA in EtOH solutions at concentration of 180 and 200 g kg^{-1} (red circles)1[6], pABA in H_2O solutions at 6 and 180 g kg^{-1} (blue triangles) and IbD experiments over the full range of concentrations, compositions and levels of supersaturation (black squares)[1]. Dashed line shows an exponential fit to the data collected through IbD at mixed solvent compositions. 82

Figure 3.6. Induction time vs. supersaturation for single temperature and multiple composition solutions of pABA in EtOH/H_2O mixtures for solutions at 26 °C[1]. Inset highlights region of mechanism change, with dashed lines showing intersect of slope change, indicating where the HEN to HON mechanism change occurred with increasing supersaturation. 83

Figure 3.7. Critical nucleus radius (solid objects) and number of molecules within the critical nucleus (hollow objects) vs supersaturation from the data obtained through IbD and TJM. IbD data shown for 81.4 g kg^{-1} pABA in EtOH/H_2O 22:78 mol % solution (black square/black hollow square), TJM data for 200 g kg^{-1} pABA in EtOH solution (red circle/red hollow circle) and 6 g kg^{-1} pABA in H_2O solution (blue triangle/blue hollow triangle). 84

Figure 4.1. Methodological workflow incorporating crystallisation analysis with molecular modelling for enhancing process understanding.....93

Figure 4.2. Chemical structures of a) eicosane, b) toluene and c) acetone. 98

Figure 4.3. Spatial grid defined around target eicosane molecule for calculation of intermolecular interaction energy calculations; (a) view along b axis; (b) view along c axis. Grid points shown by green dot symbols. 98

Figure 4.4. Representative polythermal data: a) Temperature (black) and transmission (blue) profiles against the time as used for measuring determination of crystallisation and dissolution temperatures (Tc and $Tdiss$, respectively), for 850 g L^{-1} eicosane in toluene solution at cooling rate (q) of 1 ºC min^{-1}; Temperature turbidity plot of a solution highlighting the observation of on-set points for Tc and $Tdiss$; (c) Plots of Tc (black squares) and $Tdiss$ (red circles) as a function of q, with the corresponding best linear fits are also given, for 850 g L^{-1} eicosane in toluene solution; (d) Concentration vs. temperature plot highlighting the equilibrium MSZW between the solubility (red circles) and supersolubility (black squares) curves, for eicosane in toluene at all concentrations studied. 101

Figure 4.5. Solubility of eicosane in toluene/acetone mixtures at different temperatures: 10 °C (black squares), 12.5 °C (red circles), 15 °C (green upward-triangles), 17.5 °C (blue downward-triangles), 20 °C (cyan diamonds), 22.5 °C (pink hexagons) and 25 °C (purple stars). 102

Figure 4.6. van't Hoff plots for eicosane in toluene/acetone mixed solvent solutions. Dashed black line represents ideal solubility, and solid lines represent experimental solubilities for different solvent compositions: y = 0 (red circle), y = 0.14 (blue up-pointing triangle), y = 0.26 (pink down-pointing triangle), y = 0.38 (green diamond), y = 0.49 (navy left-pointing triangle), y = 0.59 (violet right-pointing triangle), y = 0.68 (purple hexagon), y = 0.77 (brown star), y = 0.85 (mustard pentagon), y = 0.93 (blue sphere), and y = 1 (turquoise cross).....106

Figure 4.7. Trends in values obtained over the compositional range studied for crystallisability, solution thermodynamics, nucleation mechanism and effective interfacial tension. a) average MSZW values over the concentration ranges studied; b) enthalpy of dissolution; c) enthalpy of mixing; d) average slope values obtained from $lnq\ vs.\ lnuc$ over the concentration ranges studied; e) average effective interfacial tension values calculated in the range of 0.59 < y < 0.93. Red dotted line in d) represents transition from IN (<3) to PN (>3).....110

Figure 4.8. Interaction energy fields of toluene (a and b) and acetone (c and d) probe molecules, with a central eicosane molecule. Toluene and acetone molecules show most negative interaction energy site. The green dots represent interaction locations of the probes, which passed the set energy filter cut-offs that are highlighted at the top left of images. ...112

Figure 4.9. Calculated intermolecular interaction energies for possible interaction types in eicosane in toluene/acetone solution, over the total interactions calculated. High-energy cut-off set at -0.5 kcal mol^{-1}. Coloured lines represent different intermolecular interactions: eicosane/eicosane (black solid line), eicosane/toluene (red dashed line), eicosane/acetone (blue dot-dash line), toluene/toluene (green dotted line), acetone/acetone (purple double line) and toluene/acetone (orange double dashed line).....112

Figure 4.10. Solvent clusters built using the intermolecular gird-search method around eicosane molecules, in different toluene/acetone ratios, with toluene molecule interactions determined first, followed by acetone molecules. a) 20:0; b) 15:5; c) 10:10; d) 5:15 and e) 0:20. i) and ii) represent different views of solvation clusters along and down the carbon backbone of eicosane, respectively.....113

Figure 5.1. Molecular structure of p-aminobenzoic acid.....126

Figure 5.2. Diagrammatic workflow outlining key steps involved in TMA screening and assessment.....127

Figure 5.3. pABA crystal structure. Left-hand side - pABA unit cell, showing carboxylic dimer -O-H···O- hydrogen bonding (synthon A) and -N-H···O- hydrogen bonding (synthon C). Inset shows dominant hydrogen bonding tetramer intermolecular interactions. Blue dashed lines show intermolecular hydrogen bonding. Right-hand side - pABA structural packing in the c-axis, showing π-π stacking of the cyclic rings of pABA (synthon B). Inset highlights π-π stacking. Taken from AMBNAC07 in Cambridge Structural Database[46].....133

Figure 5.4. Molecular structures of pABA and the selection of seven TMAs, which are closely related in their molecular structure to pABA.....134

Figure 5.5. Most favourable interactions of a) pABA:pABA, b) pABA:ANBA3, c) pABA:AMBA2 and d) pABA:AMBA3, calculated from intermolecular grid search. Hydrogen bonding shown by blue dashed lines. Additional functional groups of TMAs are highlighted in the dotted circles.....136

Figure 5.6. Interaction clusters of 5 pABA molecules around the calculated most energetically favourable (a) pABA:pABA, (b) pABA:ANBA3, (c) pABA:AMBA2 and (d) pABA:AMBA3 dimers. Dimers are shown with ball and stick style. pABA probe molecules are shown with capped stick style. Strongest pABA intermolecular interactions with each dimer are shown with pABA molecules with light green cyclic rings. Blue dashed lines represent intermolecular hydrogen bonding for strongest pABA interaction with dimer. 138

Figure 5.7. Fractional charges calculated for each atom of pABA, ANBA3, AMBA2 and AMBA3. 140

Figure 5.8. Visualisation of a) ANBA3, b) AMBA2 and c) AMBA3 within the pABA unit cell, based on the calculated strongest interaction geometry. i) View along b axis, ii) view along c axis. TMAs shown by thicker bonding molecules. Nitro and methoxy moieties would inhibit pABA molecules close to them from packing in the required pABA unit cell structure. Crystal structure taken from AMBNAC07 in CCDC[46]. 141

Figure 5.9. Floating column chart displaying Tc (bottom of columns) and $Tdiss$ (top of columns) values determined for pABA in ethanol solution with and without the presence of TMAs. Error bars show standard deviations of results. Numeric value within columns represents dynamic MSZW in °C. Values at bottom of plot are the strongest interaction energies for each dimer, calculated from the intermolecular grid search, in kcal mol^{-1}. 143

Figure 5.10. Plots for KBHR analysis for pABA:ANBA3 in ethanol solution at a concentration of 0.21 g g-1. Left-hand side - Plot of uc vs q in ln-ln coordinates for determination of nucleation mechanism. Right-hand side - Plot of uc vs lnq for determination of nucleation kinetic parameters. 146

Figure 6.1. Transmission profiles as a function of temperature for eicosane in toluene solution with no IA (left) and 0.5 wt% IA (right) at 250 g L^{-1}, with a heating cycle rate of 0.25 °C min^{-1}. 162

Figure 6.2. Transmission profiles as a function of solution temperature for eicosane in toluene solutions with 10wt% IA treat rate, at heating cycle rates of 0.25 °C min^{-1}, over the range of solution concentrations studied. a) 250 g L^{-1}. b) 350 g L^{-1}. c) 450 g L^{-1}. d) 550 g L^{-1}. Regions defined in a) demonstrate the phase transition processes that occurred for the 3-phase system: A is the crystallisation of IA, B is the crystallisation of eicosane, C is the dissolution of eicosane and D is the dissolution of IA. Inset in c) highlights increase in transmission prior to the onset of eicosane crystallisation. 163

Figure 6.3. a) Plots of eicosane Tc (red circles) and $Tdiss$ (black squares) as a function of cooling rate (q) with the corresponding best linear fits for eicosane in toluene solutions with 10wt% IA at 550 g L^{-1}. b) Supersolubility (Tc, l) as a function of IA treat rate for given solution concentrations of 250 g L^{-1} (black squares), 350 g L^{-1} (red circles), 450 g L^{-1} (blue triangles) and 550 g L^{-1} (magenta diamonds). Data is fitted with two linear regressions for each concentration. c) MSZW for eicosane in toluene solution with 3wt% IA loading. Solid lines represent solubility, with dashed lines representing supersolubility. Data is fitted with simple exponentials. d) Increase in average MSZW as a function of IA treat rate. ..165

Figure 6.4. van't Hoff plots for eicosane in toluene solution with different IA loadings. Dashed black line represents ideal solubility, and solid lines represent experimental solubilities for different IA treat rates: 0wt% (red circle), 0.1wt% (green up-pointing triangle), 0.5wt% (blue down-pointing triangle), 2wt% (cyan diamond), 3wt% (pink left-pointing triangle), 5wt% (yellow right-pointing triangle), 10wt% (brown hexagon).....167

Figure 6.5. $lnuc$ vs. lnq plots for eicosane crystallising from toluene solution without IA and with 3 wt% IA treat rate, over the range of solution concentrations studied. 250 g L^{-1} no IA (black squares), 350 g L^{-1} no IA (red circles), 450 g L^{-1} no IA (green upwards pointing triangles), 550 g L^{-1} no IA (blue downwards pointing triangles) 250 g L^{-1} 3 wt% IA (cyan diamonds), 350 g L^{-1} 3 wt% IA (pink left pointing triangles), 450 g L^{-1} 3 wt% IA (yellow right pointing triangles) and 550 g L^{-1} 3 wt% IA (brown hexagons). Legend on graph gives values of slope for linear regressions fitted, for each concentration.....168

Figure 7.1. Effect that the antisolvent (acetone) temperature had upon the final solution temperature. a) acetone added to different volumes of toluene that were held at 20 °C. b) Exothermic and endothermic mixing behaviour observed when toluene was held at different temperatures. Coloured points and linear regressions represent different thermal mixing trends. Coloured regions represent different enthalpic mixing behaviour (red – exothermic, blue- endothermic).

Figure 7.2. Induction time predictions from statistical models. a) Actual vs. predicted log induction times for all data using a non-linear regression model. b) Actual (observed) vs. predicted induction time using a multiple linear regression (MLR) model and a non-linear regression model (NL) for $S = 2.44$ and $T = 26$ °C.

Figure 7.3. Effect upon solution temperature of adding a second solvent at controlled rates to a solution maintained at a set temperature. a) Water at room temperature added to 40 ml ethanol held at 25 °C at varying addition rates of 10 (black line), 17.5 (red line) and 31 (blue line) ml min^{-1}. Grey lines on x-axis show the start of water addition. b) Propanol at room temperature added at a rate of 50 ml min^{-1} to 300 ml of water held at 30 °C, with a power compensation coil set at a 5 °C compensation.

Figure 7.4. Execution output and process flowsheet from gPROMS FormulatedProducts simulation using KBHR kinetic models for methyl stearate crystallisation from kerosene solution.

List of Tables

Table 2.1. Thermodynamic parameters together with linear dependence of Υ on x derived from solubility analysis for varying compositions of pABA in EtOH/H_2O solutions. 50

Table 2.2. Solution compositions, concentrations and supersaturations over the range of initial solution volumes selected. 'fr' denotes solutions where the required antisolvent temperature to maintain solution temperature was too low and would cause the water antisolvent to freeze. 'nc' denotes solutions that would not crystallise due to too low supersaturations. 'lv' denotes solutions that underwent the described experimental procedure but where the solution volume was too low for accurate induction time detection. 'Final Solution' refers to the solution after antisolvent addition. 54

Table 2.3. Kinetic parameters, γeff, $r*$ and $i*$, calculated from antisolvent induction time experiments as a function of solution concentration and composition over a range of supersaturations. 57

Table 3.1. Calculated values of effective interfacial tension and the CNT kinetic parameter, $lnkmd$, for all solutions studied through TJM and IbD, alongside induction times and supersaturation ranges for all solution compositions and concentrations. SE denotes standard error in results. Dashes indicate where data was not calculated due to a limited number of data points obtained for a given solution composition.....81

Table 4.1. Solubility (Te), supersolubility (Tc, l) and steady-state MSZW data of eicosane in toluene/acetone solvent mixture solutions, together with values of the slopes of the linear regressions of $lnuc$ vs. lnq plots for the range of solvent compositions studied, with the resultant nucleation mechanism determined from the "rule of three" KBHR analysis. The '' denotes a low correlation fitting and as such the analysis has a lower confidence value and may be a potentially unreliable result.....104*

Table 4.2. Thermodynamic parameters and activity coefficients (Υ) as a function of temperature calculated from van't Hoff analysis.....107

Table 4.3. Values of effective interfacial tension (γeff), critical nuclei radius ($r*$) and number of molecules within the critical nuclei ($i*$) for the PN systems. 108

Table 4.4. Solvation energies and intermolecular interaction energies between toluene and acetone molecules in the solvation shell for the solvation of eicosane at different toluene/acetone molecular ratios. 114

Table 5.1. Strongest interaction energies for pABA:pABA and pABA:TMA from intermolecular grid search along with Van der Waals, hydrogen bonding and electrostatic interaction contributions to total energy. 135

Table 5.2 Solvation energies of 20 ethanol molecules interacting with pABA:pABA and pABA:TMAs.....137

Table 5.3. Equilibrium crystallisation and dissolution temperatures determined over a range of concentrations as well as steady-state MSZWs for pABA and pABA:ANBA3 in ethanol solutions.....144

Table 5.4. Nucleation mechanisms determined from slope of uc vs q in ln-ln coordinates and calculated nucleation kinetic parameters obtained for pABA:ANBA3 in ethanol solutions from KBHR analysis. Data presented for pABA in ethanol solutions over a comparable concentration range, taken from Turner et al[49].....145

Table 6.1. Solubility (Te) and supersolubility (Tc, l) data of eicosane in toluene solution with different treat rates of IA, together with the calculated steady-state MSZW over four concentrations (200–500 g L^{-1} for 0.1 wt% IA solution and 250–550 g L^{-1} for all other solutions).....164

Table 6.2. Thermodynamic parameters and activity coefficients calculated from van't Hoff analysis of solubility data. 167

Table 6.3. Nucleation mechanisms determined from slopes of uc vs q in ln-ln coordinates for eicosane in toluene solution with different IA loadings.....169

Table 6.4. Nucleation kinetics parameters and nucleation rates of eicosane crystallising from toluene solution at different IA treat rates. The critical radius ($r*$) and number of molecules within the cirtical cluster ($i*$) are calculated at $uc = 0.004$, corresponding to the average value of uc for eicosane in toluene solution without IA, are displaye…171

Nomenclature

a – Dimensionless molecular latent heat of crystallisation (where specified)

a – Activity (where specified)

A - Pre-exponential parameter

a_e – Activity of a saturated solution

b – Dimensionless thermodynamic parameter

c – Solute concentration (m^{-3})

c^* – Solution equilibrium concentration (m^{-3})

c_s – Solute concentration at the crystal/solution interface (m^{-3})

c_0– Concentration of nucleation sites and/or instantaneously nucleated crystallites (m^{-3})

Δc_{max} – Maximum concentration difference (m^{-3})

d – Dimensionality of crystallite growth

D – Diffusivity (m^2s)

$\frac{dc^*}{dt}$ – Rate of solubility change with temperature ($m^{-3}K^{-1}$)

dG – Change in Gibbs energy ($J\ mol^{-1}$)

dS – Change in entropy ($J\ mol^{-1}K^{-1}$)

dU – Change in internal energy

dV – Change in volume (m^3)

$f_{e,s}$ – Molecular attachment frequency per growth site (s^{-1})

f^* – Frequency of monomer attachment to the nucleus (s^{-1})

fe^* – Frequency of monomer attachment to the nucleus at $\Delta\mu$=0 (s^{-1})

G – Growth rate (ms^{-1})

H – Enthalpy ($Jmol^{-1}$)

i – Subscript to refer to single component

i_c – Number of molecules within critical nucleus

J – Nucleation rate ($m^{-3}s^{-1}$)

k – Boltzmann constant (JK^{-1})

k_G – Growth Nucleation rate constant ($m^{-3}s^{-1}$)

k_J – Kinetic factor ($m^{-3}s^{-1}$)

$k_{m,t}$ – Mass transfer coefficient (ms^{-1})

k_n – Nucleus numerical shape factor

k_v – Crystallite growth shape factor (m^{3-d})

m, n – Nucleation growth exponents

N – Number of crystallites

N_{det} – Number of detectable crystallites

q – Cooling/heating rate (Ks^{-1})

q_o – Parameter in the u_c dependence

r – Nucleus radius (m)

r_c – Critical nucleus radius (m)

R – Ideal gas constant ($JK^{-1}mol^{-1}$)

S – Supersaturation ratio (where specified)

S – Entropy ($JK^{-1}mol^{-1}$) (where specified)

T – Solution Temperature (K)

T_0 – Temperature at which crystallites spontaneously nucleate (K)

T_c – Crystallisation temperature (K)

$T_{c,e}$ - Crystallisation temperature at the kinetic limit/Equilibrium crystallisation temperature (K)

T_{diss} – Dissolution temperature (K)

T_e – Equilibrium saturation (K)

T_f – Solute fusion temperature (K)

u – Relative undercooling

u_0 – Relative undercooling at moment of crystallisation for IN

u_c – Relative critical undercooling

v_o – Volume occupied by solute molecule in the crystal (m^3)

V – Volume of solution (m^3)

V_c – Total volume of crystallites (m^3)

V_N – Volume of single crystallite (m^3)

x – Mol fraction of solute in solution

x_i – Mol fraction of component i

x_{ideal} – Solute mol fraction in an ideal solution

x_{real} – Solute mol fraction in a real solution

Z – Number of molecules in a unit cell

z – Zeldovich factor (where specified)

z - mole fraction in solid phase (where specified)

α – Fraction of crystallised volume

α_{det} – detectable fraction of crystallised volume

γ – Interfacial surface energy between crystal and supersaturated solution

γ_{eff} – Effective interfacial tension (Jm^{-2})

Γ - Complete gamma function

σ - Relative supersaturation

ΔC_p – Molar hear capacity ($Jmol^{-1}K^{-1}$)

ΔG – Gibbs free energy ($Jmol^{-1}$)

ΔG^E – Total excess Gibbs free energy ($Jmol^{-1}$)

ΔG_v – Free energy change per unit volume associated with phase change (Jm^3)

ΔH^E – Enthalpy excess function ($Jmol^{-1}$)

ΔH_{diss} – Molar enthalpy of dissolution (J/mol)

ΔH_{fus} – Molar enthalpy of fusion ($Jmol^{-1}$)

ΔH_m – Molar enthalpy of melting ($Jmol^{-1}$)

ΔH_{mix} – Molar enthalpy of mixing ($Jmol^{-1}$)

ΔS_{diss} – Molar entropy of dissolution ($Jmol^{-1}K^{-1}$)

ΔS^E – Entropy excess function ($Jmol^{-1}K^{-1}$)

ΔS_{fus} – Molar entropy of fusion ($Jmol^{-1}K^{-1}$)

ΔS_m – Molar entropy of melting ($Jmol^{-1}K^{-1}$)

ΔS_{mix} – Molar entropy of mixing ($Jmol^{-1}K^{-1}$)

ΔT – Undercooling (K)

ΔT_c – Critical undercooling (K)

$\Delta\mu$ – Supersaturation in terms of chemical potential difference (J)

λ – Molecular latent heat of crystallisation (J)

τ – Induction time (s)

μ – Chemical potential (J)

Υ– Activity coefficient

φ – Activity factor

ω – Denotes a positive number

List Of Abbreviations

ACM – Acetaminophen

ATR-FTIR – Attenuated total reflection-Fourier transform infrared

API – Active pharmaceutical ingredient

BINOL – 1,1'-bi-2-naphthol

BZC – Benzocaine

CCAC – Combined cooling antisolvent crystallisation

CFI – Cold-flow improver

CNT – Classical Nucleation Theory

CSD – Crystal Size Distribution

C.S.D. – Cambridge Structural Database

DHA – 1,3-dihydroxyacetone

EAA – Ethylene/acrylic acid (15%) copolymer

HEN – Heterogeneous nucleation

HON – Homogeneous nucleation

IA – Commercially available cold-flow improver additive

IbD – Isothermal by Design

IN – Instantaneous nucleation

IPA – Isopropanol

KBHR – Kashchiev-Borissova-Hammond-Roberts approach

KJMA – Kolmogorov-Johnson-Mehl-Avrami approach

LOA – *L*-ornithine aspartate

MSZW – Metastable zone width

NPLIN - Nonphotochemical laser-induced nucleation

PABA – Para-aminobenzoic acid

PDMS – Poly-(N,N-dimethylacrylamide)

PETI – Predicting Efficacy Through Intermolecular Interactions

PN – Progressive nucleation

PO – Preferred orientation

PS – Polystyrene

PSD - Particle size distribution

rpm - Revolutions per minute

RIG - Rough interfacial growth

TJM – Temperature-jump isothermal method

XRD – X-ray diffraction

Chapter 1 Introduction

Summary: This chapter provides a background of the research and the report. Initially, the context of the research is discussed together with the aims and objectives and a delivery plan of how the objectives are met. Details of the project management are presented, with the structure of the report then laid out.

1.1 Research Context

Crystallisation is a key purification and isolation technique that is commonly utilised in numerous particle-processing industries. Although, for the most part, it is a desirable process that is vital in the production of drugs, pigments, agrochemicals, confectionary, and other fine chemicals, a number of products and/or processes are negatively impacted by its occurrence. Unwanted crystallisation of material within formulated products can have disastrous consequences on product efficacy, such as in fuels, agrochemicals and pharmaceuticals, where products may no longer work as effectively/at all after crystallisation of components. This is further exacerbated by the fact that unwanted crystallisation is not easily predicted, even when it is known that it will occur at some point within a products operational window/lifetime.

Crystallisation itself is a process by which randomly organised molecules, atoms or ions form a three-dimensional structure, known as a crystal and it is known to occur through a driving force of supersaturation (in a solution, this is when the solution phase contains more dissolved material than could be dissolved under normal conditions by the solvent). The crystallisation process encompasses two distinct transformational stages - Nucleation and Growth, whereby nucleation is the birth of a crystalline phase (nuclei) from a mother phase and growth is the development of a nuclei to a macroscopic crystal. Therefore, in studying unwanted crystallisation events, we must focus upon the process of nucleation, as this defines the primary phase transformation stage responsible for this phenomenon.

The study of nucleation, however, presents many challenges; not least, the fact that the process by which nucleation occurs is not yet fully understood. For over half a century nucleation has commonly been described through a theory known as classical nucleation theory (CNT). CNT proposes a mechanism whereby solute molecules cluster to form a structured nucleus and grow to a macroscopic crystal, overcoming one free energy barrier in the process. However, more recent research suggests that this may not be the case in a number of systems and in fact nucleation may take place through different mechanisms, such as where a prenucleation cluster that is not arranged in the crystal structure is first formed before a crystalline structure is generated, overcoming multiple free energy barriers to complete the nucleation stage. An improved knowledge of the mechanisms by which nucleation takes place could definitively aid the study of unwanted nucleation events, specifically with regards to stopping it from happening. In this, knowledge of the steps (type and number) required for a nuclei to form could aid in an understanding of how to theoretically hinder one or more of these steps, and in doing so, stop the process entirely.

Nevertheless, even if the nucleation process was better understood, its characterisation and predictability is still so difficult that we are, at this moment in time, unable to do either accurately. For instance, when trying to gain meaningful knowledge about the kinetics of nucleation, two main experimental methodologies are often employed – isothermal and polythermal crystallisation. The latter gradually increases the level of supersaturation in a system to the point that the driving force is large enough for the energy barrier to nucleation to be overcome, reaching the limit of what is termed the metastable zone, which signifies the kinetic limit of nucleation in a system. The former method relies on the time lag to nucleation upon the generation of a set level of supersaturation within a system, termed the induction time. However, neither method truly captures when nucleation actually occurs, due to the extremely small time and length scales associated with the process. To add to this, nucleation is stochastic, due to the probabilities involved in generating the required number and types of necessary intermolecular interactions within a crystallising system, meaning that even when repeating the exact same procedures for the most perfectly controlled systems, nucleation will not occur at the same time or place twice. Relate this to formulated products that are practically 'uncontrolled' due to storage and/or use in different environments depending upon the product type, such as storage of pharmaceuticals on shelves in pharmacies or fuels within parked road vehicles, and this difficulty is exaggerated. This means that unwanted nucleation events can occur across wide timescales, ranging from seconds to years, and given that products are often brought to market as rapidly as possible, it is not common practice to search for these unwanted events over long time scales.

One routinely used method that is employed in industry to determine a products stability in terms of its thermal shelf life is a thermal stability test. In this, a product is held at elevated temperatures for relatively short periods, with any changes in the product noted. An Arrhenius relationship is used to extrapolate and predict the thermal stability of the product over a much longer time period at temperatures where the product will be stored, such as room temperature. This procedure enables the prediction of events that occur over long periods of time from tests that can be performed in a reasonable timeframe associated with experimental testing. Unfortunately, unlike thermal stability, there is currently no routine way to rapidly test for unforeseen nucleation events that may occur over long timescales. Therefore, theoretically, the same predictive nature of thermal stability tests could be used in an accelerated nucleation methodology, making it possible to predict nucleation events over an extended period of time from tests that take a much shorter time that are feasible for routine laboratory testing. This could be achieved through the generation of high supersaturation conditions, drastically increasing the driving force to nucleation and as such, accelerating the nucleation process. Although this concept can be effectively described in a manner of a few sentences, the nuances

involved in such an endeavour make this an extremely challenging task. For instance, how can one routinely and effectively generate such high supersaturations in a system to alter the occurrence of nucleation events over vast orders of magnitude in timescales? How can one not only accurately characterise when nucleation might occur, but also the kinetics associated with the process? What techniques should be employed to achieve an accelerated testing procedure? With such a stochastic process, how could one accurately predict when a nucleation event might occur over long time periods? This concept of accelerated nucleation testing forms the major focus of this study and it is hoped that through the methodologies presented the problem of unwanted nucleation can be better addressed and predicted more routinely. However, when studying unwanted nucleation it is not enough to predict its occurrence, instead an understanding of how it can be eradicated in the first place must also be gained.

In order to eradicate unwanted nucleation from formulated products, it is necessary to fully understand how the nucleation process can be disrupted, both by compounds that can be added to a crystallising system and by changes in solution structure that may occur due to the range of compounds present in complex formulations, which commonly utilise mixed-solvents. This must be characterised at the molecular level in order to understand the fundamental interactions influencing the nucleation process. Although the experimental characterisation methods outlined above cannot do this themselves, these techniques can be coupled with molecular modelling tools to enable a holistic view of the nucleation process, from its kinetics to the types and orientations of intermolecular interactions necessary for its occurrence. Although numerous modelling methodologies have been developed to gain fundamental insight into molecular scale processes, a computationally inexpensive and effective method is desirable for routine industrial employment.

The ability to not only disrupt the nucleation process, but also to predict when it might happen has been a long-standing endeavour in both academic and industrial environments. Clearly then, in order to tackle this problem more thoroughly and fundamentally a high level of design is required, both in terms of the experimental and modelling procedures that can complement each other and in the design of new experimental procedures and set-ups that can better tackle these tasks.

Through the generation of an accelerated nucleation method and an improved knowledge of how the nucleation process can be disrupted, it is envisaged that a number of industries can be positively impacted. For example, in diesel fuels, long chain alkanes form large flat plate-like wax crystals at lower temperatures, which can aggregate together to form impermeable cakes that can block vehicular fuel filters, shown in Figure 1.1, reducing operating efficiency and

eventually resulting in a failure of operation. Currently, this problem is addressed by developing chemistries known as cold flow improver (CFI) additives, which are able to lower the temperature required for the wax components to nucleate (cloud point). However, this does not eradicate the issue of crystal formation, and as such, fuel efficiency is reduced at more extreme low temperatures and the risk of fuel filter blockages is still present. An ability to extend the operability of diesel fuel to lower temperatures through improved additive chemistries and more accurate prediction as to the efficacy of CFIs could provide substantial benefits to the fuels sector.

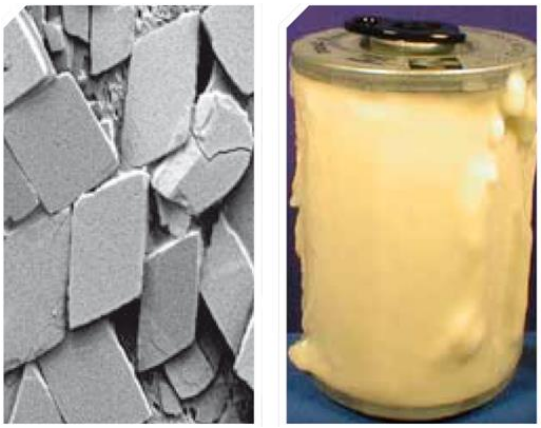


Figure 1.1 - Flat plate-like wax crystals formed in fuel and a blocked vehicle fuel filter as a result of wax crystal agglomeration[1].

Furthermore, in the agrochemical industry, almost all crop protection products contain organic molecules that crystallise readily at lower temperatures or due to metastable solution conditions, caused by highly concentrated formulations. This means that nucleation can occur relatively easily in these products, creating unwanted solids, as well as undesirable polymorphs, solvates and/or hydrates. These products are stored over long time periods, and are required to be in liquid form to enable spraying of them over large areas and to provide adequate cover over crops. Therefore, nucleation in these products is catastrophic as crystalline material can form during storage and sink to the bottom of the storage tank, creating a highly concentrated mostly solid base, unusable as crop protection and negatively impacting upon the spraying process, as demonstrated in Figure 1.2. Predicting formulation stability could be invaluable in both product development and knowledge of product storage capabilities.

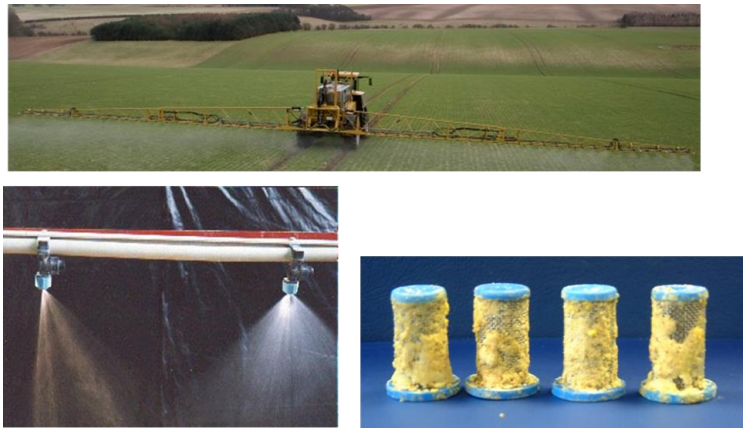


Figure 1.2. Unwanted nucleation events within crop protection products negatively impacting the spraying of the product over crops.

In the pharmaceutical industry, the increasing complexity of active pharmaceutical ingredients (APIs) means that more novel dosage forms are required to ensure drugs are both delivered safely to the right target area/s and have good bioavailability in order to be effective. This can often take the form of liquid or semi-solid dosage forms, where drugs are dissolved or suspended in solutions. However, this provides increased challenges with regards to unwanted nucleation events. Ritonavir, for example, is an antiviral Acquired Immunodeficiency Syndrome (AIDS) drug that had to be removed from the drugs market two years after release due to an unwanted nucleation event that altered its polymorphic form, shown in Figure 1.3, making it ineffective in the dosage form used at that time.

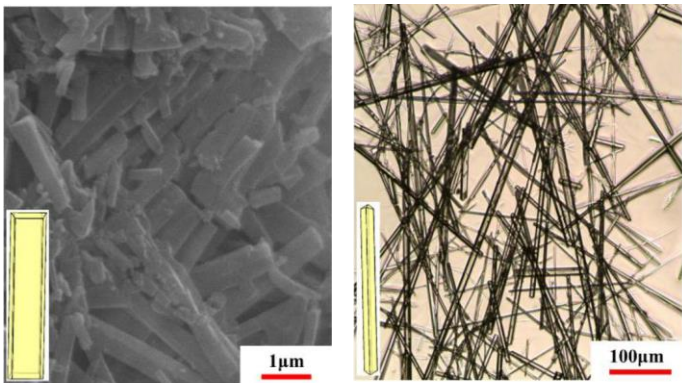


Figure 1.3. Images of Ritonavir crystals Form I (Left) and Form II (Right) crystallised from acetone solutions[2].

Overall, the overarching concepts that underpin this work, although extremely complex, provide an avenue for an indepth and novel research study that could provide beneficial research outputs in a number of areas. In order to outline the boundaries of this study, a set of aims and objectives must first be defined.

1.2 Aims & Objectives

The research question that underpins this thesis is:

Can unwanted nucleation events within solution environments be both predicted and fully inhibited?

This question is addressed through the following main objectives:

Objective #1. Design and develop experiments to generate high supersaturation conditions within solutions and, as such, drastically increase the rate of nucleation.

Objective #2. Develop a procedural workflow to aid in standardised accelerated nucleation testing and extrapolation of kinetics from high to low supersaturation conditions.

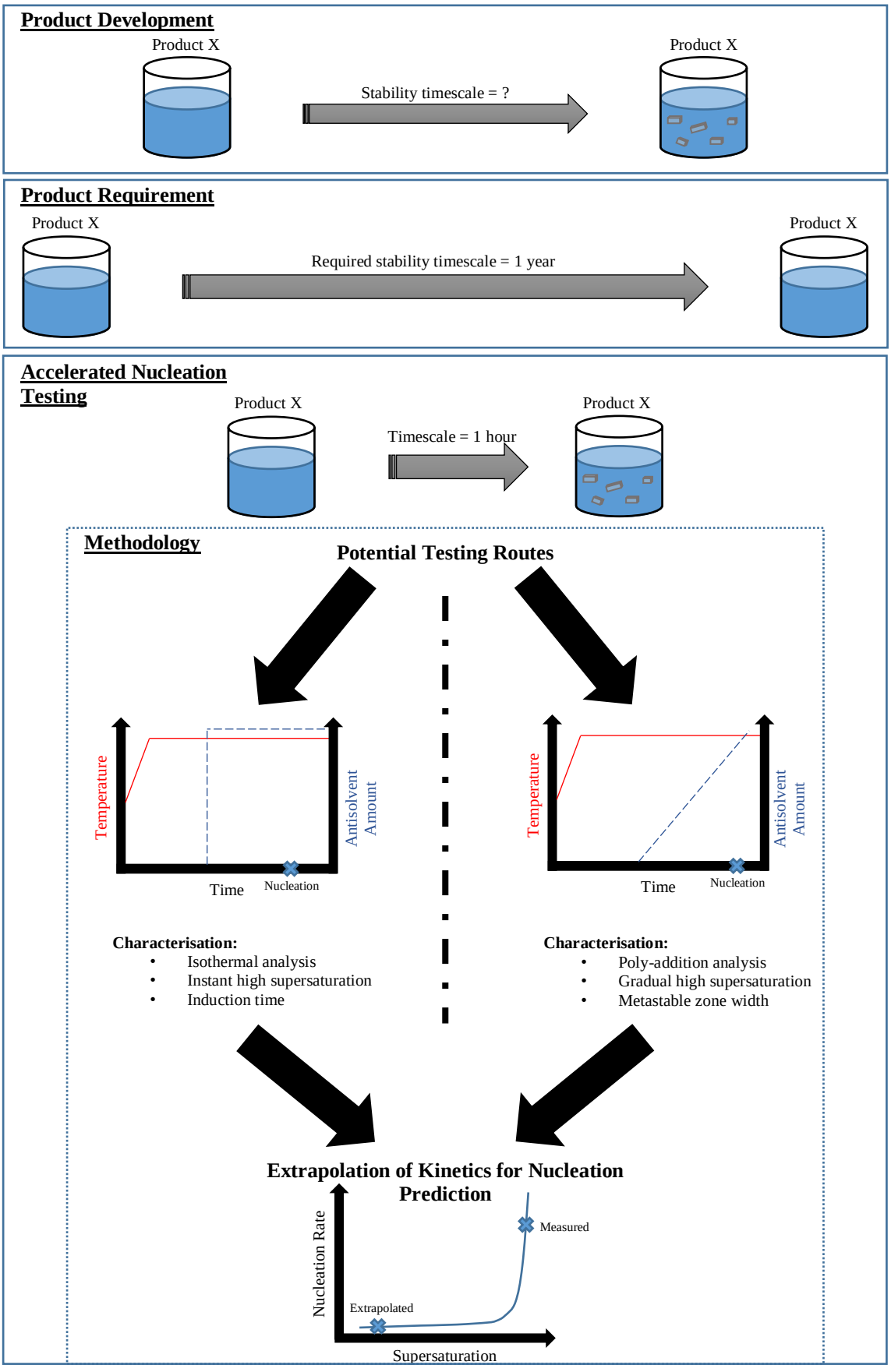
Objective #3. Determine how the types and relative strengths of intermolecular interactions within solutions can influence the nucleation process by altering solution structure.

Objective #4. Develop a procedure to aid in the understanding of how additives can inhibit nucleation on a molecular/atomic level.

Objective #5. Perform a case study on a commercially available cold-flow improver additive to determine its potential nucleation inhibition effect on a model compound.

Objective #6. Generate a numerical solution to the Kashchiev-Borissova-Hammond-Roberts kinetic analysis approach and link to the developed accelerated nucleation testing procedure.

In fully meeting these objectives, it is envisaged that a cyclic research and development system could be implemented to limit unwanted nucleation events in formulations. This is displayed schematically in Figure 1.4. In simple terms, an accelerated nucleation test could be employed during product development to predict the stability of a product. If the stability does not meet product requirements then an assessment of nucleation inhibition capabilities utilising additives and/or alterations in product compositions could be made to extend product stability. Reemploying the accelerated nucleation test could then provide vital information, not only as to the potential improved stability of the product, but also the effectiveness of the nucleation inhibition route taken. This information could then be utilised to aid in the future development of nucleation inhibition capabilities of similar products.


Product Development
Product X
Stability timescale = ?
Product X
Product Requirement
Product X
Required stability timescale = 1 year
Product X
Accelerated Nucleation Testing
Product X
Timescale = 1 hour
Product X
Methodology
Potential Testing Routes
Temperature
Antisolvent Amount
Time
Nucleation
Characterisation:
Isothermal analysis
Instant high supersaturation
Induction time
Temperature
Antisolvent Amount
Time
Nucleation
Characterisation:
Poly-addition analysis
Gradual high supersaturation
Metastable zone width
Extrapolation of Kinetics for Nucleation Prediction
Nucleation Rate
Measured
Extrapolated
Supersaturation

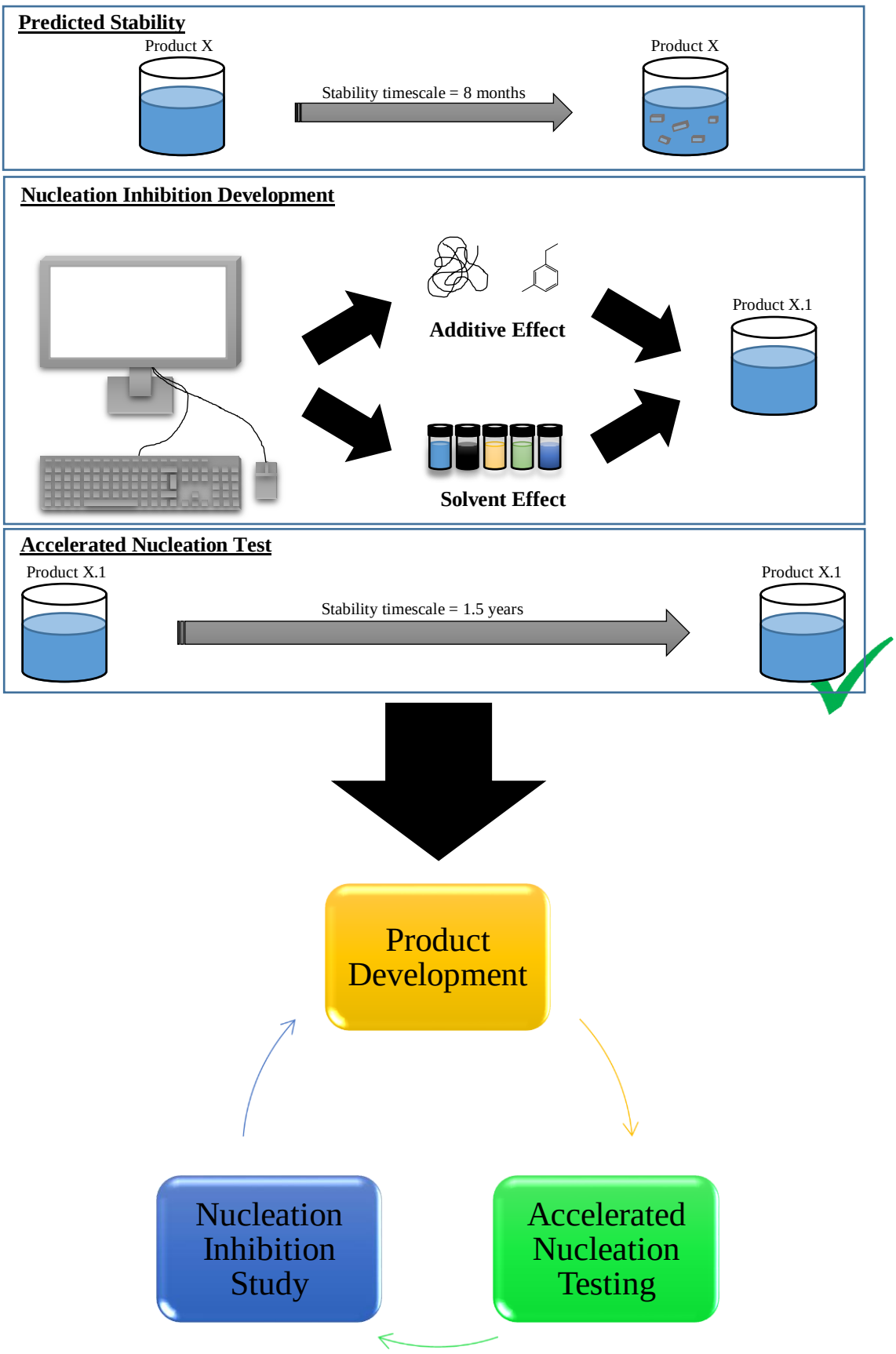


Figure 1.4. Schematic of underpinning project and methodological concepts.

1.3 Delivery Plan

In order to obtain results that address these objectives, two main system types are studied as part of this work, both hydrophilic and hydrophobic systems. These contrasting system types are selected in order to encompass the wide range of solution types present in industrial formulated products that may undergo unwanted nucleation events.

The hydrophilic systems studied utilise, as their major solute, p-aminobenzoic acid (pABA), within ethanolic and aqueous ethanolic solutions. pABA was chosen as the major crystallisation compound for these systems due to the large number of research studies focussing upon various aspects of its crystallisation behaviour, with knowledge of its fundamental nucleation behaviour from various solution environments already investigated. The hydrophobic systems studied focus upon the crystallisation of the long-chain alkane, eicosane, from toluene and mixed acetone/toluene solutions. Eicosane is representative of waxes present in diesel fuels that undergo unwanted nucleation events and its crystallisation behaviour is relatively well characterised.

As well as defining the systems studied to meet the proposed objectives, the potential methodologies that could be utilised must be assessed and selected. For example, there are numerous experimental methodologies that are able to generate high rates of nucleation within solution environments, including antisolvent, crash cooling, sono, gassing and substrate crystallisation. Literature focussing on each of these potential routes is reviewed in Appendix B. Although each of these methodologies are viable routes to potential accelerated nucleation testing, antisolvent crystallisation was selected for use in this work. In this, a solvent that the solute has a low solubility in (the antisolvent) is added to an already formed solution, lowering the overall solubility of the solvent and, as such, increasing the level of supersaturation. Depending upon the solution volumes studied, antisolvent crystallisation can be utilised in one of two ways, either by controlled addition of the antisolvent over time or, for low solution volumes enabling high mixing rates, addition of the antisolvent at one instant of time. This is highlighted in figure 1.4 as two potential routes for an accelerated testing method. Furthermore, the relatively simple procedure makes this readily applicable to both hydrophilic and hydrophobic systems. The flexibility, universal applicability and ease to which high supersaturations can be generated makes this an attractive method for accelerated nucleation testing.

Selection of polythermal and/or isothermal crystallisation methodologies must also be made to tackle each objective. Isothermal crystallisation is an attractive method for crystallisation

analysis, as it enables key nucleation parameters, including the rate of nucleation, to be determined. It could also be useful for an accelerated nucleation testing procedure as it can directly define the time at which a system can remain metastable prior to nucleation, effectively defining the stability timeframe of a formulated product. However, at solution volumes that are often utilised for 'high-throughput' crystallisation testing, which would be useful for an accelerated nucleation test to provide many results and repeats in a rapid manner, results obtained by this method can have high variability. In this, induction time measurements are known to range considerable for the same system studied in the exact same manner, providing some uncertainty in results. This behaviour is observed due to the stochastic nature of nucleation and the methodological concept utilised, in which one effectively 'waits' for a nucleation event to take place. In contrast, polythermal crystallisation somewhat overcomes this drawback through driving the process of nucleation forward by reaching the limit of metastability and, as such, is not as limited by the stochastic nature of nucleation. Most polythermal data analysis routes, however, are empirically based, limiting the fundamental knowledge that can be gained from these experiments. Nevertheless, one theoretically based analysis route is the Kashchiev-Borissova-Hammond-Roberts (KBHR) approach, which provides a viable route to understanding the nucleation kinetics and the route to nucleation of a crystallising system. However, currently the KBHR approach is analytically solved through the confinement of certain inequalities that limit its applicability at very high supersaturation environments, such as those that might be obtained during accelerated nucleation testing. Therefore, although it is currently an extremely useful method for 'standard' crystallisation analysis, it must be solved numerically for it to be applicable towards accelerated nucleation testing. The polythermal method utilised through this approach could potentially then be incorporated towards a poly-addition antisolvent concept, linking the supersaturation generation to the aforementioned controlled antisolvent addition method. The outlined methodologies are discussed in more detail in Appendix A. Both methodologies are utilised in this project with the isothermal technique adapted and used as part of the development of an accelerated nucleation procedure and the polythermal technique used for the assessment of solubility, crystallisability, solution thermodynamic and standard nucleation kinetic analysis.

A number of computational methods that enable the crystallisation to be investigated are also available to gain fundamental insight into how unwanted nucleation may be disrupted. One such method, which is used as part of this project, is grid-based molecular modelling. In this, a simulation is performed using rigid molecules that are placed within a defined grid-space, with the interactions between molecules calculated. This particular method has been utilised in numerous research studies to gain insight into the molecular scale processes that relate to crystallisation behaviour. It is also an attractive method as it can be used on standard computer

equipment, without the need for high performance computing that is often not readily available to researchers in industrial sectors.

Overall, the combination of different crystallisation systems, different experimental methodologies and a flexible and readily available molecular modelling tool provides an ideal platform for delivering the objectives put forth for this project.

1.4 Project Management

This study has been carried out within the Centre for Doctoral Training in Complex Particulate Products and Processes (CDT CP^3), which is collaboratively funded by the Engineering and Physical Sciences Research Council (EPSRC), industry and the University of Leeds. The industrial sponsorship of this project is provided mostly by Infineum UK Ltd and partly by Syngenta UK Ltd.

The work detailed in this report is completed under the main supervision of Professor Kevin J. Roberts and the co-supervision of Dr Nicholas J. Warren, at the University of Leeds. Supervision is also provided by Professor Pete Dowding and Dr Ruth Downie, at Infineum UK Ltd. and Dr Neil George, at Syngenta UK.

Quarterly meetings with Infineum UK Ltd. and separately with Syngenta UK Ltd. supervisors were carried out to present the work conducted and the progress made on achieving the outlined objectives. The directions of the work and impact of research findings towards industrial operations were discussed.

Collaborations with other researchers in my research group were formed to utilise individual expertise in various crystallisation research areas. Guangyi Xu provided solubility data used for the development of an accelerated nucleation methodology. Dr Thomas D. Turner provided induction time data on two crystallisation systems to compare with the developed accelerated nucleation data, whilst also helping with the comparative analysis. Dr Ian Rosbottom provided the atomic charges for molecular modelling studies used as part of this research project and helped in the design and analysis of modelling results. Finally, Dr Diana M. Camacho Corzo provided ideal solubility data for eicosane. These collaborations were instrumental in achieving the research outputs from this work.

This project, and its philosophical outlook, was directly and drastically impacted by the COVID-19 pandemic, which meant that some of the research plans that were underway prior

to the pandemic were not able to be completed and, as such, not all of the aforementioned objectives are met. This is more thoroughly discussed in the accompanying COVID-19 statement document and outlined within the conclusions and future work section of this thesis.

1.5 Structure of Report

Following this chapter:

Chapter 2 presents the publication outlining the developed accelerated nucleation methodology that enables the generation of high supersaturations that could enable predictive nucleation testing. A workflow is proposed to aid future studies in this area.

Chapter 3 presents the publication that compares results obtained from the developed accelerated nucleation methodology with previous work that utilised an established nucleation assessment methodology. A critical analysis of the methods is presented and insight into the impact of mixed-solvents is obtained. Both chapters 2 and 3 focus upon objectives 1 and 2 outlined above, with the work in chapter 3 having some relevance to objective 3.

Chapter 4 presents the publication that focusses on the effect of solution structure on the nucleation process when crystallising from mixed-solvent solutions. A workflow is developed to aid future studies in this area. This work concentrates heavily on objective 3 of this study.

Chapter 5 presents the publication focussing on the potential of structurally related molecules to inhibit nucleation from solution. A workflow is developed to aid future studies in this area. Objective 4 is the target of the research presented in this chapter.

Chapter 6 presents the publication that researchers the impact of a commercially available CFI on inhibiting nucleation at different concentrations within solution is examined. This work tackles the proposed objective 5 of this study.

Chapter 7 concludes this work and provides a critical review of research outcomes from this doctoral study. Detailed information outlining future work that has been started and could be further developed to build upon the findings of this study is given.

A schematic description of the thesis content is presented in Figure 1.5.

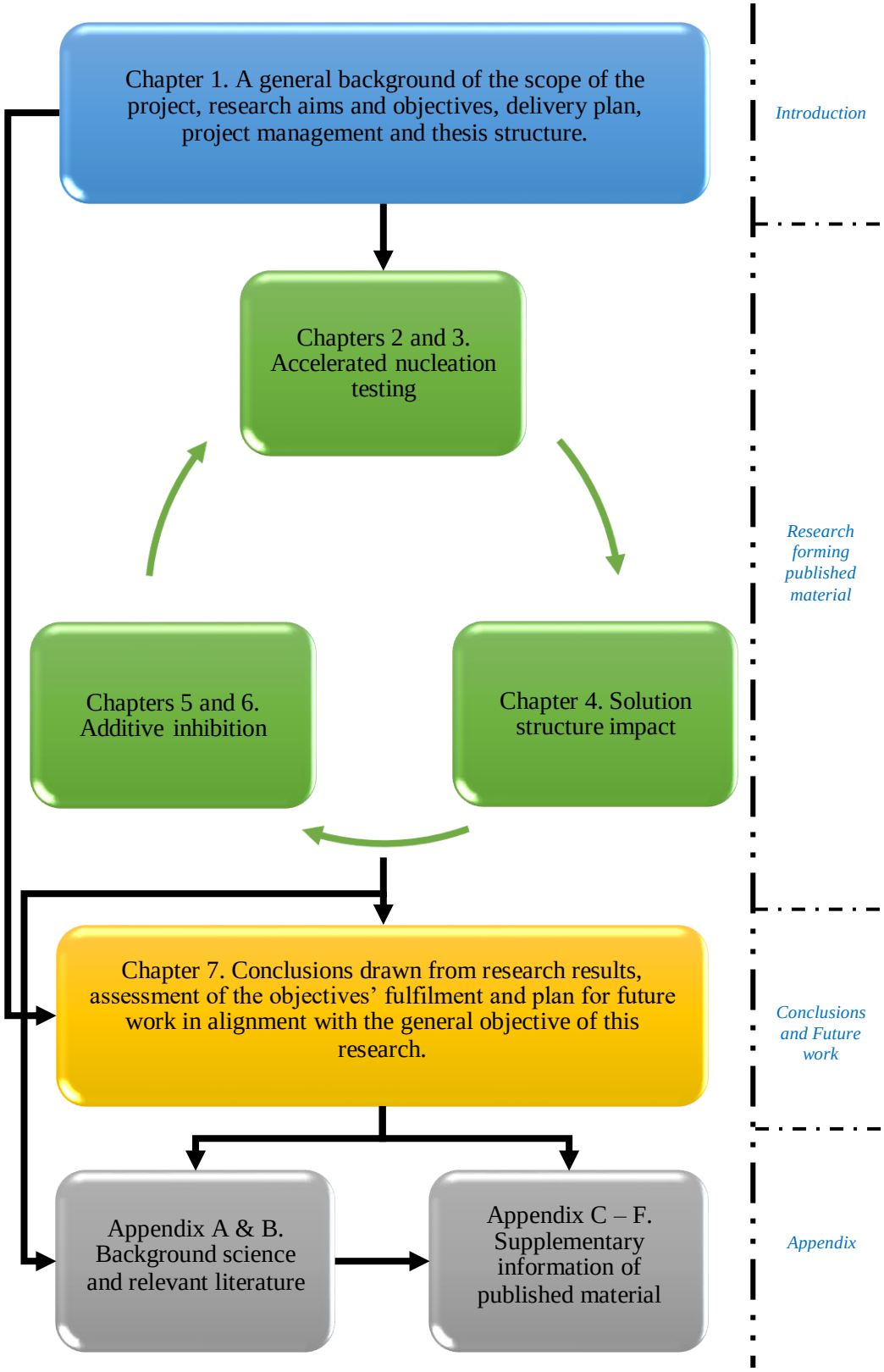


Figure 1.5 – Schematic description of the route map for the thesis.

1.6 References

1. ATC - Technical Committee of Petroleum Additive Manufacturers in Europe. Fuel Additives: Use and Benefits. 68 (2013).
2. Wang, C. *et al.* Molecular, Solid-State and Surface Structures of the Conformational Polymorphic Forms of Ritonavir in Relation to their Physicochemical Properties. *Pharm. Res.* **38**, 971–990 (2021).

Chapter 2 Isothermal by design: An accelerated approach to the prediction of the crystallisability of slowly nucleating systems

2.1 Abstract

A route to the accelerated nucleation of α-para-aminobenzoic acid (pABA) in ethanol/water (EtOH/H_2O) mixed solvent solutions, using antisolvent crystallisation, is presented. An '*isothermal by design*' approach is adopted, whereby the exothermic enthalpy of mixing associated with antisolvent addition is offset by the control of the temperature of the antisolvent added. Induction times (τ) are found to be reduced by over three orders of magnitude using this methodology, consistent with the use of this approach as a nucleation acceleration technique. Calculation of the nucleation kinetic parameters for a range of solution concentrations, compositions and supersaturations (S) reveal that effective interfacial tensions (γ_{eff}) varies from 8.4 to 2.3 mJ m^{-2} from solutions in H_2O solvent and EtOH solvent, respectively, in line with the trend in solubility. The critical nucleus radius (r^*) is calculated to decrease from 1.98 nm to 0.40 nm associated with a decrease in the number of molecules in the critical nucleus (i^*) from 196 to 2 molecules. A change in nucleation mechanism from heterogeneous nucleation (HEN) to homogeneous nucleation (HON) is observed to take place at $S \approx 1.5$. Limitations, particularly with focus towards larger scale operation, are highlighted together with potential solutions to overcome such aspects.

2.2 Introduction

Crystallisation is a highly energy-efficient key unit operation for isolation and purification within the manufacture of drugs, pigments, agrochemicals, confectionary and other fine chemicals[1]. Nevertheless, crystallisation can also be an unwanted phenomenon, e.g. in cases such as fuels operating in cold weather or drugs stabilised in highly concentrated liquid-formulations[2].

The driving force for crystallisation is supersaturation and this process encompasses two distinct transformational stages - nucleation and growth[3]. In solution crystallisation nucleation signifies the structural pathway by which solute molecules cluster together to form 3-D nuclei, which when meet a critical cluster size, termed the critical nucleus radius (r^*), with a defined number of molecules in the critical nucleus (i^*), growth is favoured.

Nucleation can be divided into two categories: heterogeneous (HEN) and homogeneous (HON) nucleation. HEN is caused when sites, usually suspended particles or impurities in the solution, provide a surface for nucleation, whereas HON describes spontaneous nucleation[4]. Nucleation behaviour can be modelled by classical nucleation theory (CNT), enabling the expression of the rate at which nucleation occurs (J) in an Arrhenius reaction rate equation:[3]

$$J = A \exp\left[-\frac{16\pi\gamma^3 {v_0}^2}{3k^3T^3(ln\,S)^2}\right] \quad 2.1$$

Which indicates that there are three main contributors to the rate of nucleation: temperature (T), degree of molar supersaturation (S) and interfacial tension (γ).[3] Further parameters in the equation include the pre-exponential factor, A, the volume occupied by a solute molecule in a crystal, v_0 and the Boltzmann constant, k.

Nucleation can occur in an infinitesimally small-time frame or it can take a period of years. This uncertainty means that tests are currently performed to screen crystalline products, which might undergo nucleation events with significant impact upon product performance, such as polymorphic screening[5], which includes solution crystallisation using a vast array of solvents as well as relatively high supersaturation conditions. However, these tests cannot, as yet, predict if/when a nucleation event may take place over an extended period of time, which would constitute a 'slowly nucleating system', due to the timescale of a nucleation event being longer than could be routinely tested under current realistic experimental timeframes in both academic and industrial settings. There are a number of examples of slowly nucleating systems, including: citric acid in water[6], fats[7], conversion of diamond to graphite, drug products[8], etc. If tests could be implemented to predict this, then perhaps steps might be taken to mitigate an unforeseen nucleation event, whether through nucleation inhibition[9] or by formulating a different solid form[10].

In chemical stability studies, accelerated approaches have been used in order to understand and hence predict properties, such as stability or reactivity, etc., through the application of elevated thermodynamic conditions. In this, products are held at relatively high temperatures for a short period to emulate the effect of storage at room temperature for an extended period[11]. In a similar manner, an accelerated methodology could be employed to predict nucleation events of slowly nucleating systems, involving the process of increasing the rate of nucleation through solution crystallisation at high supersaturations. Numerous avenues exist in which to try and achieve this, such as antisolvent crystallisation (also known as drown out crystallisation)[12–14], crash cooling crystallisation[15], sono[16–18] and/or gassing[19,20] crystallisation, or substrate crystallisation[21–23]. Each one of these techniques produce a higher nucleation rate than could perhaps be achieved through standard crystallisation processes, such as cooling, isothermal or evaporative crystallisation processes. Although each technique has different intricacies related to various methodological aspects, antisolvent crystallisation has been shown to yield effective high supersaturation results with relatively ease[5,12]. Therefore, it is the methodology that was undertaken during this research study.

In antisolvent crystallisation, two completely miscible solvents, each with substantial difference in the solubility for the solute, are used. The solute is crystallised by isothermally adding the low solubility solvent (antisolvent) to a concentrated solution of the other, with the difference in solubility increasing the solution supersaturation and as such driving the crystallisation process. Antisolvent crystallisation has been studied extensively with different research focus on the effect it has upon certain crystallisation systems, such as different addition flow rates[24], solvent composition[25], polymorphism[26], crystal size distribution (CSD)[27], antisolvent control[28], combined antisolvent and cooling (CCAC)[29] and antisolvent in continuous crystallisers[30]. Although this process has been well studied, a simple methodology to apply this approach to screen potential crystallising systems and measure their kinetics has not, as of yet, been proposed.

A significant problem with performing antisolvent crystallisations for isothermal nucleation kinetic analysis, however, is that when a second solvent is added to a solution, there is usually an exothermic enthalpy of mixing, which can cause considerable increases in the overall solution temperature. Such variations in solution temperature can make it quite challenging to derive meaningful nucleation kinetics from the analysis of such data. This is particularly problematic for the case of crystallisation at relatively high solution supersaturations, where crystallisation occurs quite rapidly, and also where the enthalpy of mixing is much higher due to a greater amount of added antisolvent.

Due to the dynamics of heat transfer, regulation of reactor temperature is not really a feasible option for process scale reactions given the difficulties associated with homogeneity of solution temperatures in large scale vessels, especially with fast changes in solution temperature, given the conductive heating control of reactor jackets[2,31–34]. An alternative approach is to offset the temperature of the antisolvent being added to the solution in a manner as to affect a heat balance with the enthalpy of mixing, hence ensuring both isothermal conditions and high supersaturations. This approach is described through the nomenclature – 'isothermal by design' (IbD). The IbD concept is demonstrated in this paper through a study of the accelerated nucleation of α-p-aminobenzoic acid (pABA) from aqueous ethanol solution, through an aqueous antisolvent addition. In such an experiment, the time to crystallise after antisolvent addition, the induction time (τ), can be measured to determine how quickly nucleation occurred. pABA in aqueous ethanol solution with aqueous antisolvent was chosen for this study due to the large amount of work carried out on pABA in this research group providing data on key nucleation parameters and solubility effects to compare the current methodology against[35–37], previous studies have determined that the metastable zone width (MSZW) of pABA was

relatively large in EtOH solvent and as such it could be used as a model system for determination of a possible nucleation acceleration methodology and it represents a model pharmaceutical compound and solvent system. A good review of the crystallisation science of pABA is described in a previous study[35].

The structure of the paper is as follows:
After this introduction, the methodology workflow is presented, followed by results and discussion.

2.3 Materials and Methods

A workflow detailing the steps required for the IbD approach for any system of study is given in Figure 2.1.

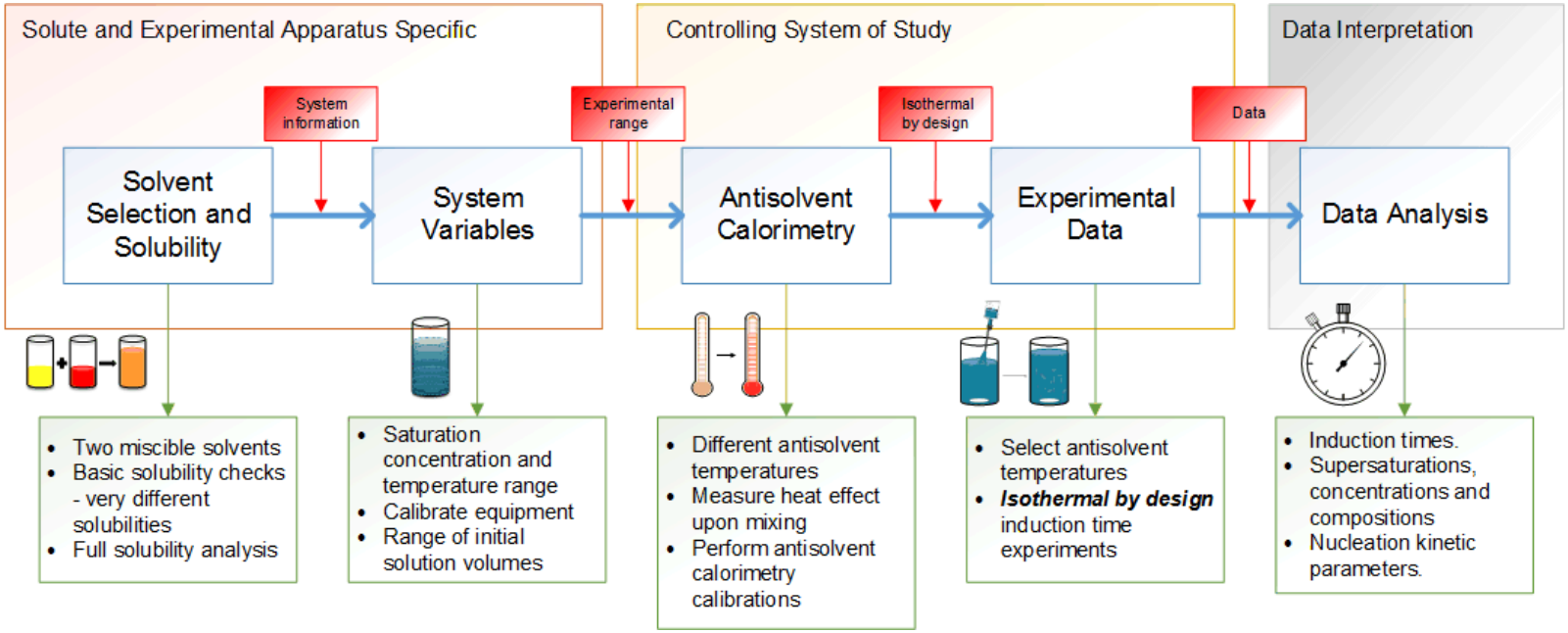


Figure 2.1. Workflow detailing the steps required in order to perform the IbD approach for any system of study

2.3.1 Materials

p-Aminobenzoic acid (99% pure) was supplied by Alfa Aesar, ethanol absolute (≥99.8% pure) was supplied by VWR and deionised water was sourced on site at the University of Leeds.

2.3.2 Experimental procedure

All the crystallisation and dissolution experiments were carried out using the Technobis Crystal 16® system[38] , which records transmission data as a function of the temperature and time. A temperature calibration of the system was performed to ensure correct temperature measurements were both taken and set under the experimental procedures undertaken.

Solubility of pABA in EtOH/H_2O mixed solutions was determined prior to antisolvent addition experiments. Solutions were prepared at a minimum of four solution concentrations, with the concentrations used dependent upon the solvent composition. Eleven solvent compositions ranging in 10 wt% increments of EtOH from pure EtOH to pure H_2O were used. Solutions were weighed on a balance with ±0.1 mg accuracy and heated to 333 K at 300 rpm for 1 hour to ensure total homogenisation of the solution. 1 ml of solution was then transferred to 1.5ml disposable glass vials for use in the experimental apparatus, which contained 7 mm x 2 mm magnetic stirrers, using a Fisherbrand 100-1000 µl micropipette with pre-heated pipette tips (30 °C) to prevent unwanted crystallisation.

The 1 ml solutions were subject to different cooling and heating cycles between 60 °C and 5 °C at set rates (q; where q = 0.3, 0.5, 0.7 and 1 °C min^{-1}), while stirring at 600 rpm. Crystallisation (T_c) and dissolution (T_{diss}) temperatures as well as crystallisation temperatures at the kinetic limit ($T_{c,l}$) and equilibrium saturation temperatures (T_e) were determined from transmission data, with the methodology undertaken to determine each of these parameters described in previous literature[39].

A van't Hoff analysis was performed from the obtained solubility data to determine how the system of study deviated from ideality, with the ideal solubility of pABA obtained from previous literature[36], based upon the Hildebrand equation (Equation 2.2). Activity coefficients (Υ) and enthalpy (ΔH_{diss}) and entropy (ΔS_{diss}) of dissolution were calculated based on the following equations, which have been derived in previous literature[39]:

$$\ln(x_{ideal}) = \frac{\Delta H_{fus}}{R}\left[\frac{1}{T} - \frac{1}{T_m}\right] \qquad 2.2$$

$$\Upsilon = \frac{x_{ideal}}{x} \quad 2.3$$

$$\ln(x) = -\frac{\Delta H_{diss}}{RT} + \frac{\Delta S_{diss}}{R} \quad 2.4$$

Where x_{ideal} is the solution concentration, x is the experimentally measured molar solubility, ΔH_{fus} is the enthalpy of fusion, R is the ideal gas constant, T is the temperature and T_m is the melting temperature.

For antisolvent calorimetry experiments, all solutions were prepared to ensure a saturation temperature of 20 °C for a mixed solvent solution of 70 wt% EtOH/30 wt% H_2O EtOH/H_2O and pABA. This temperature was chosen at it was low enough to ensure minimal solvent evaporation during the experiments. The solvent composition was selected due to solubility studies highlighting that small additions of H_2O to pABA in EtOH solution increased solubility, whereas over the temperature range used, any addition of H_2O to a 70 wt% EtOH/30 wt% H_2O composition only decreased solubility, whilst providing a large range of solvent compositions to be examined in the performed experiments. Solution volumes used ranged from 0.80 ml to 0.20 ml, in 0.05 ml increments, with all solution volumes made up to 1 ml after antisolvent addition.

Calibrations based upon solution calorimetry were performed, to ensure an IbD approach, with 5 initial volumes selected for the calibration at a selected temperature (ranging from 20 °C to 28 °C in 2 °C increments), with four different antisolvent temperatures selected. Solutions were held at constant temperature, stirring at 900 rpm, with the antisolvent held at constant temperature, stirring at 700 rpm. The calibrations were performed by placing a digital thermometer into the solution vials and then withdrawing the full antisolvent volume with a 1 ml syringe with attached needle, and transferring the contents into the solution vial rapidly, inducing high mixing. The speed of addition meant that the antisolvent was added almost instantaneously, leading to this procedure being described as 'instant addition'. The temperature of the solution was recorded after each addition by taking the value of the highest recorded temperature on the digital thermometer, within 1 second after antisolvent addition. Each calibration was repeated four times. Plots of selected antisolvent temperatures against the temperature of solutions after antisolvent addition were made and linear regressions were plotted with extrapolations to the desired solution temperature indicating the required antisolvent temperature to maintain solution temperature upon addition. This was then used to determine which antisolvent temperature should be used for each induction time experiment at that temperature. This was subsequently tested to ensure that the calibrations were accurate and that the solution temperatures were maintained upon addition of the antisolvent at the

determined calibration temperatures. It was observed that deviations in solution temperature upon addition of H_2O, over a range of four repeats, were at most ± 0.2 °C, with solutions quickly returning to set temperatures in a manner of a few seconds. Therefore, this effect was deemed to be negligible.

After the calorimetry calibrations were completed, the induction time experiments were performed. The same procedure was undertaken as described for the calibrations leading to an 'instant addition' methodology, however, all selected solution volumes were used, antisolvent temperatures were selected based upon the calibrations and no digital thermometer was placed in the vials, ensuring no effect on nucleation by introducing another surface on which to crystallise upon. Sixteen repeats were performed for each initial solution volume used at each selected temperature. The induction time to nucleation was determined from the collected transmission data.

The isothermal transmittance data was used to calculate the time between when the antisolvent was added to the vials and when nucleation had occurred, giving the induction time. The point at which antisolvent was added was also determined by the transmission data. This process is described in Appendix C, along with a more detailed description of the experimental procedures undertaken.

2.3.3 Analysis of Nucleation Kinetics and Mechanism

Molar supersaturations for each solution were calculated according to:

$$S = \frac{c}{c^*} \tag{2.5}$$

Where c is the absolute solute concentration and c^* is the saturation concentration.

The rate of nucleation was taken to be related to the induction time obtained from the experiments, under the relationship described through the equation:[3]

$$\tau \propto J^{-1} \tag{2.6}$$

The induction time data (τ as a function of S) were analysed using classical nucleation theory (CNT)[4,40], according to:

$$ln\left\{\tau[S(S-1)^{md}]^{\frac{1}{1+md}}\right\} = \ln k_{md} + \frac{B}{[(1+md)(kT\ln S)^2]} \tag{2.7}$$

$$k_{md} = \left[\frac{(1+md)\alpha_{det}}{k_v z f_e^* c_s d_0^d f_{e,s}^{md}}\right]^{\frac{1}{(1+md)}} \tag{2.8}$$

$$B = \frac{16\pi v_0^2 \gamma_{eff}^3}{3kT} \quad 2.9$$

Where m is the crystallite growth exponent, with $m = 1$ for pABA[35], d is related to the dimensionality of crystal growth, with $d = 1$ for pABA[35], α_{det} is the fraction of detectable crystallised volume, k_v is the crystallite growth shape factor, z is the Zeldovich factor, f_e^* is the frequency of monomer attachment to the nucleus at $\Delta\mu = 0$, c_s is the solution concentration at crystal solution interface, d_0 is the molecular diameter $\approx \left(\frac{6v_o}{\pi}\right)^{1/3}$, $f_{e,s}$ is the frequency of molecular attachment per growth site at $\Delta\mu = 0$, crystal and γ_{eff} is the effective interfacial tension.

A derivation of Equation 2.7 is given in a previous research article[41].

$ln\left\{\tau[S(S-1)^{md}]^{\frac{1}{1+md}}\right\}$ was plotted as a function of $\frac{1}{T^3(\ln S)^2}$ and a linear regression was fitted through the data, with the slope (SL_{lin}) equating to $\frac{16\pi v_0^2 \gamma_{eff}^3}{3(1+md)k^3}$. This enabled calculation of the effective interfacial tension. From this the critical nucleus radius (r^*) and the number of molecules in the critical nucleus (i^*) was calculated:

$$r^* = \frac{2\gamma_{eff} v_0}{kT ln\, S} \quad 2.10$$

$$i^* = \frac{4\pi {r^*}^3}{3v_0} \quad 2.11$$

Plots of $(\log S)^{-2}$ vs. $\log \tau$ were constructed to determine if a nucleation mechanism change occurred during the nucleation at higher supersaturations, given that:

$$\log \tau \propto \left[\frac{{\gamma_{eff}}^3}{T^3(\log S)^2}\right] \quad 2.12$$

Large increases in the linear fit slopes would suggest a change from HEN, at lower supersaturations, to HON, at higher supersaturations[3].

2.4 Results and Discussion

2.4.1 Solubility analysis

Small additions of H_2O to pure EtOH solutions were seen to increase pABA solubility, followed by subsequent decreasing solubility after further addition (Figure 2.2). This effect has been noted in previous research performed by Rosbottom et al.[37] for pABA in mixed

EtOH/Nitromethane (NMe) solutions. The effect is temperature dependent, with higher temperatures creating a more dramatic increase in solubility and at lower temperatures the increasing solubility with H_2O addition does not occur and the solubility of the system is highest in pure EtOH.

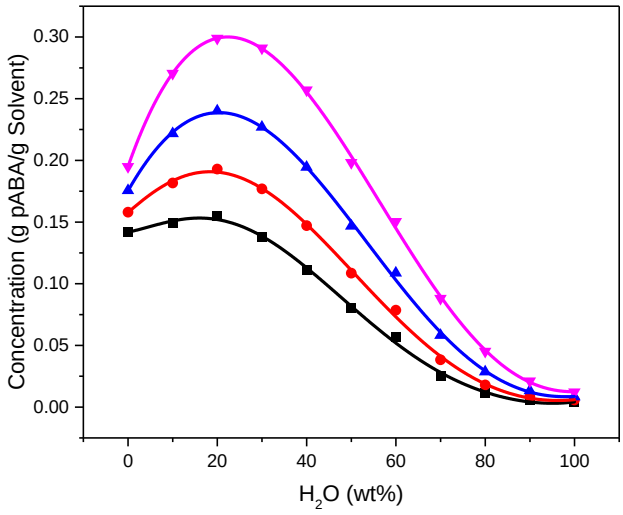


Figure 2.2. Solubility of pABA in EtOH/H_2O mixtures at different temperatures collected by dissolution studies. 50 °C (▼), 40 °C (▲), 30 °C (●) and 20 °C (■).

van't Hoff analysis provides information on the interactions between the solute and solvent molecules. In an ideal solution, the interactions are all the same, but a positive deviation from ideality indicates solute-solvent interactions are the strongest, whereas negative deviations suggest that solute-solute interactions are the strongest and dominate the solution. Solubility data obtained for varying solution compositions, (Figure 2.3) easily fit a linear regression model, this along with visual inspection of the crystals and no previous finding of other pABA polymorphs than the alpha form crystallising from ethanolic solutions indicated that there was no difference in the solid state form of pABA over the range of temperatures used.

The values of the enthalpy (ΔH_{diss}) and entropy (ΔS_{diss}) of dissolutions calculated from the slope and y-axis intercepts of the van't Hoff plots, respectively, and the linear dependence of the calculated activity coefficients (Υ) on the experimentally measured molar solubility (x) are displayed in Table 2.1. Less than ideal behaviour was observed for all pABA EtOH/H_2O solutions with values of Υ for all solutions found to be above 1 over the temperature range of 10 - 50 °C, demonstrating that the solute-solute interactions were strongest. However, the gradient of the plots were not all found to be equal to that of the ideal solution, showing that at lower temperatures, some solutions show more than ideal behaviour although this does not

occur until, for example, 1 °C for the pure EtOH solution. This change was also observed for pABA solutions in mixed EtOH/NMe solvent in a previous study[37]. It is noticeable that solution behaviour of pABA in EtOH deviates largely from those containing some/only H_2O (Figure 2.3b). This difference in solution behaviour could be due to the different solvation energies for pABA in EtOH and H_2O[36]. The fairly comparable slopes of the mixed solvent and pure H_2O solvent solutions demonstrates that for these solutions the entropic component was changing, whereas for pure ethanolic solvent solutions, the enthalpic component was changing. The enthalpic gradient observed for the pure ethanolic solution is consistent with the determined solubility data, corroborating the finding that at higher temperatures, small additions of H_2O increase solubility, whereas at lower temperatures this effect does not occur. Turner et al.[36] calculated values of Υ for pABA in EtOH and H_2O to be 1.10 and 63.05, respectively, which correlates strongly with the calculated values here, with $61.7 < \Upsilon < 87.5$ for H_2O in the temperature range 27 - 48 °C and $1.4 < \Upsilon < 2.1$ for EtOH in the temperature range 20 - 51 °C, providing confidence in the reported values.

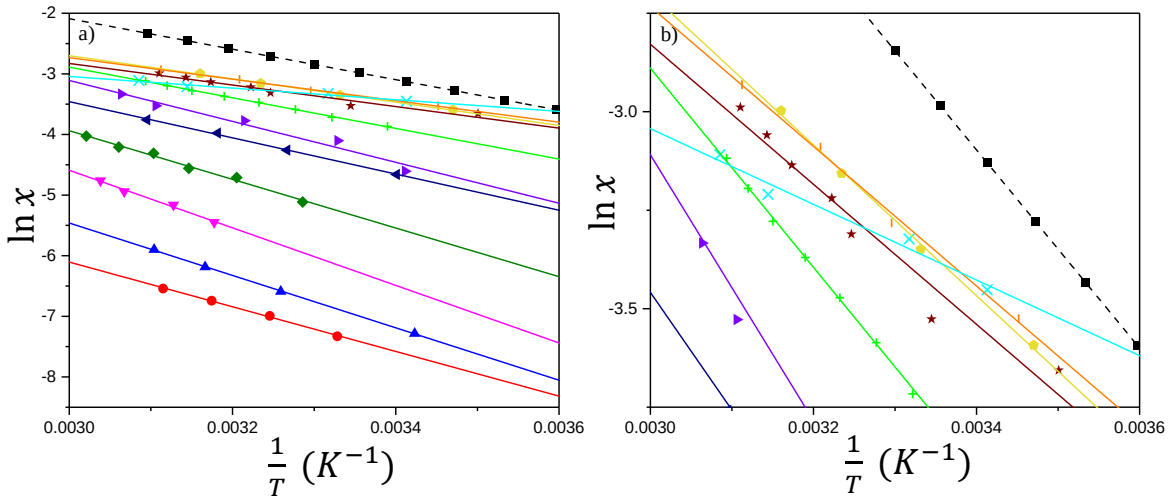


Figure 2.3. van't Hoff plot for pABA in EtOH/H_2O mixed solvent solutions. Dashed black line represents ideal solubility and solid lines represent experimental solubilities for different solvent compositions: 100 wt% EtOH (X), 90 wt% EtOH (|), 80 wt% EtOH (⬟), 70 wt% EtOH (★), 60 wt% EtOH (+), 50 wt% EtOH (▶), 40 wt% EtOH (◀), 30 wt% EtOH (♦), 20 wt% EtOH (▼), 10 wt% EtOH (▲), 100 wt% H_2O (●). a) plots for all compositions studied. b) Plot over a smaller range of molar solubility, showing more clearly the variation observed with EtOH solubility as a function of temperature.

Table 2.1. Thermodynamic parameters together with linear dependence of Υ on x derived from solubility analysis for varying compositions of pABA in EtOH/H_2O solutions.

	Thermodynamic Parameters

	ΔH_{diss} (kJ mol^{-1})	ΔS_{diss} (kJ K^{-1} mol^{-1})	$\ln Y = ax + b$
H_2O	30.64	0.041	$-0.32 \ln x + 2.07$
10:90 EtOH/H_2O	35.93	0.062	$-0.42 \ln x + 1.09$
20:80 EtOH/H_2O	39.47	0.080	$-0.47 \ln x + 0.32$
30:70 EtOH/H_2O	33.37	0.067	$-0.38 \ln x + 0.35$
40:60 EtOH/H_2O	24.82	0.046	$-0.16 \ln x + 0.82$
50:50 EtOH/H_2O	28.06	0.058	$-0.28 \ln x + 0.13$
60:40 EtOH/H_2O	21.01	0.039	$-0.004 \ln x + 0.8$
70:30 EtOH/H_2O	14.13	0.019	$0.36 \ln x + 1.73$
80:20 EtOH/H_2O	15.93	0.025	$0.31 \ln x + 1.45$
90:10 EtOH/H_2O	14.74	0.021	$0.41 \ln x + 1.77$
EtOH	7.99	-0.001	$1.55 \ln x + 5.65$

2.4.2 Calorimetry - effect of antisolvent temperature

The addition temperature of H_2O to the pABA in EtOH/H_2O mixed solvent solutions was found to have a large impact on the solution temperature, providing evidence of just how pronounced the effect of controlling antisolvent temperature can be. The amount by which the antisolvent temperature altered the solution temperature varied depending upon the amount added, with a greater volume of antisolvent having a larger impact on solution temperature (Figure 2.4).

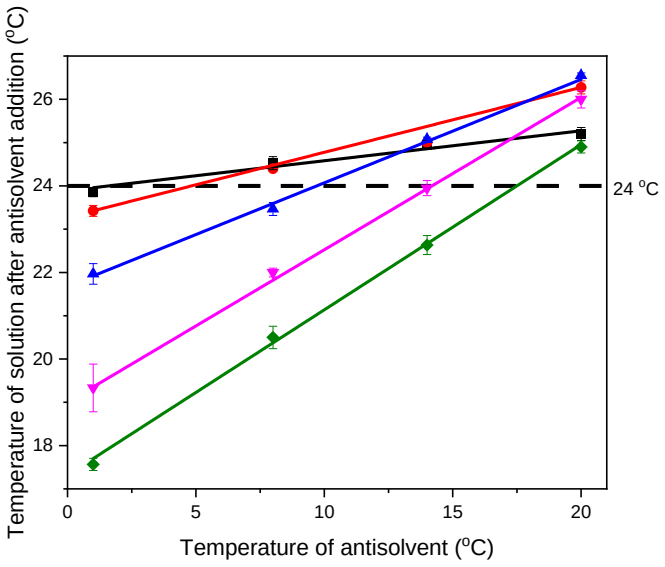


Figure 2.4. Effect antisolvent temperature had on solutions of pABA in EtOH/H_2O mixed solvent held at constant temperature (24 °C). Effect of antisolvent temperature on 0.2 ml initial solution (♦), 0.3 ml initial solution (▼), 0.5 ml initial solution (▲), 0.65 ml initial solution (●) and 0.8 ml initial solution (■) shown by the gradients of the linear relationships.

A total calibration for solution volumes and temperatures was created (Figure 2.5) to enable the IbD approach to this study. It is worth mentioning that these calibrations are specific to this system and experimental setup, with different pieces of equipment yielding potentially different results based upon heat transfer efficiency, mixing, etc.

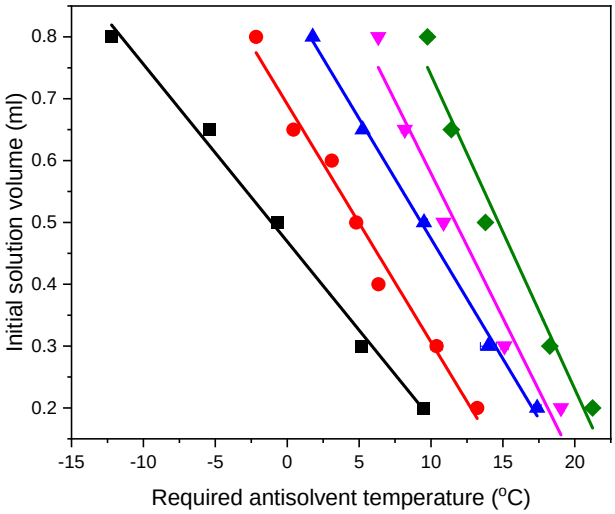


Figure 2.5. Antisolvent temperature calibration for addition of water to pABA in 70:30 wt% EtOH/H_2O solution held at set temperatures [28 °C (♦), 26 °C (▼), 24 °C (▲), 22 °C (●) and 20 °C (■)], in order to maintain solution temperatures. Temperature of the antisolvent is plotted against the initial amount of solution used.

The discrepancies in nucleation induction time results obtained when the antisolvent temperature was controlled through the described methodology compared to uncontrolled antisolvent temperature, where the antisolvent was held at the same temperature as the solution (Figure 2.6) was found to be large. For controlled antisolvent temperature, the induction times were mainly much smaller than for the experiments performed without control, which can be attributed to the heat of mixing increasing the solution temperature for uncontrolled experiments and as such decreasing the supersaturation, before subsequent slow and uncontrolled cooling to the solution set temperature as the experimental system re-equilibrated the solution temperature. Furthermore, the standard deviations of the controlled experiments were much lower than in the uncontrolled experiments. This was due to the IbD approach in the controlled experiments, meaning deviations in results were due to the stochasticity of nucleation as opposed to the added effect of temperature variations, which was a component of the uncontrolled experiments.

It is noticeable that lower initial solution volumes have a lower standard deviation than higher initial solution volumes. This is due to the higher initial solution volumes generating a lower supersaturation, as less antisolvent was added, and as such this lower driving force generating more variation in the stochasticity of nucleation. This will be discussed in more detail in the next section.

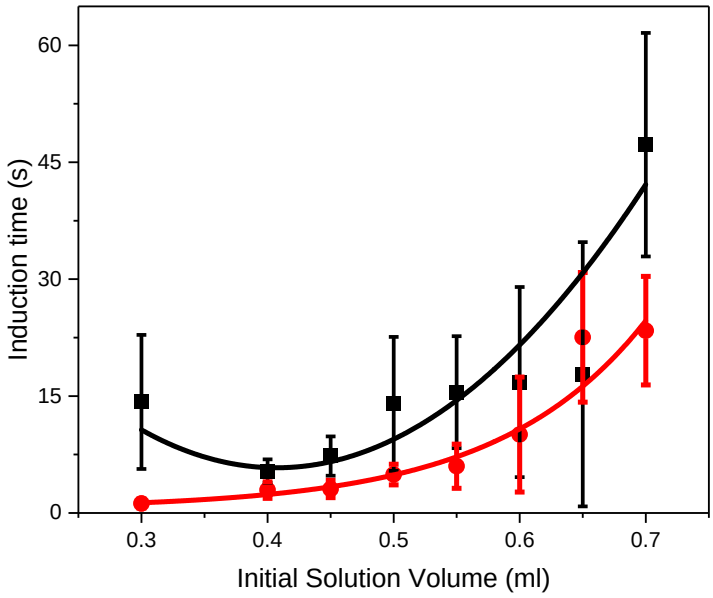


Figure 2.6. Difference in induction time measurements for uncontrolled (■) and controlled (●) antisolvent temperature addition for a solution temperature of 22 °C. Error bars show standard deviation of repeats. Trend lines fitted for both data sets to highlight deviation.

2.4.3 Compositions, Concentrations and Supersaturations

The experimental methodology applied to accelerating nucleation was able to cover a wide range of solution compositions from 11 - 53 wt% EtOH, concentrations from 22.4 - 104.3 g pABA kg^{-1} solvent and supersaturations from 1.08 - 4.73 (Table 2.2). It is important to note that other systems studied through this methodology could achieve different and potentially greater variations in compositions and concentrations, as well as higher supersaturations, which will be discussed in Section 2.5.2 of this article.

Table 2.2. Solution compositions, concentrations and supersaturations over the range of initial solution volumes selected. 'fr' denotes solutions where the required antisolvent temperature to maintain solution temperature was too low and would cause the water antisolvent to freeze. 'nc' denotes solutions that would not crystallise due to too low supersaturations. 'lv' denotes solutions that underwent the described experimental procedure but where the solution volume was too low for accurate induction time detection. 'Final Solution' refers to the solution after antisolvent addition.

Initial Solution Volume (ml)	**Final Solution H_2O Content (wt%)**	**Final Solution EtOH Content (wt%)**	**Final Solution Concentration (g pABA kg^{-1} solution)**	**Supersaturation at solution temperature of 20 °C**	**Supersaturation at solution temperature of 22 °C**	**Supersaturation at solution temperature of 24 °C**	**Supersaturation at solution temperature of 26 °C**	**Supersaturation at solution temperature of 28 °C**
0.8	47	53	104.3	fr	1.08	nc	nc	nc
0.75	51	49	96.5	fr	1.15	1.09	nc	nc
0.7	55	45	88.9	fr	1.25	1.17	1.10	nc
0.65	59	41	81.4	fr	1.37	1.28	1.20	1.12
0.6	62	38	74.2	fr	1.51	1.41	1.32	1.23
0.55	66	34	67.2	1.82	1.69	1.57	1.46	1.36
0.5	69	31	60.3	2.06	1.91	1.77	1.64	1.52
0.45	73	27	53.6	2.36	2.18	2.01	1.86	1.72
0.4	76	24	47.0	2.72	2.51	2.31	2.12	1.96
0.35	79	21	40.7	3.16	2.90	2.66	2.44	2.24
0.3	83	17	34.4	3.68	3.36	3.07	2.80	2.55
0.25	86	14	28.4	4.25(lv)	3.85(lv)	3.49(lv)	3.16(lv)	2.86(lv)
0.2	89	11	22.4	4.73(lv)	4.23(lv)	3.79(lv)	3.40(lv)	3.06(lv)

An overall non-linear decreasing trend of τ with increasing supersaturation, and hence an increased rate of nucleation (Figure 2.7), for pABA crystallising from EtOH/H_2O mixtures, was observed. At high solution supersaturations, changes in τ were smaller than at lower supersaturations, where even small changes in *S* had a pronounced effect on induction times.

At relatively low supersaturations high standard deviations in induction time results were observed. This stochasticity and lack of reproducibility of induction time measurements at low *S* has led to the use of probability distribution functions in induction time studies to determine nucleation parameters[42], meaning a very large number of repeats are needed for each supersaturation used. However, due to supersaturation being the driving force for crystal nucleation, it was seen that at the higher supersaturations, and lower induction times, where the

stochastic nature of nucleation is somewhat overcome, the results were more reproducible, with less deviation from one experiment to the next (Figure 2.8).

For all concentrations and compositions used, it is noticeable that the change in induction times using the proposed method was substantial, with changes from periods of hours to seconds (Figure 2.7b). Furthermore, it provides significant information regarding when crystallisation would occur at different supersaturations, meaning great control could be achieved over the process of pABA crystallising from EtOH/H_2O solutions. This 'control' could be of considerable impact to systems that are required to remain uncrystallised for a certain duration of time or conversely need to crystallise at a specific time, such as diesel fuel, agrochemical products, pharmaceutical supersaturated dosage forms, etc.

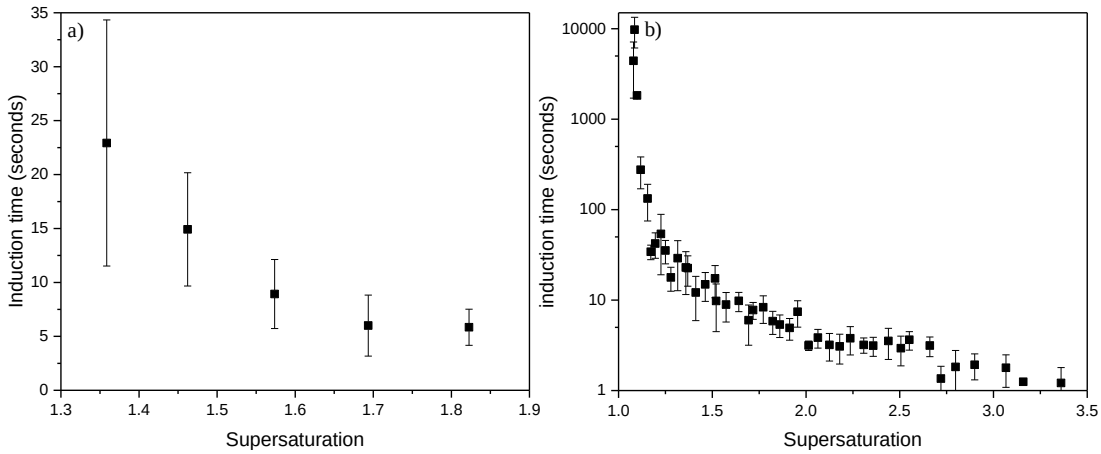


Figure 2.7. Induction time vs. supersaturation for pABA in EtOH/H_2O mixture solutions, with error bars showing standard deviation of 16 repeats for each data point. a) Data obtained at a final solution concentration of 67.2 g pABA kg^{-1} solvent mixture at all temperatures, b) All concentrations and compositions at all temperatures (log scale used for y-axis).

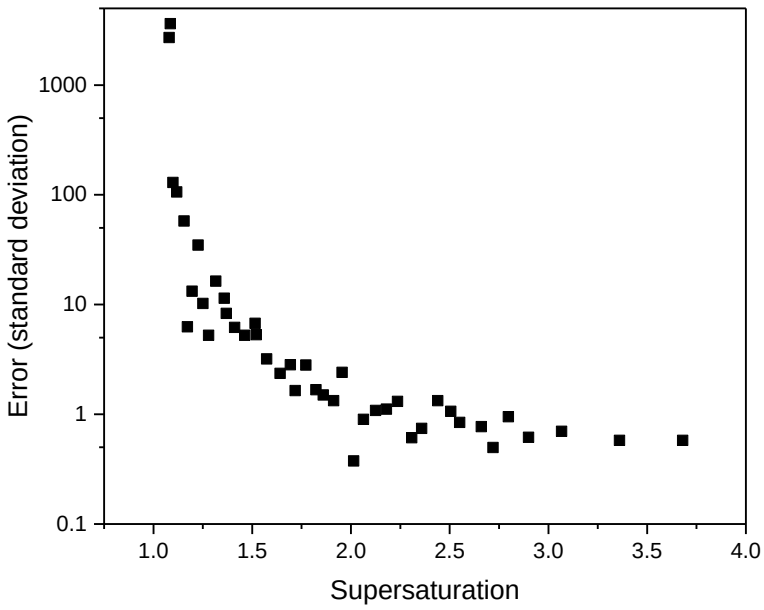


Figure 2.8. Change in standard deviation of induction time measurements, over 16 repeats, as a function of supersaturation.

Furthermore, high supersaturations were achieved at a very fast rate under this 'instant addition' methodology, unlike other crystallisation methodologies to produce high supersaturations, such as crash cooling, which can take minutes to reach a desired level of supersaturation[43] and as such can be subject to unwanted crystallisation before the level is reached. This was very important for the higher supersaturation experiments performed as the induction times themselves were only one or more seconds, meaning that other methodologies might not have been able to produce such supersaturation level for the system of study, such as conventional cooling crystallisation, evaporative crystallisation, isothermal crystallisation, etc. For example, for pABA in EtOH, in order to achieve S = 2 at 20 °C, a saturation temperature of 86 °C was required, which is above the boiling point of EtOH, meaning normal isothermal approaches are not feasible, providing further evidence of the benefits of this IbD antisolvent approach to achieving high supersaturations.

An alternative explanation to how induction times were reduced so substantially under the proposed IbD methodology is that 'cold spots' were created upon addition of the colder antisolvent to the higher temperature solution, creating areas of localised high supersaturations. However, given that the mixing times would be short in comparison to the induction times, even at higher solution supersaturations, this is not the case and the high supersaturations and low induction times were achieved by direct mixing of the antisolvent with solution and subsequent homogeneity of solution temperature in a very short time period, before subsequent nucleation. Nevertheless, at larger scales, such as industrial scales, this could be a problem due

to difficulties in mixing and temperature regulation[31,34]. This will be discussed further in Section 2.5.3.

A comparative method to IbD outlined here is combined cooling and antisolvent crystallisation (CCAC)[29], which utilises a polythermal cooling crystallisation methodology with a controlled addition of antisolvent to achieve high supersaturations. The advantages of IbD over CCAC are twofold: IbD has a greater simplicity to CCAC, with just control of antisolvent temperature being prevalent as opposed to trying to control cooling rate, enthalpies of mixing and antisolvent addition rate, all at once. Also, IbD utilises direct mixing to maintain solution temperature, whereas CCAC utilises conduction cooling from a reactor jacket, which can be cause difficulties in solution homogeneity at larger industrial scales, as discussed in the introduction section.

2.4.4 Nucleation Kinetics Analysis

Induction time (τ) data was collected as a function of supersaturation (S) for a range of concentrations and compositions of pABA in EtOH/H_2O mixed solutions. The data collected was used to calculate interfacial tensions (γ_{eff}) for solution concentrations between 88.9 and 34.4 pABA kg^{-1} solvent mixture, using Equation 2.7 and the slope from the linear relationship (SL_{lin}), equal to $\frac{16\pi v_0^2 \gamma_{eff}^3}{3(1+md)k^3}$. Example plots of the linear relationship are given in Appendix C. Calculated values of γ_{eff}, r^* and i^* for the range of concentrations and compositions used are displayed in Table 2.3.

Table 2.3. Kinetic parameters, γ_{eff}, r^* and i^*, calculated from antisolvent induction time experiments as a function of solution concentration and composition over a range of supersaturations.

Final Solution Concentration (g kg^{-1})	**EtOH/H_2O Solvent Ratio** (wt%)	**Temperature Range** (°C)	γ_{eff} (mJ m^{-2})	***Supersaturation Range***	r^* (nm)	i^* (molecules)
34.4	17 : 83	20 - 28	8.39	3.7 - 2.6	0.53 - 0.71	4 - 9
40.7	21 : 79	20 - 28	7.86	3.2 - 2.2	0.56 - 0.78	4 - 12
47.0	24 : 76	20 - 28	6.39	2.7 - 2.0	0.52 - 0.76	4 - 11
53.6	27 : 73	20 - 28	5.29	2.4 - 1.7	0.50 - 0.78	3 - 12
60.3	31 : 69	20 - 28	4.50	2.1 - 1.5	0.51 - 0.85	3 - 16

67.2	34 : 66	20 - 28	3.35	1.8 - 1.4	0.46 - 0.87	2 - 17
74.2	38 : 62	22 - 28	2.77	1.5 - 1.2	0.54 - 0.1.08	4 - 32
81.4	41 : 59	22 - 28	2.11	1.4 - 1.1	0.55 - 1.51	4 - 87
88.9	45 : 55	22 - 26	2.32	1.3 - 1.1	0.84 - 1.98	15 - 196

2.4.4.1 Effective interfacial tension

Calculated γ_{eff} values showed a marked decrease as the supersaturation and H_2O content decreased. The compositional effect on γ_{eff} correlates with the solubility of the system, with a lower solubility attributed to a higher γ_{eff}[44]. Furthermore, a higher rate of decrease in γ_{eff} was observed for higher H_2O contents, with the rate decreasing along with H_2O content, showing a similar trend to induction time results. This result provides evidence that it may be possible to extrapolate γ_{eff} values over the compositional range, even to the single solvent system boundaries, however, further work is clearly needed to probe this possibility.

Sullivan et al.[45] and Toroz et al.[35] recently reported values of γ_{eff} for pABA in acetonitrile, 2-propanol and ethyl acetate and ethanol, respectively, using isothermal experimental methodologies, in the range of 1.33 - 2.44 mJ m^{-2} over $1.08 < S < 1.35$ and 0.85 - 1.31 mJ m^{-2} over the smaller range of $1.04 < S < 1.15$, respectively. The calculated values of Sullivan et al. compare well with those calculated in a similar supersaturation range in this study, providing confidence in the results obtained. However, these studies were concerned with single solvent systems and to the authors' knowledge no current open literature provides details of values of γ_{eff} for EtOH/H_2O mixed systems. Jiang & ter Horst[42] previously studied a similar compound in a similar solvent system, m-aminobenzoic acid (mABA) in mixed EtOH/H_2O solution, and determined the value of γ_{eff} for this system to be 8.7 mJ m^{-2}, which correlates well with the higher γ_{eff} values calculated in this study.

Interestingly, although it has been previously found that for pABA in EtOH solutions, a lower pABA concentration correlates to lower values of γ_{eff}[35], the same trend was not followed for these results. Instead, the opposite occurs, with a lower concentration correlating to a higher γ_{eff}. This result suggests that either the supersaturation or the compositional effects dominate γ_{eff}, although it is not possible to disentangle these factors under this experimental procedure due to the supersaturation and composition being intrinsically linked.

Furthermore, induction time data over single temperatures, i.e. multiple compositions, was studied. Figure 2.9 displays data collected for a single temperature of 26 °C. For temperatures of 22 - 28 °C there were two linear relationships found for the experimental data, showing two distinct slopes. This is indicative of a mechanistic change in the nucleation of pABA from the mixed solvent system, changing from HEN to HON as the supersaturation reached a sufficient level. This finding has been observed in a number of research studies with critical supersaturations attributed to this mechanistic change being varied depending upon the system of study. Kim & Kim[12] found the HEN to HON critical supersaturation level of S = 1.7 for aqueous sodium chloride solution using methanol as an antisolvent, whereas Sohnel & Mullin[46] found S = 20 for reaction crystallisation of calcium carbonate from aqueous sodium carbonate solution. In the case of pABA in EtOH/H_2O solutions in this study the change occurred at $S \approx$ 1.5.

This slope change was not observed at the set temperature of 20 °C, which is due to the lowest level of supersaturation achieved being above the $S \approx 1.5$ threshold.

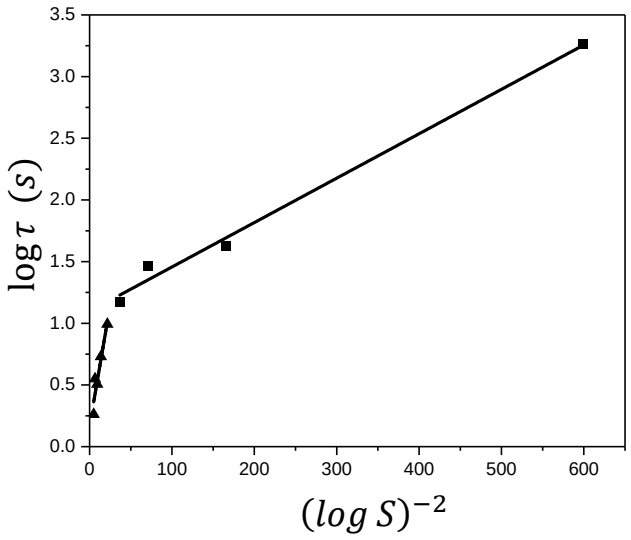


Figure 2.9. Induction time vs. supersaturation for single temperature and multiple composition solutions of pABA in EtOH/H_2O mixtures for solutions at 26 °C.

2.4.4.2 Critical Nucleus Radius and Number of Molecules in the Critical Nucleus

Values of r^* and i^* both showed a similar trend to the obtained induction time measurements as a function of supersaturation for the pABA in EtOH/H_2O mixed solutions, i.e. lower values correlate with higher supersaturations (Figure 2.10), which is a trend previously observed with pABA in ethanolic solutions[35] and is expected with the supersaturation dependence (Equations

2.10 and 2.11). Additionally, the nonlinear trend is also consistent, with smaller changes in values observed at higher supersaturations and larger variation achieved at lower supersaturations. However, a higher supersaturation did not solely dictate r^* and i^*, as lower values of r^* and i^* were determined at lower supersaturations in some cases. This is compositional dependency, as the values of γ_{eff} varied with the solubility of the systems studied, as described previously, meaning that although supersaturation has a strong effect on the size of the critical nucleus, the composition has a larger effect, due to the γ_{eff} associated with forming a critical nucleus.

Values of i^* as low as 2 and 3 were calculated for this system at relatively high supersaturations and at certain compositions. In a previous study by this research group[35] it was determined through small angle x-ray studies that stable dimers are formed in equilibrium with pABA in EtOH solution, which is suggestive that i^* should be larger than 2, otherwise critical nuclei would exist in an undersaturated state. Nevertheless, this is suggestive of a non-classical nucleation route and as such the use of CNT, as the analysis methodology in this study, can determine that i^* = 2. Furthermore, in the previously highlighted study, an isothermal methodology was also used to determine key nucleation parameters and calculated i^* values as low as 3 using CNT, at lower supersaturations than were achieved in this current study, giving confidence in the results obtained here under a CNT methodology.

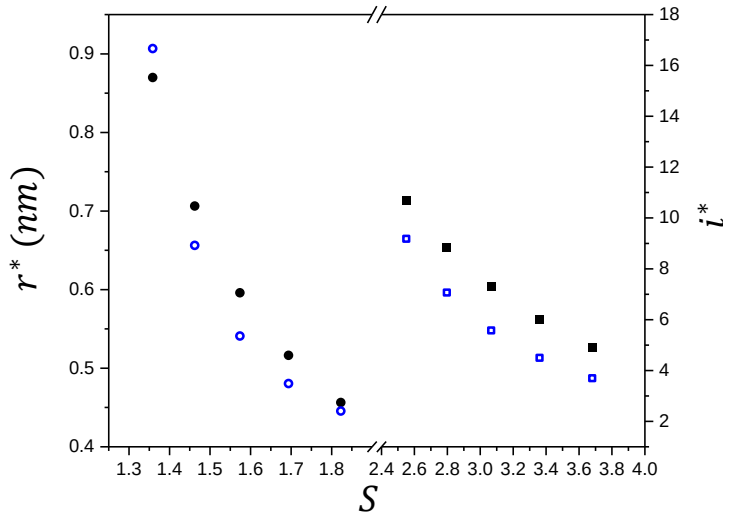


Figure 2.10. r^* (solid objects) and i^* (hollow objects) vs. supersaturation from data obtained at a final solution concentration of 34.4 g pABA kg^{-1} solvent mixture (■/□) and a final solution concentration of 67.2 g pABA kg^{-1} solvent mixture (●/○). Break applied to graph between 1.9 to 2.4.

2.5 Conclusions

2.5.1 Conclusions of this study

Overall, a comprehensive experimental investigation was undertaken, introducing a simple methodology to accelerate crystal nucleation and enable key kinetic parameters to be determined, which would otherwise be unachievable through conventional crystallisation methods, whilst also providing a possibility for a future predictive ability of the nucleation of slowly nucleating systems.

A route to the accelerated nucleation of α-para-aminobenzoic acid (pABA) in ethanol/water (EtOH/H_2O) mixed solvent solutions, using antisolvent crystallisation, was presented using an 'isothermal by design' approach. Supersaturations that were accessible through the IbD methodology of this system were higher than could be achieved through traditional crystallisation methods, achieving $S > 4$. Initial solubility studies determined that small additions of H_2O to pABA in EtOH solutions increased the solubility, but further additions decreased solubility. All solutions of pABA in EtOH/H_2O mixed solvent solution were less than ideal.

The enthalpy of mixing upon addition of H_2O as an antisolvent had a dramatic effect on the solution temperature and as such the induction time results. Control of antisolvent addition temperature, through calorimetry calibrations, ensured that the IbD experiments provided the relevant information for accurate and comparable nucleation kinetic analysis. Induction times were controlled with ease, with significant changes from solutions at low supersaturations and high supersaturations by four orders of magnitude. The high driving force to nucleation for solutions at high supersaturations reduced the standard deviation of induction time results when compared to low supersaturation conditions.

Nucleation kinetics of a range of solution compositions and concentrations were determined from the obtained experimental data. Values of γ_{eff} decreased with decreasing supersaturation and H_2O content, and increasing concentration. The observed nonlinear trend of changing γ_{eff} with composition was similar to that observed for induction time measurements. A change of nucleation mechanism from heterogeneous nucleation (HEN) to homogeneous nucleation (HON) was found as the supersaturation was increased to a critical value of around 1.5. Values of r^* and i^* both showed an expected trend with respect to an increased supersaturation being met with smaller critical nucleus sizes. However, the results demonstrated that r^* and i^* were also compositionally dependent, with supersaturation not solely determining the critical nucleus

size, showing that solubility plays a large role in the nucleation kinetics of pABA crystallising from ethanol/water mixtures.

2.5.2 Future Work and Current Limitations

This study has detailed a useful and novel methodology for determining key nucleation parameters more effectively over a vast range of supersaturations. However, it is currently subject to certain limitations and could be improved further.

One limitation of using the current system is the previously highlighted solubility of pABA in mixed EtOH/H_2O solvents. This is due to an increased pABA solubility upon small additions of H_2O to EtOH solvent, limiting compositions accessible to solely increase supersaturations, limiting the supersaturations that could be achieved in the allowable working solution volume of the experimental apparatus used. Many other systems would not be subject to this limitation however, such as α-lactose in isopropanol/water and acetone/water mixtures[47].

Another limitation is that in order to undertake the IbD methodology for accelerated nucleation studies, a 'reasonable' solubility is required for the initial solvent with the second solvent having a much lower solubility, as highlighted in the workflow given in Figure 2.1. However, this could easily be mitigated by continuous crystallisation IbD methodologies, where the issue of solubility would be negated by the low volumes mixed at one instance, such as use with T-mixer geometries[12].

Furthermore, supersaturations were limited under this system of study as a minimum detection time of one second was applicable for the experimental apparatus used. Therefore, if different apparatus and/or process analytical techniques (PAT) were used then resolution of results could be improved. Nevertheless, systems that nucleate slower than the one in this study would not be effected by this limitation and detection could be more accurate.

Induction time data can be dependent upon the stochastic nature of nucleation and as such can be affected by relatively high standard deviations of repeats, as discussed in Section 2.4.3. This can mean that crystallisation parameters calculated from induction data can be subject to some variability. Further use of PAT to determine the point of detectable nucleation more accurately, such as use of complimentary FTIR[48], UV/Vis[49], microscopy[50], etc. could ensure that key crystallisation parameters are calculated more accurately, however, at the scales used for the current study (1 ml) and the experimental apparatus these are not applicable.

The calculated values of γ_{eff} showed a trend in decreasing value alongside a decrease in H_2O solvent content. This trend needs to be further studied to understand if it is possible to extrapolate calculated values of γ_{eff} to various other solvent compositions. Furthermore, a statistical analysis of results could provide an avenue in which to model the effect of supersaturation on induction time as well as the standard deviations associated with the induction time measurements.

2.5.3 Potential for Transferring IbD Methodology to Industrial Scales

The methodology outlined in this study would be useful in an industrial R&D environment, enabling key crystallisation parameters to be determined more accurately prior to large operation, aiding in improved large scale operation and greater control of product performance, particularly with respect to the physical stability of materials, such as undiscovered polymorphs. Furthermore, current tests to predict nucleation events of slowly nucleating systems involve large timescales for experiments, which hinder progression of products to manufacture and market. This methodology would speed up this step and enable a product to get to market quicker.

Also, the methodology provides clarity on the large effect that antisolvent addition can have upon otherwise well controlled solution conditions, which, given the larger volumes used at industrial scales, can be even more problematic. This important aspect of the methodology highlights the fact that the antisolvent temperature must be offset in comparison to the solution temperature in order to ensure as accurate solution conditions as possible and, as such, greater product control, regardless of scale or industry application.

Nevertheless, the addition of antisolvent at controlled temperatures did cause slight heating/cooling effects to the ‘isothermal’ solution, but as described previously, this was negligible and quick to return to solution temperature at the scale studied. However, at larger scales this could be more problematic and a longer time period to return to set solution temperature could occur. This could be controlled through very accurate antisolvent addition calorimetry calibrations, but it should be noted that this slight effect is much smaller than would occur without the IbD methodology in place.

Furthermore, issues with cold spots, as eluded to previously, and inhomogeneous mixing at industrial scales could be problematic with the IbD methodology outlined. However, these issues can be overcome with appropriate internals to ensure homogenous solutions are formed, which could be achieved through baffles, correct internals material choice and rotation

speed[32,33], etc. Also, manipulation of antisolvent addition technique, such as an antisolvent distributor or sparging, which is currently under research, could overcome these issues. Furthermore, if this methodology is utilised with gas antisolvent (GAS) then issues with mixing would be negligible[51]. This could also be negated by continuous crystallisation processes[52,53], where mixing can be extremely rapid in a much smaller volume.

2.6 References

1. Khan, S., Ma, C. Y., Mahmud, T., Penchev, R. Y. & Roberts, K. J. In-process monitoring and control of supersaturation in seeded batch cooling crystallisation of l-glutamic acid: From laboratory to industrial pilot plant. *Org. Process Res. Dev.* **15**, 540–555 (2011).
2. Camacho Corzo, D. ., Ma, C. ., Ramachandran, V., Mahmud, T. & Roberts, K. . Crystallisation Route Map. in *Engineering Crystallography: From Molecule to Crystal to Functional Form. NATO Science for Peace and Security Series A: Chemistry and Biology* (eds. Roberts, K. ., Docherty, R. & Tamura, R.) 179–213 (Springer, 2017).
3. Mullin, J. W. *Crystallization*. (Butterworth-Heinemann, 2001).
4. Kashchiev, D. *Nucleation*. (Butterworth-Heinemann, 2000).
5. Kwokal, A. Preparation, Stabilisation and Advantages of Metastable Polymorphs. in *Engineering Crystallography: From Molecule to Crystal to Functional Form. NATO Science for Peace and Security Series A: Chemistry and Biology* (eds. Roberts, K. ., Docherty, R. & Tamura, R.) 247–260 (Springer, 2017).
6. Groen, H. & Roberts, K. J. Nucleation, growth, and pseudo-polymorphic behavior of citric acid as monitored in situ by attenuated total reflection fourier transform infrared spectroscopy. *J. Phys. Chem. B* **105**, 10723–10730 (2001).
7. MacMillan, S. D. *et al.* In Situ Small Angle X-ray Scattering (SAXS) Studies of Polymorphism with the Associated Crystallization of Cocoa Butter Fat Using Shearing Conditions. *Cryst. Growth Des.* **2**, 221–226 (2002).
8. Bauer, J. *et al.* Ritonavir: An Extraordinary Case of Conformational Polymorphism. *Pharm. Res.* **18**, 859–866 (2001).
9. Heffernan, C., Ukrainczyk, M., Zeglinski, J., Hodnett, B. K. & Rasmuson, Å. C. Influence of Structurally Related Impurities on the Crystal Nucleation of Curcumin. *Cryst. Growth Des.* **18**, 4715–4723 (2018).
10. McAfee, D. A., Hadgraft, J. & Lane, M. E. Rotigotine: The first new chemical entity for transdermal drug delivery. *Eur. J. Pharm. Biopharm.* **88**, 586–593 (2014).
11. Bajaj, S., Singla, D. & Sakhuja, N. Stability testing of pharmaceutical products. *J. Appl. Pharm. Sci.* **2**, 129–138 (2012).

12. Kim, K. J. & Kim, J. K. Nucleation and supersaturation in drowning-out crystallization using a T-mixer. *Chem. Eng. Technol.* **29**, 951–956 (2006).
13. Pina, C. M., Fernández-Díaz, L., Prieto, M. & Veintemillas-Verdaguer, S. Metastability in drowning-out crystallization: Precipitation of highly soluble sulphates. *J. Cryst. Growth* **222**, 317–327 (2001).
14. Croker, D. M. *et al.* Demonstrating the Influence of Solvent Choice and Crystallization Conditions on Phenacetin Crystal Habit and Particle Size Distribution. *Org. Process Res. Dev.* **19**, 1826–1836 (2015).
15. Musumeci, D., Hunter, C. A. & McCabe, J. F. Solvent effects on acridine polymorphism. *Cryst. Growth Des.* **10**, 1661–1664 (2010).
16. Kordylla, A., Koch, S., Tumakaka, F. & Schembecker, G. Towards an optimized crystallization with ultrasound: Effect of solvent properties and ultrasonic process parameters. *J. Cryst. Growth* **310**, 4177–4184 (2008).
17. Lyczko, N., Espitalier, F., Louisnard, O. & Schwartzentruber, J. Effect of ultrasound on the induction time and the metastable zone widths of potassium sulphate. *Chem. Eng. J.* **86**, 233–241 (2002).
18. Bari, A. H., Chawla, A. & Pandit, A. B. Sono-crystallization kinetics of K2SO4: Estimation of nucleation, growth, breakage and agglomeration kinetics. *Ultrason. Sonochem.* **35**, 196–203 (2017).
19. Kleetz, T., Funke, F., Sunderhaus, A., Schembecker, G. & Wohlgemuth, K. Influence of Gassing Crystallization Parameters on Induction Time and Crystal Size Distribution. *Cryst. Growth Des.* **16**, 6797–6803 (2016).
20. Wohlgemuth, K. Induced Nucleation Processes during Batch Cooling Crystallization. (2012).
21. Curcio, E. *et al.* Regulating nucleation kinetics through molecular interactions at the polymer-solute interface. *Cryst. Growth Des.* **14**, 678–686 (2014).
22. Diao, Y., Myerson, A. S., Hatton, T. A. & Trout, B. L. Surface design for controlled crystallization: The role of surface chemistry and nanoscale pores in heterogeneous nucleation. *Langmuir* **27**, 5324–5334 (2011).
23. Wijethunga, T. K., Baftizadeh, F., Stojaković, J., Myerson, A. S. & Trout, B. L. Experimental and Mechanistic Study of the Heterogeneous Nucleation and Epitaxy of Acetaminophen with Biocompatible Crystalline Substrates. *Cryst. Growth Des.* **17**, 3783–3795 (2017).
24. Sangwal, K. & Mielniczek-Brzóska, E. Antisolvent crystallization of aqueous ammonium dihydrogen phosphate solutions by addition of methanol. *J. Cryst. Growth* **451**, 139–149 (2016).
25. Granberg, R. A., Bloch, D. G. & Rasmuson, C. Crystallization of paracetamol in acetone

— water mixtures. *J. Cryst. Growth* **198/199**, 1287–1293 (1999).

26. Roelands, C. P. M. *et al.* Antisolvent crystallization of the polymorphs of L-histidine as a function of supersaturation ratio and of solvent composition. *Cryst. Growth Des.* **6**, 955–963 (2006).
27. Hermanto, M. W., Chow, P. S. & Tan, R. B. H. Operating strategy to produce consistent CSD in combined antisolvent-cooling crystallization using FBRM. *Ind. Eng. Chem. Res.* **51**, 13773–13783 (2012).
28. Sheikhzadeh, M., Trifkovic, M. & Rohani, S. Adaptive MIMO neuro-fuzzy logic control of a seeded and an unseeded anti-solvent semi-batch crystallizer. *Chem. Eng. Sci.* **63**, 1261–1272 (2008).
29. Lindenberg, C., Kra, M., Cornel, J. & Mazzotti, M. Design and Optimization of a Combined Cooling / Antisolvent Crystallization Process. *Cryst. Growth Des.* **9**, 1124–1136 (2009).
30. Yang, Y. & Nagy, Z. K. Combined Cooling and Antisolvent Crystallization in Continuous Mixed Suspension, Mixed Product Removal Cascade Crystallizers: Steady-State and Startup Optimization. *Ind. Eng. Chem. Res.* **54**, 5673–5682 (2015).
31. Bentham, E. J., Heggs, P. J. & Mahmud, T. CFD modelling of conjugate heat transfer in a pilot-scale unbaffled stirred tank reactor with a plain jacket. *Can. J. Chem. Eng.* **97**, 573–585 (2019).
32. Liang, K. *et al.* An examination into the effect of stirrer material and agitation rate on the nucleation of L-glutamic acid batch crystallized from supersaturated aqueous solutions. *Cryst. Growth Des.* **4**, 1039–1044 (2004).
33. Liang, K. *et al.* Examination of the Process Scale Dependence of l -Glutamic Acid Batch Crystallized from Supersaturated Aqueous Solutions in Relation to Reactor Hydrodynamics. *Ind. Eng. Chem. Res.* **43**, 1227–1234 (2004).
34. Al-Marri, M., Mahmud, T. & Roberts, K. J. A flexible heat transfer model for simulating the performance of batch cooling crystallization as a function of process scale size. in *Proceedings of the 17th International Symposium on Industrial Crystallization* (eds. Ulrich, J., Jansens, P. & Roelands, M.) 613–620 (Vol. 2, 2008).
35. Toroz, D. *et al.* Towards an understanding of the nucleation of alpha-para amino benzoic acid from ethanolic solutions: a multi-scale approach. *Faraday Discuss.* **179**, 79–114 (2015).
36. Turner, T. D. *et al.* The influence of solution environment on the nucleation kinetics and crystallisability of para-aminobenzoic acid. *Phys. Chem. Chem. Phys.* **18**, 27507–27520 (2016).
37. Rosbottom, I. *et al.* Influence of Solvent Composition on the Crystal Morphology and Structure of p-Aminobenzoic Acid Crystallized from Mixed Ethanol and Nitromethane

Solutions. *Cryst. Growth Des.* **17**, 4151–4161 (2017).

38. Technobis. Crystal16. (2020). Available at: https://www.crystallizationsystems.com/crystal16.
39. Tang, X. *et al.* Solubility and crystallisability of the ternary system: Hexadecane and octadecane representative in fuel solvents. *Fuel* **226**, 665–674 (2018).
40. Sangwal, Mk. *Additives and Crystallization Processes: From Fundamentals to Applications*. (John Wiley & Sons Ltd., 2007).
41. Camacho Corzo, D. M. *et al.* Nucleation mechanism and kinetics from the analysis of polythermal crystallisation data: methyl stearate from kerosene solutions. *CrystEngComm* **16**, 974–991 (2014).
42. Jiang, S. & Ter Horst, J. H. Crystal nucleation rates from probability distributions of induction times. *Cryst. Growth Des.* **11**, 256–261 (2011).
43. Black, J. Solvent & additive effects on the appearance of polymorphs of p-aminobenzoic acid. (Manchester, 2016).
44. Nielsen, A. E. & Söhnel, O. Interfacial tensions electrolyte crystal-aqueous solution, from nucleation data. *J. Cryst. Growth* **11**, 233–242 (1971).
45. Sullivan, R. A. *et al.* Revealing the roles of desolvation and molecular self-assembly in crystal nucleation from solution: Benzoic and p -aminobenzoic acids. *Cryst. Growth Des.* **14**, 2689–2696 (2014).
46. Söhnel, O. & Mullin, J. W. A method for the determination of precipitation induction periods. *J. Cryst. Growth* **44**, 377–382 (1978).
47. MacFhionnghaile, P., Svoboda, V., McGinty, J., Nordon, A. & Sefcik, J. Crystallization Diagram for Antisolvent Crystallization of Lactose: Using Design of Experiments to Investigate Continuous Mixing-Induced Supersaturation. *Cryst. Growth Des.* **17**, 2611–2621 (2017).
48. Feng, L. & Berglund, K. A. ATR-FTIR for Determining Optimal Cooling Curves for Batch Crystallization of Succinic Acid. *Cryst. Growth Des.* **2**, 449–452 (2002).
49. Simone, E., Saleemi, A. N., Tonnon, N. & Nagy, Z. K. Active polymorphic feedback control of crystallization processes using a combined raman and ATR-UV/Vis spectroscopy approach. *Cryst. Growth Des.* **14**, 1839–1850 (2014).
50. Li, R. F. *et al.* Particle shape characterisation via image analysis: From laboratory studies to in-process measurements using an in situ particle viewer system. *Org. Process Res. Dev.* **12**, 837–849 (2008).
51. Gallagher, P. M., Coffey, M. P., Krukonis, V. J. & Klasutis, N. Gas Antisolvent Recrystallization: New Process To Recrystallize Compounds Insoluble in Supercritical Fluids. in *Supercritical Fluid Science and Technology* (eds. Johnson, K. P. & Penninger, J. M. L.) **406**, 334–354 (ACS Symposium Series, 1989).

52. Zauner, R. & Jones, A. G. Scale-up of continuous and semibatch precipitation processes. *Ind. Eng. Chem. Res.* **39**, 2392–2403 (2000).

53. Yu. Shekunov, B., Baldyga, J. & York, P. Particle formation by mixing with supercritical antisolvent at high Reynolds numbers. *Chem. Eng. Sci.* **56**, 2421–2433 (2002).

Chapter 3 Isothermal by Design: Comparison with an Established Isothermal Nucleation Kinetics Analysis Method

3.1 Abstract

The nucleation kinetics of the alpha form p-aminobenzoic acid from ethanolic and aqueous solutions is examined through a comparative examination of temperature-jump and anti-solvent drown-out isothermal crystallisation methodologies. Analysis of the data reveals the measured induction times and calculated effective interfacial tensions as a function of supersaturation show broadly equivalent behaviour for the aqueous ethanol mixed solvent-drown out and temperature-jump ethanol solution systems, confirming the comparability of the two methodologies. The results also highlight poorer agreement with the temperature-jump pure aqueous system highlighting the importance of the strength of solvation/desolvation as being the key rate-limiting process for the overall nucleation behaviour.

3.2 Introduction

Isothermal by design (IbD)[1] is an antisolvent crystallisation methodology for studying solution phase nucleation kinetics, which has been shown to be applicable over a wide range of supersaturations (S), particularly accessing supersaturations that can be challenging to attain through conventional temperature-jump cooling-based isothermal crystallisation methodologies (TJM). Whilst IbD has been shown to enable key nucleation kinetic information to be determined[1], such data has not, as of yet, been directly cross-correlated with those obtained by using temperature-jump isothermal methodology (TJM) for the same crystallisation system.

TJM is a prominent methodology for assessing nucleation kinetics that has been used extensively and successfully to understand how crystallisation solution systems nucleate[2–6]. It involves cooling an undersaturated solution to a given level of supersaturation and the time it takes to crystallise from this set point is taken as the induction time (τ), which is a combination of three time components: the relaxation time for molecular cluster distribution, the time to form a stable nucleus and the time for growth to a detectable size (τ_r, τ_n and τ_g, respectively)[7]. However, difficulty in achieving relatively high levels of solution supersaturation through this methodology are created due to the initial cooling required to achieve a certain solution supersaturation, which can impact upon the induction time and as such effect the calculation of the associated nucleation kinetics.

In contrast, IbD utilises an antisolvent methodology, whereby a miscible second solvent is added to a solution, which lowers the solubility of a given solute, increasing the level of supersaturation and therefore the rate of nucleation (J), following the relationship $J \propto S$. This

relationship is outlined through classical nucleation theory (CNT), which is the crystallisation analysis pathway used in this study for IbD and TJM. However, the enthalpy of mixing associated with the addition of a second miscible solvent to a solution can cause a change in the solution temperature. IbD takes account for this and through simple antisolvent calorimetry calibrations, whereby the antisolvent temperature is offset to ensure that the desired solution temperature is maintained, enabling the same analysis methodology to be undertaken as with TJM.

This work focusses on a comparison of nucleation kinetic data obtained through IbD and TJM, detailing the advantages and drawbacks of both techniques, whilst comparing the results obtained through IbD with those from TJM over a similar supersaturation range. Results from IbD are obtained from a previous study focusing on the crystallisation of para-aminobenzoic acid (pABA) from ethanol/water (EtOH/H_2O) mixed solvent solutions[1], whilst those from TJM are a combination of work from a previous study for pABA in EtOH[6,8] and H_2O solutions[8]. The system choice of pABA from these solvent systems represents a well-studied model pharmaceutical compound used in many crystallisation processes.

3.3 Materials and Methods

3.3.1 Materials

pABA (99% pure) was supplied by Alfa Aesar and Sigma, ethanol absolute (≥99.8% pure) was supplied by VWR and deionised water was sourced on site at the University of Leeds.

3.3.2 Experimental Procedure

All TJM and IbD crystallisation experiments were performed on the Technobis Crystal16 system[9] at a 1 ml scale with magnetic stirring.

3.3.2.1 TJM

The temperature-jump isothermal methodology induction time experiments were performed by initially preparing solutions with concentrations of 180 g kg^{-1} and 200 g kg^{-1}, for pABA in EtOH solutions, and 6 g kg^{-1} and 8 g kg^{-1}, for pABA in H_2O solutions. The measurements were carried out at values of supersaturation ranging from 1.03–1.10 (solution temperatures: 26 – 30 °C) and 1.07–1.15 (solution temperatures: 30 – 34 °C) respectively, for EtOH solutions, and 1.17-1.27 (solution temperatures: 23 – 25 °C) and 1.17-1.32 (solution temperatures: 29 – 32 °C) respectively, for H_2O solutions. The values of supersaturation were calculated using solubility

data collected from Turner et al.[8,10]. Solutions were then heated to 10 °C above the dissolution temperature and held for one hour to ensure complete dissolution of the solute. Solutions were then subjected to rapid cooling at 5 °C min^{-1} to the desired holding temperature within the MSZW. The measured induction time was taken as the difference from the start time after reaching the set solution temperatures to the time of the measured transmittance decrease, from 100% to below 90%, indicating crystallisation. Experiments at each level of supersaturation were repeated 8 times at the relevant concentration to provide an average induction time measurement.

3.3.2.2 IbD

The IbD experiments were performed over a large compositional range of pABA in EtOH/H_2O mixed solutions, with five solution temperatures, from 20 to 28 °C in 2 °C increments, denoting the temperatures at which nucleation occurred using this methodology. Initial solutions were prepared with a pABA saturation concentration of 20 °C in a 70:30 EtOH/H_2O wt% solution, with the composition chosen based on solubility data. Solubility was determined over the full solvent compositional range, with eleven solvent compositions ranging in 10 wt% increments of EtOH from pure EtOH to pure H_2O used. The solutions were decanted into 1.5 ml glass vials in varying volumes, from 0.2 to 0.8 ml, which would be made up to 1 ml in volume after addition of H_2O antisolvent with a 1 ml needle and syringe. This addition methodology would result in minor volume variations in antisolvent addition, however, these were assumed to have a negligible effect on induction times in comparison to the innate variability obtained for induction time results for repeats of the same solution composition.

Antisolvent calorimetry calibrations were performed, following the workflow outlined in Kaskiewicz et al.[1], to ensure that the exothermic heating effect caused upon H_2O addition to the pABA solution was nullified. Calorimetry calibrations were performed by varying the antisolvent temperature and measuring the solution temperature after antisolvent addition at each selected solution temperature, over a range of initial solution volumes. Plots of antisolvent temperature vs. final solution temperature were made and linear regression models fitted to determine the required antisolvent temperature to maintain the solution temperature and ensure an isothermal antisolvent addition process. This was subsequently tested to ensure that isothermal conditions were maintained upon antisolvent addition at the determined required antisolvent temperatures, with minimal deviation in temperature changes found.

Following the calorimetry calibrations, induction time experiments were performed over the full range of initial solution volumes, varying in 0.05 ml increments, using the five solution

temperatures, previously described, and the calibrated antisolvent temperatures. Values of induction time were determined using transmission data, in the same manner as the TJM experiments, but the onset of supersaturation was determined through an initial change in transmission upon antisolvent addition followed by a return to 100% transmission after mixing, which denoted time zero for induction time measurements, which took around 1-2 seconds to achieve after mixing. Given the low solution volumes used and the high mixing induced by the antisolvent addition method, this was deemed to be sufficient time for the solutions to mix and homogenise. Experiments were repeated sixteen times for each initial solution volume and temperature to provide an average induction time measurement.

A full description of the methodology used to determine solubility and to perform all stages of the IbD methodology is described elsewhere[1].

3.3.3 Nucleation Kinetics Analysis

Molar supersaturations for each solution were calculated according to:

$$S = \frac{c}{c^*} \tag{3.1}$$

Where c is the absolute solute concentration and c^* is the saturation concentration.
The rate of nucleation was taken to be related to the induction time obtained from the experiments, under the relationship described through the equation:[7]

$$\tau \propto J^{-1} \tag{3.2}$$

The induction time data (τ as a function of S) were analysed using classical nucleation theory (CNT)[11,12], according to:

$$ln\left\{\tau[S(S-1)^{md}]^{\frac{1}{1+md}}\right\} = \ln k_{md} + \frac{B}{[(1+md)(kT\ln S)^2]} \tag{3.3}$$

Where:

$$k_{md} = \left[\frac{(1+md)\alpha_{det}}{k_v z f_e^* c_s d_0^d f_{e,s}^{md}}\right]^{\frac{1}{(1+md)}} \tag{3.4}$$

$$B = \frac{16\pi v_0^2 \gamma_{eff}^3}{3kT} \tag{3.5}$$

Where m is the crystallite growth exponent, with $m = 1$ for pABA, indicating growth through diffusion of solute through a stagnant layer around the crystal[13], d is related to the dimensionality of crystal growth, with $d = 1$ for pABA due to its needle-like morphology, k is the Boltzmann constant, α_{det} is the fraction of detectable crystallised volume and is equal to $\frac{V_c}{V}$, where V_c is the crystallised volume and V is the solution volume, k_v is the crystallite growth

shape factor, z is the Zeldovich factor, f_e^* is the frequency of monomer attachment to the nucleus at $\Delta\mu = 0$, c_s is the concentration of sites in the system on which clusters of the new phases can form, d_0 is the molecular diameter $\approx \left(\frac{6v_o}{\pi}\right)^{1/3}$, $f_{e,s}$ is the frequency of molecular attachment per growth site at $\Delta\mu = 0$, v_0 is the volume occupied by a solute molecule in a crystal and γ_{eff} is the effective interfacial tension. A full derivation of equation 3 is given in a previous research article[4].

For all solutions studied using TJM and solution compositions (initial starting solution volume) ranging from 24 – 8 mol% EtOH for IbD studies, plots of $ln\left\{\tau[S(S-1)^{md}]^{\frac{1}{1+md}}\right\}$ vs. $\frac{1}{T^3(\ln S)^2}$ were constructed, over the range of temperatures used to study each individual solution composition. This provided data for varying supersaturation with constant solution composition, and a linear regression was fitted to the data, with the slope equating to $\frac{16\pi v_0^2 \gamma_{eff}^3}{3(1+md)k^3}$, enabling the calculation of γ_{eff}. This parameter could not be determined for solution compositions of 31 and 27 mol% EtOH using IbD, due to a limited number of data points over a substantial temperature range, this prohibited an accurate calculation of effective interfacial tension in this compositional range. The intercept of the linear regression was equal to $\ln k_{md}$. From the slope the critical nucleus radius (r^*) and the number of molecules in the critical nucleus (i^*) were calculated, according to:

$$r^* = \frac{2\gamma_{eff} v_0}{kT ln\, S} \tag{3.6}$$

$$i^* = \frac{4\pi {r^*}^3}{3v_0} \tag{3.7}$$

Also, $(\log S)^{-2}$ was plotted as a function of $\log \tau$, given the relationship:

$$\log \tau \propto \left[\frac{{\gamma_{eff}}^3}{T^3(\log S)^2}\right] \tag{3.8}$$

With any changes in the trend of data over a single temperature resulting in large increases in the linear regression fit of data, suggesting a change in nucleation mechanism for heterogeneous nucleation (HEN), at lower supersaturations, to homogeneous nucleation (HON), at higher supersaturations[7,14,15].

3.4 Results and Discussion

3.4.1 IbD Calorimetry Calibrations

Figure 3.1, displays calorimetry calibration data collected from pABA in mixed EtOH/H_2O solutions held at 24 °C, with different antisolvent addition temperatures over a range of initial solution volumes[1]. Antisolvent temperature was found to have a significant effect on the final solution temperature, which, for example, can be seen by a required antisolvent temperature over 20 °C lower than that of the solution temperature for a 0.8 ml initial solution volume, in order to maintain the solution temperature at 24 °C.

This substantial variation in required antisolvent temperature, when compared to solution temperature, as well as a large difference in required antisolvent temperature with different addition quantities, demonstrates the importance for off-setting the antisolvent temperature for antisolvent crystallisation processes. Therefore, understanding the system as a whole to ensure accurate and precise measurements are taken, creating reliable data for which to analyse, is extremely important.

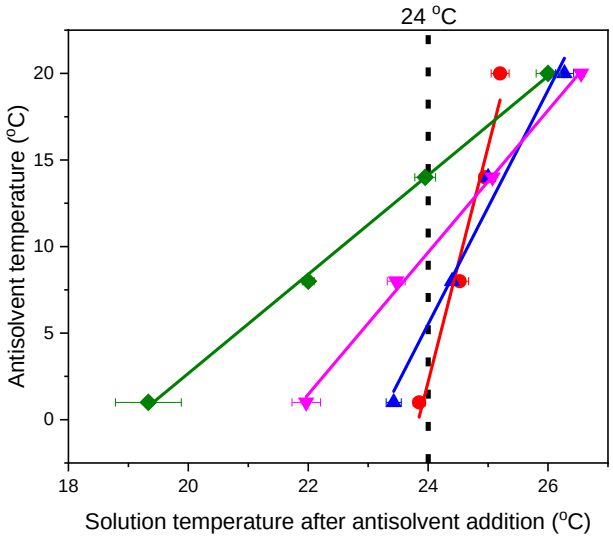


Figure 3.1. Effect of antisolvent temperature upon solutions of pABA in EtOH/H_2O mixed solvent system held at constant temperature (24 °C). Effect of antisolvent temperature on 0.3 ml initial solution (green diamond), 0.5 ml initial solution (pink down-pointing triangle), 0.65 ml initial solution (blue up-pointing triangle) and 0.8 ml initial solution (red circle), shown by the gradients of the linear relationships. Dotted line shows solution temperature prior to antisolvent addition[1].

3.4.2 Induction Time Measurements

Induction time data were collected as a function of supersaturation for pABA in pure EtOH and pure H_2O solvents under TJM and for a range of compositions under IbD, from 31:69 to 11:89 EtOH/H_2O mol%, respectively, highlighted in Figure 3.2.

A comparison of the collected data demonstrates the ability of the IbD methodology to enable the collection of induction time data at higher levels of supersaturation compared to TJM. This is extremely useful for accelerated testing capabilities, allowing higher rates of nucleation to be attained and also for understanding the crystallisation process at high supersaturation. For reliable induction time data under TJM, the cooling time to reach the set level of supersaturation must be negligible with respect to the induction time, ensuring that the time to cool has no real impact upon the determined induction time value. However, if the cooling time increases and as such the induction time decreases, the cooling time can have a significant effect on the induction time, making results unreliable. Therefore, this limits the achievable level of supersaturation using TJM and as such makes it less effective under these solution conditions. For example, for pABA in EtOH solution at a concentration of 180 g kg^{-1}, in order to achieve S = 1.3 it would take 306 seconds of idealised linear cooling at the rate of 5 °C min^{-1} from saturation temperature. However, the results obtained through IbD demonstrate that at this level of supersaturation, the induction time would only be around 20 seconds, over 15 times shorter than the time to cool. It is clear that the time to cool would be much larger than and the induction time and so would have a substantial effect upon it, rendering it unreliable. It would also be unlikely that the solution could reach this level of supersaturation given that the cooling time is so long compared to the induction time. This is further exacerbated by the fact that a high cooling rate of 5 °C min^{-1} was used for the 1 ml solutions in this study, but this cooling rate would not be achievable if the solution volume was scaled up, which would potentially create an even longer cooling period and, as such, a lower achievable level of supersaturation.

What is further evident from the S vs τ data is that the reproducibility of results decreases at lower levels of supersaturation. This can be seen with an increase in the coefficient of variation as the induction time increased (Figure 3.3).This might be due to a number of factors, such as: minor changes in supersaturation having a large effect on induction time, caused with temperature control systems, also, any 'foreign' particulates within the solution vials impacting upon the nucleation process through a heterogeneous nucleation mechanism and importantly that the process of nucleation is stochastic, which can lead to large variations in induction time results for the same experiment regardless if all experimental conditions remained consistent. This aspect has led, in other studies[2], to the use of a large number of repeats (~80 repeats for

each supersaturation) requiring the application of probability distribution functions to analyse induction time data. This requires a large number of experiments to be carried out, and remains a very experimentally time-consuming process. At the higher levels of supersaturation accessible through IbD coefficients of variation were found to be lower, due to a higher driving force to nucleation somewhat overcoming the stochasticity of nucleation. This is highly beneficial as it indicates data with an increase in reproducibility and it provides more confidence in results obtained through analysis of induction time data at these levels of supersaturation.

The results obtained from TJM and IbD methodologies also demonstrate that the mixed solvent solutions used with IbD follow a similar trend to results obtained for pABA in pure EtOH solutions, but not those obtained for pABA in pure H_2O solutions. A higher level of supersaturation was found to be required for the nucleation of pABA in H_2O solutions, for a similar induction time to those of the other systems in this study. The mixed solvent solutions used with the IbD methodology ranged in composition from 8 - 25 mol% EtOH, meaning all solutions had a higher H_2O content compared to EtOH. However, despite this, these solutions were found to follow a similar S vs τ trend as those of pABA in EtOH solution, which could be due to the strong solvation power of EtOH. EtOH molecules have both hydrophobic (alkyl) and hydrophilic (alcohol) moieties and hence are able to solvate the polar and apolar electronic components of the pABA molecule. In contrast, for H_2O, much of the surface area of the pABA molecules is largely inaccessible due to the hydrophobic nature of the benzene ring and therefore this solvent system has much weaker solvation properties and as such a much lower solubility[10,16,17]. This means that although much lower amounts of EtOH are in solution, EtOH molecules could dominate the solvation process. This aspect would be consistent with pABA in mixed EtOH/H_2O solvent solutions, used with IbD, being similar in nucleation properties to pABA in EtOH solutions, as studied using TJM.

The similar trend at low supersaturation of pABA in EtOH solutions to the mixed solvent solutions suggests that it may be possible to extrapolate data obtained from the mixed solvent solutions used through IbD to a single solvent system that is being studied for accelerated testing. Therefore, it may be possible to probe a high level of supersaturation to accelerate a very slow nucleating system and determine how the system behaves at low supersaturation conditions. The data also provides validity with the IbD results, as data collected in the same range of supersaturation had similar values of induction time, shown by the inset in Figure 3.2.

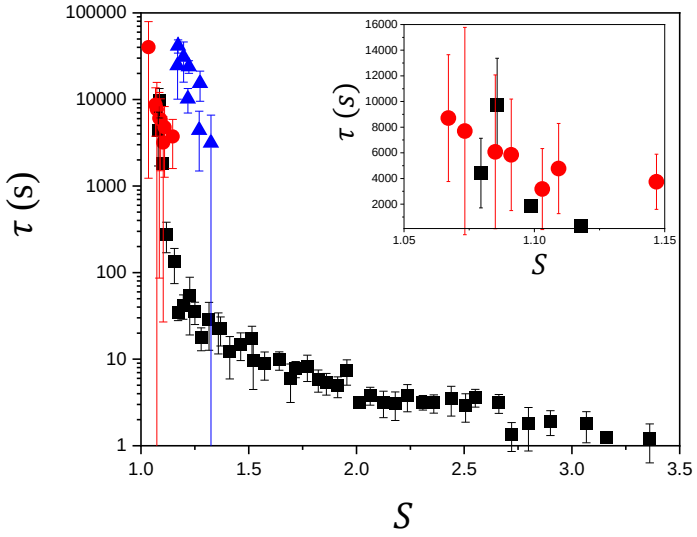


Figure 3.2. Supersaturation vs. induction time data collected from pABA in EtOH solutions at concentration of 180 and 200 g kg^{-1} (red circles), pABA in water solutions at 6 and 180 g kg^{-1} (blue triangles) and IbD experiments over the full range of concentrations, compositions and supersaturations[1] (black squares). Standard deviations of repeats are displayed. $\boldsymbol{\tau}$ *axis in log format. Inset shows data collected for 100 s <* $\boldsymbol{\tau}$ *< 16000, from 1.0 <* $\boldsymbol{S}$ *< 1.15.*

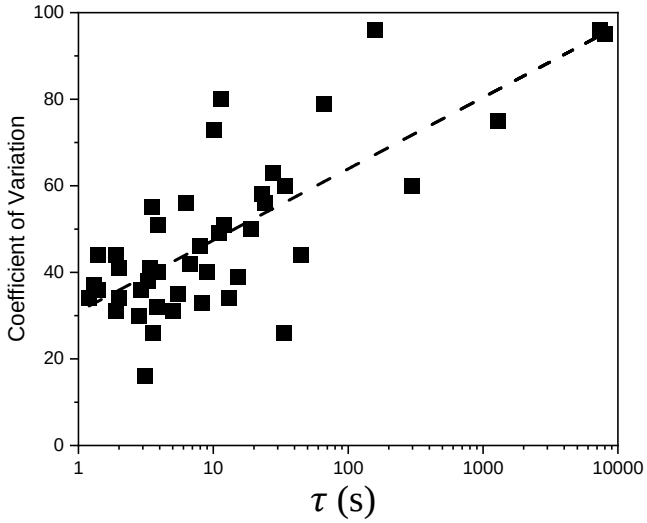


Figure 3.3. Coefficient of variation calculated for the IbD experiments, as a function of induction time. Dashed line shows linear regression fitted to data.

3.4.3 Nucleation Kinetic Parameters

3.4.3.1 Effective Interfacial Tension

An example plot for the determination of effective interfacial tension for pABA in H_2O solution at 6 g kg^{-1} is shown in Figure 3.4. A comparison of calculated effective interfacial tension values from the different methodologies shows a stark difference between those calculated through TJM and IbD, Table 3.1. Given that effective interfacial tension is strongly influenced by solvent environment, this result is expected. Effective interfacial tension calculated from IbD compares well to a previous study performed by Jiang & ter Horst[2], which studied a very similar compound, m-aminobenzoic acid, using the same solvent composition that was used for IbD, mixed EtOH/H_2O solution. This study used TJM and the probability distribution method of induction time analysis, calculating effective interfacial tension of 8.7 mJ m^{-2}. This provides some confidence in the results obtained through IbD.

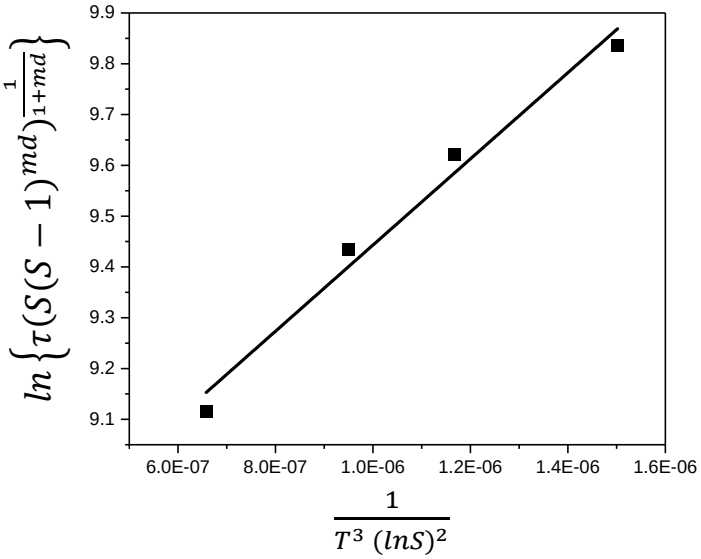


Figure 3.4. Induction time data to determine linear slope values for calculation of effective interfacial tension from data obtained for pABA in water solution at 6 g kg^{-1} concentration.

Examination of Equation 3.3 reveals that an increase in the effective interfacial tension is consistent with an increase in the induction time, for a given supersaturation. However, from Table 3.1 it is clear that for the IbD data, effective interfacial tension increased with a decrease in induction time. In this, the kinetic parameter, ln k_{md}, would therefore have to be lower, in order to be consistent with a decrease in induction time and also for the observed similar τ vs. S behaviour of the mixed solvent IbD and pure EtOH TJM systems. The calculated values of ln k_{md} are given in Table 3.1.

A decrease in $\ln k_{md}$ was calculated for the mixed solvent solutions when compared to the pure EtOH and H_2O solutions, with the trend of decreasing $\ln k_{md}$ over the range of solution compositions studied through IbD also found to be consistent with an increase in effective interfacial tension. It should be noted that although a negative $\ln k_{md}$ value was determined for the IbD mixed solvent solution at 8 mol% EtOH, given the slight calculated error, this is likely to be a very small positive value. From Equation 3.4, it is clear that a decrease in $\ln k_{md}$ would be caused due to a decrease in α_{det} and/or an increase in one or more of the kinetic parameters in the denominator ($z, f_e^*, c_s,$ and $f_{e,s}^{md}$). Unfortunately, it is not possible to quantify the changes in each of the kinetic parameters of $\ln k_{md}$ under the applied methodologies, however, estimations can be made as to the likely changes in values.

Given the lower solution concentrations studied through IbD, it can be confidently stated that there was a likely decrease in α_{det}. Nevertheless, given that the solution concentration of pABA in H_2O is 1 or 2 orders of magnitude lower than those of pABA in EtOH and in the mixed solvent solution, it is clear that the kinetic parameters have a large effect on the induction time results. An increase in supersaturation is known to negligibly increase z, f_e^* and $f_{e,s}^{md}$,[11] which would therefore be unlikely to be the contributing factor to the decrease in $\ln k_{md}$. Solution environment would also have an influence on f_e^* and $f_{e,s}^{md}$, given they are controlled by the diffusion of solute molecules through solution to the growing nuclei. pABA has been shown to be highly solvated by EtOH molecules, but very weakly solvated by H_2O molecules, with around twice the interaction energy calculated for EtOH interacting with a pABA molecule than for H_2O[10,17]. Therefore, it would be expected that the pABA molecules in the mixed solvent solutions would encounter less resistance to movement through the bulk solution to a nuclei, compared to pABA in EtOH solutions, meaning f_e^* and $f_{e,s}^{md}$ would be larger values. The low concentration of pABA in the H_2O solutions would limit the attachment frequency, and so these parameters would also be lower in value than the mixed solvent solutions.

Furthermore, although it has been shown that c_s does not vary dramatically for pABA in solution with EtOH or H_2O[10], it is exponentially dependent upon supersaturation and is influenced strongly by solution concentration,[11] and as such would contribute to the lowering of $\ln k_{md}$ seen for the IbD results. Overall, it is expected that the kinetic parameters of pABA in the mixed solutions studied through IbD would be larger than those of pABA in EtOH and H_2O solutions studied through TJM. It can be assumed that the larger kinetic parameters of the IbD solutions contribute to the similar τ vs. S behaviour of the mixed solvent and EtOH

solutions seen in Figure 3.2, with the smaller kinetic parameters being responsible for the differing behaviour observed for pABA in H_2O solutions.

Table 3.1. Calculated values of effective interfacial tension and the CNT kinetic parameter, $ln\, k_{md}$, for all solutions studied through TJM and IbD, alongside induction times and supersaturation ranges for all solution compositions and concentrations. SE denotes standard error in results. Dashes indicate where data was not calculated due to a limited number of data points obtained for a given solution composition.

Conc. (g kg $^{-1}$)	**Composition (mol% EtOH)**	**γ_{eff} (mJ m^{-2})**	**ln k_{md}**	**SE - ln k_{md}**	**Induction Time Range (s)**	**Supersaturation Range**
TJM Ethanol Solutions						
180	100	0.85	6.66	0.18	40260 - 3180	1.0 - 1.1
200	100	1.31	6.89	0.02	7700 - 3746	1.0 - 1.15
TJM Water Solutions						
6	0	2.1	8.59	0.09	41631 - 15405	1.2 - 1.3
8	0	2.6	6.96	0.20	20064 - 3153	1.2 - 1.3
IbD Mixed Solutions						
104.3	31	-	-	-	4424	1.1
96.5	27	-	-	-	9751 - 133	1.1 - 1.15
88.9	24	2.32	1.34	0.52	1830 - 24	1.1 - 1.3
81.4	22	2.11	2.14	0.25	276 - 23	1.1 - 1.4
74.2	19	2.77	1.77	0.22	54 - 10	1.2 - 1.5
67.2	17	3.35	1.54	0.12	23 - 6	1.4 - 1.8
60.3	15	4.5	1.18	0.29	10 - 4	1.5 - 2.1
53.6	13	5.29	0.56	0.23	8 - 2	1.7 - 2.4
47	11	6.39	0.35	0.49	7 - 1	2.0 - 2.7
40.7	9	7.86	0.02	0.52	4 - 1	2.2 - 3.2
34.4	8	8.39	-0.22	0.35	4 - 1	2.6 - 3.7

Interestingly, the trend in decreasing effective interfacial tension with increasing EtOH content for the IbD results, which follows the trend outlined by the solubility, suggests that it may be feasible to extrapolate values of effective interfacial tension from the mixed solvent compositions (see black squares of Figure 3.5) to pure solvent solutions (see red circles of Figure 3.5), shown by the exponential fitted dashed line in Figure 3.5. However, such an

extrapolation did not correlate with pABA in H_2O solution (see blue triangles in Figure 3.5). This differential between the behaviour of the two pure solvent systems seems to follow a similar trend to that also observed in the τ vs. S data, Figure 3.2, where the data collected from IbD and from pABA in EtOH solution from TJM show similar behaviour, but not for pABA in H_2O solution. Clearly, more work is needed to probe this aspect.

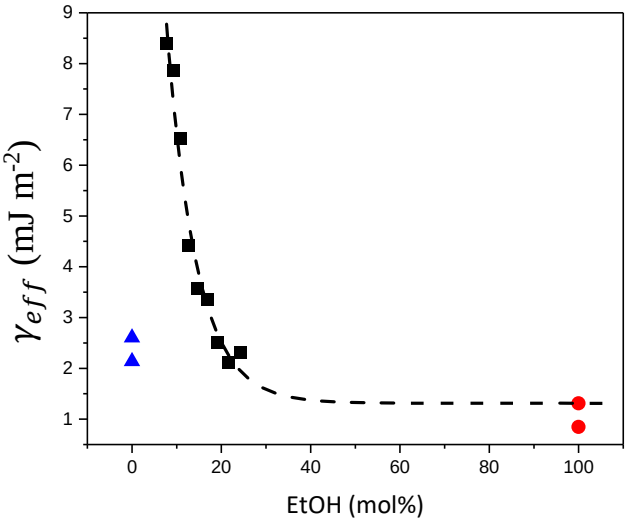


Figure 3.5. Calculated values of effective interfacial tension from pABA in EtOH solutions at concentration of 180 and 200 g kg^{-1} (red circles)1[6], pABA in H_2O solutions at 6 and 180 g kg^{-1} (blue triangles) and IbD experiments over the full range of concentrations, compositions and levels of supersaturation (black squares)[1]. Dashed line shows an exponential fit to the data collected through IbD at mixed solvent compositions.

Due to the large range of supersaturation studied through IbD a change in nucleation mechanism, from HEN to HON was observed at a transition point of $S \approx 1.5$, with this level indicating a high enough driving force to nucleation to enable HON to occur. This mechanism change was determined through an observed change in effective interfacial tension through a plot of $(\log S)^{-2}$ vs. $\log \tau$ and the relationship given in Equation 8. A sharp change in gradient of the linear correlation of the data in this plot demonstrates this mechanism change[14,15], and is provided in Figure 3.6. This insight into the nucleation of pABA in the studied solutions was attained through the IbD methodology but not through TJM, due to the limitations in the range of supersaturation that can be studied through this crystallisation methodology and highlights one of the critical benefits of this methodology.

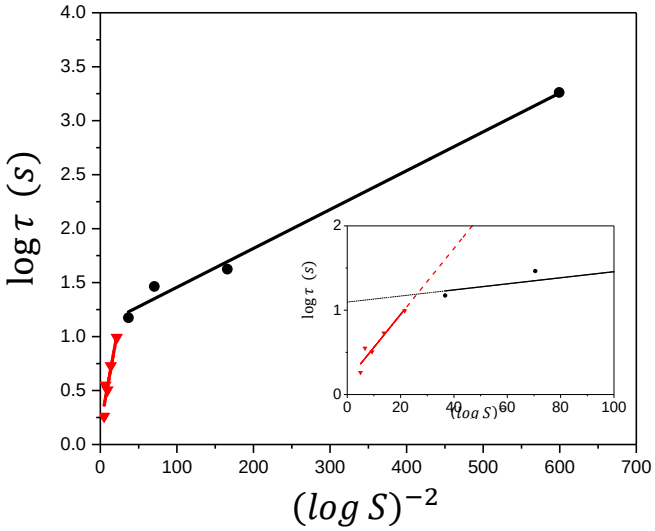


Figure 3.6. Induction time vs. supersaturation for single temperature and multiple composition solutions of pABA in EtOH/H₂O mixtures for solutions at 26 °C[1]. Inset highlights region of mechanism change, with dashed lines showing intersect of slope change, indicating where the HEN to HON mechanism change occurred with increasing supersaturation.

3.4.3.2 Critical Nucleus

Values of critical cluster radius and the number of molecules within the critical nucleus calculated from induction time data from IbD for 81.4 g kg^{-1} pABA in EtOH/H_2O 22:78 mol % solution and from TJM for 200 g kg^{-1} pABA in EtOH solution and 6 g kg^{-1} pABA in H_2O solution are displayed in Figure 3.7. All results show a consistent trend of decreasing r^* and i^* with increasing supersaturation, due to an increased driving force, meaning a smaller critical nucleus size is required for nucleation. However, supersaturation was not the only factor affecting the values of r^* and i^*, with solution composition also impacting these values. This is evident in Figure 3.6, with lower values of r^* and i^* determined for pABA in EtOH solution, than for pABA in H_2O and mixed solvent solutions, even at lower supersaturations.

The values of r^* and i^* for 81.4 g kg^{-1} pABA in EtOH/H_2O 22:78 mol % solution and 6 g kg^{-1} pABA in H_2O solution were found to be very similar across the overlapping range of supersaturations studied. This is due to the values of effective interfacial tension for the mixed EtOH/H_2O 22:78 mol % solvent solution and that of the H_2O solvent solution being 2.11 and 2.13 mJ m^{-2}, respectively, with similar temperature ranges studied. From Equations 3.6 and 3.7, it is clear that the parameters that effect the change in r^* and i^* across the range of solutions studied are effective interfacial tension, supersaturation and solution temperature, therefore, this comparison shows that when solution conditions are similar, regardless of whether the

experimental methodology undertaken was IbD or TJM, pABA nucleates in a similar manner, providing validity to the IbD results.

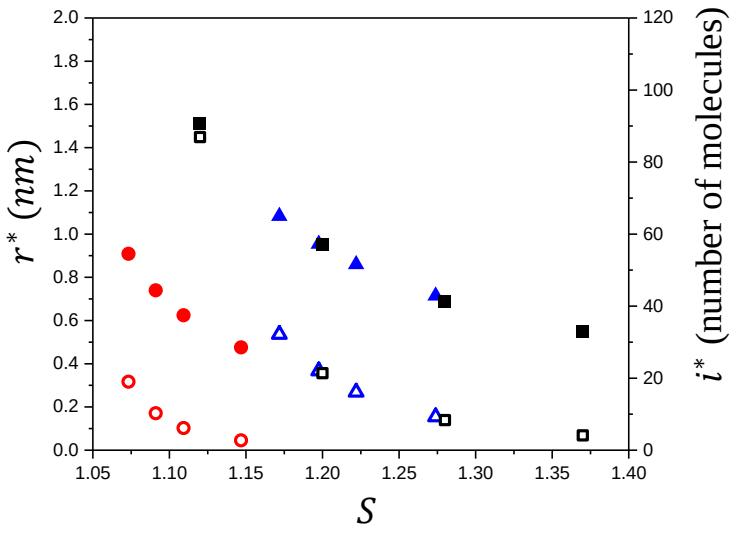


Figure 3.7. Critical nucleus radius (solid objects) and number of molecules within the critical nucleus (hollow objects) vs supersaturation from the data obtained through IbD and TJM. IbD data shown for 81.4 g kg^{-1} pABA in EtOH/H_2O 22:78 mol % solution (black square/black hollow square), TJM data for 200 g kg^{-1} pABA in EtOH solution (red circle/red hollow circle) and 6 g kg^{-1} pABA in H_2O solution (blue triangle/blue hollow triangle).

3.4.4 Advantages and Disadvantages of TJM and IbD

The temperature-jump methodology to determine induction time enables key nucleation kinetic information to be obtained in a relatively simple way, involving rapid cooling to a set temperature followed by a temperature hold. This simplicity and capability has made it a very commonly used experimental methodology in the field of crystallisation science and engineering. However, one drawback of TJM is that the levels of supersaturation that can be achieved by using it are relatively low, creating a low driving force to nucleation and as such the induction time results are subject to large variation, meaning a very high number of repeats is required to obtain reproducible results that can provide accurate and reliable kinetic data. Furthermore, this limitation in achievable level of supersaturation means that it is not a suitable or viable method for accelerated nucleation testing, but is able to provide a comparison and validation of results obtained through IbD over the overlapping range of supersaturation studied through both methodologies.

In contrast, the IbD methodology enabled a much greater range of supersaturation to be studied and as such, through its use, accelerated nucleation testing can be achieved. However, it does involve the addition of a second solvent to the system of study, which requires much more solubility data to be obtained over the full compositional range. Moreover, the final nucleation kinetic parameter results are obtained for mixed solvent systems and not for the original single solvent system that could be the system of interest, which requires accelerated nucleation testing. Nevertheless, the results shown in this study suggest that there is a link between the single solvent system required to be accelerated and the mixed solvent system for pABA in EtOH and H_2O solutions. The addition of a second solvent also creates the necessity for calorimetry calibrations to offset the heat of mixing created upon antisolvent addition to a solution, which requires more experimental effort. The added experimental effort required through IbD can be somewhat offset by the lower number of repeats required to collect reliable and reproducible data at higher levels of supersaturation when compared to TJM.

However, in order for IbD to be an effective methodology for accelerated nucleation testing for predictive purposes, data collected at high levels of supersaturation have to be able to be extrapolated to low supersaturation. The current challenge with this is that the data collected over the range of supersaturations involves two different nucleation mechanisms, HEN and HON. Therefore, these must be decoupled to allow for accurate extrapolations of results obtained in either of the observed mechanism regimes and ensure that each regime is not impacting on the extrapolation of the other. This is a current limitation, but statistical analysis work is being completed to understand whether accurate predictions can be made through extrapolation of results at high supersaturation using IbD.

3.5 Conclusions

A comparison of two nucleation kinetic analysis routes has been undertaken, with data collected from pABA in mixed EtOH/H_2O solutions using IbD and data collected for both pABA in EtOH solutions and H_2O solutions using TJM compared with respect to supersaturation, induction time, effective interfacial tension, critical nucleus size and number of molecules within the critical nucleus.

Induction time data collected over a comparable range of supersaturation for IbD in mixed EtOH/H_2O solutions and pABA in EtOH solutions TJM results showed a similar trend, with similar values of induction time. In contrast, results obtained for pABA in H_2O solutions from TJM showed the same trend in terms of non-linear decreasing induction time with increasing supersaturation but values were offset, with regards to both TJM results from pABA in EtOH

solutions and IbD results, with induction time being larger for a given supersaturation. This 'offset' of induction time values was consistent with the higher driving forces needed to overcome the higher effective interfacial tension value of H_2O when compared to EtOH and also reflecting the weak solvation power of H_2O to pABA. In contrast, the solvation power of the mixed solvent solution used with the IbD methodology appeared to be dominated by the stronger solvation abilities of the EtOH molecules, leading to a similar S vs. τ trend for these systems.

The effective interfacial tension values calculated through IbD ranged from 2.3 - 8.4 mJ m^{-2}. In contrast, for TJM experiments effective interfacial tension values ranging from 0.85 - 1.31 mJ m^{-2} for pABA in EtOH solutions and 2.1 - 2.6 mJ m^{-2} for pABA in H_2O solutions, depending on solution concentration. This increased effective interfacial tension suggested that changes in kinetic parameters must be responsible for the aforementioned τ vs. S data trends observed. An analysis of the kinetic parameters suggested a decrease in α_{det} would occur with a lowering of solution concentration with an increase in $z, f_e^*, c_s,$ and $f_{e,s}^{md}$ likely for the IbD solutions studied, given the mixed solvent environment and the higher levels of solution supersaturation achieved through this methodology. These changes were able to provide an explanation as to the τ vs. S behaviour of the TJM and IbD systems. A comparison of results also showed that it may be possible to extrapolate values of effective interfacial tension of the mixed solvent solutions to the solutions containing EtOH only, with an exponential relationship. A comparison of results obtained for analysis of the critical nucleus, r^* and i^*, demonstrated that for all methodologies, r^* and i^* decreased non-linearly with increasing levels of supersaturation and that over a similar range of effective interfacial tension and supersaturation, results were comparable. Overall, results obtained through TJM validated data collected through IbD over a similar range of supersaturation and provide confidence in the data collected at higher levels of supersaturation achievable through IbD.

In future work, TJM studies on mixed pABA in mixed EtOH/H_2O solutions, particularly to probe the detailed nature of the induction time offset observed between these two single solvents would be particularly useful. However, direct correlation of the two approaches over the full range of supersaturation studied through IbD is clearly not feasible, due to the limitations in achieving higher supersaturation through TJM. Furthermore, another interesting study would result from the use of IbD of a different system, such as a non-aqueous system, that would probe the applicability of IbD to wide ranging crystallisation systems.

3.6 References

1. Kaskiewicz, P. L. *et al.* Isothermal by Design: An Accelerated Approach to the Prediction of the Crystallizability of Slowly Nucleating Systems. *Org. Process Res. Dev.* **23**, 1948–1959 (2019).
2. Jiang, S. & Ter Horst, J. H. Crystal nucleation rates from probability distributions of induction times. *Cryst. Growth Des.* **11**, 256–261 (2011).
3. Mealey, D., Croker, D. M. & Rasmuson, Å. C. Crystal nucleation of salicylic acid in organic solvents. *CrystEngComm* **17**, 3961–3973 (2015).
4. Camacho Corzo, D. M. *et al.* Nucleation mechanism and kinetics from the analysis of polythermal crystallisation data: methyl stearate from kerosene solutions. *CrystEngComm* **16**, 974–991 (2014).
5. Black, J. F. B. *et al.* Crystal nucleation and growth in a polymorphic system: Ostwald's rule,: P -aminobenzoic acid and nucleation transition states. *CrystEngComm* **20**, 768–776 (2018).
6. Toroz, D. *et al.* Towards an understanding of the nucleation of alpha-para amino benzoic acid from ethanolic solutions: a multi-scale approach. *Faraday Discuss.* **179**, 79–114 (2015).
7. Mullin, J. W. *Crystallization*. (Butterworth-Heinemann, 2001).
8. Turner, T. D. Molecular Self-Assembly, Nucleation Kinetics and Cluster Formation Associated with Solution Crystallisation. (University of Leeds, 2015).
9. Technobis. Crystal16. (2020). Available at: https://www.crystallizationsystems.com/crystal16.
10. Turner, T. D. *et al.* The influence of solution environment on the nucleation kinetics and crystallisability of para-aminobenzoic acid. *Phys. Chem. Chem. Phys.* **18**, 27507–27520 (2016).
11. Kashchiev, D. *Nucleation*. (Butterworth-Heinemann, 2000).
12. Sangwal, Mk. *Additives and Crystallization Processes: From Fundamentals to Applications*. (John Wiley & Sons Ltd., 2007).
13. Kashchiev, D. & Firoozabadi, A. Induction time in crystallization of gas hydrates. *J. Cryst. Growth* **250**, 499–515 (2003).
14. Söhnel, O. & Mullin, J. W. A method for the determination of precipitation induction periods. *J. Cryst. Growth* **44**, 377–382 (1978).
15. Kim, K. J. & Kim, J. K. Nucleation and supersaturation in drowning-out crystallization using a T-mixer. *Chem. Eng. Technol.* **29**, 951–956 (2006).
16. Rosbottom, I. *et al.* Influence of Solvent Composition on the Crystal Morphology and Structure of p-Aminobenzoic Acid Crystallized from Mixed Ethanol and Nitromethane

Solutions. *Cryst. Growth Des.* **17**, 4151–4161 (2017).

17. Rosbottom, I., Pickering, J., Hammond, R. B. & Roberts, K. J. A Digital Workflow Supporting the Selection of Solvents for Optimising the Crystallisability of Para Aminobenzoic Acid. *Org. Process Res. Dev.* **24**, 500–507 (2020).

Chapter 4 Influence of Solution Chemistry on the Solubility, Crystallisability and Nucleation Behaviour of Eicosane in Toluene/Acetone Mixed-Solvents

4.1 Abstract

The interplay between the solution chemistry and crystallisability of eicosane in mixed toluene/acetone solutions is examined over the full compositional range from pure toluene to pure acetone, using a combination of polythermal crystallisation experiments and molecular modelling. Enthalpies of dissolution and mixing, as well as metastable zone widths increase with increasing acetone content, up to a mol fraction of 0.85 acetone, followed by a decrease in values to pure acetone solutions. Nucleation is found to occur via an instantaneous pathway for the pure solvent systems and also when toluene is in excess, in contrast to solutions where acetone is in excess, which are found to nucleate progressively. Rationalisation through molecular modelling highlights likely changes in the solution structure, whereby eicosane can be expected to be preferentially solvated by toluene, with this solvated cluster being surrounded by a 'cage' of acetone molecules. This proposed structure is consistent with a model whereby solute diffusion and hence clustering is hindered when acetone is in excess, decreasing the crystallisability of the solution and effecting a change in the mechanism of nucleation. However, above a critical acetone composition, the potential for a complete toluene solvation is restricted and easier crystallisation is enabled.

4.2 Introduction

Solution phase crystallisation is an energy-efficient physical process widely utilised to isolate and/or purify solid-form ingredients. The majority of speciality chemicals are crystallised in multi-substance batch reactors, which provide limited opportunities for specialised reactor designs and for optimising crystal product properties[1]. However, selection of a mixed-solvent crystallisation system, comprising two or more miscible components, provides an alternative opportunity for the control and optimisation of the crystallisation process. Mixed-solvent crystallisation systems have been intensively studied, due to compositional variation affecting solubility[2], solid-form produced[3–5], crystal growth[6], habit[7], crystal size[8], crystallisability[9–12] and nucleation[13–15].

Crystallisation from mixed-solvent solution systems can be directed, either through cooling of an initial solvent blend[7,16] or through antisolvent crystallisation[15,17]. Both routes require miscible solvents, with the latter requiring significant differences in the solubility of the solute between the solvent and antisolvent, the addition of which lowers solute solubility and hence generates supersaturated conditions. In the design of mixed-solvent crystallisation processes, it is helpful to have developed workflows for the characterisation of the solubility and solution

properties over the full range of compositions used and, through this, optimise process parameters to ensure desired crystal product characteristics[18,19].

For the design of antisolvent crystallisation processes knowledge of the solubility-temperature relationship as a function of the composition of solvent mixture is important for control of the solution supersaturation generated upon addition of the lower solubility solvent. Depending upon the magnitude of the enthalpy of mixing the addition of a second solvent can change the solution temperature[15,17] and hence a detailed knowledge of solution mixed-solvent thermodynamics is also needed.

Changes in solution properties can, in turn, also impact upon solute mass transport within the solution phase and through this, impact upon the overall crystallisability of the material. Hence, characterisation of the metastable zone width (MSZW) as a function of solvent composition is required in order to define the operational conditions for large-scale crystallisation processes.

Variation in mixed-solvent composition can also change the nature of the intermolecular interactions associated with solute desolvation and clustering, which can directly affect the ability of the solute to nucleate, impacting, in turn, on the nucleation kinetics and associated mechanism[15,17,20]. In the latter respect, nucleation can occur either through instantaneous (IN) or progressive (PN) nucleation mechanisms[21], whereby IN describes the process in which all nuclei form instantly and subsequently undergo crystal growth, whereas in PN the nuclei continuously form in the presence of growing crystals. Such mechanistic changes can impact on the crystal product properties, e.g. IN could, in principle, result in a more uniform crystal size distribution of product. Previous studies in other organic solvents have highlighted the fact that changes in solution environment, relating to solution solvent and concentration[20,22] as well as the inclusion of nucleation inhibition additives[23], can alter the mechanism of nucleation. The IN mechanism has been shown to occur when solute clustering is present in solution prior to the nucleation stage[24], in line with van't Hoff isotherms suggesting strong solute:solute interactions within solution[20]. The relationship between solute clustering, solution structure and nucleation mechanism is examined to provide insight into these effects.

In this study, the crystallisation of the long-chain hydrocarbon, eicosane ($C_{20}H_{42}$), from mixed toluene/acetone solutions is examined. Alkanes, in general, are known to be highly soluble in toluene[25] but can be expected to be much less soluble in more polar solvents, such as acetone. The work presented here investigates this mixed-solvent system, examining the interplay between solvent composition and solution chemistry, in terms of the solutions solubility and crystallisability, thermodynamics and nucleation kinetics and mechanism. In this, the approach

adopted encompasses experimental polythermal crystallisation/dissolution measurements[26–28] to characterise the solution solubility and nucleation kinetics and mechanisms coupled with molecular-scale grid-based modelling[29] of solute:solvent interactions. The latter seeks to compliment the experimental studies providing an insight into the likely molecular-scale solvation process for the mixed-solvent system and through this, produce a more complete understanding of the intermolecular interactions taking place within the solution phase, together with their concomitant impact upon the crystallisation process.

4.3 Materials & Methods

4.3.1 Workflow

The methodological workflow used in this study is given in Figure 4.1, providing a standardised assessment for the characterisation of mixed-solvent solutions and their crystallisation, through an integrated approach, coupling experimental and modelling techniques.

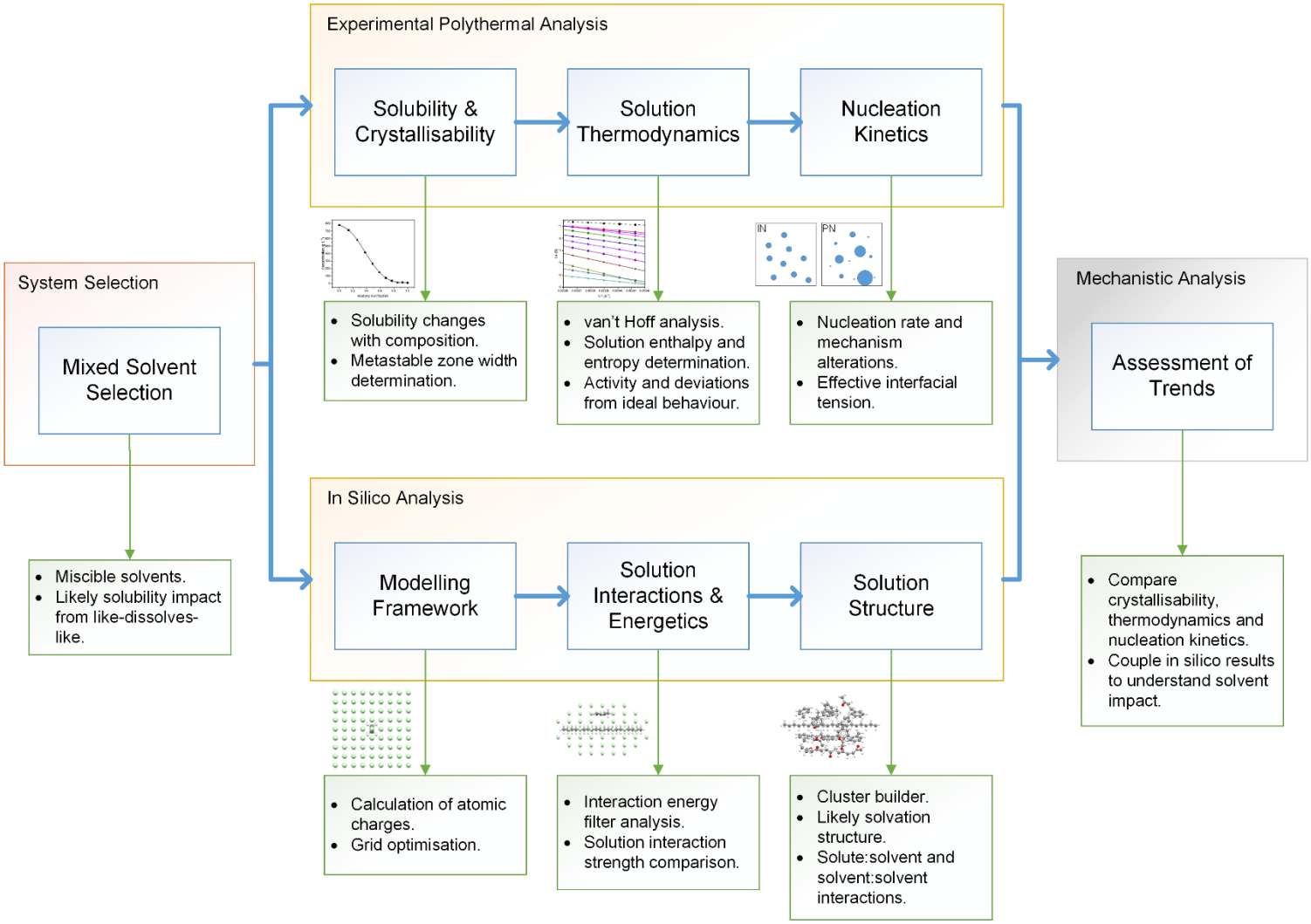


Figure 4.1. Methodological workflow incorporating crystallisation analysis with molecular modelling for enhancing process understanding.

4.3.2 Materials

Eicosane (99% pure) was supplied by Sigma-Aldrich, toluene (≥99.3% pure) was supplied by Honeywell and acetone (99.5+% pure) was supplied by Arcos Organics. All materials were used as received without further purification.

4.3.3 Experimental Procedure

4.3.3.1 DSC Measurements and Data Analysis

The latent heat of crystallisation and melting temperature of eicosane were measured using a Mettler Toledo Differential Scanning Calorimetry DSC 1 STARe system. 3 mg of eicosane was weighed into 40 µl aluminium standard pans and was subject to a temperature profile initiated by heating to 40 °C, where it was held for an hour to ensure complete homogenization, and then cooled to -15 °C, where it was also held for an hour to allow equilibration. A constant rate (q) of 0.25 °C min^{-1} was used in both the heating and cooling segments. The temperature cycle was repeated five times to obtain mean values of the latent heat of crystallisation and melting temperature, which were determined from the integration of the corresponding exothermic and endothermic peaks using Origin software[30].

4.3.3.2 Solution Preparation and Polythermal Measurements

All solutions were prepared at a minimum of four solution concentrations, ranging from 5 - 850 g L^{-1} over the full compositional range of toluene/acetone mixtures, e.g. 250 - 850 g L^{-1} for eicosane in pure toluene and 5 - 35 g L^{-1} for eicosane in pure acetone solutions, with concentrations varying with solvent composition to take into account changes in solubility. A total of eleven compositions of the toluene/acetone solvent mixtures in 10% volume increments were used.

Solutions were prepared by weighing eicosane into 15 ml prewashed glass vials, using a weighing scale that could measure with ±0.1 mg accuracy. A Fisherbrand 500-5000 µl micropipette was used to add the respective solvent to each concentration sample, with 5 ml total solvent volume used. A magnetic stirrer was placed into the glass vials and the mixtures were placed on a stirrer hot plate and held at 35 ºC for 30 minutes under constant agitation, in order to form a homogeneous liquid solution. 1 ml of solution was added to the 1.5 ml glass vials and a standard 7 x 2 mm magnetic stirrer was added to each vial.

Crystallisation experiments were performed using the Technobis Crystal 16® system[31] with crystallisation and dissolution onset points detected by optical turbidity methods. The 1 ml

solutions were subject to different cooling and heating cycles. Each temperature cycle began by heating the solutions to 35 ºC, before being held at this temperature for one hour to ensure that complete homogenisation had taken place and was the solution was then subsequently cooled at a set rate to -15 ºC. This temperature was then held for an hour to allow equilibration, followed by an increase in temperature back to 35 ºC at the same specified rate. This temperature profile was performed for each concentration of each composition at rates (q) of 0.25, 1, 2 and 3.2 ºC min^{-1} for both the cooling and heating segments of the temperature cycles and at a constant stirring rate of 300 rpm. Each temperature cycle was performed five times to obtain mean and standard deviation (STD) values for the rate-dependent crystallisation and dissolution temperatures determined.

4.3.3.3 Solubility and Crystallisability Assessment

The individual crystallisation (T_c) and dissolution temperatures (T_{diss}) were determined from transmission (optical turbidity) vs. temperature profiles. The values for sample transmittance were calibrated from 100%, for a homogeneous liquid solution, to 0%, for a fully crystallised solution. T_c was taken as the onset point where the light transmittance dropped to approximately 95% and T_{diss} was taken as the point where the light transmittance reached 100% for all measurements. The polythermal data was used to extrapolate both $T_c(q)$ and $T_{diss}(q)$ lines back to a cooling rate of 0 ºC min^{-1} so that the crystallisation temperatures at the kinetic limit ($T_{c,l}$) and equilibrium saturation temperatures (T_e) could be determined, respectively. The difference between $T_{c,l}$ and T_e was taken as a measure of the steady-state metastable zone width (MSZW).

A van't Hoff analysis was performed on the solubility data determined from the saturation temperatures. The solution ideality was determined with respect to the ideal solubility as obtained from DSC analysis, based upon the Hildebrand equation (Equation 4.1). Activity coefficients (Υ), enthalpy (ΔH_{diss}) and entropy (ΔS_{diss}) of dissolution were calculated based on Equations (4.2) and (4.3), respectively[25]:

$$\ln(x_{ideal}) = \frac{\Delta H_{fus}}{R}\left[\frac{1}{T} - \frac{1}{T_m}\right] \quad 4.1$$

$$\Upsilon = \frac{x_{ideal}}{x} \quad 4.2$$

$$\ln(x) = -\frac{\Delta H_{diss}}{RT} + \frac{\Delta S_{diss}}{R} \quad 4.3$$

Where x_{ideal} is the solution concentration, x is the experimentally measured molar solubility, ΔH_{fus} is the enthalpy of fusion, R is the ideal gas constant, T is the temperature and T_m is the melting temperature.

The calculated activity coefficients were fitted with respect to the variation in temperature, by:

$$\ln \Upsilon = aT + c \quad 4.4$$

Where a and c are constants.

The enthalpy (ΔH_{mix}) and entropy (ΔS_{mix}) of mixing were calculated from the deviation in ΔH_{diss} and ΔS_{diss} from ideality, through the relationships:

$$\Delta H_{mix} = \Delta H_{diss} - \Delta H_{diss}^{ideal} \quad 4.5$$

$$\Delta S_{mix} = \Delta S_{diss} - \Delta S_{diss}^{ideal} \quad 4.6$$

4.3.3.4 Nucleation Kinetic Analysis

The KBHR approach[26–28], utilised in this study, enables the distinction between instantaneous (IN) and progressive (PN) nucleation in a crystallising system, with the latter referring to continuous birth of new crystallites amongst already growing ones and the former being characterised by all crystallites appearing at once in the solution, followed by only growth, without subsequent nucleation events. In the PN case, the number of crystallites increases as a function of time, with a large distribution of crystallite sizes, whereas in the IN case there are a fixed number of crystallites of equal sizes, assuming a consistent growth rate. IN occurs when a number of strongly active nucleation sites are present in solution, which can occur due to foreign particles within solution, resulting in heterogeneous nucleation, or when solutions are seeded with crystallites, either externally or self-seeded, or when, as previous studies have highlighted[23,24], solutions are subject to strong solute clustering, resulting in a number of prenucleation clusters that nucleate at once.

Regardless of the mechanism by which nucleation occurs, the solution remains apparently unaffected until a critical level of undercooling is reached corresponding to the limit of the MSZW, at which point the amount of formed crystallites are detectable by the monitoring technique. This undercooling is dependent upon the nucleation, growth and cooling rates. The KBHR approach utilises the relationship between the relative critical solution undercooling (u_c) and the cooling rate (q) to enable the determination of crystallisation parameters. u_c was determined by:

$$u_c = \frac{\Delta T_c}{T_e} \quad 4.7$$

Where, $\Delta T_c = T_e - T_c$

The mechanism of nucleation was determined through the "rule of three", from ln-ln plots of u_c vs q, the slopes of which were fitted by linear regressions, whereby a slope >3 signifies a PN pathway and a slope <3 indicates an IN pathway[26,27].

For the PN case, the final expression for $u_c(q)$ dependence, when expressed through the number of crystallites at the detection point (N_{det}), can be defined as:

$$\ln q = \ln q_0 + a_1 \ln u_c - \frac{a_2}{(1-u_c)u_c^2} \quad 4.8$$

Plots of u_c vs. $\ln q$ fitted with Equation 4.8 enable the free parameters to be determined for the calculation of the nucleation parameters and the effective interfacial tension (γ_{eff}), Equation 4.9. This enables the calculation of the critical nucleus radius (r^*), assuming spherical nuclei, and the number of molecules in the critical nucleus (i^*), through Equations 4.10 and 4.11.

$$b = \frac{k_n v_0^2 {\gamma_{eff}}^3}{kT_e \lambda^2} \quad 4.9$$

$$r^* = \frac{2\gamma_{eff} v_0}{\lambda u} \quad 4.10$$

$$i^* = \frac{2bkT_e}{\lambda u^3} \quad 4.11$$

Where k_n is the nuclei numerical shape factor, v_0 is the volume occupied by a solute molecule in the crystal, λ is the molecular latent heat of crystallisation, k is the Boltzmann constant and the dimensionless thermodynamic parameter b is related to the nucleation rate, by:

$$J(t) = K_J e^{-\frac{b}{[(1-u_c)u_c^2]}} \quad 4.12$$

Where J is the nucleation rate and K_J is the nucleation rate constant, which is related to the Zeldovich factor (Z), the attachment frequency of monomers to the nucleus (f^*) and the concentration of nucleation sites (C_0).

More detailed descriptions of the KBHR approach have been described previously[26–28].

4.3.4 Molecular Modelling

4.3.4.1 Molecular Structure Building

The molecular structures of eicosane, toluene and acetone, provided in Figure 5.2, were built within Biovia Materials Studio[32], with structural optimisation and atomic fractional charges derived from a calculation of the electrostatic potential using Gaussian09[33], with a grid-based method (ChelpG) scheme[34], a 6-31G* basis set and the Becke three-parameter[35] Lee-Yang Parr exchange-correlation function[36]. Although eicosane is likely to exist in a number of conformations within solution, due to its long-chain nature, structural optimisation was performed to generate the lowest energy eicosane molecular structure, representative of a likely structure within the solution environment, with accurate calculated atomic fractional charges.

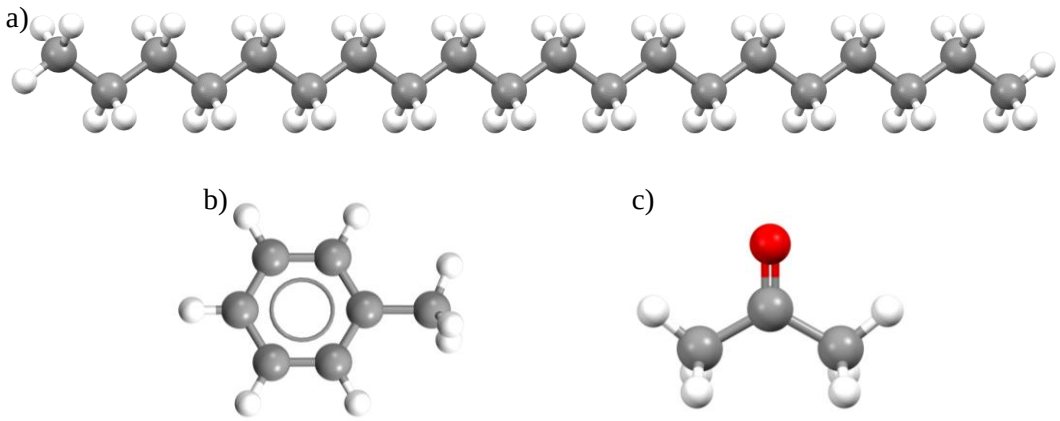


Figure 4.2. Chemical structures of a) eicosane, b) toluene and c) acetone.

4.3.4.2 Molecule-Molecule Solvation Grid-Search

Solute:solute and solute:solvent interactions were examined using intermolecular grid search methods[37,38], with a spatial grid defined around a central target molecule, Figure 4.3. A grid optimisation was performed and an orthogonal grid shape with size 15, 15 and 35 Å in the X, Y and Z planes, respectively was found to be optimal for energy calculations. In each plane, the number of grid points was defined with 8, 8, 10 steps of grid points on the X, Y and Z planes, respectively. This provided a grid with total points of 891, Figure 4.3. During the intermolecular interaction energy calculation procedure, a probe molecule was placed on each point of the grid and rotated through a set of Euler angles, which were set at 4º for the x-axis, y-axis and z-axis. This resulted in a heterogeneous six-dimensional search space, and at each point in this search space the interaction energy between the probe and target molecules was calculated using an atom-atom approach, through the Momany intermolecular potential[16,39]. Intermolecular interactions in the form of van der Waals, hydrogen bonding and electrostatic interactions were calculated, with the summation of the repulsive and attractive components of each of these interaction types providing the total intermolecular interaction energy.

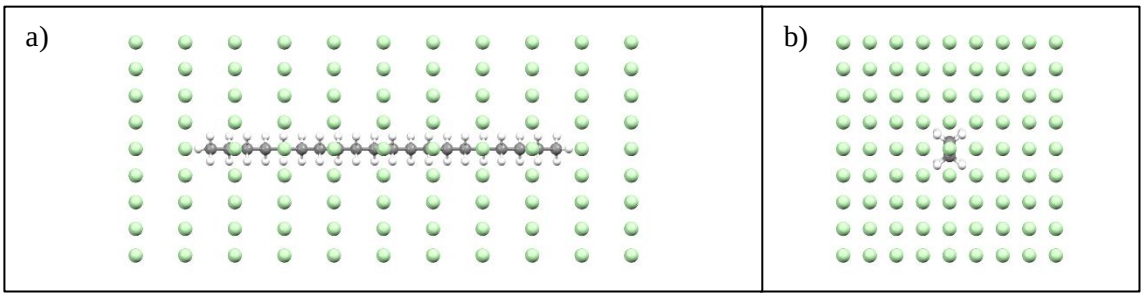


Figure 4.3. Spatial grid defined around target eicosane molecule for calculation of intermolecular interaction energy calculations; (a) view along b axis; (b) view along c axis. Grid points shown by green dot symbols.

The solvating power of toluene and acetone to eicosane was assessed by comparison of the intermolecular interaction strengths of the solvents (probes) with eicosane (target). A low-pass energy filter was be applied to remove interactions below given interaction strengths, which were set at -0.5, -1.0, -1.5 and 2.0 kcal mol^{-1} for toluene interactions and -0.5, -1.0, -1.2 and 1.4 kcal mol^{-1} for acetone interactions. The more negative energy filters highlighted the most favourable interaction sites with an eicosane molecule. A total of 331,986,600 points (location + rotation) were searched for each simulation.

All possible solvent and solute intermolecular interactions within the solution phase (eicosane/eicosane, eicosane/toluene, eicosane/acetone, toluene/toluene, acetone/acetone and toluene/acetone) were calculated using the intermolecular grid search method. A low-pass energy filter of -0.5 kcal mol^{-1} was used to screen out low energy interactions with the screen resulting in over 4000 possible intermolecular interaction energies for each interaction type.

4.3.4.3 Solvation Shell Grid-Search

Solvation energies and solution structure were assessed via the grid-search method, using cluster building. In this, a probe molecule was located at the lowest-energy site in the grid around a target, with this molecular-pair becoming a new fixed-target for a subsequent probe molecule, which was then placed on the next available lowest-energy site. This process was repeated until the positions for a shell of molecules had been located. The intermolecular interaction energy between each subsequent probe and target as well as probe-probe interactions were calculated. 20 solvent molecules were used as probes around the target eicosane molecule, in different toluene/acetone mixed solvent ratios of 0:20, 5:15, 10:10, 15:5 and 20:0 molecules. Software procedures required one set of solvent:solute interactions to be calculated prior to the other. A previous study demonstrated that, in solubility mismatched mixed-solvent solutions, such as the system studied here, the local solvation environment of a nucleating solute could be dominated by the strongly solvating solvent, due to the much higher intermolecular interaction strengths[17]. Therefore, for the current procedure the interactions of toluene molecules with eicosane were calculated first, followed by the acetone molecules. Whilst this molecular modelling technique provides an attractive and representative molecular-scale assessment as to likely solute:solvent ordering within the solution, it is limited by fixed interaction procedure imposed by the chosen grid size that does not directly allow for molecular conformational flexibility nor deals with random solute:solvent interactions.

The overall cluster structures generated were optimised using the Forcite module within Biovia Materials Studio. The SMART algorithm and a very fine tolerance was used to distinguish intra

and inter-molecular interactions, ensuring solvation energies could be determined. For this, Gasteiger[40,41] atom point charges were utilised. All structures were visualised using the CCDC's Mercury[42] software package.

4.4 Results

4.4.1 Assessment of Solubility and Crystallisability

Examples of polythermal heating-cooling and turbidity profiles used for the temperature cycles are displayed in Figures 4.4(a) and (b), highlighting the determination of T_{diss} and T_c. The equilibrium solubility (T_e) and supersolubility ($T_{c,l}$) temperatures obtained from extrapolation of T_{diss} and T_c back to 0 ºC min^{-1} are given in Table 4.1, together with their MSZW (ΔT_c) for eicosane crystallising from toluene/acetone mixture solutions. Examples of the linear regression plots of T_{diss} and T_c vs. q together with their standard deviation values from five repeats and the resulting solubility-supersolubility curves are given in Figures 4.4(c) and (d), respectively. Experimental data from all of the experiments is provided in Appendix D. To our knowledge, no current open-literature data is available on the solubility in the ternary system studied. All the solutions measured in this study showed high repeatability from five repeats of cycling experiments, with low standard deviation values.

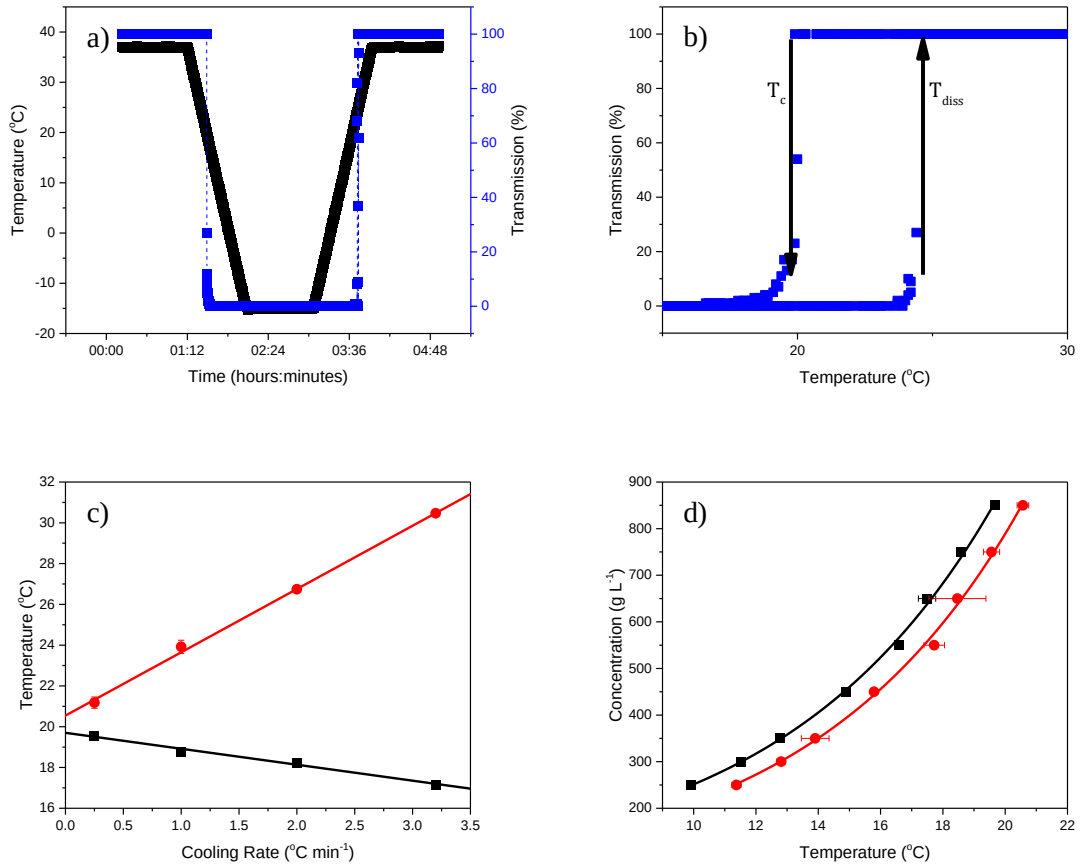


Figure 4.4. Representative polythermal data: a) Temperature (black) and transmission (blue) profiles against the time as used for measuring determination of crystallisation and dissolution temperatures (T_c and T_{diss}, respectively), for 850 g L^{-1} eicosane in toluene solution at cooling rate (q) of 1 °C min^{-1}; Temperature turbidity plot of a solution highlighting the observation of on-set points for T_c and T_{diss}; (c) Plots of T_c (black squares) and T_{diss} (red circles) as a function of q, with the corresponding best linear fits are also given, for 850 g L^{-1} eicosane in toluene solution; (d) Concentration vs. temperature plot highlighting the equilibrium MSZW between the solubility (red circles) and supersolubility (black squares) curves, for eicosane in toluene at all concentrations studied.

As expected, the solubility of eicosane was found to be highest in toluene, with increasing acetone composition causing a decrease in solubility over the full range of compositions studied, as shown in Figure 4.5. This can be justified in terms of the adage 'like-dissolves-like', with eicosane being a negligibly polar molecule and as such being more likely to dissolve in a non-polar solvent. Toluene has a small dipole moment (0.36 D)[43] in comparison to acetone (2.90 D)[44], therefore, eicosane can be expected to have greater affinity towards toluene rather than acetone molecules in solution, consistent with a higher solubility with increased toluene composition. The limited solvation power of acetone perhaps represents an antisolvent, as opposed to a true solvent for eicosane, thus demonstrating the ability of this system to be used both as an initial solvent blend for crystallisation and/or for an antisolvent crystallisation methodology. However, at lower

solution temperatures, below around 15 °C, and above an acetone mol fraction (y) of 0.85, eicosane solubility increased with small additions of acetone, perhaps suggesting alterations in solution structure that could influence solute:solvent interactions and hence eicosane solubility.

Previous studies have highlighted that in mixed-solvent solutions solute solubility can increase with small additions of lower solubility solvents[7,15], suggesting that the lower solubility solvent has the ability to solvate parts of the solute molecule that the higher solubility solvent cannot, hence contributing to and enhancing the overall solution solvation power of the mixed solvent system. This behaviour was observed for eicosane in toluene/acetone mixed-solvent solutions at 25 °C. However, below this temperature the addition of acetone was found to only reduce eicosane solubility, perhaps demonstrating acetone's comparatively poor ability to solvate the eicosane molecule when compared to toluene. The temperature dependence of this behaviour is interesting in that it demonstrates, perhaps, that a critical level of molecular mobility should be reached in order for the lower solubility solvent to access potential solute solvation sites that are not fully solvated by the higher solubility solvent within the mixed-solvent.

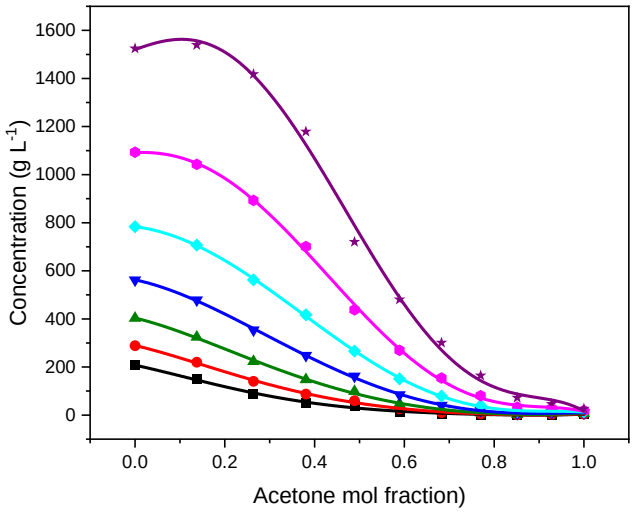


Figure 4.5. Solubility of eicosane in toluene/acetone mixtures at different temperatures: 10 °C (black squares), 12.5 °C (red circles), 15 °C (green upward-triangles), 17.5 °C (blue downward-triangles), 20 °C (cyan diamonds), 22.5 °C (pink hexagons) and 25 °C (purple stars).

MSZW data provides an indication of the ease of which a solution overcomes its inherent nucleation barrier and crystallises, with a narrower MSZW being consistent with a tendency towards easier nucleation. For all concentrations and compositions studied the MSZWs were found to be around 0.5 – 2.2 °C, in broad agreement with previous work[25,45–48], but quite small when compared to other typical organic solution phase systems[20,49]. For solution compositions

from $0 < y < 0.49$ and $0.93 < y < 1$ the MSZW was found, in general, to be roughly inversely proportional to the solution concentration. This would be consistent with nucleation being easier with a higher number of solute molecules within solution, which might be expected given that this would offer a greater chance for solute:solute interactions. In contrast, for solutions within the compositional range of $0.59 < y < 0.85$, the opposite trend was observed, with, in general, an increase in MSZW with increasing concentration. This could indicate changes in solution chemistry and nucleation mechanisms over the compositional ranges studied, perhaps reflecting the changing nature of the intermolecular interactions within the solution state.

Table 4.1. Solubility (T_e), supersolubility ($T_{c,l}$) and steady-state MSZW data of eicosane in toluene/acetone solvent mixture solutions, together with values of the slopes of the linear regressions of $\ln u_c$ vs. $\ln q$ plots for the range of solvent compositions studied, with the resultant nucleation mechanism determined from the "rule of three" KBHR analysis. The '' denotes a low correlation fitting and as such the analysis has a lower confidence value and may be a potentially unreliable result.*

Conc. (g L^{-1})	$T_{c,l}$ (°C)	T_e (°C)	MSZW (°C)	$\ln u_c$ vs. $\ln q$ slope	Nucleation mechanism	Conc. (g L^{-1})	$T_{c,l}$ (°C)	T_e (°C)	MSZW (°C)	$\ln u_c$ vs. $\ln q$ slope	Nucleation mechanism
y = 0						**y = 0.14**					
250	9.92	11.37	1.46	2.87	IN	**200**	10.39	11.85	1.46	2.80	IN
350	12.78	13.90	1.13	2.51	IN	**300**	13.47	14.46	0.98	2.26	IN
450	14.88	15.79	0.91	2.25	IN	**400**	15.47	16.48	1.01	2.37	IN
550	16.58	17.72	1.14	2.45	IN	**500**	16.57	17.82	1.26	3.15	PN*
y = 0.26						**y = 0.38**					
200	12.81	14.30	1.49	3.50	PN	**200**	15.05	16.51	1.47	2.87	IN
300	15.45	16.80	1.35	2.87	IN	**300**	17.61	18.36	0.75	2.05	IN
400	17.18	18.24	1.06	2.37	IN	**400**	18.87	19.74	0.88	2.41	IN
500	18.70	19.20	0.50	1.64	IN	**500**	20.20	20.94	0.74	2.01	IN
y = 0.49						**y = 0.59**					
150	15.42	17.09	1.67	2.82	IN	**150**	18.39	19.88	1.49	2.70	IN
250	18.69	19.76	1.07	2.32	IN	**250**	20.64	22.37	1.73	3.08	PN
350	20.26	21.28	1.02	2.53	IN	**350**	21.94	23.67	1.74	3.41	PN
450	21.31	22.67	1.36	2.67	IN	**450**	22.97	24.58	1.61	3.32	PN
y = 0.68						**y = 0.77**					
150	20.80	22.44	1.65	3.16	PN	**100**	21.59	23.23	1.64	3.18	PN
250	22.63	24.16	1.53	3.58	PN	**200**	24.29	25.84	1.55	3.27	PN
350	23.80	25.75	1.95	3.82	PN	**300**	25.45	26.92	1.47	3.04	PN
450	24.58	26.41	1.83	3.25	PN	**400**	26.02	28.22	2.20	3.91	PN

y = 0.85						y = 0.93					
75	23.17	25.00	1.82	3.61	PN	**20**	18.80	20.60	1.81	2.84	IN
175	26.27	28.16	1.89	4.00	PN	**60**	25.09	26.85	1.77	3.74	PN
275	27.29	29.34	2.05	3.84	PN	**100**	27.29	29.00	1.71	3.70	PN
375	27.90	29.98	2.09	4.04	PN	**140**	28.36	30.18	1.83	3.92	PN
y = 1											
5	11.92	13.08	1.16	1.68	IN						
15	20.27	21.53	1.26	2.28	IN						
25	23.48	24.76	1.28	4.16	PN						
35	25.81	26.57	0.76	1.95	IN						

4.4.2 Analysis of the Solution Thermodynamics

van't Hoff analysis provides further indication of the nature of the solution behaviour in terms of the impact of solvent and compositional effects. The van't Hoff plots, as a function of solvent composition, were found to fit well by linear regression for all the solutions studied, as shown in Figure 4.6. The enthalpy (ΔH_{diss}) and entropy (ΔS_{diss}) of dissolution values, enthalpy (ΔH_{mix}) and entropy (ΔS_{mix}) of mixing values and the activity coefficients (Υ) calculated from van't Hoff analysis are summarised in Table 4.2.

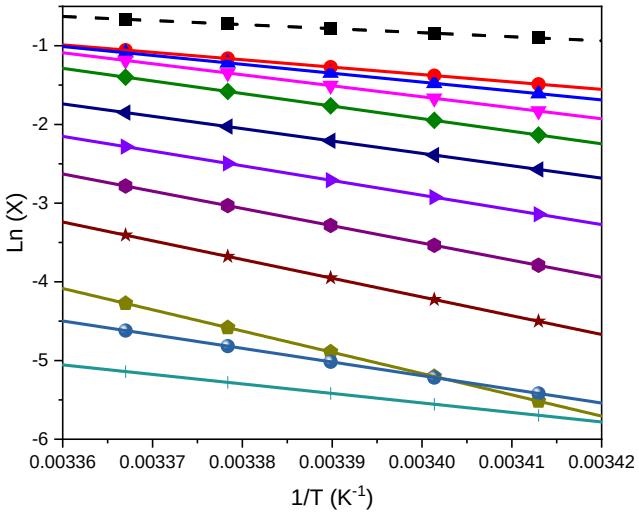


Figure 4.6. van't Hoff plots for eicosane in toluene/acetone mixed solvent solutions. Dashed black line represents ideal solubility, and solid lines represent experimental solubilities for different solvent compositions: y = 0 (red circle), y = 0.14 (blue up-pointing triangle), y = 0.26 (pink down-pointing triangle), y = 0.38 (green diamond), y = 0.49 (navy left-pointing triangle), y = 0.59 (violet right-pointing triangle), y = 0.68 (purple hexagon), y = 0.77 (brown star), y = 0.85 (mustard pentagon), y = 0.93 (blue sphere), and y = 1 (turquoise cross).

Less than ideal behaviour was observed for all the solutions with Υ greater than 1 for the temperature range studied. This behaviour is consistent with a solution structure whereby homogeneous (solute:solute and solvent:solvent) intermolecular interactions are preferred with respect to heterogenous (solute:solvent) intermolecular interactions. In line with the trend observed for the solubility studies, toluene solutions were found to show the most ideal behaviour, with larger deviations from ideal behaviour being observed with increasing acetone composition. This behaviour is consistent with toluene having much stronger intermolecular interactions with eicosane comparative to acetone, with high content acetone solutions not only having likely stronger solute:solute interactions, but also likely stronger solvent:solvent

interactions, making for easier eicosane desolvation and hence crystallisation from solution. This is evidenced in the calculated ΔH_{diss} values, in Table 4.2, highlighting that, in general, ΔH_{diss} is larger at the higher solution acetone compositions.

However, ΔH_{diss} was found to decrease with increasing acetone composition above y = 0.85, which given the low solubility of eicosane in high acetone compositions solutions, this would seem to be counter-intuitive. However, the change in van't Hoff plot slopes for these solutions suggest decreasing effects of enthalpy and entropy within solution. This is corroborated with a similar trend in the enthalpy of mixing results, suggesting that the solute:solvent interactions decreased in strength with increasing acetone solution content, until a critical acetone composition created a change in the ratio between solute:solute/solvent:solvent and solute:solvent interactions.

Interestingly, the slopes of the van't Hoff plots were found to be relatively similar for solutions with excess toluene and for higher solution acetone content above y = 0.85. Deviations found for the mixed-solvent solutions with excess acetone content demonstrated changing temperature dependence of solution activity, and as such, solution structure, as a function of composition, as outlined by the varying values of aT in Table 4.2.

Values of ΔH_{diss}, ΔS_{diss} and the range of Υ calculated for eicosane in toluene solution were close to those calculated in a previous study by Tang et al.[25], which focussed on hexadecane and octadecane mixtures crystallising from three fuel representative solvents, including toluene. Values of around 69 kJ mol^{-1}, 0.24 kJ mol^{-1} K^{-1} and the range 1.40 – 1.59 were calculated in the aforementioned study, for ΔH_{diss}, ΔS_{diss} and the range of Υ over the concentration range studied, respectively.

Table 4.2. Thermodynamic parameters and activity coefficients (Υ) as a function of temperature calculated from van't Hoff analysis.

Acetone mol fraction (y)	**Enthalpy of dissolution (kJ mol^{-1})**	**Entropy of dissolution (kJ mol^{-1} K^{-1})**	**Enthalpy of mixing (kJ mol^{-1})**	**Entropy of mixing (kJ mol^{-1} K^{-1})**	**Concentration Range (g L^{-1})**	$ln\,\Upsilon = aT + c$
0	78.36	0.255	35.50	0.116	250 - 850	-0.05T + 1.60
0.14	93.99	0.307	51.13	0.169	200 - 800	-0.07T + 2.16
0.26	116.28	0.382	73.42	0.243	200 - 500	-0.11T + 3.01
0.38	132.89	0.436	90.02	0.297	200 - 500	-0.13T + 3.76
0.49	130.71	0.425	87.85	0.286	150 - 450	-0.12T + 4.12
0.59	155.35	0.504	112.48	0.365	150 - 450	-0.16T + 5.32

0.68	182.22	0.590	139.36	0.452	150 - 450	-0.19T + 6.64
0.77	198.03	0.638	155.17	0.500	100 - 400	-0.21T + 7.73
0.85	224.72	0.721	181.86	0.582	75 - 375	-0.24T + 9.38
0.93	144.45	0.448	101.58	0.309	20 - 140	-0.14T + 7.24
1	100.52	0.296	57.65	0.157	5 - 35	-0.08T + 6.41

4.4.3 Analysis of the Nucleation Kinetics

For eicosane in mixed toluene/acetone solutions the resultant nucleation mechanisms, Table 4.1, varied as a function of solution composition and concentration, in line with the trends observed for the solution thermodynamics and MSZW analysis. For solution compositions from $0 < y < 0.49$ and $y = 1$, the nucleation mechanism was found to be predominantly IN, which is consistent with a previous study that focussed on the nucleation of hexandecane/octadecane mixtures from single solvent solutions, with both alkanes being found to predominantly nucleate via IN pathway[22]. In contrast, for solution compositions ranging from $0.59 < y < 0.93$, the predominant nucleation mechanism was found to be PN.

For the PN cases, the calculated effective interfacial tensions, critical nuclei radius and number of molecules within the critical nuclei are given in Table 4.3. Comparatively, low values of effective interfacial tension, ranging from 0.38 – 1.94, were calculated for all PN systems studied, consistent with data on other long-chain hydrocarbons[28], and consistent with the nucleation process being predominantly heterogeneous. The latter may also explain the low calculated values for the critical nucleus size and number of molecules within the critical nucleus. Nonetheless, the overall behaviour of interfacial tension as a function of composition was found to closely mirror the variations observed for crystallisability and solution thermodynamics over the range of compositions studied.

Table 4.3. Values of effective interfacial tension (γ_{eff}), critical nuclei radius (r^*) and number of molecules within the critical nuclei (i^*) for the PN systems.

Conc. (g L^{-1})	**γ_{eff} (mJ m^{-2})**	**r^* (nm)**	**i^***
y = 0.59			
250	0.38	0.28 - 0.12	0.18 - 0.01
350	0.86	0.62 - 0.29	1.95 - 0.20
450	0.87	0.62 - 0.28	2.20 - 0.19
y = 0.68			
150	0.89	0.51 - 0.23	1.10 - 0.10
250	1.19	0.73 - 0.35	3.26 - 0.37

350	1.41	0.72 - 0.36	3.14 - 0.40
450	1.02	0.54 - 0.26	1.33 - 0.14
y = 0.77			
100	1.15	0.56 - 0.26	1.44 - 0.14
200	1.16	0.61 - 0.28	1.92 - 0.19
300	0.96	0.52 - 0.23	1.20 - 0.10
400	1.94	0.72 - 0.40	3.06 - 0.53
y = 0.85			
75	1.54	0.64 - 0.32	2.23 - 0.28
175	1.72	0.73 - 0.39	3.19 - 0.50
275	1.62	0.67 - 0.34	2.48 - 0.32
375	1.86	0.71 - 0.38	3.03 - 0.46
y = 0.93			
60	1.19	0.81 - 0.40	4.46 - 0.55
100	1.00	0.77 - 0.39	3.82 - 0.50
140	1.28	0.84 - 0.45	4.89- 0.77

4.4.4 Compositional Trends

Examination of the results of the crystallisability, solution thermodynamics and nucleation kinetics data clearly demonstrate concurrent trends over the full compositional range for the eicosane in toluene/acetone mixed-solvent system. For all solution compositions, the average MSZWs, over the range of concentrations studied, were found to increase for compositions ranging from $0 < y < 0.85$. This was subsequently followed by a decrease in average MSZW with increasing solution acetone content to a solution composition of $y = 1$. This same trend was observed for values of enthalpies of dissolution and mixing, the average slope values from linear regressions fitted to plots of $\ln u_c$ vs. $\ln q$, over the full compositional range studied and the values of effective interfacial tension, Figure 4.7. This demonstrates a clear link between the crystallisability, solution thermodynamics and nucleation kinetics and mechanism, which are all dominated by the solution structure.

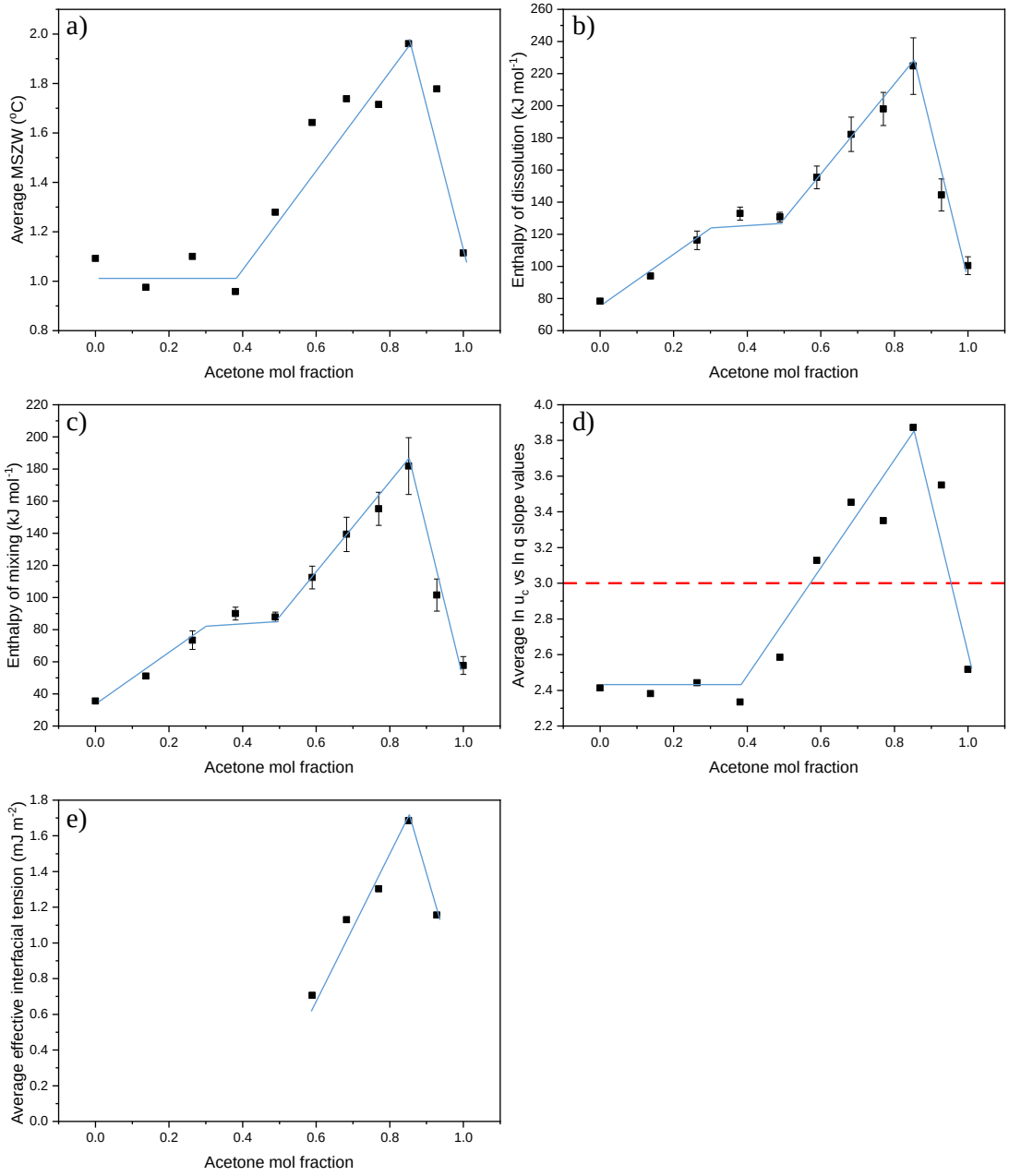


Figure 4.7. Trends in values obtained over the compositional range studied for crystallisability, solution thermodynamics, nucleation mechanism and effective interfacial tension. a) average MSZW values over the concentration ranges studied; b) enthalpy of dissolution; c) enthalpy of mixing; d) average slope values obtained from $\ln q \ vs. \ln u_c$ *over the concentration ranges studied; e) average effective interfacial tension values calculated in the range of 0.59 < y < 0.93. Red dotted line in d) represents transition from IN (<3) to PN (>3).*

4.4.5 Intermolecular Grid-Search Modelling

Results summarising the calculated solvation sites for a single eicosane molecule solvated with toluene and acetone, using different low-pass energy cut-off filters, are given in Figure 4.8.

Examination of the energy-filtered data reveals that both toluene and acetone can easily solvate the surfaces of eicosane, with the strongest binding interactions with the carbon backbone of the eicosane molecule, where the number of potential atom-atom van der Waals interactions is highest. However, higher energy cut-off filtering revealed that acetone's solvation propensity diminished quite rapidly. In contrast, toluene was found to maintain strong solvation propensity over the majority of the eicosane molecule, even at the highest energy cut-offs. The full solvation site analysis is given in Appendix D.

Figure 4.9 shows the distribution of binding site energies as a function of the number of calculated interactions. As might be expected on the basis of molecular weight, the strength of intermolecular interaction energies of eicosane with other eicosane molecules were much higher than for other possible solution interaction types, correlating well with the less than ideal solution behaviour observed. Furthermore, in terms of solute:solvent interactions, toluene was found to interact more strongly with eicosane than acetone was, in line with measured relative solubilities, with acetone/eicosane interactions found to be the weakest interaction type calculated, suggesting that in solution acetone may have been more likely to interact with either itself or toluene, instead of eicosane. This is in line with calculated atomic fractional charges for the studied molecules, provided in Appendix D, which demonstrate increasing charge distribution from eicosane < toluene < acetone. Acetone, therefore, would have stronger electrostatic interactions with itself or toluene than with eicosane in the solution environment.

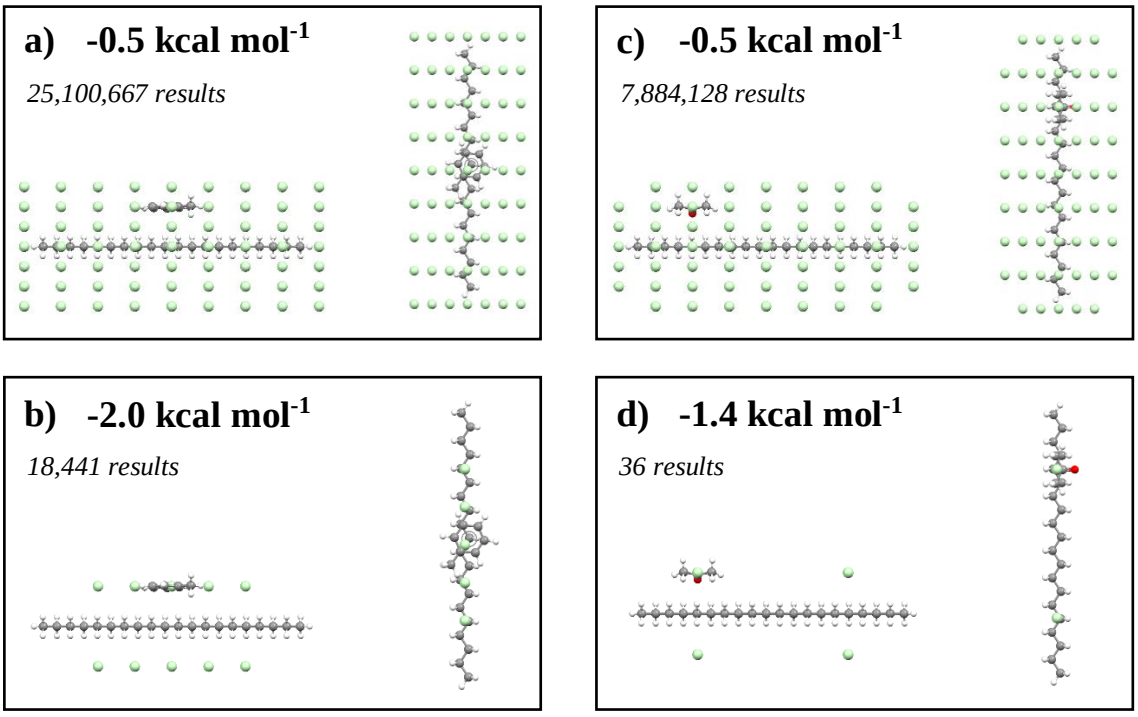


Figure 4.8. Interaction energy fields of toluene (a and b) and acetone (c and d) probe molecules, with a central eicosane molecule. Toluene and acetone molecules show most negative interaction energy site. The green dots represent interaction locations of the probes, which passed the set energy filter cut-offs that are highlighted at the top left of images.

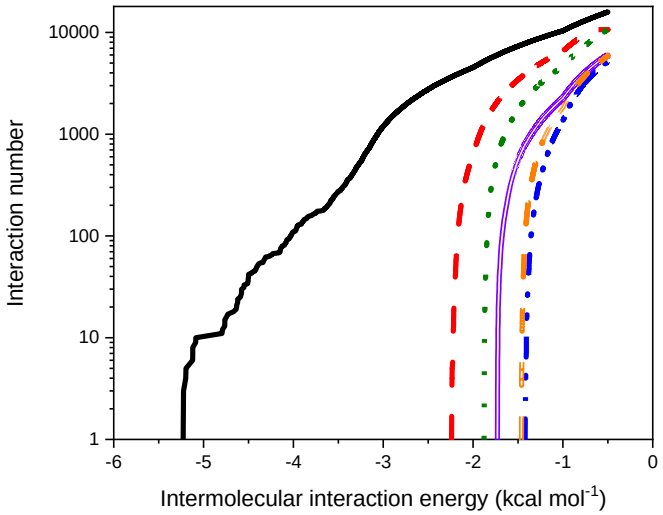
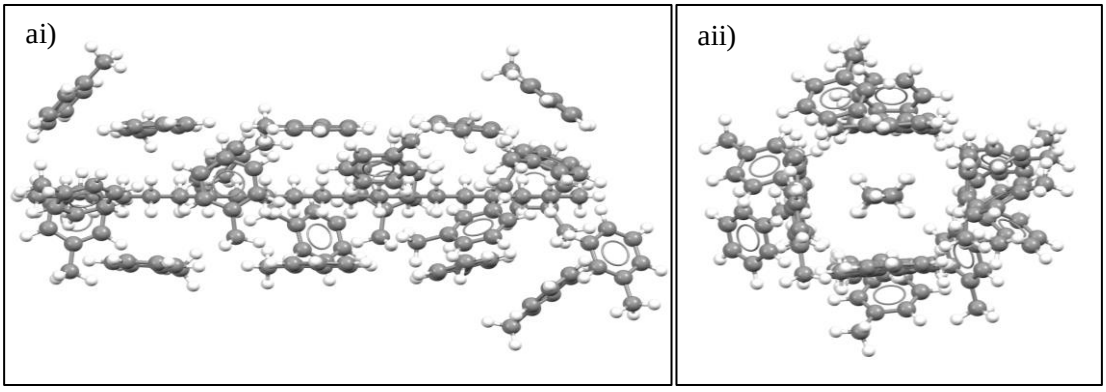


Figure 4.9. Calculated intermolecular interaction energies for possible interaction types in eicosane in toluene/acetone solution, over the total interactions calculated. High-energy cut-off set at -0.5 kcal mol^{-1}. Coloured lines represent different intermolecular interactions: eicosane/eicosane (black solid line), eicosane/toluene (red dashed line), eicosane/acetone (blue dot-dash line), toluene/toluene (green dotted line), acetone/acetone (purple double line) and toluene/acetone (orange double dashed line).

Figure 4.10 summarises the results of the solute:solvent simulation highlighting the predicted solvation shell structure based upon different toluene/acetone ratios. The simulation data reveals that for the 10:10 and 15:5 ratios of toluene/acetone, the acetone molecules preferentially bind to the toluene molecules, creating, what is effectively, a 'second shell' around the primary toluene solvation of eicosane rather than filling the potential empty solvation sites.



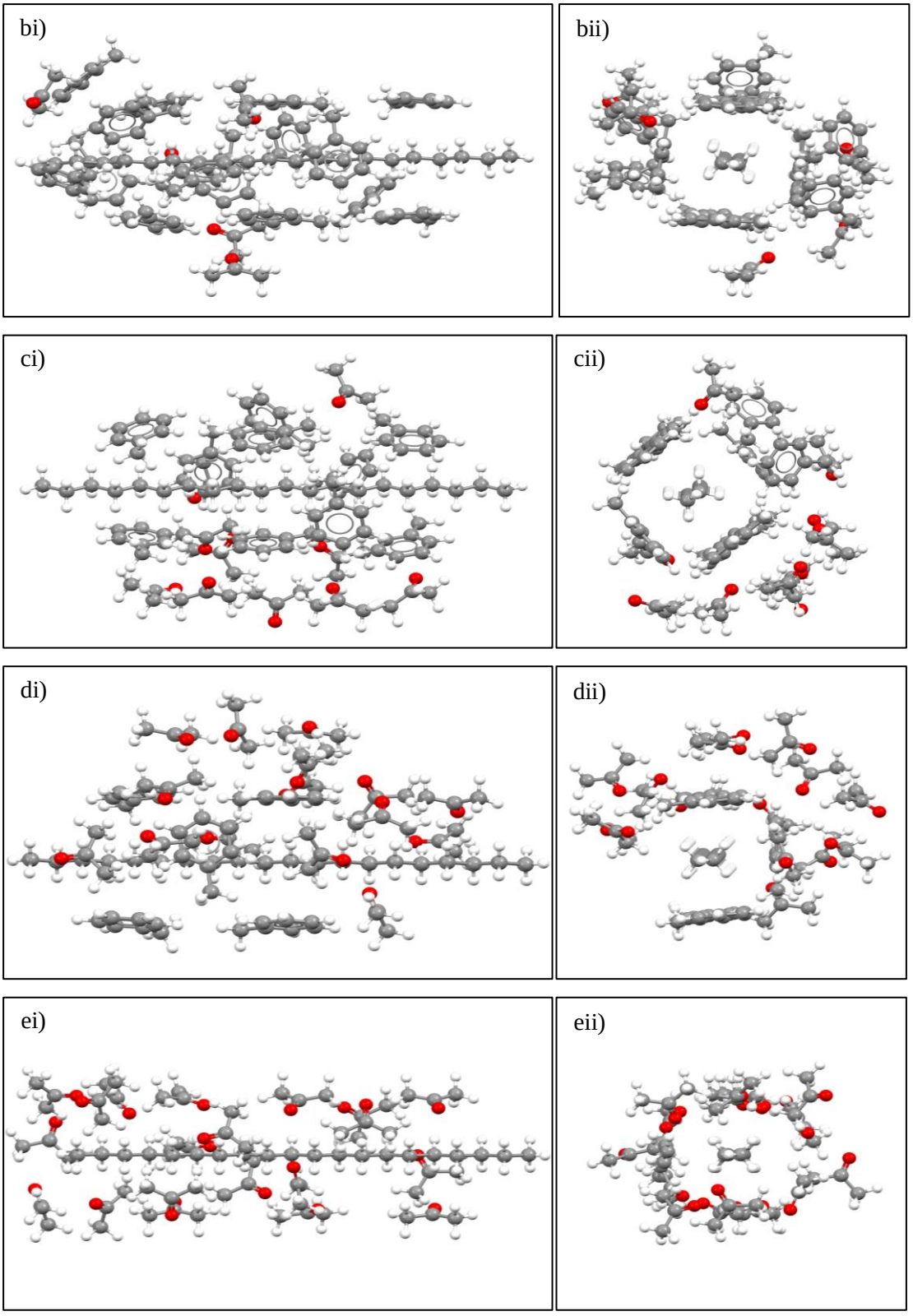


Figure 4.10. Solvent clusters built using the intermolecular gird-search method around eicosane molecules, in different toluene/acetone ratios, with toluene molecule interactions determined first, followed by acetone molecules. a) 20:0; b) 15:5; c) 10:10; d) 5:15 and e) 0:20. i) and ii) represent different views of solvation clusters along and down the carbon backbone of eicosane, respectively.

For the 5:15 ratio of toluene/acetone intermolecular grid search result the acetone molecules were still found to create a 'second' solvation shell around the toluene molecules that were solvating the eicosane molecule, but some free eicosane solvation sites were filled with acetone molecules. This suggests that when the ratio of acetone to toluene was high enough, the acetone molecules would more strongly solvate the eicosane molecule. Therefore, for the studied solutions, above a critical acetone composition the disruptive solvent:solvent interaction effect is likely to be somewhat overcome.

Examination of the calculated solvation energies based on these cluster structures, as well as the intermolecular solvent:solvent interaction energies within the solvation shell are given in Table 4.4. In general, the total solvation energy was found to decrease with an increase in acetone composition, in line with the trend observed in measured solubility over the mixed-solvent compositional range studied. However, a slight increase in solvation energy was calculated from a toluene/acetone ratio of 5:15 to 0:20. This correlates well to the observed solubility behaviour at lower solution temperatures, where eicosane solubility increased from solutions with a high acetone composition to pure acetone solutions and suggests a changing nature of solvent:solvent interactions affecting solvation power.

The solvent:solvent interactions in the solvation shell were found to be strongest for 10:10 toluene/acetone with decreased total intermolecular interaction energies for 5:15 and 15:5 toluene/acetone ratios. This further suggests that strong toluene/acetone interactions were present in the mixed solvent solutions, with a decrease in interaction intensity with an excess of one of the solvents in solution.

Table 4.4. Solvation energies and intermolecular interaction energies between toluene and acetone molecules in the solvation shell for the solvation of eicosane at different toluene/acetone molecular ratios.

Toluene/Acetone Molecular Ratio	**Interaction Energy (kcal mol^{-1})**	
	Total Solvation	**Toluene/Acetone**
20:0	-54.71	-
15:5	-52.39	-27.80
10:10	-46.54	-41.96
5:15	-38.84	-30.69
0:20	-43.72	-

4.5 Discussion

Intermolecular grid-search results suggest that acetone molecules could be more likely to 'solvate' toluene molecules and disrupt the solute:solvent interactions, until a critical acetone composition is reached whereby acetone molecules solvate eicosane more readily. These predictions provide insight into the increasing enthalpies of dissolution and mixing values up to a solution composition of y = 0.85, due to strong interactions between acetone and toluene in the solvation shell, decreasing the solvation power towards eicosane and, as such, decreasing solute:solvent interaction strengths, followed by a decrease in enthalpic values, due to increased acetone solvation.

This behaviour also provides a potential insight into the similar trends in MSZW and changes in the nucleation mechanism. An IN pathway represents solutions containing stable prenucleation clusters and at a critical level of supersaturation, there is sufficient driving force for nucleation to occur for all clusters present. Practically, this represents the case whereby all nucleation events within the solution occur at one instance, with only crystal growth occurring after this stage. In contrast, PN suggests that the prenucleation clusters would have a lower stability, therefore only certain clusters would be able to overcome the free energy barrier required for nucleation to occur at one instance of time, resulting in concomitant crystal nucleation and growth processes occurring within solution as crystallisation progresses in the system

For the PN systems, the solution environments had an excess of acetone molecules, with respect to toluene. This change in nucleation mechanism perhaps suggests that when acetone is in excess in solution, there was a more complicated solution structure, whereby the solvation layer around eicosane molecules is more disordered, containing a high number of heterogeneous and homogeneous solvent:solvent interactions. Such a structure could disrupt the diffusive transport of eicosane molecules into the prenucleation clusters, seen when toluene is in excess, given acetone's limited intermolecular interactions with eicosane. This would have the effect of lowering the attachment frequency of eicosane to a growing cluster, hence reducing the nucleation rate constant, K_J, and, as such, the rate of nucleation (Equation 4.12). Thus, only some of the eicosane clusters might reach a critical cluster size and be able to nucleate, before a stable equilibrium in solution was reached. This would result in the case of nucleation events occurring over time, creating concomitant nucleation and growth processes at different locations within solution, in line with the PN mechanism.

In contrast, for the IN cases the solutions either had an excess toluene component with respect to acetone or a single solvent environment, with potentially less disruptive heterogeneous solvent:solvent interactions and hence a lower barrier to the formation of stable prenucleation clusters within solution. Therefore, a distribution of stable prenucleation clusters could be able to form prior to the nucleation stage, once a critical level of supersaturation corresponding to the limit of the MSZW had been reached, with all clusters nucleating at once. Although speculative, at this stage such a model could also explain the increase in MSZW with increasing acetone composition, and as such a lower ease of crystallisation, until a critical acetone composition was reached, in which this behaviour was reversed. Further support for this comes with the calculated values of effective interfacial tension, which mirror the behaviour of the MSZW with mixed-solvent composition, notably in such a case that a higher level of supersaturation would be needed to overcome the energy barrier required to create a solid nucleus surface. This suggests that strong interactions between acetone and toluene molecules might lead to weaker interactions with eicosane clusters, thereby increasing the barrier to the formation of nuclei surfaces, driving up the effective interfacial tension and lowering the crystallisability. This would be consistent with an increase in the thermodynamic parameter *b* associated with the nucleation rate expression (Equation 4.12), which would reduce the rate of nucleation of eicosane in these solutions. This, coupled with a reduction in the nucleation rate constant, would essentially create a more thermodynamically controlled nucleation process, more consistent with the progressive nucleation pathway.

The resulting changes in nucleation behaviour and mechanism as a function of mixed-solvent composition, also align well with previous studies that have demonstrated that, in single solvent solutions, the IN mechanism is associated with stable prenucleation clusters in solution[24] and a shift towards a PN pathway can be associated with a disruption of the ability of solutions to form stable clusters prior to nucleation[23]. This demonstrates a wider applicability of the results outlined in this study towards other crystallising systems.

The changing nature of solution behaviour above a critical acetone solution content at around y = 0.85 could also represent increased solvent structuring in solution, as demonstrated by decreasing values of the entropy of dissolution and mixing. Acetone is known to structure through strong carbonyl intermolecular interactions in its crystal structure and liquid state[50], which could enable free interactions between the methyl groups and solute molecules within solutions, with a high concentration of acetone molecules. This could provide an additive solubilising effect towards eicosane in solution alongside the more strongly interacting toluene molecules, which could be responsible for the observed increases in solubility at lower solution

temperatures, for solutions with a high acetone content above y = 0.85. However, further study is needed to investigate this possible behaviour.

4.6 Conclusions

Eicosane in mixed toluene/acetone solvent solutions was studied over a range of solution compositions from pure toluene to pure acetone, revealing comparatively small MSZWs for all solution compositions in comparison to other organic crystallising systems, highlighting their ease of crystallisability. A broadly inverse relationship between solution concentration and MSZW was found for solution compositions at acetone mol fractions (y) of $0 < y < 0.49$ and $0.93 < y < 1$. In contrast, the opposite relationship was observed for solution compositions of $0.53 < y < 0.85$.

The solubility of eicosane was found, in general, to decrease with increasing solution acetone content. At higher solution temperatures, small additions of acetone to pure toluene solutions were found to increase solubility, whereas at lower solution temperatures this behaviour was not observed and when acetone was in excess, further additions of acetone increased solubility above a solution composition of y = 0.85. All solutions revealed less than ideal behaviour, with activity coefficient temperature dependency altering as a function of mixed-solvent composition. Both the enthalpies of dissolution and mixing were found to increase over the compositional range of $0 < y < 0.85$, followed by a decrease with higher acetone content, demonstrating a change in solution chemistry above a critical solution acetone composition.

Intermolecular grid search results from energy cut-off calculations were in good agreement with the solubility findings, with toluene molecules being found to interact much more strongly with eicosane than did acetone molecules. The strongest solvation sites were found to be along the carbon backbone of the eicosane molecule, where closer atom-atom contacts and strong van der Waals interactions were readily available. Intermolecular interaction energies revealed eicosane/eicosane interactions to be the strongest, in line with the less than ideal behaviour observed for all solutions. Acetone was found to interact more strongly with itself and toluene than with eicosane, suggesting that it would have limited interaction with eicosane in a mixed-solvent solution environment.

Analysis of nucleation kinetic data revealed that solution compositions in the range $0 < y < 0.49$ and y = 1, nucleated via an IN mechanism, whilst in contrast, solution compositions ranging from $0.59 < y < 0.85$ were found to predominantly nucleate via the PN pathway, the latter suggesting a more thermodynamically-controlled system. The kinetic and thermodynamic

dependencies of the nucleation of these solutions were found to correlate to the dependency of the MSZW vs. the solution concentration behaviour observed. PN solutions crystallised with low effective interfacial tensions, in line with previous studies on alkane systems, but were found to increase with increasing acetone composition up to y = 0.85, above which, the effective interfacial was found to decrease again.

The key crystallisation process metrics were all found to follow the same consistent behaviour as a function of mixed-solvent composition, notably: MSZW, enthalpies of dissolution/mixing, interfacial tension and the balance between the thermodynamic and kinetic factors on the nucleation process, calculated by the IN/PN determination slopes. Analysis of solvation energies and cluster structures was found to provide an insight into the potential intermolecular clustering behaviour within this mixed-solvent solution, notably acetone interacts more strongly with toluene than with eicosane, with the latter not being effectively solvated by acetone molecules in the mixed-solvent solutions. A 'cage' of acetone molecules created due the stronger toluene/acetone interactions limited the ability of eicosane to form stable prenucleation clusters throughout solution, altering the nucleation mechanism from IN to PN when acetone was in excess. Above a critical acetone content this effect was overcome.

Overall, the solution chemistry and structure were found to directly relate to crystallisation behaviour and this was integrated within a methodological workflow, developed to aid future research into mixed solvent solution crystallisation processes.

4.6.1 Future Work and Current Limitations

The molecular grid-search based modelling of indicative solution structure could be enhanced in future work through its integration with more atomistically detailed modelling molecular dynamic (MD) simulations, which would have the potential to provide a more complete and extended structural insight into the solution environment, associated with solvation by mixed solvent systems. Through this, the longer-range solution structure and its relationship, as well as its relationship with the solute mass transfer, could be directly related to the subsequent nucleation kinetics.

Furthermore, small angle neutron scattering (SANS) of mixed-solvent systems using deuteration to confirm specific solvent species within the mixed-solvent environments, could potentially validate the solvation structural ordering proposed in this work.

4.7 References

1. Myerson, A. S., Decker, S. E. & Welplng, F. Solvent Selection and Batch Crystallization. *Ind. Eng. Chem. Process Des. Dev.* **25**, 925–929 (1986).
2. Zhu, Y. *et al.* Study of the solubility and the metastable zone of 1,3-dihydroxyacetone for the drowning-out process. *J. Cryst. Growth* **257**, 370–377 (2003).
3. Roelands, C. P. M. *et al.* Antisolvent crystallization of the polymorphs of L-histidine as a function of supersaturation ratio and of solvent composition. *Cryst. Growth Des.* **6**, 955–963 (2006).
4. Jiang, S., Horst, J. H. & Jansens, P. J. Concomitant Polymorphism of o-Aminobenzoic Acid in Antisolvent Crystallization. *Cryst. Growth Des.* **8**, 37–43 (2008).
5. Wantha, L., Punmalee, N., Sawaddiphol, V. & Flood, A. E. Effect of ethanol on crystallization of the polymorphs of L-histidine. *J. Cryst. Growth* **490**, 65–70 (2018).
6. Granberg, R. A., Bloch, D. G. & Rasmuson, C. Crystallization of paracetamol in acetone — water mixtures. *J. Cryst. Growth* **198/199**, 1287–1293 (1999).
7. Rosbottom, I. *et al.* Influence of Solvent Composition on the Crystal Morphology and Structure of p-Aminobenzoic Acid Crystallized from Mixed Ethanol and Nitromethane Solutions. *Cryst. Growth Des.* **17**, 4151–4161 (2017).
8. Plasari, E., Grisoni, P. H. & Villermaux, J. Influence of process parameters on the precipitation of organic nanoparticles by drowning-out. *Chem. Eng. Res. Des.* **75**, 237–244 (1997).
9. Sangwal, K. On the interpretation of metastable zone width in anti-solvent crystallization. *Cryst. Res. Technol.* **45**, 909–919 (2010).
10. Sangwal, K. & Mielniczek-Brzóska, E. Antisolvent crystallization of aqueous ammonium dihydrogen phosphate solutions by addition of methanol. *J. Cryst. Growth* **451**, 139–149 (2016).
11. Zou, F. *et al.* Determination of metastable zone widths and the primary nucleation and growth mechanisms for the crystallization of disodium guanosine 5′-monophosphate from a water-ethanol system. *Ind. Eng. Chem. Res.* **54**, 137–145 (2015).
12. Zhang, Y., Jiang, Y., Zhang, D., Qian, Y. & Wang, X. Z. Metastable zone width, crystal nucleation and growth kinetics measurement in anti-solvent crystallization of β-artemether in the mixture of ethanol and water. *Chem. Eng. Res. Des.* **95**, 187–194 (2015).
13. Gao, Z. *et al.* Self-Induced Nucleation during the Antisolvent Crystallization Process of Candesartan Cilexetil. *Cryst. Growth Des.* **18**, 7655–7662 (2018).
14. Roelands, C. P. M., Ter Horst, J. H., Kramer, H. J. M. & Jansens, P. J. Analysis of nucleation rate measurements in precipitation processes. *Cryst. Growth Des.* **6**, 1380–

1392 (2006).

15. Kaskiewicz, P. L. *et al.* Isothermal by Design: An Accelerated Approach to the Prediction of the Crystallizability of Slowly Nucleating Systems. *Org. Process Res. Dev.* **23**, 1948–1959 (2019).
16. Hammond, R. B., Pencheva, K., Ramachandran, V. & Roberts, K. J. Application of grid-based molecular methods for modeling solvent-dependent crystal growth morphology: Aspirin crystallized from aqueous ethanolic solution. *Cryst. Growth Des.* **7**, 1571–1574 (2007).
17. Kaskiewicz, P. L. *et al.* Isothermal by Design: Comparison with an Established Isothermal Nucleation Kinetics Analysis Method. *Chem. Eng. Technol.* **43**, 1971–1980 (2020).
18. Muller, F. L., Fielding, M. & Black, S. A practical approach for using solubility to design cooling crystallisations. *Org. Process Res. Dev.* **13**, 1315–1321 (2009).
19. Black, S. & Muller, F. On the effect of temperature on aqueous solubility of organic solids. *Org. Process Res. Dev.* **14**, 661–665 (2010).
20. Turner, T. D. *et al.* The influence of solution environment on the nucleation kinetics and crystallisability of para-aminobenzoic acid. *Phys. Chem. Chem. Phys.* **18**, 27507–27520 (2016).
21. Kashchiev, D. *Nucleation*. (Butterworth-Heinemann, 2000).
22. Tang, X. Crystal Structure, Phase Behaviour and Kinetics Associated with the Crystallisation of Octadecane, Hexadecane, and Mixtures Thereof. (2017).
23. Kaskiewicz, P. L. *et al.* Understanding and Designing Tailor-Made Additives for Controlling Nucleation: Case Study of p-Aminobenzoic Acid Crystallizing from Ethanolic Solutions. *Cryst. Growth Des.* (2021). doi:https://dx.doi.org/10.1021/acs.cgd.0c01209
24. Toroz, D. *et al.* Towards an understanding of the nucleation of alpha-para amino benzoic acid from ethanolic solutions: a multi-scale approach. *Faraday Discuss.* **179**, 79–114 (2015).
25. Tang, X. *et al.* Solubility and crystallisability of the ternary system: Hexadecane and octadecane representative in fuel solvents. *Fuel* **226**, 665–674 (2018).
26. Kashchiev, D., Borissova, A., Hammond, R. B. & Roberts, K. J. Effect of cooling rate on the critical undercooling for crystallization. *J. Cryst. Growth* **312**, 698–704 (2010).
27. Kashchiev, D., Borissova, A., Hammond, R. B. & Roberts, K. J. Dependence of the critical undercooling for crystallization on the cooling rate. *J. Phys. Chem. B* **114**, 5441–5446 (2010).
28. Camacho Corzo, D. M. *et al.* Nucleation mechanism and kinetics from the analysis of polythermal crystallisation data: methyl stearate from kerosene solutions.

CrystEngComm **16**, 974–991 (2014).

29. Rosbottom, I., Pickering, J., Hammond, R. B. & Roberts, K. J. A Digital Workflow Supporting the Selection of Solvents for Optimising the Crystallisability of Para Aminobenzoic Acid. *Org. Process Res. Dev.* **24**, 500–507 (2020).
30. OriginLab Corporation. Version 2014. Origin(Pro).
31. Technobis. Crystal16. (2020). Available at: https://www.crystallizationsystems.com/crystal16.
32. BIOVIA Dassault Systèmes. Materials Studio. *2019* Available at: https://www.3dsbiovia.com/portfolio/materials-studio.html.
33. Frisch, M. J. *et al*. Gaussian09, Revision D.01. (2016).
34. Breneman, C. M. & Wiberg, K. B. Determining atom-centered monopoles from molecular electrostatic potentials. The need for high sampling density in formamide conformational analysis. *J. Comput. Chem.* **11**, 361–373 (1990).
35. Becke, A. D. A new mixing of Hartree-Fock and local density-functional theories. *J. Chem. Phys.* **98**, 1372–1377 (1993).
36. Lee, C., Yang, W. & Parr, R. G. Development of the Colle-Salvetti correlation-energy formula into a functional of the electron density. *Phys. Rev. B* **37**, 785–789 (1988).
37. Hammond, R. B., Ma, C., Roberts, K. J., Ghi, P. Y. & Harris, R. K. Application of systematic search methods to studies of the structures of urea-dihydroxy benzene cocrystals. *J. Phys. Chem. B* **107**, 11820–11826 (2003).
38. Hammond, R. B., Hashim, R. S., Ma, C. & Roberts, K. J. Grid-based molecular modeling for pharmaceutical salt screening: Case example of 3,4,6,7,8,9-hexahydro-2H-pyrimido (1,2-a) pyrimidinium acetate. *J. Pharm. Sci.* **95**, 2361–2372 (2006).
39. Momany, F. A., Carruthers, L. M., McGuire, R. F. & Scheraga, H. A. Intermolecular potentials from crystal data. III. Determination of empirical potentials and application to the packing configurations and lattice energies in crystals of hydrocarbons, carboxylic acids, amines, and amides. *J. Phys. Chem.* **78**, 1595–1620 (1974).
40. Gasteiger, J. & Marsili, M. A new model for calculating atomic charges in molecules. *Tetrahedron Lett.* **19**, 3181–3184 (1978).
41. Gasteiger, J. & Marsili, M. Iterative partial equalization of orbital electronegativity-a rapid access to atomic charges. *Tetrahedron* **36**, 3219–3228 (1980).
42. The Cambridge Crystallographic Data Centre (CCDC). Mercury. (2020). Available at: https://www.ccdc.cam.ac.uk/solutions/csd-system/components/mercury/.
43. Nguyen, T. T. H., Hammond, R. B., Roberts, K. J., Marziano, I. & Nichols, G. Precision measurement of the growth rate and mechanism of ibuprofen {001} and {011} as a function of crystallization environment. *CrystEngComm* **16**, 4568–4586 (2014).
44. Swalen, J. D. & Costain, C. C. Internal Rotation in Molecules with Two Internal Rotors:

Microwave Spectrum of Acetone. *J. Chem. Phys* **31**, 1562 (1959).

45. Gerson, A. R., Roberts, K. J. & Sherwood, J. N. An instrument for the examination of nucleation from solution and its application to the study of precipitation from diesel fuels and solutions of n-alkanes. *Powder Technol.* **65**, 243–249 (1991).
46. Gerson, A. R., Roberts, K. J., Sherwood, J. N., Taggart, A. M. & Jackson, G. The role of growth environment on the crystallization of normal alkanes in the homologous series from C18H38 to C29H60. *J. Cryst. Growth* **128**, 1176–1181 (1993).
47. Taggart, A. M., Voogt, F., Clydesdale, G. & Roberts, K. J. An examination of the nucleation kinetics of n-alkanes in the homologous series C13H28 to C32H66, and their relationship to structural type, associated with crystallization from stagnant melts. *Langmuir* **12**, 5722–5728 (1996).
48. Roberts, K. J., Sherwood, J. N. & Stewart, A. The nucleation of n-eicosane crystals from solution in n-dodecane in the presence of homologous impurities. *J. Cryst. Growth* **102**, 419–426 (1990).
49. Mealey, D., Croker, D. M. & Rasmuson, Å. C. Crystal nucleation of salicylic acid in organic solvents. *CrystEngComm* **17**, 3961–3973 (2015).
50. Ferrer, P., Da Silva, I. & Puente-Orench, I. Solid acetone structure dependence on pressure: A new fibre textured thin film crystallographic structure studied by grazing-incidence X-ray diffraction. *CrystEngComm* **18**, 8220–8228 (2016).

Chapter 5 Understanding and Designing Tailor-Made Additives for Controlling Nucleation: Case Study of p-Aminobenzoic Acid Crystallising from Ethanolic Solutions

5.1 Abstract

A workflow for tailor-made additive screening and crystallisation control using a combination of molecular modelling and experimental techniques is presented. The impact of seven structurally analogous additives, the majority of which containing a carboxylic acid group, on the nucleation of alpha-para-aminobenzoic acid is assessed. Intermolecular grid-search modelling is used to determine dimer interaction energies. Of these, three tailor-made additives are found to form stronger carboxylic group dimer interactions with the compound. Solvation energy calculations demonstrate the stability of these dimers in solution. Subsequent intermolecular interaction assessment demonstrates an ability of one of the tailor-made additives to interfere with the molecular preassembly route to nucleation, with molecular charge distributions providing an insight into this effect. Polythermal crystallisation experimental screening confirms the effectiveness of these tailor-made additives to inhibit nucleation. Interestingly, the nucleation mechanism is found to change from instantaneous to progressive nucleation in the absence and presence of the tailor-made additives in solution, respectively, together with an increase in the effective interfacial tension.

5.2 Introduction

Crystallisation is a process that is extensively utilised in industry to produce a pure and stable solid form with defined physical and chemical properties. It is also, under certain conditions, an inevitable natural process that cannot be avoided, even when it is not desirable. To this latter end, steps can be taken to try and inhibit unwanted crystallisation, through e.g. solvent selection, to try and gain greater 'control' over the crystallisation processes to alter solubility[1], crystallisability[2], polymorphic[3–5] or solvated forms[6], etc. Additives are also often employed to aid in the control of crystallisation events[7].

The ability of additives to interfere with the crystallisation process has been well studied with respect to both inorganic[8–11] and organic[12–17] systems, as well as utilising computational modelling methodologies to try and understand their effect at a molecular level[18–20]. Studies on the influence of additives on the crystallisation process have focused heavily on tailor-made additives (TMAs), which refer to compounds added to a crystallisation system that act as imposter molecules, having only slight differing moieties than the solute to be crystallised, and as such, a similar molecular structure to the target solute[17]. TMA research has concentrated on their effect on crystal growth[18,19,21–23], however, their effect on the nucleation process has been an area of growing focus. These additives have the capacity to disrupt/aid the nucleation process

by interacting with nuclei cluster formation and/or cluster reorientation[24–27]. However, the process by which this can occur is extremely complex.

Although research into the effects of TMAs on nucleation has become a more prominent area of study[28], TMA selection can still be a somewhat empirical approach, whereby nucleation inhibition TMAs may be selected for study based on their molecular structure alone. However, this does not take into account the structural arrangement and binding energetics associated with the specific intermolecular (synthonic) interactions, relating to the nucleation stage of crystallisation. Such knowledge can greatly enhance understanding of how specific molecular moieties can disrupt nucleation, hence providing a resource and workflow for crystallisation process design. On a fundamental level, this can also give an indication into which solute:solute interactions are dominant in the pre-nucleation clustering process. Reflecting this, we introduce an in silico TMA screening tool that, whilst being computationally efficient, can provide an insight into both the relative strength of solute:solute and solute:TMA intermolecular interactions respectively, as well as their structural orientation in space, which when integrated with crystallographic structure can provide valuable insight into TMA effectiveness.

Grid-based molecular modelling tools have been successfully utilised for a number of fundamental crystallisation studies[20,29–35], including studies of the interaction of solvent molecules with pABA to aid in solvent selection and crystallisation process design[36]. In this paper, the grid-search approach has been used to understand the dominant molecular interactions between pABA and the TMAs, in terms of their synthonic interaction structures and energetics.

An experimental polythermal assessment was utilised for validation of in silico results and to provide insight into TMA influence on the nucleation process. The crystallisability, in terms of the steady-state metastable zone width (MSZW) to crystallisation as well as solution thermodynamics were assessed. These factors have previously been studied to gain an understanding of the effects of varying solvents and solute compositions on the crystallisation process[2]. The Kashchiev-Hammond-Borissova-Roberts (KBHR) approach[37–39], which has been used in a number of research studies, was employed to determine nucleation kinetic parameters and distinguish the mechanism by which the solutions nucleated, either through instantaneous or progressive nucleation (IN or PN, respectively). IN describes the process in which all nuclei form instantly and subsequently undergo crystal growth, whereas in PN nuclei continuously form in the presence of growing crystals.

This work focusses on a case study of the nucleation of p-aminobenzoic acid (pABA), Figure 5.1, from ethanol solution, in the presence of a selection of TMAs. pABA was selected for this study due to its functional groups being representative of many pharmaceutical compounds and is well studied in terms of polymorphism[40–44], morphology[45,46], solution structure[6,36,47–49], TMAs[27], nucleation[1,50–53] and growth[54]. A previous study by Black et al.[27] focused on the influence of two TMAs, 4-amino-3-methoxybenzoic acid (AMBA3), and 4-amino-3-nitrobenzoic acid (ANBA3), on pABA crystallisation and found that they were able to lower both the nucleation and growth kinetics, as well as direct polymorphic forms at a given solution scale. This work takes on a synthonic engineering perspective[55] and aims to more thoroughly elucidate the specific intermolecular interactions underpinning the ability of TMAs to disrupt pABA nucleation as well as provide a standardised TMA assessment procedure through the tools used in this study. In order to aid future studies in the area of TMA assessment and understanding, a multilayer workflow is presented.

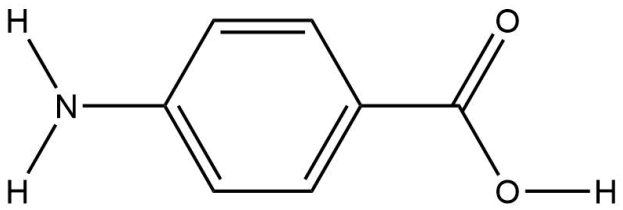


Figure 5.1. Molecular structure of p-aminobenzoic acid.

5.3 Workflow, Materials & Methods

A methodological workflow outlining the proposed steps for simple nucleation inhibition TMA screening and assessment, using the tools outlined in this work, is provided in Figure 5.2. This workflow was developed and utilised for TMA screening and assessment and is presented in order to try and aid future TMA selection and understanding. The stages presented outline the structure of the materials & methods and results & discussion sections of this article.

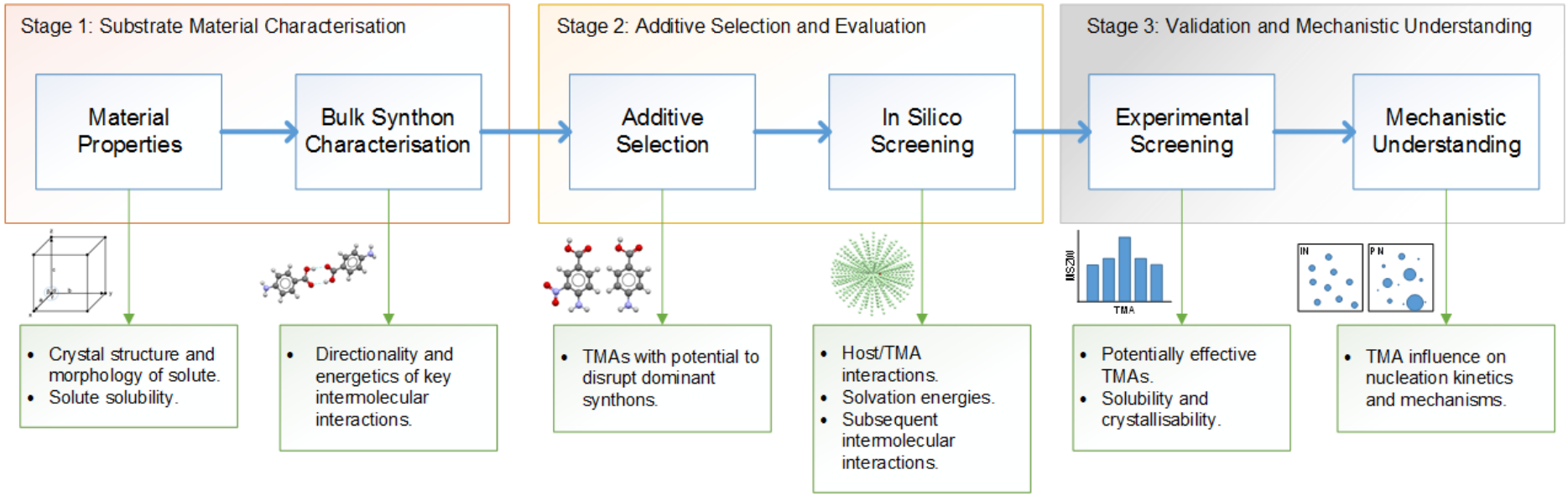


Figure 5.2. Diagrammatic workflow outlining key steps involved in TMA screening and assessment.

5.3.1 Material Properties & Bulk Synthon Characterisation

Material selection for TMA assessment in industrial environments is often dominated by product development, which dictates the solute that is studied. Knowledge of basic material properties of the target solute, such as crystal structure, morphology and solubility must be gained to optimise process design and aid in TMA assessment.

Knowledge of key synthons within the solute crystal structure can be obtained through experimental and/or computational material property assessment to determine key crystallographic data or through prior research/crystal databases, such as the Cambridge Structural Database (CSD)[56].

5.3.2 Additive Selection

In order to ensure experimental validation and assessment could take place, TMAs that were commercially available were used in this study. The criteria for TMA selection focussed upon molecular similarity to pABA as well as the bulk synthonic characterisation results, whereby TMAs were selected that could have potential strong intermolecular interactions with the dominant synthons present in the pABA crystal structure.

5.3.3 In Silico Screening

5.3.3.1 Calculation of TMA Interaction

Intermolecular grid searches were performed by using the molecular interaction energy predictor, available within the VisualHABIT synthonic engineering tool set[30]. These searches took pABA as the target molecule, centred around which a 3D spatial grid was defined, and a probe molecule (pABA or a TMA). A spherical grid with radius of 15 Å from the target molecule (pABA) with 10 steps of grid points on the radius, the polar angle and on the equator, provided a grid with total points of 921, which was defined for energy calculations. A description of the grid optimisation procedure used as well as visualisations of the grid are given in Appendix E. At each point on the grid, the probe molecule was placed and rotated through a grid of Euler angles, which were set at 4º for the x-axis, y-axis and z-axis. This resulted in a heterogeneous six dimensional search space, and at each point in this search space the interaction energy of the probe and target assemblies was calculated using the

Dreiding[57] potential. All grid based intermolecular interaction calculations were performed using a standard PC with CPU times in the range of minutes and hours.

Atomic fractional charges were derived from a calculation of the electrostatic potential at the density functional theory, using a 6-31G* basis set and the Becke three-parameter[58], Lee-Yang Parr exchange-correlation function[59], using Gaussian09[60]. This was completed using high performance computing with CPU times of less than one hour for each molecule studied.

Intermolecular interactions in the form of van der Waals, hydrogen bonding and electrostatic interactions were calculated. The strongest intermolecular interactions for pABA:pABA and pABA:TMAs were compared and the target and probe assemblies for the strongest interactions predicted were assessed, in terms of their geometrical arrangement, using the Biovia Materials Studio[61] software package to visualise the most prominent molecular interaction orientations.

The subsequent most energetically favourable dimer structures of each interaction pair were used to calculate the likely interactions of further pABA molecules. Five pABA molecules were used as probes, with the dimers used as the grid search target structures. The same grid dimensions and Euler angles, as well as interaction energy and interaction geometry assessment method, as aforementioned, were used.

5.3.3.2 Calculation of Solvation Energies

The intermolecular grid search method was also used to calculate the solvation energies of the most energetically favourable dimer structures determined from the pABA:pABA/TMA intermolecular interaction calculations. Twenty ethanol molecules were used as the probes, providing enough solvent molecules to ensure the target dimers were well solvated. A slightly smaller grid size of 14 Å with 9 steps of grid points on the radius, the polar angle and on the equator, was used, slightly reducing the number of grid points to enable the software to calculate interactions with the high number of probe molecules. Further optimisation of the calculated interaction shell, using the Forcite module within Biovia Materials Studio was performed. The SMART algorithm and a very fine tolerance was used to distinguish intra and inter-molecular interactions, ensuring solvation energies alone could be determined. For this, Gasteiger[62,63] atom point charges were utilised.

5.3.4 Experimental Screening

5.3.4.1 Materials

pABA, 3-aminobenzoic acid (mABA) and 4-nitrophenol (pNP) were supplied by Alfa Aesar, 4-amino-3-methoxybenzoic acid (AMBA3), 4-amino-2-methoxybenzoic acid (AMBA2), 4-amino-3-nitrobenzoic acid (ANBA3) and 4-amino-2-nitrobenzoic acid (ANBA2) were supplied by Fluorochem, 4-aminosalicyclic acid (pASA) was supplied by LKT Laboratories Inc. and ethanol absolute was supplied by Sigma-Aldrich. All materials were used as received without further purification.

5.3.4.2 Experimental Procedure

All experiments were performed using the Technobis Crystal16 system[64] at a 1 ml solution scale.

A TMA screen was performed through determination of changes in solution crystallisation temperature (T_c) in the presence of TMAs, using a polythermal analysis[2]. Solutions at a concentration of 0.17g (99 mol% pABA: 1 mol % TMA) g^{-1} ethanol were subjected to heating cycles at a rate of 0.5 °C min^{-1} between 37 °C and -15 °C, with constant magnetic stirrer bar agitation at 300 rpm. Temperature cycles were repeated 12 times to get average T_c and dissolution temperatures (T_{diss}). T_c and T_{diss} were determined through transmissivity data as a function of temperature, as described in a previous research article[2].

5.3.4.3 Mechanistic Understanding

The most effective TMA was further analysed and compared to the crystallisation of pABA from ethanol solution. Steady-state metastable zone width (MSZW) analysis, van't Hoff analysis and nucleation kinetic analysis through the KBHR approach, subsequently described, were performed. pABA in ethanol at concentrations of 0.14, 0.15, 0.16 and 0.17 g g^{-1} and pABA:TMA (99:1 mol%) in ethanol at concentrations of 0.18, 0.19, 0.20 and 0.21 g g^{-1} were studied. Heating cycles at rates of 0.3, 0.5, 0.7 and 0.9 °C min^{-1} in the temperature range 37 °C to -15 °C were used with a minimum of 5 repeats for pABA in ethanol solutions. For pABA:TMA in ethanol solutions, additional heating cycle rates of 0.4, 0.6 and 0.8 °C min^{-1} were used. T_c, T_{diss}, the equilibrium crystallisation temperature at the kinetic limit ($T_{c/l}$) and the equilibrium dissolution temperature (T_e) were determined as described elsewhere[2]. The difference between $T_{c/l}$ and T_e provided the steady-state MSZW.

A van't Hoff analysis was performed from the obtained solubility data to determine how the systems of study deviated from ideality, with the ideal solubility of pABA obtained from previous literature[49]. Activity coefficients (Υ), enthalpy (ΔH_{diss}) and entropy (ΔS_{diss}) of dissolution were calculated based on the following equations[65,66]:

$$\ln(x_{ideal}) = \frac{\Delta H_{fus}}{R}\left[\frac{1}{T} - \frac{1}{T_m}\right] \quad 5.1$$

$$\Upsilon = \frac{x_{ideal}}{x} \quad 5.2$$

$$\ln(x) = -\frac{\Delta H_{diss}}{RT} + \frac{\Delta S_{diss}}{R} \quad 5.3$$

Where x_{ideal} is the solution concentration, x is the experimentally measured mole fraction, ΔH_{fus} is the enthalpy of fusion, R is the ideal gas constant, T is the temperature and T_m is the melting temperature.

The KBHR approach was undertaken to gain an insight into the mechanism by which pABA:TMA in ethanol solutions nucleated in comparison to pABA in ethanol solutions, as well as to determine nucleation kinetic parameters to assess changes in the effective interfacial tension (γ_{eff}) to nucleation, giving an insight into the ease by which the systems crystallised. The KBHR approach relates the relative critical undercooling (u_c) to the cooling rate (q), utilising classical nucleation theory (CNT). u_c was calculated through the relationship:

$$u_c = \frac{\Delta T_c}{T_e} \quad 5.4$$

Where, $\Delta T_c = T_e - T_c$

Plots of u_c vs q in ln-ln coordinates were produced, with slopes of fitted linear regressions providing information as to the mechanism of nucleation. A slope <3 indicated an instantaneous nucleation pathway, whereas a slope >3 signified a progressive nucleation pathway. IN describes the pathway by which all nucleation active sites in a system (in this case a solution) have practically equal activities. Therefore, when a level of supersaturation is reached, corresponding to the critical level of supersaturation required for nucleation, all nucleation events occur at one instance. In contrast, PN describes the pathway by which nucleation active centres have a range of activities and therefore this non-uniform distribution of energies results in nucleation events occurring over a range of time, once individual nuclei reach the critical cluster size required for nucleation, where nucleation events can take place in the presence of already growing crystals.

For the case of PN, The final expression for $u_c(q)$ dependence, when expressed through the number of crystallites at the detection point (N_{det}), is defined as:

$$\ln q = \ln q_0 + a_1 \ln u_c - \frac{a_2}{(1-u_c)u_c^2} \quad 4.5$$

Plots of u_c vs. ln q fitted with equation 5 enabled parameters to be determined for the calculation of the nucleation kinetic parameters of γ_{eff}, the critical nucleus radius (r^*) and the number of molecules in the critical nucleus (i^*).

A full description of the KBHR analysis approach methodology is outlined in a previous research article[39].

5.4 Results & Discussion

5.4.1 Material Properties

pABA has a number of polymorphic forms, but has two major polymorphs, α- and β-pABA, with α-pABA being the most commonly observed form. This paper concerns the α-polymorph, which is subsequently referred to simply as pABA. pABA crystallises in the monoclinic crystal system, with space group $P2_1/n$ and 2 molecules in the asymmetric unit. The mix of polar and apolar structural groups of pABA, as well as the structurally distinct polymorphs with very different physical properties, make this an attractive model compound. The needle-like alpha form of pABA often dominates the crystallisation from organic solvents and has been shown to be highly soluble in ethanol[48].

5.4.2 Bulk Synthon Characterisation

Synthon analysis of pABA has been previously studied, with the results summarised here. The solid-state packing of pABA is made up of -O-H···O- dimer hydrogen bonding (synthon A), head-to-head π-π stacking of the phenyl rings (synthon B) and amine to carboxylic group -N-H···O- hydrogen bonding (synthon C) synthons (Figure 5.3)[46]. Several studies of the nucleation rates in different solvents and pre-nucleation structure has indicated that the desolvation of the carboxylic acid group, along with the subsequent formation of the pABA:pABA OH…O H-bond, is an important step for the nucleation of the alpha-form[45,47,48,52,67]. However, computational and experimental studies in water and nitromethane have implied that disruption of the π-π stacking interactions can also impact upon the nucleation behaviour of pABA[6,27,51] and may be the dominant synthon type in controlling the

nucleation of pABA from solution[27,51]. Although there is evidence to support both the synthon A and the synthon B hypothesis for pABA nucleation control, open literature is more suggestive of synthon A dominance in ethanol solution, which is the basis of the work presented in this paper. A thorough discussion on these contrasting views in provided in Appendix E.

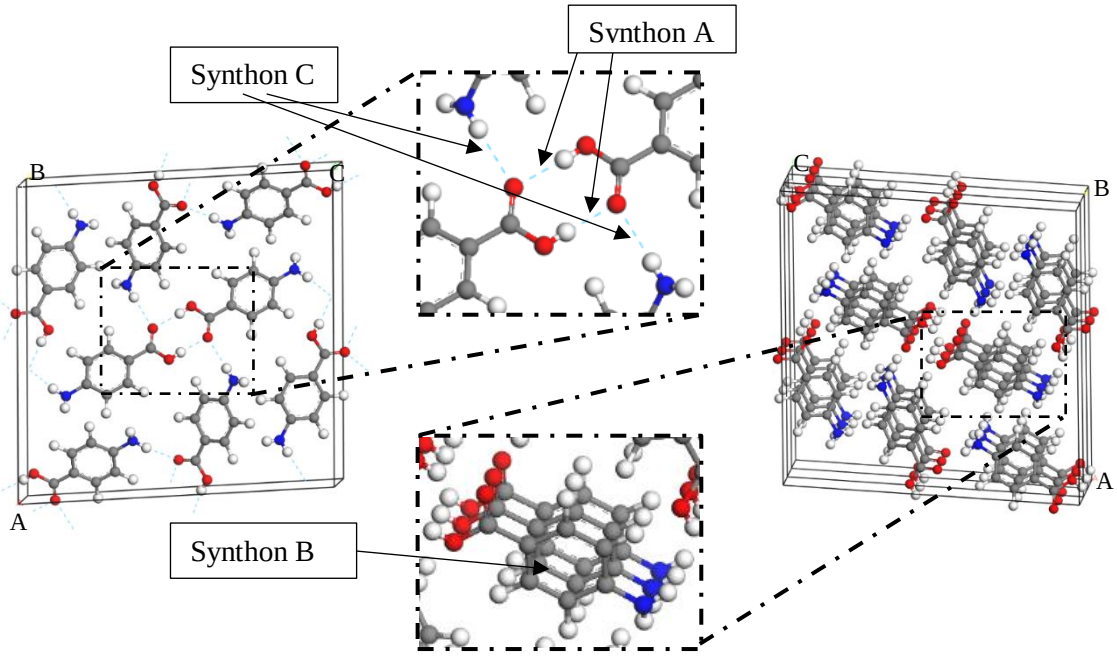


Figure 5.3. pABA crystal structure. Left-hand side - pABA unit cell, showing carboxylic dimer -O-H···O- hydrogen bonding (synthon A) and -N-H···O- hydrogen bonding (synthon C). Inset shows dominant hydrogen bonding tetramer intermolecular interactions. Blue dashed lines show intermolecular hydrogen bonding. Right-hand side - pABA structural packing in the c-axis, showing π-π stacking of the cyclic rings of pABA (synthon B). Inset highlights π-π stacking. Taken from AMBNAC07 in Cambridge Structural Database[46].

5.4.3 Additive Selection

Potential nucleation inhibition additives were selected based on two factors. Firstly, in order to meet the criteria of being termed TMAs, as outlined by the seminal work of the Weizmann Institute[17], additives that had molecular similarity to pABA were selected. Also, knowledge gained from the aforementioned pABA bulk synthon characterisation[45] was used to aid selection of TMAs that could potentially impact upon the important pABA crystallographic synthons, i.e. through exploiting electrostatic or steric hindrance effects, in an effort to inhibit nucleation. The molecular structures of pABA and all TMAs studied are given in Figure 5.4.

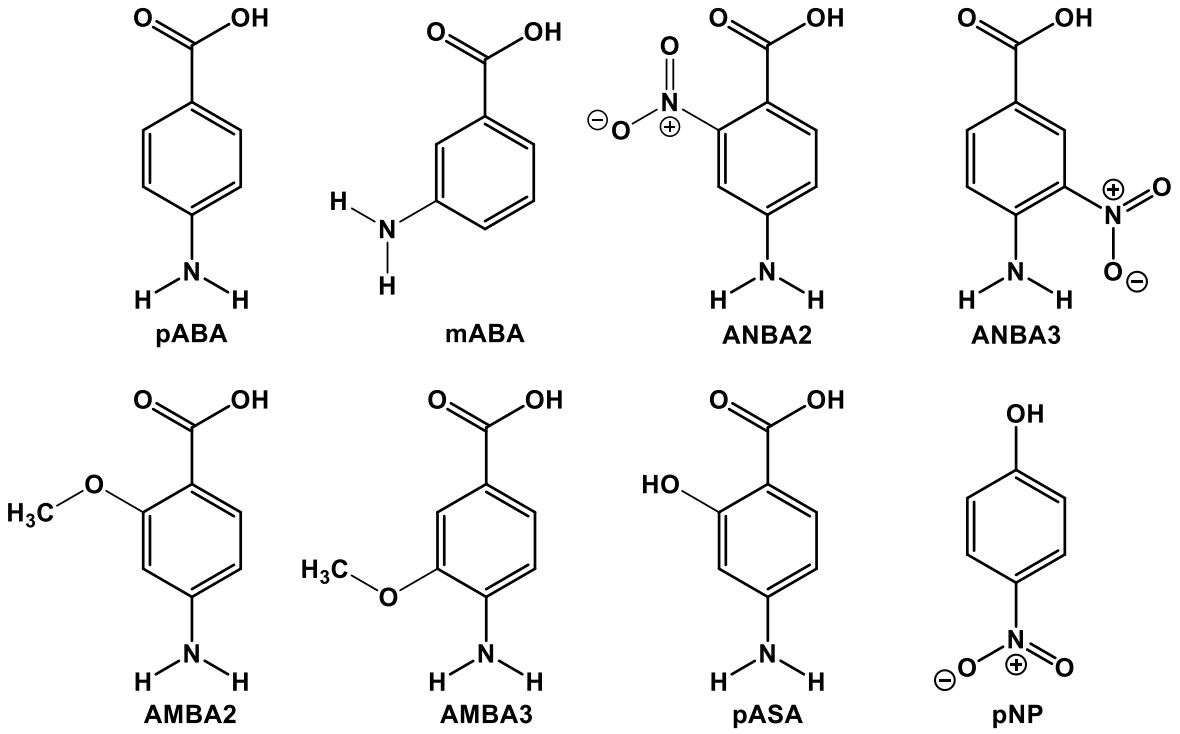


Figure 5.4. Molecular structures of pABA and the selection of seven TMAs, which are closely related in their molecular structure to pABA.

5.4.4 In Silico Screening

5.4.4.1 In Silico Intermolecular Grid Search TMA Screen - Dimers

A comparison of the strongest intermolecular interaction energy values, determined from the grid-search analysis, between pABA:pABA and pABA:TMAs is summarised in Table 5.1. The variation in calculated intermolecular interaction energies were found to be relatively small between the dimer interactions, except for pABA:pNP, which showed a larger variation. Given that the same calculation procedure was undertaken for all intermolecular interaction calculations and all TMAs, except pNP, had strong interacting carboxylic and amine groups, these calculated values were taken to provide a trend in intermolecular interaction strengths between pABA:pABA and pABA:TMAs.

The data indicates that for pABA:ANBA3, pABA:AMBA2 and pABA:AMBA3 intermolecular interactions energies were calculated to be stronger (more negative) than for those of pABA:pABA. We theorise that the stronger binding of these structurally related TMA's may disrupt the formation of a critical sized nucleus for pABA nucleation. In contrast, the other tested TMAs were calculated

to bind more weakly with pABA and thought to be less likely to inhibit nucleation. No significant changes were observed in trends for decreasing pABA:TMA interaction energies over the range of interactions calculated. An analysis of over 3000 calculated intermolecular interaction energies for each pABA:TMA system, as well as pABA:pABA, is provided in Appendix E.

Table 5.1. Strongest interaction energies for pABA:pABA and pABA:TMA from intermolecular grid search along with Van der Waals, hydrogen bonding and electrostatic interaction contributions to total energy.

Molecule in dimer with pABA	Van der Waals interaction energy (kcal mol^{-1})	Hydrogen bonding interaction energy (kcal mol^{-1})	Electrostatic interaction energy (kcal mol^{-1})	Total interaction energy (kcal mol^{-1})	% Variation in total interaction energy compared to pABA:pABA
pABA	0.80	-5.33	-4.50	-9.03	0.00
mABA	1.35	-5.50	-4.81	-8.96	+0.78
ANBA2	1.02	-4.74	-5.21	-8.93	+1.11
ANBA3	1.16	-5.84	-4.71	-9.39	-3.99
AMBA2	1.25	-5.63	-4.93	-9.31	-3.10
AMBA3	1.89	-5.63	-5.54	-9.28	-2.77
pASA	1.27	-5.13	-5.16	-9.02	+0.11
pNP	0.68	-4.06	-3.40	-6.78	+24.92

For the strongest intermolecular interaction energies calculated, hydrogen bonding tended to be the dominant intermolecular interaction type, with a high electrostatic contribution and a low/repulsive Van der Waals contribution to the overall intermolecular interaction energies calculated, which matched the trend observed for pABA:pABA and suggested strong hydrogen bonded carboxylic group dimer formation (synthon A).

The most energetically favourable intermolecular interaction geometries of pABA:pABA, pABA:ANBA3, pABA:AMBA2 and pABA:AMBA3 are displayed in Figure 5.5. All strongest calculated interactions were the OH…O H-bonding dimer, which is analogous to the strongest synthon in the alpha pABA structure (synthon A). This suggests that ANBA3, AMBA2 and AMBA3 are able to disrupt the important pABA:pABA dimer formation, which has been experimentally suggested to form prior to nucleation of alpha pABA and template the self-assembly of this

structure[48]. For all pABA:TMA intermolecular interactions studied, synthon A was found to be the most energetically favourable interaction type, with the exception of pABA:pNP, due to pNP lacking the carboxylic acid group moiety. This similarity across the interactions studied also highlights the relatively small changes in intermolecular interaction energies calculated for these systems. It also suggests that energy scaling/normalization based on molecular size would not be necessary for a comparison of interaction energies, as all interactions, except for pABA:pNP, were the same type. The most favourable interactions calculated for each pABA:TMA are given in Appendix E.

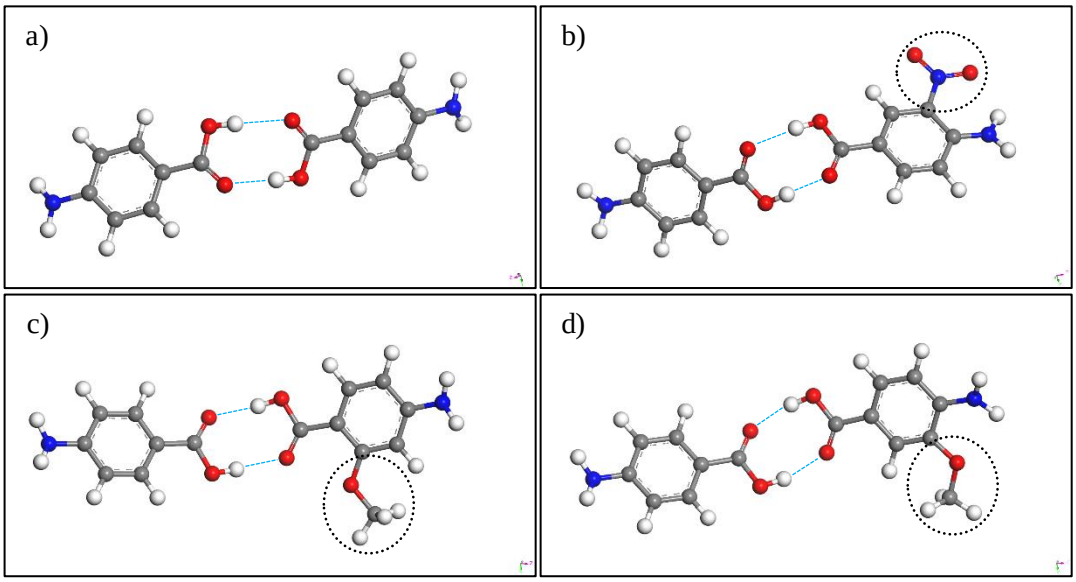


Figure 5.5. Most favourable interactions of a) pABA:pABA, b) pABA:ANBA3, c) pABA:AMBA2 and d) pABA:AMBA3, calculated from intermolecular grid search. Hydrogen bonding shown by blue dashed lines. Additional functional groups of TMAs are highlighted in the dotted circles.

5.4.4.2 In Silico Intermolecular Grid Search TMA Screen - Solvation

The calculated solvation energies of the most energetically favourable calculated dimers of pABA:pABA, pABA:ANBA3, pABA:AMBA2 and pABA:AMBA3 are given in Table 5.2.

All potential most energetically favourable pABA:TMA dimers were found to be more strongly solvated than the pABA:pABA dimer. This is likely due to the additional moieties on the TMA molecules, which enabled stronger interactions with the ethanol molecules. The strongest solvation energy of the three determined most likely pABA:TMA dimers was pABA:ANBA3. A stronger solvation demonstrates that the dimers would be more stable within solution and would be harder to desolvate for subsequent pABA intermolecular interactions to take place through the key secondary synthons B and C, making nucleation more difficult.

Table 5.2 Solvation energies of 20 ethanol molecules interacting with pABA:pABA and pABA:TMAs.

Molecule in dimer with pABA	pABA	ANBA3	AMBA2	AMBA3
Solvation Energy (kcal mol^{-1})	-58.71	-76.03	-60.43	-73.52

5.4.4.3 In Silico Intermolecular Grid Search TMA Screen – pABA Interactions with Stable Dimers

For 5 pABA molecules interacting with the studied dimers, the total interaction energies calculated with the pABA:TMAs were found to be stronger than with of pABA:pABA. This is consistent with the ethanol solvation results and is again likely due to the additional moieties of the TMAs having an effect on the oriented intermolecular interactions of pABA with the dimers. Therefore, intermolecular interactions of pABA molecules with the dimers in solution would be more favourable with the pABA:TMA dimers than with the pABA:pABA dimer. This suggests that if the TMAs were required to be removed from the prenucleation clusters in order for the pABA crystal structure to form and nucleation to occur, more energy would be required to achieve this. This mechanism of nucleation inhibiting additives being required to be removed from the prenuclei to enable nucleation to occur has been suggested in previous literature[24]. The intermolecular interaction energies calculated for 5 pABA molecules interacting with all pABA:pABA and pABA:TMA dimers are given in Appendix E.

The interaction geometries of the 5 pABA molecules with the most stable pABA:pABA dimer and the three most stable pABA:TMA dimers (ANBA3, AMBA2 and AMBA3) are displayed in Figure 5.6. These geometries provide information as to the likely effect of the important secondary synthonic interactions of pABA necessary for nucleation in ethanol solution to occur. For pABA molecules interacting with the pABA:pABA, pABA:AMBA2 and pABA:AMBA3 dimers, the strongest intermolecular interaction was synthon C, with the amine group of the pABA molecule interacting with the carboxylic acid groups of the dimers. This relates strongly to the pre assembly mechanism of pABA. In contrast, the strongest intermolecular interaction with a pABA molecule and the pABA:ANBA3 dimer does not relate to the important secondary synthons B or C. Instead, the amine group of the interacting pABA molecule interacts with the nitro group of ANBA3, directing strong non-crystallographic synthons. This suggests that ANBA3 has the strongest pABA nucleation inhibition capabilities of any of the TMAs studied, with its meta-position nitro group having a large effect on the ability of pABA molecules to form key synthonic interactions and nucleate.

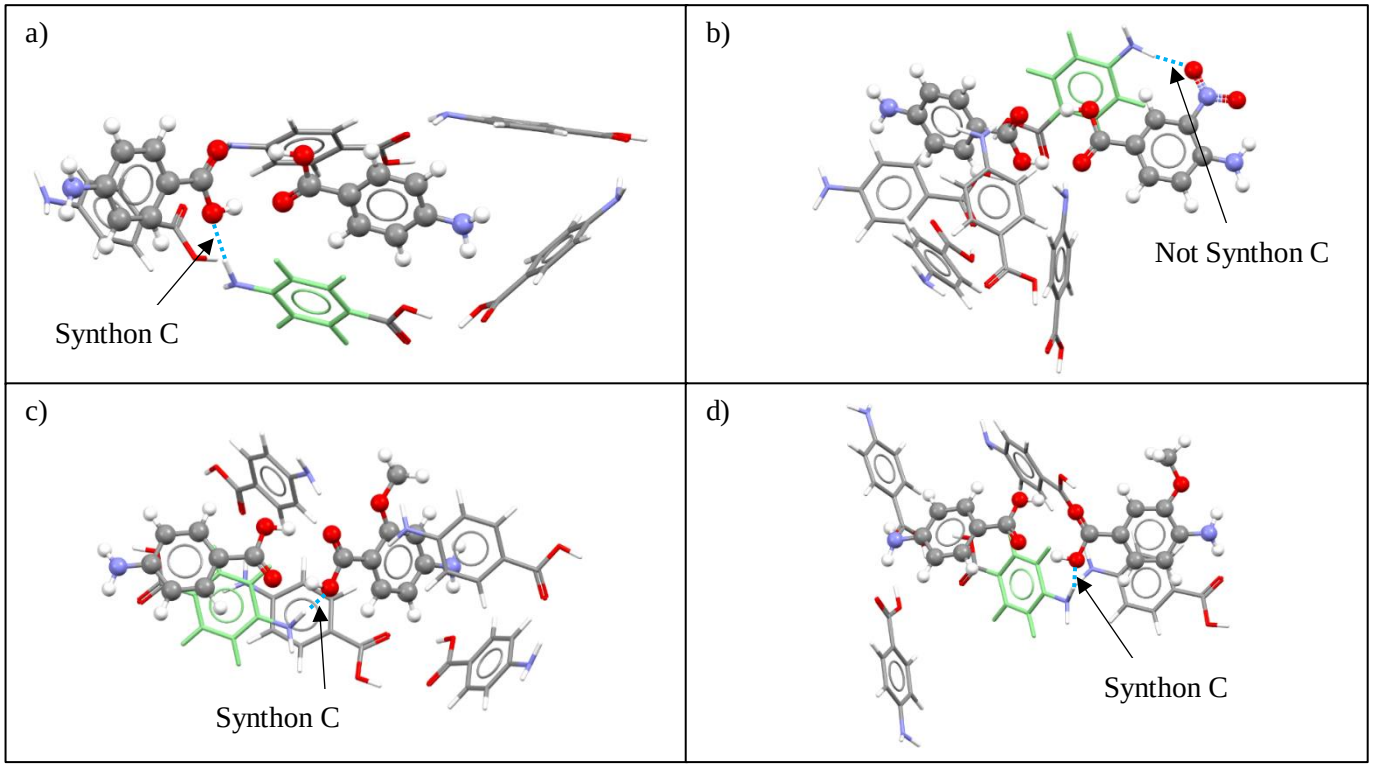


Figure 5.6. Interaction clusters of 5 pABA molecules around the calculated most energetically favourable (a) pABA:pABA, (b) pABA:ANBA3, (c) pABA:AMBA2 and (d) pABA:AMBA3 dimers. Dimers are shown with ball and stick style. pABA probe molecules are shown with capped stick style. Strongest pABA intermolecular interactions with each dimer are shown with pABA molecules with light green cyclic rings. Blue dashed lines represent intermolecular hydrogen bonding for strongest pABA interaction with dimer.

5.4.4.4 In Silico Intermolecular Grid Search TMA Screen – Atomic Charges

The calculated fractional charges of atoms on ANBA3, AMBA2 and AMBA3, Figure 5.7, provide further insight into the possible pABA nucleation inhibition effect of these TMAs. Charges calculated over the nitro group on ANBA3 ranged from 0.69 to -0.45, whereas the methoxy group charges of AMBA2 and AMBA3 ranged from -0.28 to 0.02. The larger charges of the nitro group suggest that ANBA3 would have a stronger influence on ethanol and pABA molecules within solution than AMBA2 or AMBA3, as seen in the solvation and pABA cluster results. A comparison of atomic charges of pABA and the selected TMAs shows somewhat minor variations in charges on amino groups of the molecules, except for ANBA3, which showed a large change in atomic charges. The nitro group of ANBA3 has strong electron withdrawing capacity towards the amino group and as such, created more positively charged hydrogen atoms and a more negative nitrogen atom (Figure 5.7). The higher positive charges of the amino group hydrogen atoms of ANBA3 would create stronger -N-H···O- intermolecular interactions with subsequent pABA molecules, and as such could potentially disrupt the pre-assembly/nucleation pathway required for nucleation of pABA from ethanol solution more than for the other TMAs studied. Therefore, it would be expected that ANBA3 would be a more effective TMA for pABA nucleation inhibition from ethanol solution than AMBA2 and AMBA3.

The charges on the cyclic rings of the TMAs were also influenced by the additional functional groups present, compared to the pABA molecule, with subtle changes in the calculated charges of the carbon atoms. These charges influence the π-π stacking synthon B interactions and as such, it is likely that the changing polarizability would influence this synthon, however, it is less clear at this stage as to the exact influence these changes would have on synthon B formation. Nevertheless, a previous study found that the synthon B interaction of both ANBA3 and AMBA3 with a pABA molecule is stronger than that of pABA with another pABA molecule, although the geometries of these interactions altered significantly from the pABA crystallographic solid state synthon B[27].

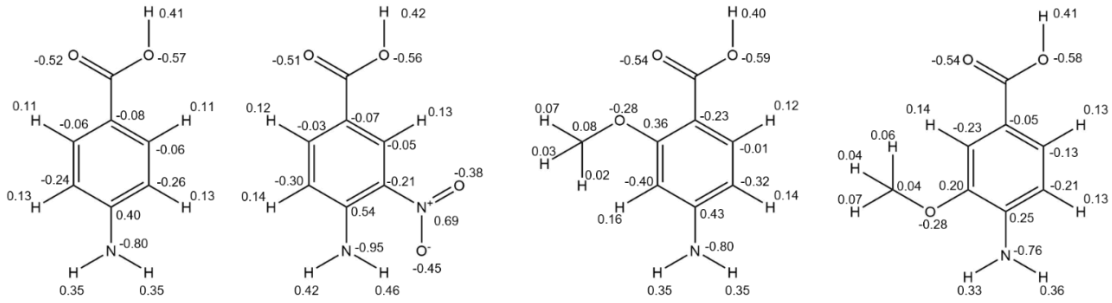


Figure 5.7. Fractional charges calculated for each atom of pABA, ANBA3, AMBA2 and AMBA3.

5.4.4.5 In Silico Intermolecular Grid Search TMA Screen –TMAs in pABA Crystal Structure

To further aid conceptualisation of how these TMAs could potentially inhibit formation of the pABA crystal structure, Figure 5.8 displays visualisations of the strongest interactions of pABA:TMAs, taken from Figure 5.6, within the pABA unit cell structure[46]. These TMAs could have a significant effect on disrupting the pABA crystal structure formation through electrostatic and steric hindrance towards subsequent pABA molecules joining the strong dimer formed in ethanol solution. The additional nitro moiety of ANBA3 and the methoxy moieties of AMBA2 and AMBA3 could disrupt pABA molecules orientating into the required crystal structure and inhibit the important crystallographic synthon B formation. Given that the nitro group is a larger moiety than the methoxy group, ANBA3 would have a larger disruptive effect on crystal structure formation. A space fill figure is provided in Appendix E to further highlight this.

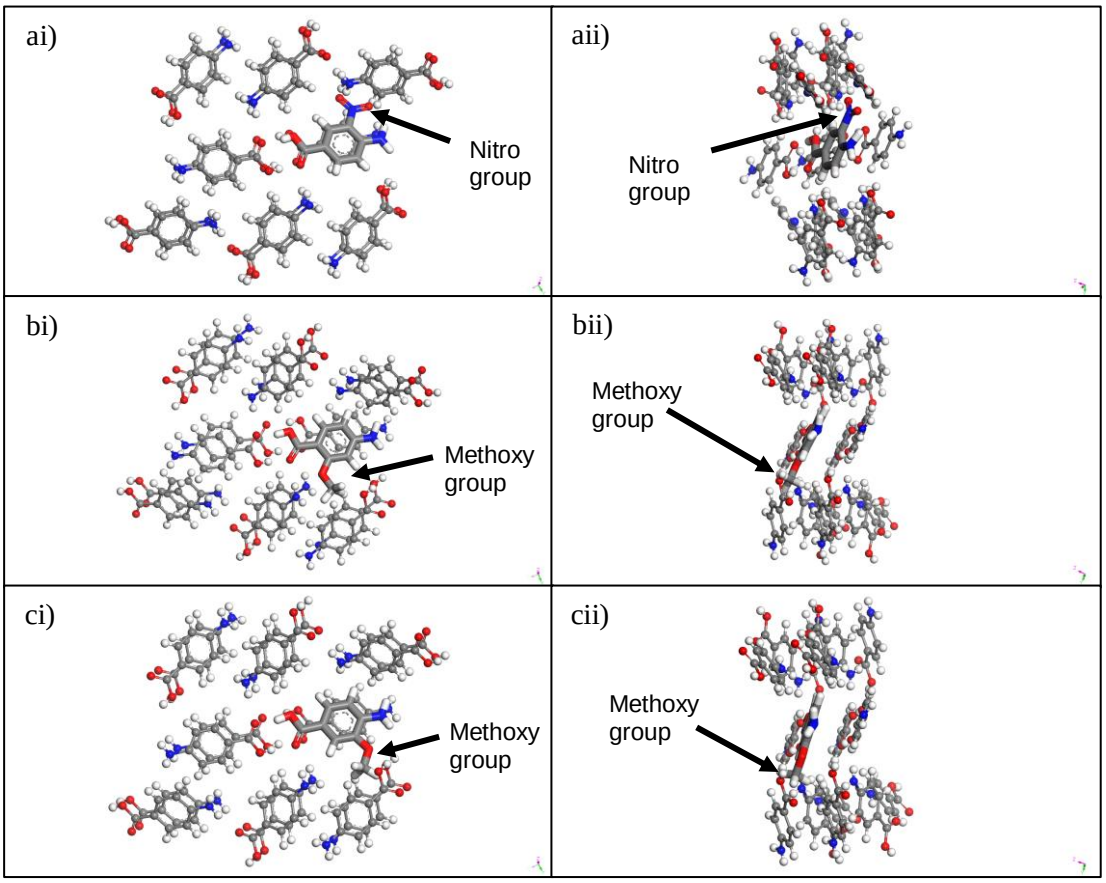


Figure 5.8. Visualisation of a) ANBA3, b) AMBA2 and c) AMBA3 within the pABA unit cell, based on the calculated strongest interaction geometry. i) View along b axis, ii) view along c axis. TMAs shown by thicker bonding molecules. Nitro and methoxy moieties would inhibit pABA molecules close to them from packing in the required pABA unit cell structure. Crystal structure taken from AMBNAC07 in CCDC[46].

The results of the intermolecular grid search pABA:TMA screen demonstrate that TMA selection should not be based solely on the molecular similarity of a target solute and an additive. This is still no guarantee of TMA competitive binding, shown by the comparison of interaction energies of ANBA3 and ANBA2. Both molecules have the same moieties, but the nitro group is present on different carbons of the cyclic ring, with the nitro group on the second carbon (ortho position) for ANBA2 and the third carbon (meta position) for ANBA3. The group placement had a large effect on intermolecular interaction energy strengths with pABA. This suggests that the nitro group moiety placement on the molecular structure had a large influence on the molecular polarity and as such on interaction strengths. This would also suggest that ANBA3 would have a larger influence on the other intermolecular interactions important for pABA self-assembly than ANBA2.

5.4.5 Experimental Screening

An experimental screen of the crystallisation of pABA:pABA and pABA:TMAs from ethanol solution, using the same TMAs that were assessed through intermolecular grid search, was undertaken to validate the results obtained through the in silico TMA screen and to demonstrate TMA effectiveness in a real solution, with the influence of solvent molecules.

The effectiveness of each TMA to inhibit pABA nucleation was assessed through a study of T_c of each solution as a function of heating cycle rate, with a lowering of T_c assumed to correlate with nucleation inhibition. Figure 5.9 shows determined average T_c and T_{diss} results obtained for each solution studied. The experimental results corroborate the findings from the intermolecular grid search screen, with the most effective TMAs being found to be ANBA3, AMBA2 and AMBA3, decreasing T_c by an average of 24.0 °C, 9.4 °C and 6.7 °C, respectively. A student T-test statistical analysis was completed to determine if deviations in average values of T_c were statistically significant. Only the TMAs: ANBA3, AMBA2 and AMBA3 were found to have statistical significance when compared to results collected with pABA in ethanol solutions. The full student t-test analysis results are provided in Appendix E. The variation in T_{diss} was found to be negligible with or without TMAs present, suggesting that the TMAs used had no significant effect on the solubility of pABA in ethanol. Dynamic MSZWs as a function

of cooling rate were determined using the values of T_c and T_{diss} for each solution and are given in figure 4.9. These further highlight the effectiveness of ANBA3, AMBA2 and AMBA3 to inhibit pABA nucleation from ethanol solution given the increase in MSZW for these systems.

ANBA3 had the greatest effect on T_c, lowering it substantially more than any other TMA, demonstrating that the nitro group of ANBA3 had a larger effect on disrupting pABA nucleation than the methoxy groups of AMBA2 and AMBA3. This highlights the importance of not just synthon A, but also synthons B and C, given that the nitro group of ANBA3 would likely influence these intermolecular interaction more than the methoxy groups of AMBA2 and AMBA3, as discussed previously. This correlates with the intermolecular interaction energy calculations and the charge calculations of these moieties discussed previously, further validating the intermolecular grid search results. Overall, these results suggest that TMAs must competitively bind at least with equivalence to the host molecule but a second criterion is that the secondary interactions must disrupt the preassembly cluster formation, in order to inhibit the nucleation process.

It should also be noted that the growth rate of pABA was likely reduced by the presence of the TMAs that influenced its nucleation. ANBA3 and AMBA3 have previously been shown to reduce the growth rate of pABA in 2-propanol solution[27]. AMBA3 was found to have a more drastic effect on reducing growth rates at lower additive loadings, although the reduction in growth rates became similar at around 1 wt% loading. However, from Figure 5.9 it is clear that ANBA3 had a larger effect on inhibiting nucleation than AMBA3. Therefore, the reduction in growth rate would likely influence the detection of crystallites in solution and could contribute to the lowering of the solution crystallisation temperatures for the pABA:ANBA3, pABA:AMBA2 and pABA:AMBA3 solutions, but it is clear that there is a larger impact of the TMAs on the nucleation process.

In order to determine whether any polymorphic transformations had occurred as a result of the presence of the TMAs with the pABA in ethanol solution, a morphological assessment was completed. Previously, it has been found that the two most dominant pABA polymorphs, α-pABA and β-pABA, have distinct morphologies, being needle-like and prismatic, respectively. Furthermore, this morphological dissimilarity has been shown to still be present in the presence of TMAs[27]. All crystals collected from the crystallisation experiments undertaken during this study were found to conform to the needle-like morphology of α-pABA, therefore, no polymorphic transformations are presumed to have taken place. Optical micrographs showing crystals collected from experiments using all TMAs are provided in Appendix E.

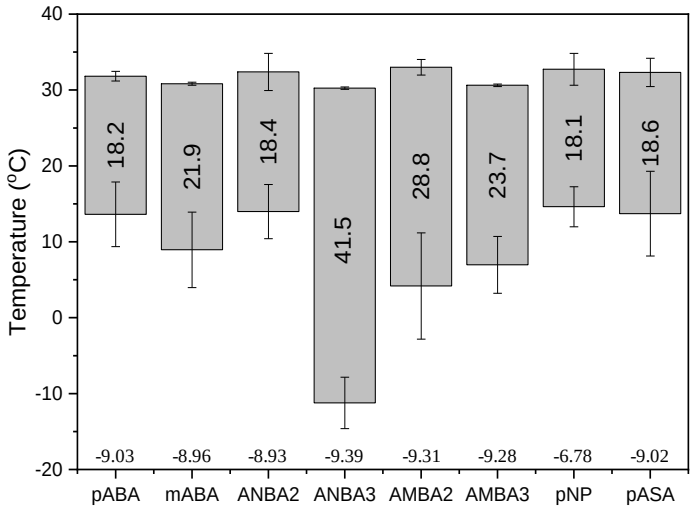


Figure 5.9. Floating column chart displaying $\boldsymbol{T_c}$ *(bottom of columns) and* $\boldsymbol{T_{diss}}$ *(top of columns) values determined for pABA in ethanol solution with and without the presence of TMAs. Error bars show standard deviations of results. Numeric value within columns represents dynamic MSZW in °C. Values at bottom of plot are the strongest interaction energies for each dimer, calculated from the intermolecular grid search, in kcal mol*$^{-1}$.

Due to the pABA nucleation inhibition from ethanol solution capabilities of ANBA3, this was the TMA that was further studied.

5.4.6 Mechanistic Understanding

5.4.6.1 Crystallisability and Solution Thermodynamics

Steady-state MSZW analysis highlighted the difference in crystallisability between pABA and pABA:ANBA3 in ethanol solutions. Over the concentration ranges studied the addition of ANBA3 increased the steady-state MSZW substantially, Table 5.4. Negligible variations in the trend of increasing equilibrium dissolution temperatures, T_e, with increasing solution concentration were determined, corroborating the previous finding of ANBA3 having a negligible effect on pABA solubility in ethanol. Therefore, the increase in the steady-state MSZW is attributed to the large decreases in the equilibrium crystallisation temperatures at the kinetic limit, $T_{c/l}$, observed. This demonstrates that pABA:ANBA3 required a much higher driving force to induce nucleation than for pABA in ethanol solution.

A van't Hoff analysis demonstrated a very similar trend, with regards to solution thermodynamics of the crystallising systems, with negligible changes in the enthalpy and

entropy of dissolution between both systems found. Full results of the van't Hoff analysis are given in Appendix E.

Table 5.3. Equilibrium crystallisation and dissolution temperatures determined over a range of concentrations as well as steady-state MSZWs for pABA and pABA:ANBA3 in ethanol solutions.

Conc. (g g^{-1})	$T_{c/l}$	T_e	MSZW (°C)	Conc. (g g^{-1})	$T_{c/l}$	T_e	MSZW (°C)
pABA				**pABA:ANBA3**			
0.14	12.9	16.4	3.5	0.18	1.8	34.0	32.2
0.15	14.7	22.2	7.5	0.19	8.2	36.4	28.2
0.16	22.3	26.4	4.1	0.20	18.0	41.4	23.4
0.17	23.0	30.6	7.6	0.21	20.8	49.6	28.8

5.4.6.2 Nucleation Kinetics

The KBHR approach was used to determine the mechanism by which nucleation occurred and the nucleation kinetic parameters for pABA:ANBA3 in ethanol solutions. An example plot of u_c vs q in ln-ln coordinates, for nucleation mechanism assessment, for pABA:ANBA3 in ethanol solution at a concentration of 0.21 g g^{-1} is shown in Figure 5.10.

Turner et al.[49] previously found that, over a comparable range of concentrations studied for pABA:ANBA3 in ethanol solutions, pABA in ethanol solutions nucleate through an IN pathway, Table 5.5. Small angle X-ray studies have previously shown that the IN mechanism associated with pABA in ethanol solutions is mediated through the existence of pABA prenucleation clusters, which nucleate when a high enough driving force of supersaturation is reached[48]. This suggests an equilibrium of pABA clusters with similar energies exist in the supersaturated solution state, whereby once a high enough driving force to nucleation is achieved, given a high enough supersaturation, this equilibrium ensures a mechanistic nucleation pathway by which all nuclei reach a critical size in one instant, before subsequent crystal growth occurs.

In contrast, pABA:ANBA3 in ethanol solutions were found to undertake the PN pathway for all concentrations studied, Table 5.5. This suggests that the equilibrium of cluster formation that could undergo nucleation at a given instance, present in pABA in ethanol solutions, was disrupted by the presence of ANBA3. From the in silico findings it is clear that there are strong

pABA:ANBA3 intermolecular interactions and the presence of ANBA3 is able to direct non-crystallographic synthons, as well as providing steric hindrance to the formation of the pABA crystal structure. Therefore, this suggests that the presence of ANBA3 in solution disrupts the ability of solute clusters in solution to form into a pABA crystal structure. This result has been found previously for TMA studies on nucleation inhibition of different crystallisation systems[24,26]. Therefore, it is assumed that a higher driving force to nucleation was required to overcome the favourable pABA:ANBA3 intermolecular interactions and remove the ANBA3 molecules from the clusters. Given the potential variation of clusters in solution, containing different numbers of ANBA3 and pABA molecules, only certain clusters would be provided with enough of a driving force to initiate the nucleation stage, once a critical nucleus size was reached, thereby altering the nucleation pathway to a state in which nucleation occurred in different areas of the solution over a period of time, in line with the PN pathway.

This novel insight into how ANBA3 affects the mechanism by which pABA nucleates from ethanol solution demonstrates that the interaction between the TMA and solute can fundamentally alter the behaviour of a nucleating system. Understanding how TMAs effect the mechanism of nucleation is extremely important as it can have a large impact on final crystal size distribution, solution hydrodynamics and system thermodynamics, etc.

Table 5.4. Nucleation mechanisms determined from slope of u_c vs q in ln-ln coordinates and calculated nucleation kinetic parameters obtained for pABA:ANBA3 in ethanol solutions from KBHR analysis. Data presented for pABA in ethanol solutions over a comparable concentration range, taken from Turner et al[49].

Concentration (g g^{-1})	**Slope**	**R^2 of linear fit**	**Mechanism**	**γ_{eff} (mJ m^{-2})**	**r^* (nm)**	**i^***
pABA (from Turner et al.[49])						
0.18	1.76	0.80	IN	-	-	-
0.19	1.56	0.53	IN	-	-	-
0.20	1.62	0.62	IN	-	-	-
pABA:ANBA3						
0.18	9.18	0.91	PN	3.74	0.93 - 0.84	20.2 - 14.8
0.19	6.70	0.95	PN	2.98	0.83 - 0.72	14.5 - 9.5
0.20	3.95	0.96	PN	1.83	0.57 - 0.44	4.8 - 2.1
0.21	5.30	0.98	PN	2.59	0.74 - 0.60	10.1 - 5.5

For the PN case of pABA:ANBA3, the KBHR approach enabled the calculation of the nucleation kinetic parameters, γ_{eff}, r^* and i^*, shown in table 3. Plots of u_c vs $\ln q$ were formed and fitted with Equation 5.5 to enable the determination of the parameters. An example of the u_c vs $\ln q$ plot for pABA:ANBA3 in ethanol solution at a concentration of 0.21 g g^{-1} is shown in Figure 5.8.

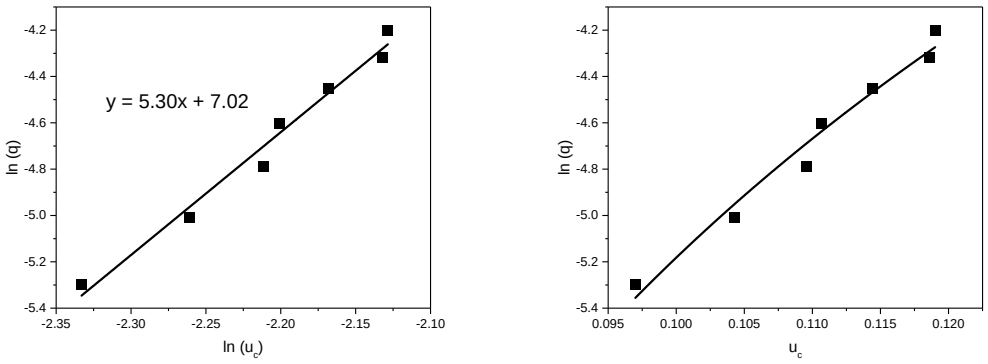


Figure 5.10. Plots for KBHR analysis for pABA:ANBA3 in ethanol solution at a concentration of 0.21 g g-1. Left-hand side - Plot of $\boldsymbol{u_c}$ *vs* $\boldsymbol{q}$ *in ln-ln coordinates for determination of nucleation mechanism. Right-hand side - Plot of* $\boldsymbol{u_c}$ *vs* $\boldsymbol{\ln q}$ *for determination of nucleation kinetic parameters.*

A previous research study determined values of γ_{eff} for pABA in ethanol solution using isothermal induction time data and CNT analysis[48]. Over a similar concentration range as studied in this work, the values of γ_{eff} were calculated to range from 0.85 - 1.31 mJ m^{-2}. In contrast values of γ_{eff} for pABA:ANBA3 in ethanol solution calculated from this analysis were found to be between 1.8 - 3.7 mJ m^{-2}. The higher γ_{eff} demonstrates that the presence of ANBA3 increased the required driving force to nucleation, which correlates well with the depression in T_c observed with experimental crystallisation studies as well as the nucleation mechanism change from IN to PN with the presence of ANBA3 in solution.

5.5 Conclusions

5.5.1 Conclusions of this Study

A workflow for TMA screening and assessment was developed and undertaken to study the nucleation inhibition effects of 7 TMAs on pABA crystallising from ethanol solution.

Intermolecular grid search results suggested that 3 out of 7 studied TMAs (ANBA3, AMBA2 and AMBA3) interacted more strongly with pABA than pABA did with itself. The other TMAs were found to have weaker intermolecular interactions. Therefore, ANBA3, AMBA2 and AMBA3 would likely form competitively to pABA in solution , forming through the important synthon A, whereas the others would have a much smaller influence on intermolecular interactions in solution.

These 3 pABA:TMA dimers were found to be more stable in solution than pABA:pABA dimers and as such, harder to desolvate. pABA:ANBA3 was also found to likely disrupt the important synthon C formation necessary for pABA nucleation. Atomic fractional charges demonstrated that ANBA3 would have stronger intermolecular interactions with subsequent pABA molecules due to strong charges on its nitro and amine groups and TMA cyclic rings had varied charges, suggesting an ability to alter synthon B and C formation. All 3 pABA:TMA dimers were found to be unlikely to fit within the pABA crystal structure and as such, would be likely to disrupt the important synthon B and other pABA intermolecular interactions necessary for pABA nucleation.

Therefore, although initial in silico testing provided an indication as to the likely interaction strengths of pABA homodimers and pABA:TMA heterodimers, through assessment of the impact of TMAs on key pABA synthons (A, B and C), stability of dimers in solution, subsequent pABA interactions, atomic fractional charges and the stereochemistry associated with TMA incorporation into the crystal structure, the impact of the TMAs on pABA nucleation was comprehensively evaluated.

Experimental screening corroborated the in silico findings, with only ANBA3, AMBA2 and AMBA3 having an ability to lower the crystallisation temperature of pABA in ethanol solution. ANBA3 was found to have the largest nucleation inhibition effect.

The crystallisability, solution thermodynamics and nucleation kinetics of pABA:ANBA3 were assessed to gain a mechanistic understanding of TMA inhibition of pABA nucleation. Large increases were observed in the steady-state MSZW with the presence of ANBA3 in solution, with little changes in the solution thermodynamics. The mechanism of nucleation was found to change from instantaneous nucleation for pABA in ethanol solution to progressive nucleation in the presence of ANBA3 in solution. This is suggested to be as a result of ANBA3 molecules influencing the ability of pABA molecules to form into their crystal structure to enable the nucleation process to occur. A higher driving force to nucleation would be needed for ANBA3 to be removed from these clusters and allow pABA nucleation to occur. This was found to be

the case, with a higher supersaturation necessary to induce nucleation of pABA:ANBA3 in ethanol solutions, as well as a higher effective interfacial tension calculated for these solutions.

5.5.2 Applications, Future Work and Current Limitations

Industrial additive selection can take the form of an initial selection of hundreds of potentially useful additives followed by an additive screen to determine the most effective. This is a long and tedious process that requires substantial experimental effort and money to complete. Furthermore, these screens provide no real information as to the mechanism of action of the additives towards the crystallisation process, which means fundamental knowledge cannot be used to aid future additive selection. The workflow produced in this study provides a step towards making the process of additive selection, as well as understanding fundamental mechanistic additive influences on the crystallisation process, more efficient, by reducing experimental expenditure and gaining greater insights to aid in future idea generation.

The workflow produced could also be implemented towards understanding how chemical synthesis impurities effect the crystallisation of desired products. This is due to these impurities being akin to TMAs, i.e. they have a similar molecular structure to the desired product. This could then aid in process understanding so that process parameters, such as solvent selection, could be altered. This could potentially change intermolecular interaction pathways to nucleation, creating a more controlled crystallisation process.

Furthermore, although not thoroughly discussed in this work, understanding how TMAs interact with preassembly/nucleation pathways can aid in directing polymorphic form. This has been shown in a previous study by Black et al.[27], whereby, at higher additive loadings and higher solution volumes to those used in this work, ANBA3 and AMBA3 were able to direct the crystallisation of β-pABA, with explanations given as to the TMAs interfering with the important synthons in α-pABA crystal structure. The workflow presented here provides a way in which to thoroughly understand these interactions and as such could be used to aid polymorphic form selectivity.

A limitation of this work is that it does not address key issues arising from TMA studies, such as understanding how TMA concentration influences nucleation inhibition or how changes in TMA solubility in the solvent influence its efficacy.

A further limitation of this work is that it focusses upon a relatively simple molecule in a model crystallisation system. Therefore, it does not take into account added complexity of many

solutions. This complexity could be the result of many factors, such as high molecular weight compounds, highly charged compounds, multi component systems, lower purity products or hydrophobic systems that do not have strong hydrogen bonding responsible for key synthons.

In order to ensure effective workflow procedures and universal applicability, it is suggested that the produced workflow should be developed and validated further, through subsequent studies on nucleation inhibition using TMAs of different systems. With further studies and successive methodological improvement it is suggested that the TMA selection workflow could become a more common and rigorously used industrial crystallisation tool.

5.6 References

1. Kaskiewicz, P. L. *et al.* Isothermal by Design: An Accelerated Approach to the Prediction of the Crystallizability of Slowly Nucleating Systems. *Org. Process Res. Dev.* **23**, 1948–1959 (2019).
2. Tang, X. *et al.* Solubility and crystallisability of the ternary system: Hexadecane and octadecane representative in fuel solvents. *Fuel* **226**, 665–674 (2018).
3. Gracin, S. & Rasmuson, Å. C. Polymorphism and crystallization of p-aminobenzoic acid. *Cryst. Growth Des.* **4**, 1013–1023 (2004).
4. Simone, E., Steele, G. & Nagy, Z. K. Tailoring crystal shape and polymorphism using combinations of solvents and a structurally related additive. *CrystEngComm* **17**, 9370–9379 (2015).
5. Simone, E., Saleemi, A. N., Tonnon, N. & Nagy, Z. K. Active polymorphic feedback control of crystallization processes using a combined raman and ATR-UV/Vis spectroscopy approach. *Cryst. Growth Des.* **14**, 1839–1850 (2014).
6. Rosbottom, I. *et al.* Influence of Solvent Composition on the Crystal Morphology and Structure of p-Aminobenzoic Acid Crystallized from Mixed Ethanol and Nitromethane Solutions. *Cryst. Growth Des.* **17**, 4151–4161 (2017).
7. Sangwal, Mk. *Additives and Crystallization Processes: From Fundamentals to Applications*. (John Wiley & Sons Ltd., 2007).
8. Buckley, H. E. Some new Features in Habit-Modification shown by KClO4 Crystals. *Zeitschrift für Krist.* **91**, 375 (1935).
9. Buckley, H. E. Habit modification in crystals as a result of the introduction of impurities during growth. *Discuss. Faraday Soc.* **5**, 243–254 (1949).
10. Butchart, A. & Whetstone, J. The effect of dyes on the crystal habits of some oxy-salts. *Discuss. Faraday Soc.* **5**, 254–261 (1949).

11. Whetstone, J. The effect of crystal habit modification on the setting of inorganic oxy-salts. *Discuss. Faraday Soc.* **5**, 261–266 (1949).
12. van Mil, J., Gati, E., Addadi, L. & Lahav, M. Useful Impurities for Optical Resolutions. 1. On the Crystallization of Photopolymerizing Dienes in the Presence of Their Chiral Topochemical Products. *J. Am. Chem. Soc.* **103**, 1248–1249 (1981).
13. Addadi, L., van Mil, J. & Lahav, M. Useful Impurities for Optical Resolutions. 2. Generality and Mechanism of the Rule of Reversal. *J. Am. Chem. Soc.* **103**, 1249–1251 (1981).
14. Addadi, L. *et al.* Resolution of conglomerates by stereoselective habit modifications. *Nature* **296**, 21–26 (1982).
15. Wireko, F. C. *et al.* Effect of solvent on the growth of organic crystals. 1. The riddle of α-resorcinol. *J. Phys. Chem.* **91**, 472–481 (1987).
16. Weissbuch, I., Addadi, L., Lahav, M. & Leiserowitz, L. Molecular recognition at crystal interfaces reduction in crystal symmetry of solid. *Science (80-.).* **253**, 637–645 (1991).
17. Weissbuch, I., Lahav, M. & Leiserowitz, L. Toward stereochemical control, monitoring, and understanding of crystal nucleation. *Cryst. Growth Des.* **3**, 125–150 (2003).
18. Clydesdale, G., Roberts, K. J., Lewtas, K. & Docherty, R. Modelling the morphology of molecular crystals in the presence of disruptive tailor-made additives. *J. Cryst. Growth* **135**, 331–340 (1994).
19. Clydesdale, G., Roberts, K. J., Lewtas, K. & Docherty, R. Modelling the morphology of molecular crystals in the presence of blocking tailor-made additives. *J. Cryst. Growth* **141**, 443–450 (1994).
20. Clydesdale, G., Hammond, R. B., Ramachandran, V., Roberts, K. J. & Mougin, P. Molecular modelling of the morphology of organic crystals in the presence of impurity species: recent applications to naphthalene, phenanthrene, and caprolactam crystals. *Mol. Cryst. Liq. Cryst.* **440**, 235–257 (2005).
21. Black, S. N., Davey, R. J. & Halcrow, M. The kinetics of crystal growth in the presence of tailor-made additives. *J. Cryst. Growth* **79**, 765–774 (1986).
22. Chen, B. D., Garside, J., Davey, R. J., Maginn, S. J. & Matsuoka, M. Growth of m-chloronitrobenzene crystals in the presence of tailor-made additives: Assignment of the polar axes from morphological calculations. *J. Phys. Chem.* **98**, 3215–3221 (1994).
23. Dowling, R. *et al.* Acceleration of crystal growth rates: An unexpected effect of tailor-made additives. *Chem. Commun.* **46**, 5924–5926 (2010).

24. Heffernan, C., Ukrainczyk, M., Zeglinski, J., Hodnett, B. K. & Rasmuson, Å. C. Influence of Structurally Related Impurities on the Crystal Nucleation of Curcumin. *Cryst. Growth Des.* **18**, 4715–4723 (2018).
25. Pons Siepermann, C. A., Huang, S. & Myerson, A. S. Nucleation Inhibition of Benzoic Acid through Solution Complexation. *Cryst. Growth Des.* **17**, 2646–2653 (2017).
26. Pons Siepermann, C. A. & Myerson, A. S. Inhibition of Nucleation Using a Dilute, Weakly Hydrogen-Bonding Molecular Additive. *Cryst. Growth Des.* **18**, acs.cgd.8b00367 (2018).
27. Black, J. F. B., Cruz-Cabeza, A. J., Davey, R. J., Willacy, R. D. & Yeoh, A. The Kinetic Story of Tailor-made Additives in Polymorphic Systems: New Data and Molecular Insights for p-Aminobenzoic Acid. *Cryst. Growth Des.* **18**, 7518–7525 (2018).
28. Ulrich, J. Solution crystallization - Developments and new trends. *Chem. Eng. Technol.* **26**, 832–835 (2003).
29. Mougin, P., Clydesdale, G., Hammond, R. B. & Roberts, K. J. Molecular and solid-state modeling of the crystal purity and morphology of ε-caprolactam in the presence of synthesis impurities and the imino-tautomeric species caprolactim. *J. Phys. Chem. B* **107**, 13262–13272 (2003).
30. Hammond, R. B., Ma, C., Roberts, K. J., Ghi, P. Y. & Harris, R. K. Application of systematic search methods to studies of the structures of urea-dihydroxy benzene cocrystals. *J. Phys. Chem. B* **107**, 11820–11826 (2003).
31. Clydesdale, G., Hammond, R. B. & Roberts, K. J. Molecular modeling of bulk impurity segregation and impurity-mediated crystal habit modification of naphthalene and phenanthrene in the presence of heteroimpurity species. *J. Phys. Chem. B* **107**, 4826–4833 (2003).
32. Harris, R. K. *et al.* Solid-state NMR and computational studies of 4-methyl-2-nitroacetanilide. *Magn. Reson. Chem.* **44**, 325–333 (2006).
33. Hammond, R. B., Hashim, R. S., Ma, C. & Roberts, K. J. Grid-based molecular modeling for pharmaceutical salt screening: Case example of 3,4,6,7,8,9-hexahydro-2H-pyrimido (1,2-a) pyrimidinium acetate. *J. Pharm. Sci.* **95**, 2361–2372 (2006).
34. Ramachandran, V. *et al.* Formulation pre-screening of inhalation powders using computational atom-atom systematic search method. *Mol. Pharm.* **12**, 18–33 (2015).
35. Rosbottom, I., Pickering, J. H., Etbon, B., Hammond, R. B. & Roberts, K. J. Examination of inequivalent wetting on the crystal habit surfaces of RS-ibuprofen using grid-based molecular modelling. *Phys. Chem. Chem. Phys.* **20**, 11622–11633 (2018).

36. Rosbottom, I., Pickering, J., Hammond, R. B. & Roberts, K. J. A Digital Workflow Supporting the Selection of Solvents for Optimising the Crystallisability of Para Aminobenzoic Acid. *Org. Process Res. Dev.* **24**, 500–507 (2020).
37. Kashchiev, D., Borissova, A., Hammond, R. B. & Roberts, K. J. Effect of cooling rate on the critical undercooling for crystallization. *J. Cryst. Growth* **312**, 698–704 (2010).
38. Kashchiev, D., Borissova, A., Hammond, R. B. & Roberts, K. J. Dependence of the critical undercooling for crystallization on the cooling rate. *J. Phys. Chem. B* **114**, 5441–5446 (2010).
39. Camacho Corzo, D. M. *et al.* Nucleation mechanism and kinetics from the analysis of polythermal crystallisation data: methyl stearate from kerosene solutions. *CrystEngComm* **16**, 974–991 (2014).
40. Svärd, M., Nordström, F. L., Hoffmann, E. M., Aziz, B. & Rasmuson, Å. C. Thermodynamics and nucleation of the enantiotropic compound p-aminobenzoic acid. *CrystEngComm* **15**, 5020–5031 (2013).
41. Black, J. F. B., Davey, R. J., Gowers, R. J. & Yeoh, A. Ostwald's rule and enantiotropy: Polymorph appearance in the crystallisation of p-aminobenzoic acid. *CrystEngComm* **17**, 5139–5142 (2015).
42. Turner, T. D., Caddick, S., Hammond, R. B., Roberts, K. J. & Lai, X. Kinetics of the Aqueous-Ethanol Solution Mediated Transformation between the Beta and Alpha Polymorphs of p-Aminobenzoic Acid. *Cryst. Growth Des.* **18**, 1117–1125 (2018).
43. Black, J. F. B. *et al.* Crystal nucleation and growth in a polymorphic system: Ostwald's rule,: P -aminobenzoic acid and nucleation transition states. *CrystEngComm* **20**, 768–776 (2018).
44. Cruz-Cabeza, A. J., Davey, R. J., Oswald, I. D. H., Ward, M. R. & Sugden, I. J. Polymorphism in p-aminobenzoic acid. *CrystEngComm* **21**, 2034–2042 (2019).
45. Rosbottom, I., Roberts, K. J. & Docherty, R. The solid state, surface and morphological properties of p-aminobenzoic acid in terms of the strength and directionality of its intermolecular synthons. *CrystEngComm* **17**, 5768–5788 (2015).
46. Sullivan, R. A. & Davey, R. J. Concerning the crystal morphologies of the α and β polymorphs of p-aminobenzoic acid. *CrystEngComm* **17**, 1015–1023 (2015).
47. Sullivan, R. A. *et al.* Revealing the roles of desolvation and molecular self-assembly in crystal nucleation from solution: Benzoic and p -aminobenzoic acids. *Cryst. Growth Des.* **14**, 2689–2696 (2014).
48. Toroz, D. *et al.* Towards an understanding of the nucleation of alpha-para amino benzoic acid from ethanolic solutions: a multi-scale approach. *Faraday Discuss.* **179**, 79–114 (2015).

49. Turner, T. D. *et al.* The influence of solution environment on the nucleation kinetics and crystallisability of para-aminobenzoic acid. *Phys. Chem. Chem. Phys.* **18**, 27507–27520 (2016).
50. Davey, R. J., Back, K. R. & Sullivan, R. A. Crystal nucleation from solutions - Transition states, rate determining steps and complexity. *Faraday Discuss.* **179**, 9–26 (2015).
51. Cruz-cabeza, A. J., Davey, R. J. & Sachithananthan, S. Aromatic stacking - a key step in nucleation. *Chem. Commun.* **53**, 7905–7908 (2017).
52. Rosbottom, I., Toroz, D., Hammond, R. B. & Roberts, K. J. Conformational and structural stability of the single molecule and hydrogen bonded clusters of para aminobenzoic acid in the gas and solution phases. *CrystEngComm* **20**, 7543–7555 (2018).
53. Nappo, V. *et al.* Effect of shear rate on primary nucleation of para-amino benzoic acid in solution under different fluid dynamic conditions. *Chem. Eng. Res. Des.* **136**, 48–56 (2018).
54. Rosbottom, I. & Roberts, K. J. Crystal Growth and Morphology of Molecular Crystals. in *Engineering Crystallography: From Molecule to Crystal to Functional Form. NATO Science for Peace and Security Series A: Chemistry and Biology* (eds. Roberts, K. J., Docherty, R. & Tamura, R.) 109–131 (Springer, 2017).
55. Roberts, K. J., Hammond, R. B., Ramachandran, V. & Docherty, R. Synthonic Engineering. in *Computational Pharmaceutical Solid State Chemistry* (ed. Abramov, Y. A.) 175–210 (John Wiley & Sons, Ltd, 2016). doi:https://doi.org/10.1002/9781118700686.ch8
56. The Cambridge Crystallographic Data Centre. Cambridge Structural Database. (2020). Available at: https://www.ccdc.cam.ac.uk/solutions/csd-system/components/csd/.
57. Mayo, S. L., Olafson, B. D. & Goddard, W. A. DREIDING: A generic force field for molecular simulations. *J. Phys. Chem.* **94**, 8897–8909 (1990).
58. Becke, A. D. A new mixing of Hartree-Fock and local density-functional theories. *J. Chem. Phys.* **98**, 1372–1377 (1993).
59. Lee, C., Yang, W. & Parr, R. G. Development of the Colle-Salvetti correlation-energy formula into a functional of the electron density. *Phys. Rev. B* **37**, 785–789 (1988).
60. Frisch, M. J. *et al.* Gaussian09, Revision D.01. (2016).
61. BIOVIA Dassault Systèmes. Materials Studio. *2019* Available at: https://www.3dsbiovia.com/portfolio/materials-studio.html.
62. Gasteiger, J. & Marsili, M. A new model for calculating atomic charges in molecules. *Tetrahedron Lett.* **19**, 3181–3184 (1978).

63. Gasteiger, J. & Marsili, M. Iterative partial equalization of orbital electronegativity-a rapid access to atomic charges. *Tetrahedron* **36**, 3219–3228 (1980).
64. Technobis. Crystal16. (2020). Available at: https://www.crystallizationsystems.com/crystal16.
65. Hildebrand, J. H. & Jenks, C. A. Solubility. IV. Solubility relations of naphthalene and iodine in the various solvents, Including a method for evaluating solubility data. *J. Am. Chem. Soc.* **42**, 2180–2189 (1920).
66. Grant, D. J. W., Mehdizadeh, M., Chow, A. H. L. & Fairbrother, J. E. Non-linear van't Hoff solubility-temperature plots and their pharmaceutical interpretation. *Int. J. Pharm.* **18**, 25–38 (1984).
67. Turner, T. D. Molecular Self-Assembly, Nucleation Kinetics and Cluster Formation Associated with Solution Crystallisation. (University of Leeds, 2015).

Chapter 6 Influence of a Polymeric Additive on the Crystallisability and Nucleation Mechanism for the Model Fuel System of Eicosane Crystallising from Supersaturated Toluene Solutions

6.1 Abstract

The impact of a commercially available cold flow improver additive (IA) on crystallisation within a model fuel system of eicosane in toluene solutions is investigated. Polythermal crystallisation method utilising turbidometric detection is used to assess the influence of IA addition upon eicosane solubility and nucleation inhibition at different solution IA treat rates, ranging from 0.1 to 10 wt%. Whilst IA is found to have negligible effect upon eicosane solubility, its nucleation is found to be disrupted, resulting in a reduction in crystallisation temperatures as a function of higher IA treat rate, with IA and eicosane phase separation also taking place at treat rates of 2wt% IA and above. A change from an instantaneous to a progressive nucleation mechanism of eicosane in the absence and presence of IA within solution, respectively, is found. This behaviour is rationalised through the proposition that IA is incorporated within developing eicosane prenucleation clusters, hence disrupting its ability to grow to a critical size for nucleation. Nucleation kinetic analysis confirms that at given solution undercoolings, higher IA treat rate reduces the rate of nucleation due to an increase in the effective interfacial tension to nucleation, in line with a higher degree of thermodynamic control of the nucleation process, as might be expected for the progressive nucleation behaviour.

6.2 Introduction

Crystallisation is a key isolation and purification process that is extensively used in a number of particle processing industries. However, under certain conditions it can be an unwanted phenomenon that has the potential to impact negatively upon formulated products. As an example, Ritonavir, a drug used for the treatment of Acquired Immuno-Deficiency Syndrome (AIDS), provides a stark example of this behaviour, undergoing an unwanted crystallisation event after a period of around two years on the market, causing a lack of efficacy in the product[1,2].

To this end, additives can often be employed to delay or even prevent unwanted crystallisation within formulated products[3–8]. In fuel, for example, polymeric-based cold-flow improvers (CFIs) are often added to supress the crystallisation of wax components under extreme low temperature operational conditions[9–13]. As well as controlling their morphology, CFIs are able to inhibit the formation of large plate-like wax crystals which otherwise would have the tendency to form large agglomerated lattices, increasing the risk of fuel system blockages[14]. Additive treat rate, which is the amount of additive added to a system, can have a large effect

on solution crystallisation, with the amounts of additives used changing dramatically depending on their efficacy and the product composition[6,15].

Crystallisation processes encompass two key stages, nucleation and growth, with the kinetics of both of these depending on the magnitude of the supersaturation driving force. Nucleation describes the 3D formation of the solid crystalline phase from the mother phase, which is followed by 2D growth upon these nuclei on the crystal habit surfaces, leading to the development of macroscopic crystals[16,17]. Hence, in order to determine the efficacy of nucleation inhibition additives, it is important to initially characterise the nucleation stage and, through this, assess the additives ability to delay or supress the formation of crystalline material from a mother phase.

In characterising nucleation, it is also important to understand any effect that an additive might have on solute solubility within the crystallisation system[18]. Solubility and the onset of nucleation can be used to define the crystallisability of a material, with the metastable zone width (MSZW) of the crystallisation system reflecting a zone of thermodynamic metastability[17]. The MSZW is cooling rate dependent, reflecting the relative balance between the kinetics of supersaturation generation and that of nucleation. Hence, a comparative characterisation of the MSZW for solutions crystallising in the absence and presence of additives provides an assessment of the nucleation suppression power of additives, with a widening of the MSZW correlating to the inhibition of nucleation[3,18–21].

Analysis of the solubility as a function of solute concentration and additive treat rate can also provide an indication as to the likely intermolecular interactions in the solution state, yielding a thermodynamic assessment of the enthalpic and entropic influences on dissolution process.

Previous studies have shown that the rate of nucleation can be affected by the presence of additives, with both small molecular[3,21] and polymeric based additives[5] being found to inhibit and reduce the rate of nucleation depending upon their relative affinity towards a solute molecule. Mechanistically, such additives have been suggested to inhibit nucleation through their integration into the bulk structure and/or onto the surface of a growing nuclei, hence disrupting the ability of further solute molecules to form into the crystal structure.

In this study, the impact of additive treat rate on the determination of additive efficacy and nucleation kinetic analysis is examined for a model fuel system comprising the paraffin eicosane ($C_{20}H_{42}$) crystallising from toluene solution. Eicosane is selected as it is representative of wax components within diesel fuels[10], with toluene representative of aromatic solvation

components within fuel[22]. Solution behaviour and the MSZW in the absence and presence of a commercially-available polymeric based CFI additive (IA) is characterised. Eicosane is known to be highly soluble in toluene[23], whereas IA is formulated to be effective in diesel fuel and therefore can be expected to be also somewhat soluble in toluene, given it is representative of aromatic compounds within fuel, but with a different solubility with respect to eicosane.

The experimental approach adopted encompasses polythermal crystallisation/dissolution procedures, with crystallisation and dissolution temperatures determined through turbidity measurements, which is a common technique for determining these parameters[22,24,25]. Through this, the mechanisms by which nucleation occurs[25–27] within the solutions as well as the nucleation kinetics are determined. Overall, this study seeks to characterise and understand the influence of additives on the nucleation behaviour of a simple model fuel system.

6.3 Materials & Methods

6.3.1 Materials

Eicosane (99% pure) and toluene (≥99.3% pure) were supplied by Sigma-Aldrich. IA was supplied by Infineum UK Ltd. All materials were used as supplied, without further purification.

6.3.2 Experimental Procedure

6.3.2.1 Solution Preparation

All solutions were prepared at four concentrations (eicosane + IA) for each IA treat rate used, ranging from 250 - 550 g L^{-1} for 0, 0.5, 2, 3, 5 and 10 wt% IA treat rate and 200 – 500 g L^{-1} for 0.1 wt% IA treat rate, with IA treat rate corresponding to wt% IA with respect to the total solution concentration, providing a total of 28 solutions for this study. Solutions were prepared by weighing eicosane and IA into 15 ml prewashed glass vials, using a weighing scale that could measure with ±0.1 mg accuracy. A Fisherbrand 500-5000 µl micropipette was used to add 5 ml toluene to each solution. A magnetic stirrer was placed into the glass vials and the mixtures were placed on a stirrer hot plate and held at 35 ºC for 30 minutes under constant agitation, in order to form a homogeneous liquid solution. 1 ml of solution was added to the 1.5 ml glass vials and a standard 7 x 2 mm magnetic stirrer was added to each vial.

6.3.2.2 Polythermal Measurements

Polythermal crystallisation and dissolution experiments were performed using the Technobis Crystal 16® system[28]. The 1 ml solutions were subject to different cooling and heating cycles. Each temperature cycle began by heating the solutions to 37 ºC, before being held at this temperature for one hour to ensure that complete homogenisation had taken place and was then subsequently cooled at a set rate to -15 ºC. This temperature was then held for an hour to allow equilibration, followed by an increase in temperature back to 37 ºC at the specified rate. This temperature profile was performed for each concentration of each composition at rates (q) of 0.25, 1, 2 and 3.2 ºC min^{-1} for both the cooling and heating segments of the temperature cycles with constant stirring at 300 rpm. Each temperature cycle was performed five times to obtain mean and standard deviation (STD) values for the crystallisation and dissolution temperatures.

Crystallisation (T_c) and dissolution temperatures (T_{diss}) were determined from transmission vs. temperature profiles. The values of transmittance were calibrated to range from 100%, for a homogeneous liquid solution, to 0%, for a fully opaque solution. Data was initially analysed through the standard route (STR)[22,25,29–32], where T_c was taken as the onset point where the light transmittance dropped to approximately 95% and T_{diss} was taken as the point where the light transmittance reached 100% for all measurements. Reanalysis of raw transmittance data was also performed (RRT), for solutions that demonstrated two distinct linear and non-linear regions in the transmission vs. temperature profiles, for both the crystallisation and dissolution processes. For these solutions T_c of eicosane was taken as the point where light transmittance began to drop in a linear and rapid manner and T_{diss} of eicosane was taken as the point where light transmittance altered from the linear increasing region to the non-linear increasing region. This created minor errors in the determination of T_{diss} of eicosane, given a transmittance of 100% was not reached before transition to the non-linear transmission region. However, this was deemed to have negligible impact upon the values of eicosane T_{diss}, given the sharp increases in transmittance observed for solutions that were not subject to two dissolution regions.

6.3.2.3 Data Analysis: Solubility

The polythermal data collected through both analysis routes was used to extrapolate both $T_c(q)$ and $T_{diss}(q)$ lines back to a cooling rate of 0 ºC min^{-1} so that the crystallisation temperatures at the kinetic limit ($T_{c,l}$) and equilibrium saturation temperatures (T_e) could be determined, respectively. The difference between $T_{c,l}$ and T_e was taken as the steady-state MSZW.

A van't Hoff analysis was performed on the solubility data with the solution ideality determined from a previous study[23], based upon the Hildebrand equation (Equation 6.1). Activity coefficients (Υ), enthalpy (ΔH_{diss}) and entropy (ΔS_{diss}) of dissolution were calculated based on Equations (6.2) and (6.3), respectively[22]:

$$\ln(X_{ideal}) = \frac{\Delta H_{fus}}{R}\left[\frac{1}{T} - \frac{1}{T_m}\right] \quad 6.1$$

$$\Upsilon = \frac{X_{ideal}}{X} \quad 6.2$$

$$\ln(X) = -\frac{\Delta H_{diss}}{RT} + \frac{\Delta S_{diss}}{R} \quad 6.3$$

Where X_{ideal} is the solution concentration, X is the solute mol fraction, ΔH_{fus} is the enthalpy of fusion, R is the ideal gas constant, T is the temperature and T_m is the melting temperature.

van't Hoff calculations for solutions containing IA were performed taking X as the mol fraction of eicosane alone, assuming a negligible impact of IA on the overall dissolution of eicosane, given its low concentration within solution.

6.3.2.4 Data Analysis: Nucleation Mechanism and Kinetics

The KBHR approach was undertaken to gain an insight into the mechanism by which eicosane nucleated and its associated nucleation kinetics. The KBHR approach relates the relative critical undercooling (u_c) to the cooling rate (q). u_c was calculated through the relationship:

$$u_c = \frac{\Delta T_c}{T_e} \quad 6.4$$

Where, $\Delta T_c = T_e - T_c$

Plots of u_c vs q in ln-ln coordinates were produced, giving linear relationships, with the slopes of fitted linear regressions providing information as to the mechanism of nucleation. A slope <3 indicated an IN pathway, whereas a slope >3 signified a PN pathway. IN describes the pathway by which all nucleation active sites in a system (in this case a solution) have practically equal activities. Therefore, when a level of supersaturation is reached, corresponding to the critical level of supersaturation required for nucleation, all nucleation events occur at one instance. In contrast, PN describes the pathway by which nucleation active sites have a range of activities. This non-uniform distribution of energies results in nucleation events occurring over a range of time where nucleation events can take place in the presence of already growing crystals.

For the PN case, the final expression for $u_c(q)$ dependence, when expressed through the number of crystallites at the detection point (N_{det}), enables the calculation of the nucleation parameters effective interfacial tension (γ_{eff}), the critical nucleus radius (r^*) and the number of molecules in the critical nucleus (i^*), along with the rate of nucleation (J), with the latter calculated through the expression:

$$J(t) = K_J e^{-\frac{b}{[(1-u_c)u_c^2]}} \qquad 6.5$$

Where b is the dimensionless thermodynamic parameter, which is associated with γ_{eff} and K_J is the nucleation rate constant that is related to the Zeldovich factor (Z), the attachment frequency of monomers to the nucleus (f^*) and the concentration of nucleation sites (C_0).

A full description of the KBHR analysis approach methodology is outlined in a previous research article[33].

6.4 Results & Discussion

6.4.1 Transmission Profiles

Analysis of the profiles of laser transmission as a function of solution temperature, for the solutions studied, provided an indication of the effect of IA on the crystallisation of eicosane from toluene solution. Standard profiles from polythermal crystallisation/dissolution experiments enable the determination of crystallisation and dissolution temperatures through sharp changes in transmission, which tend to follow single regions of a decrease or increase in transmission, respectively[22]. This relationship was observed for eicosane in toluene solutions with no IA present and for relatively low IA treat rates, up to 0.5 wt% IA, as shown in Figure 6.1, suggesting that for these solutions the crystallisation and dissolution processes occurred for eicosane alone, with IA remaining in solution throughout these stages.

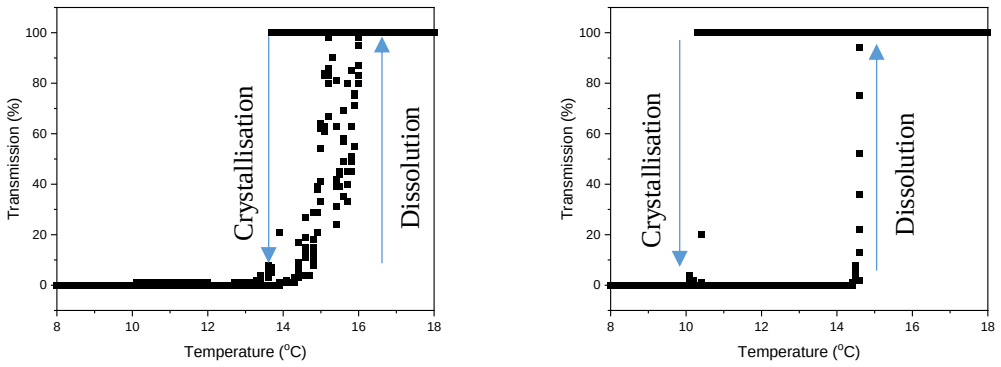


Figure 6.1. Transmission profiles as a function of temperature for eicosane in toluene solution with no IA (left) and 0.5 wt% IA (right) at 250 g L^{-1}, with a heating cycle rate of 0.25 °C min^{-1}.

However, at IA treat rates at 2 wt% and above, phase separation was observed for all solution concentrations and heating rates studied, as evidenced by observation of two regions for crystallisation and dissolution processes, one linear and one non-linear, as shown in Figure 6.2. In this, the linear regions were consistent with the crystallisation and dissolution of eicosane, whereas the non-linear regions identify the crystallisation and dissolution of IA, respectively.

Consideration of the dissolution region reveals that the overall dissolution process was initiated by eicosane crystals dissolving into solution, followed by IA. The dissolution of eicosane was found to be quite rapid, occurring over a short time and small temperature change. In contrast, the dissolution of IA was found to be much slower, with the whole process occurring over a much larger range of solution temperatures. Such behaviour is probably a reflection of the range of molecular weights (MW) for the polymers within IA additive, each of which would be expected to have a different solubility in toluene, i.e. with the lower MWs having the largest solubility.

In contrast, the trend in the decrease of transmission was initiated by a non-linear decrease followed by a sharp linear decrease, demonstrating that IA crystallised prior to eicosane, with the different MW polymer chains of IA crystallising at different times, with the larger chains crystallising first. Eventually, enough IA dropped out of solution that it became ineffective at inhibiting the nucleation of eicosane within solution, resulting in its crystallisation.

Interestingly, prior to the crystallisation of eicosane the transmission was found to consistently slightly increase, as shown in the inset in Figure 6.2(c), suggesting that small amounts of IA may have re-dissolved into solution, even though the solution temperature was continuously decreasing. Whilst this may seem to be somewhat counterintuitive, given the decrease in solubility with lowering solution temperatures, it could provide potential insight into the nucleation behaviour of eicosane. Indeed, alkanes are known to nucleate through the formation of prenucleation clusters within solution prior to the rearrangement of these structures into the crystal structure[34]. Although speculative, the observed decrease in turbidity directly prior to the onset of eicosane nucleation could be taken as indicative of eicosane desolvation and hence formation of solute clusters prior to nucleation, which would, in turn, increase the effective concentration of toluene molecules, enabling them to solvate IA instead of eicosane.

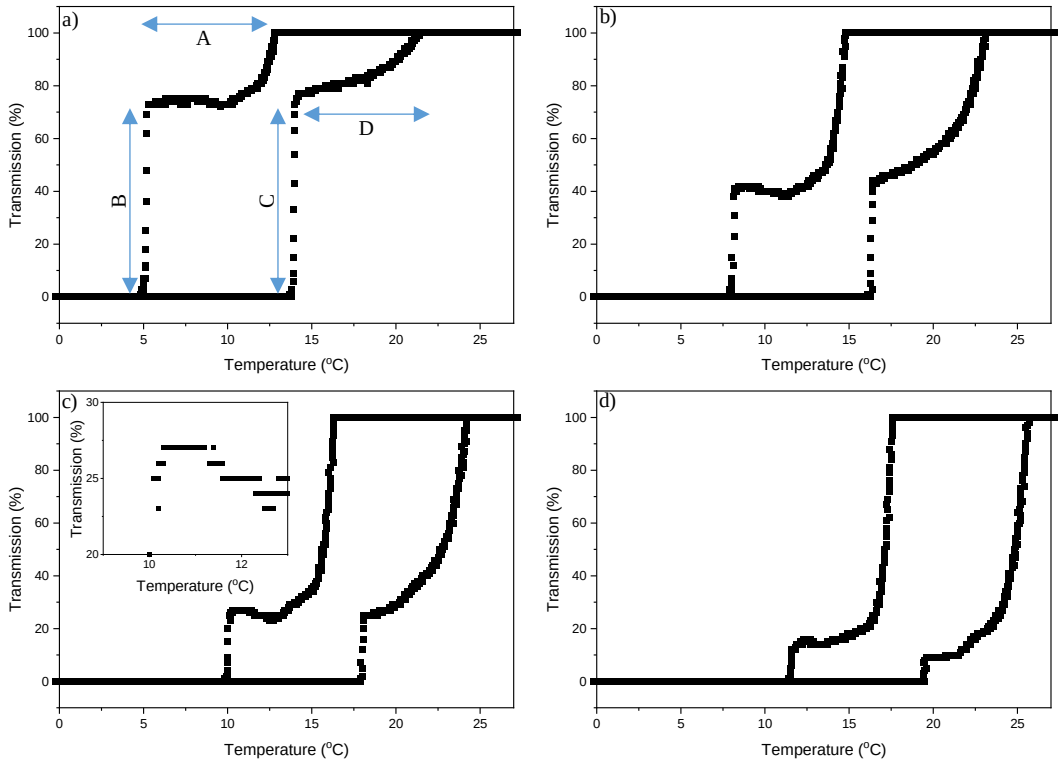


Figure 6.2. Transmission profiles as a function of solution temperature for eicosane in toluene solutions with 10wt% IA treat rate, at heating cycle rates of 0.25 °C min^{-1}, over the range of solution concentrations studied. a) 250 g L^{-1}. b) 350 g L^{-1}. c) 450 g L^{-1}. d) 550 g L^{-1}. Regions defined in a) demonstrate the phase transition processes that occurred for the 3-phase system: A is the crystallisation of IA, B is the crystallisation of eicosane, C is the dissolution of eicosane and D is the dissolution of IA. Inset in c) highlights increase in transmission prior to the onset of eicosane crystallisation.

6.4.2 Characterisation of Crystallisability and Solubility

The equilibrium solubility (T_e) and supersolubility ($T_{c,l}$) temperatures calculated from T_c and T_{diss} analysis are given in Table 6.1, together with their steady-state MSZWs for eicosane in toluene solutions at different IA treat rates. An example of the linear regression plot of T_c and T_{diss} vs. q together with standard deviation values from five repeats are given in Figure 6.3a. The full list of T_c and T_{diss} determined for each solution are provided in Appendix F.

The presence of 0.1 wt% IA in solution was found to slightly decrease the solubility of eicosane in toluene, with further IA treat rate having negligible impact on the solubility of eicosane over the range of treat rates studied. This consistent solubility behaviour over the IA treat rate range

studied suggests that the small thermodynamic effect on solution phase change processes observed reached a critical level at the lowest IA treat rate studied, with further addition not having any observable influence. This observation also suggests that the IA additive was not incorporated into the eicosane crystals during the crystal growth process.

Figure 6.3(b) shows that the crystallisation temperatures decreased as a function of increasing IA treat rate, and that the trend appeared to be quite similar for each of the solution concentrations studied. The data reveals there was a relatively sharp decreases in $T_{c,l}$ observed upon addition of 0.1wt% IA to the eicosane in toluene solutions, followed by a linear, less pronounced, further decrease with increasing IA treat rate. This crystallisation inhibition behaviour probably reflects a decrease in the nucleation and growth kinetics of eicosane, due to chemical and steric interactions between solute and IA molecules within the crystallising solutions. Mostly, these occur via van der Waals interactions formed between IA and solute molecules in solution, as other potential intermolecular interactions, such as electrostatic interactions, would not likely to be dominant due to the low polarizability of the eicosane molecules[23].

Table 6.1. Solubility (T_e) and supersolubility ($T_{c,l}$) data of eicosane in toluene solution with different treat rates of IA, together with the calculated steady-state MSZW over four concentrations (200–500 g L^{-1} for 0.1 wt% IA solution and 250–550 g L^{-1} for all other solutions).

Conc. (g L^{-1})	**$T_{c,l}$ (°C)**	**T_e (°C)**	**MSZW (°C)**	**Conc. (g L^{-1})**	**$T_{c,l}$ (°C)**	**T_e (°C)**	**MSZW (°C)**	**Conc. (g L^{-1})**	**$T_{c,l}$ (°C)**	**T_e (°C)**	**MSZW (°C)**
0 wt% IA				**0.1 wt% IA**				**0.5 wt% IA**			
250	9.9	11.4	1.5	**200**	7.4	11.4	4.0	**250**	8.7	12.8	4.1
350	12.8	13.9	1.1	**300**	10.8	14.5	3.7	**350**	11.8	15.3	3.5
450	14.9	15.8	0.9	**400**	13.2	16.8	3.6	**450**	13.7	17.1	3.4
550	16.6	17.7	1.1	**500**	15.0	18.2	3.2	**550**	15.1	18.5	3.4
2 wt% IA				**3 wt% IA**				**5 wt% IA**			
250	8.0	12.8	4.8	**250**	7.7	12.9	5.2	**250**	6.6	12.6	6.0
350	10.8	15.1	4.3	**350**	10.4	15.1	4.7	**350**	9.2	14.9	5.7
450	12.6	16.9	4.3	**450**	12.2	16.8	4.6	**450**	11.2	16.5	5.3
550	14.3	18.3	4.0	**550**	13.8	18.1	4.3	**550**	12.3	18.1	5.7
10 wt% IA											
250	4.5	12.2	7.8								
350	7.2	14.8	7.6								
450	9.0	16.4	7.4								
550	10.4	17.7	7.2								

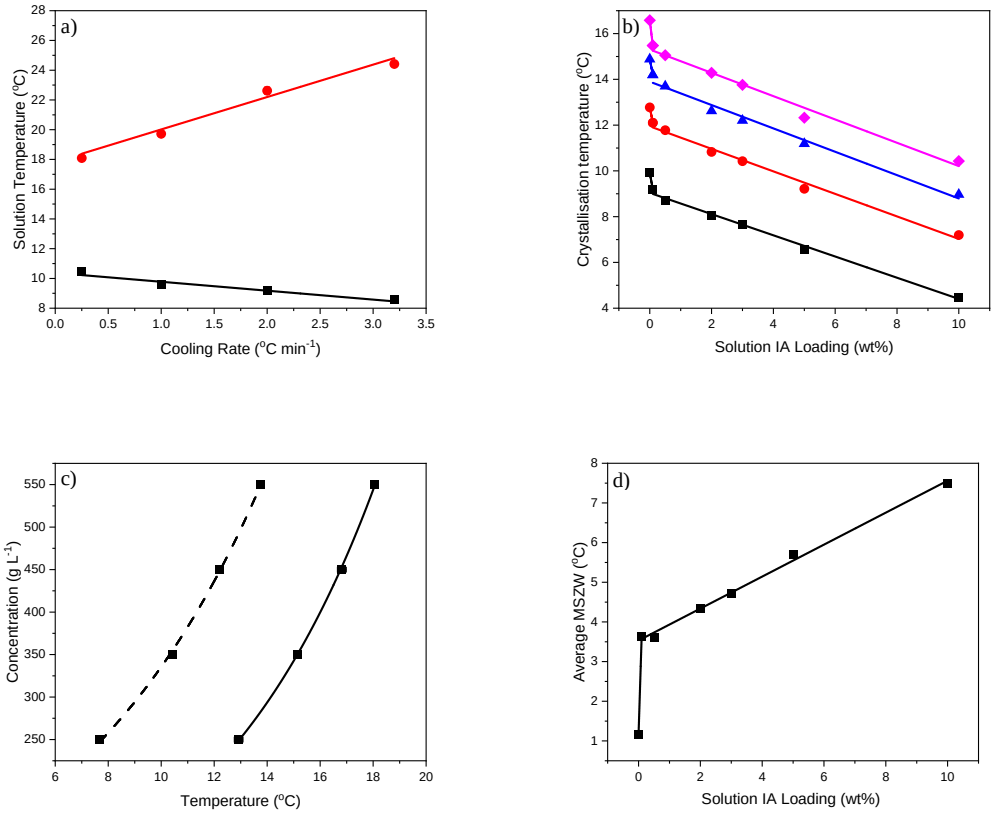


Figure 6.3. a) Plots of eicosane T_c (red circles) and T_{diss} (black squares) as a function of cooling rate (q) with the corresponding best linear fits for eicosane in toluene solutions with 10wt% IA at 550 g L^{-1}. b) Supersolubility ($T_{c,l}$) as a function of IA treat rate for given solution concentrations of 250 g L^{-1} (black squares), 350 g L^{-1} (red circles), 450 g L^{-1} (blue triangles) and 550 g L^{-1} (magenta diamonds). Data is fitted with two linear regressions for each concentration. c) MSZW for eicosane in toluene solution with 3wt% IA loading. Solid lines represent solubility, with dashed lines representing supersolubility. Data is fitted with simple exponentials. d) Increase in average MSZW as a function of IA treat rate.

Extrapolated cooling-rate corrected dissolution (T_e) and crystallisation ($T_{c,l}$) temperatures were found to follow a distinct trend with respect to IA treat rate, Figure 6.3(c), enabling the accurate determination of eicosane solubility over the full range of solution concentrations studied. Solution MSZWs were found to increase with IA treat rate, Figure 6.3(d), suggesting that IA was effective at hindering the nucleation of eicosane from solution. The average MSZW was found to more than triple with the addition of just 0.1 wt% IA to the eicosane crystallising solution, highlighting its ability to inhibit eicosane nucleation even at small treat rates. This was followed by a linear increase in average MSZW with increasing IA treat rate, in line with the

linearly decreasing values of $T_{c,l}$ observed. The latter analysis suggests that the impact of IA on the MSZW could be predicted over a range of IA loadings.

Overall, solution MSZWs were found to be dependent upon solution concentration, with a higher solution concentration correlating with a lower MSZW. This suggests that the crystallisability of solutions increased as the solution concentration was increased. This might be expected, given that a higher solution concentration would tend to crystallise more easily, due to the higher concentration of solute molecules within solution providing a greater chance for critical nucleus sizes to form, required for crystal nucleation to occur.

6.4.3 Analysis of Solution Thermodynamics

Figure 6.4 shows the van't Hoff plots, revealing a good fit by linear regression for all solutions studied, consistent with no change in the solid form of the precipitated material. Table 6.3 shows the calculated enthalpy (ΔH_{diss}) and entropy (ΔS_{diss}) of dissolution values, together with the associated activity coefficients (Υ), as calculated from van't Hoff analysis. The data reveal less than ideal behaviour for all solutions and at all IA treat rates over the temperature range studied, consistent with a preference for solute:solute and/or solvent:solvent intermolecular interactions being the strongest interaction types in solution. Only slight, but consistent changes were found in the variation of van't Hoff plots for the different IA treat rate solutions, although larger deviation was observed in comparison to solutions containing no IA, with higher values of ΔH_{diss} and ΔS_{diss} as a function of increasing IA treat rate.

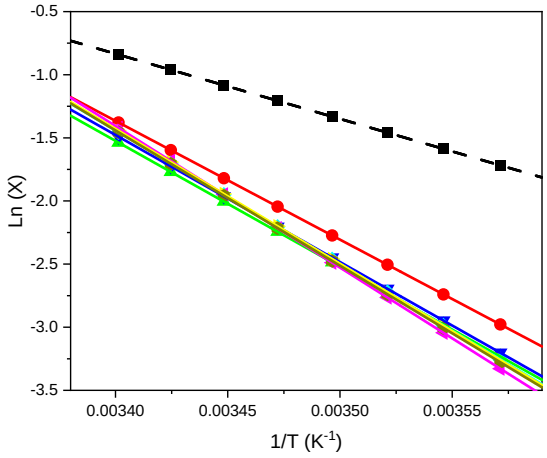


Figure 6.4. van't Hoff plots for eicosane in toluene solution with different IA loadings. Dashed black line represents ideal solubility, and solid lines represent experimental solubilities for different IA treat rates: 0wt% (red circle), 0.1wt% (green up-pointing triangle), 0.5wt% (blue down-pointing triangle), 2wt% (cyan diamond), 3wt% (pink left-pointing triangle), 5wt% (yellow right-pointing triangle), 10wt% (brown hexagon).

Table 6.2. Thermodynamic parameters and activity coefficients calculated from van't Hoff analysis of solubility data.

IA treat rate (wt%)	Enthalpy of dissolution (kJ mol^{-1})	Entropy of dissolution (kJ mol^{-1} K^{-1})	Activity Range
0.0	78.21	0.25	2.07 - 2.78
0.1	82.86	0.27	2.31 - 3.44
0.5	83.65	0.27	2.18 - 3.06
2.0	88.00	0.29	2.18 - 3.11
3.0	93.22	0.31	2.17 - 3.16
5.0	88.81	0.29	2.2.1 - 3.16
10.0	89.05	0.29	2.26 - 3.24

6.4.4 Analysis of Nucleation Mechanism

An example plot of u_c vs q in ln-ln coordinates fitted with linear regressions, for eicosane crystallising from toluene solution with no IA and 3 wt% IA is given in Figure 6.5. Results of nucleation mechanism analysis for all solutions studied are given in Table 6.4.

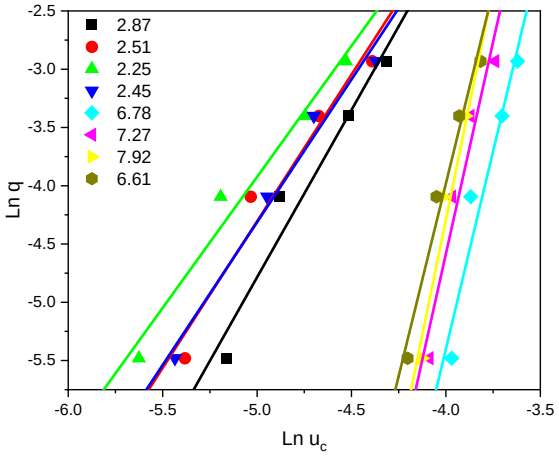


Figure 6.5. $\ln u_c$ vs. $\ln q$ plots for eicosane crystallising from toluene solution without IA and with 3 wt% IA treat rate, over the range of solution concentrations studied. 250 g L^{-1} no IA (black squares), 350 g L^{-1} no IA (red circles), 450 g L^{-1} no IA (green upwards pointing triangles), 550 g L^{-1} no IA (blue downwards pointing triangles) 250 g L^{-1} 3 wt% IA (cyan diamonds), 350 g L^{-1} 3 wt% IA (pink left pointing triangles), 450 g L^{-1} 3 wt% IA (yellow right pointing triangles) and 550 g L^{-1} 3 wt% IA (brown hexagons). Legend on graph gives values of slope for linear regressions fitted, for each concentration.

In the absence of IA, the nucleation pathway was found to be IN for all solution concentrations studied. In contrast, solutions containing IA were found to nucleate via a PN mechanism, for all the IA wt% treat rates and solution concentrations studied. Previous studies have highlighted that the mechanism of nucleation can be altered by changing solution concentration[24], the solvent used[24,34] and also by the inclusion of tailor-made additives[21] in a crystallising solution. An IN mechanism represents a crystallising solution with a high number of nucleation active sites, each with the potential to act as a host for stable prenucleation clusters prior to the nucleation stage. Such clusters could be expected to have similar stabilities and thus, once a critical level of supersaturation is reached, nucleation would be expected to take place for all clusters at one instance. Such a model would be consistent with previous results, which have suggested that alkane crystallisation is initiated by an IN mechanism associated with the presence of prenucleation clusters[34], albeit their structure has yet to be determined.

For solutions containing IA, the high concentration of IA crystallised from solution prior to the nucleation of eicosane would suggest that this precursor crystallisation should provide nucleation sites needed within solution to promote IN nucleation, mindful that this nucleation pathway is associated with heterogeneous nucleation[35]. However, IA containing solutions were found to nucleate by a PN mechanism. This switch towards a PN pathway suggests that IA, in some way, disrupts the formation of stable eicosane prenuclei in solution and, as such, prevents the formation of a uniform distribution of stable prenucleation clusters.

Small molecular additives have been shown previously to change the nucleation mechanism from IN to PN through their ability to disrupt the formation of the stable prenucleation solute clusters that form the precursor of macroscopic crystals of solute, via strong binding to the solute and form non-crystallographic intermolecular interactions (synthons) that inhibit orientation into the crystal structure[21]. The nucleation inhibition power of IA, therefore, is probably due to its strong van der Waals interactions with eicosane molecules in solution. These interactions could also cause IA to be incorporated into growing eicosane nuclei, and as such, disrupt eicosane's ability to readily assemble into the required crystal structure for nucleation. Therefore, nucleation could only occur once a high enough driving force of supersaturation was

generated in solution in order to overgrow the incorporated IA from the growing nuclei. At these higher supersaturations the required critical nucleus size for nucleation would be much lower, enabling smaller eicosane clusters to nucleate. Furthermore, given the polymers higher molecular weights and greater conformational flexibility, IA would be likely to have a large steric impact upon the mass transfer associated with the formation of eicosane nuclei, inhibiting the movement of eicosane molecules through solution and their ability to transfer and interact with growing eicosane prenucleation clusters. Such behaviours would result in only certain eicosane clusters in solution having the ability to grow to a critical size and undergo nucleation, creating a crystallisation process by which nucleation events take place in the presence of already growing crystals, in line with a PN mechanism. The above putative mechanism is though speculative and further studies probing molecular ordering phenomena are clearly needed to quantify this effect.

The progressive nature of nucleation was found to generally increase with IA treat rate, as evidenced by an increase in the slope value of the fitted linear regressions of u_c vs q in ln-ln coordinate plots. This observation suggests that the higher concentration of IA in solution had a larger impact on the disruption of eicosane to form homogeneous clusters in solution and orientate into the required crystal structure, potentially due to the higher level of IA:eicosane interactions and steric hindrance, caused by the increased concentration of polymeric molecules within solution. For high IA treat rate solutions, it is perhaps probable that nucleation was only possible once sufficient IA had dropped out of solution to limit IA:eicosane interactions in solution. This supposition is supported by the data presented in Figure 6.2, whereby at both high solution concentrations, and high IA concentrations, more IA dropped out of solution prior to the nucleation of eicosane, as shown by the larger decreases in transmission of the non-linear region.

Table 6.3. Nucleation mechanisms determined from slopes of u_c vs q in ln-ln coordinates for eicosane in toluene solution with different IA loadings.

Conc. (g/l)	**Slope**	**R^2**	**Nucleation mechanism**	**Conc. (g/l)**	**Slope**	**R^2**	**Nucleation mechanism**
0 wt% IA				**0.1 wt% IA**			
250	2.87	0.95	IN	**200**	6.34	0.92	PN
350	2.51	0.96	IN	**300**	5.47	0.94	PN
450	2.25	0.97	IN	**400**	5.69	0.96	PN
550	2.45	0.98	IN	**500**	5.15	0.93	PN
0.5 wt% IA				**2 wt% IA**			
250	5.35	0.64	PN	**250**	7.08	0.88	PN

350	5.88	0.96	PN	**350**	7.02	0.96	PN
450	6.01	0.97	PN	**450**	7.70	0.92	PN
550	5.86	0.89	PN	**550**	5.90	0.98	PN
3 wt% IA				**5 wt% IA**			
250	6.78	0.93	PN	**250**	10.54	0.94	PN
350	7.27	0.93	PN	**350**	11.21	0.97	PN
450	7.92	0.96	PN	**450**	10.05	0.96	PN
550	6.61	0.97	PN	**550**	3.66	0.91	PN
10 wt% IA							
250	10.20	0.88	PN				
350	13.85	0.89	PN				
450	14.73	0.97	PN				
550	11.21	0.99	PN				

6.4.5 Assessment of the Nucleation Kinetics

Calculated nucleation kinetic parameters for the eicosane in toluene solutions containing IA are displayed in Table 6.5. The dimensionless thermodynamic parameter b, was found to increase by an order of magnitude from a 0.1 wt% to 10 wt% IA loading, in line with a doubling of the values of effective interfacial tension over the same increased IA loading range. The values of effective interfacial tension at the higher IA treat rates are above those previously observed in the crystallisation of eicosane from solution in the absence of any additives[10,23]. This demonstrates a decrease in eicosane crystallisability as a function of increasing IA treat rate, as evidenced also by the increasing MSZW and the shift towards a PN mechanism, all of which is consistent with IA surface adsorption to a growing eicosane prenucleation cluster, increasing the barrier to the formation of a critically sized eicosane nucleus. This is supported by analysis of the nucleation kinetics parameters, revealing critical nucleus size and the number of molecules in the critical nucleus both increased with IA treat rate, with the latter increasing by an order of magnitude over the full range of IA treat rates studied for a given level of undercooling corresponding to the MSZ limit of eicosane crystallising from toluene solution in the absence of IA.

Table 6.4. Nucleation kinetics parameters and nucleation rates of eicosane crystallising from toluene solution at different IA treat rates. The critical radius (r^*) and number of molecules within the cirtical cluster (i^*), are calculated at $u_c = 0.004$, corresponding to the average value of u_c for eicosane in toluene solution without IA, are displayed.

IA loading	Conc. (g L^{-1})	b	γ_{eff} (mJ m^{-2})	r^* (nm)	i^*	IA loading	Conc. (g L^{-1})	b	γ_{eff} (mJ m^{-2})	r^* (nm)	i^*
0.1wt%	200	5.48E-04	2.13	3.97	520	**0.5wt%**	250	3.84E-04	1.90	3.52	362
	300	3.50E-04	1.84	3.43	335		350	3.45E-04	1.84	3.41	329
	400	3.29E-04	1.80	3.37	318		450	3.30E-04	1.82	3.36	317
	500	2.41E-04	1.63	3.04	233		550	3.46E-04	1.85	3.42	333
2wt%	250	8.62E-04	2.58	4.53	774	**3wt%**	250	9.57E-04	2.77	4.60	810
	350	6.57E-04	2.36	4.15	594		350	8.60E-04	2.68	4.45	734
	450	7.56E-04	2.48	4.36	688		450	8.75E-04	2.70	4.49	751
	550	4.22E-04	2.04	3.59	386		550	5.86E-04	2.37	3.93	506
5wt%	250	2.13E-03	3.51	6.10	1892	**10wt%**	250	3.61E-03	4.19	7.27	3194
	350	2.00E-03	3.44	5.99	1791		350	4.65E-03	4.57	7.93	4150
	450	1.54E-03	3.16	5.50	1387		450	4.55E-03	4.54	7.89	4084
	550	3.70E-04	1.97	3.43	335		550	3.11E-03	4.01	6.96	2804

6.5 Conclusions

An investigation into the nucleation inhibition effect of a commercially available CFI additive (IA) on the crystallisation behaviour of the simple model fuel system, eicosane in toluene solution, highlighted the utility of turbidity measurements and analysis for the characterisation of nucleation behaviour in complex systems, such as providing a revealing insight into the fundamental nucleation inhibition behaviour of the CFI.

Two turbidity analysis routes were presented, using the standard assessment route (STR), whereby changes in light transmittance were assumed to correlate with crystallisation and dissolution phase changes of eicosane, and a reanalysed raw data route (RRT), whereby transmission vs. temperature profiles showing two distinct trends due to phase separation, could be assessed to divulge phase changes in IA and eicosane. At IA treat rates of 2 wt% and above, data collected through STR analysis was found to be inaccurate for characterisation of eicosane crystallisation behaviour, with the RRT method being found to accurately characterise eicosane crystallisation and dissolution processes in the presence of CFI additives.

IA was found to negligibly effect the solubility of eicosane within solution over the full range of IA treat rates studied, suggesting limited thermodynamic impact of IA within solution and little/no IA incorporation within the eicosane crystals. The crystallisation temperature was found to reduce with an increase in IA treat rate, corresponding to an increased MSZW, demonstrating IA's nucleation inhibition power and its increased effectiveness at higher

solution loadings. All solutions showed less than ideal behaviour, with solution thermodynamic parameters being found to be relatively consistent over the range of IA treat rates studied.

Eicosane crystallising from toluene solutions in the absence of the CFI additive were found to nucleate via an instantaneous nucleation mechanism, which switched to a progressive nucleation pathway upon addition of the additive. This change in nucleation mechanism would be consistent with strong intermolecular binding between IA and solute molecules, disrupting the solute's ability to form prenucleation clusters required for their development into crystals at nucleation.

Nucleation kinetic analysis showed that for a given solution undercooling there was an increase in the effective interfacial tension, affecting a higher degree of difficulty of nucleation. Such an increase was consistent with an increase in the progressive nature of nucleation.

Overall, the study revealed an increased fundamental knowledge of the nucleation inhibition behaviour of CFIs such as IA, providing, in turn, an insight into characterisation methods for assessment and screening additive efficacy.

6.6 References

1. Bauer, J. *et al*. Ritonavir: An Extraordinary Case of Conformational Polymorphism. *Pharm. Res.* **18**, 859–866 (2001).
2. Wang, C. *et al*. Molecular, Solid-State and Surface Structures of the Conformational Polymorphic Forms of Ritonavir in Relation to their Physicochemical Properties. *Pharm. Res.* **38**, 971–990 (2021).
3. Anwar, J., Boateng, P. K., Tamaki, R. & Odedra, S. Mode of action and design rules for additives that modulate crystal nucleation. *Angew. Chemie - Int. Ed.* **48**, 1596–1600 (2009).
4. Frank, D. S., Zhu, Q. & Matzger, A. J. Inhibiting or Accelerating Crystallization of Pharmaceuticals by Manipulating Polymer Solubility. *Mol. Pharm.* **16**, 3720–3725 (2019).
5. Ilevbare, G. A., Liu, H., Edgar, K. J. & Taylor, L. S. Maintaining supersaturation in aqueous drug solutions: Impact of different polymers on induction times. *Cryst. Growth Des.* **13**, 740–751 (2013).
6. Trasi, N. S. & Taylor, L. S. Effect of polymers on nucleation and crystal growth of amorphous acetaminophen. *CrystEngComm* **14**, 5188–5197 (2012).
7. Weissbuch, I., Addadi, L., Lahav, M. & Leiserowitz, L. Molecular recognition at crystal

interfaces reduction in crystal symmetry of solid. *Science (80-.).* **253**, 637–645 (1991).

8. Weissbuch, I., Lahav, M. & Leiserowitz, L. Toward stereochemical control, monitoring, and understanding of crystal nucleation. *Cryst. Growth Des.* **3**, 125–150 (2003).
9. Gerson, A. R., Sherwood, J. N., Roberts, K. J. & Hausermann, D. Novel kinetic and structural studies of wax crystallisation. *J. Cryst. Growth* **99**, 145–149 (1990).
10. Roberts, K. J., Sherwood, J. N. & Stewart, A. The nucleation of n-eicosane crystals from solution in n-dodecane in the presence of homologous impurities. *J. Cryst. Growth* **102**, 419–426 (1990).
11. Gerson, A. R., Roberts, K. J. & Sherwood, J. N. An instrument for the examination of nucleation from solution and its application to the study of precipitation from diesel fuels and solutions of n-alkanes. *Powder Technol.* **65**, 243–249 (1991).
12. Zhang, J., Wu, C., Li, W., Wang, Y. & Han, Z. Study on performance mechanism of pour point depressants with differential scanning calorimeter and X-ray diffraction methods. *Fuel* **82**, 1419–1426 (2003).
13. Marie, E., Chevalier, Y., Eydoux, F., Germanaud, L. & Flores, P. Control of n-alkanes crystallization by ethylene-vinyl acetate copolymers. *J. Colloid Interface Sci.* **290**, 406–418 (2005).
14. Gerson, A. R., Roberts, K. J., Sherwood, J. N., Taggart, A. M. & Jackson, G. The role of growth environment on the crystallization of normal alkanes in the homologous series from C18H38 to C29H60. *J. Cryst. Growth* **128**, 1176–1181 (1993).
15. Pino-García, O. & Rasmuson, Å. C. Influence of additives on nucleation of vanillin: Experiments and introductory molecular simulations. *Cryst. Growth Des.* **4**, 1025–1037 (2004).
16. Mullin, J. W. *Crystallization*. (Butterworth-Heinemann, 2001).
17. Camacho Corzo, D. ., Ma, C. ., Ramachandran, V., Mahmud, T. & Roberts, K. . Crystallisation Route Map. in *Engineering Crystallography: From Molecule to Crystal to Functional Form. NATO Science for Peace and Security Series A: Chemistry and Biology* (eds. Roberts, K. ., Docherty, R. & Tamura, R.) 179–213 (Springer, 2017).
18. Sangwal, Mk. *Additives and Crystallization Processes: From Fundamentals to Applications*. (John Wiley & Sons Ltd., 2007).
19. Hennessy, A. J., Neville, A. & Roberts, K. J. An examination of additive-mediated wax nucleation in oil pipeline environments. *J. Cryst. Growth* **198**–**199**, 830–837 (1999).
20. Myerson, A. S. & Jang, S. M. A comparison of binding energy and metastable zone width for adipic acid with various additives. *J. Cryst. Growth* **156**, 459–466 (1995).
21. Kaskiewicz, P. L. *et al.* Understanding and Designing Tailor-Made Additives for Controlling Nucleation: Case Study of p-Aminobenzoic Acid Crystallizing from Ethanolic Solutions. *Cryst. Growth Des.* (2021).

doi:https://dx.doi.org/10.1021/acs.cgd.0c01209

22. Tang, X. *et al.* Solubility and crystallisability of the ternary system: Hexadecane and octadecane representative in fuel solvents. *Fuel* **226**, 665–674 (2018).
23. Kaskiewicz, P. L. *et al.* Influence of Solution Chemistry on the Solubility, Crystallisability and Nucleation Behaviour of Eicosane in Toluene/Acetone Mixed-Solvents. *CrystEngComm* **23**, 3109–3125 (2021).
24. Turner, T. D. *et al.* The influence of solution environment on the nucleation kinetics and crystallisability of para-aminobenzoic acid. *Phys. Chem. Chem. Phys.* **18**, 27507–27520 (2016).
25. Camacho Corzo, D. M. *et al.* Nucleation mechanism and kinetics from the analysis of polythermal crystallisation data: methyl stearate from kerosene solutions. *CrystEngComm* **16**, 974–991 (2014).
26. Kashchiev, D., Borissova, A., Hammond, R. B. & Roberts, K. J. Effect of cooling rate on the critical undercooling for crystallization. *J. Cryst. Growth* **312**, 698–704 (2010).
27. Kashchiev, D., Borissova, A., Hammond, R. B. & Roberts, K. J. Dependence of the critical undercooling for crystallization on the cooling rate. *J. Phys. Chem. B* **114**, 5441–5446 (2010).
28. Technobis. Crystal16. (2020). Available at: https://www.crystallizationsystems.com/crystal16.
29. Jiang, S. & Ter Horst, J. H. Crystal nucleation rates from probability distributions of induction times. *Cryst. Growth Des.* **11**, 256–261 (2011).
30. Toroz, D. *et al.* Towards an understanding of the nucleation of alpha-para amino benzoic acid from ethanolic solutions: a multi-scale approach. *Faraday Discuss.* **179**, 79–114 (2015).
31. Rosbottom, I. *et al.* Influence of Solvent Composition on the Crystal Morphology and Structure of p-Aminobenzoic Acid Crystallized from Mixed Ethanol and Nitromethane Solutions. *Cryst. Growth Des.* **17**, 4151–4161 (2017).
32. Kaskiewicz, P. L. *et al.* Isothermal by Design: An Accelerated Approach to the Prediction of the Crystallizability of Slowly Nucleating Systems. *Org. Process Res. Dev.* **23**, 1948–1959 (2019).
33. Camacho, D. M., Roberts, K. J., More, I. & Lewtas, K. Solubility and Nucleation of Methyl Stearate as a Function of Crystallization Environment. *Energy and Fuels* **32**, 3447–3459 (2018).
34. Tang, X. Crystal Structure, Phase Behaviour and Kinetics Associated with the Crystallisation of Octadecane, Hexadecane, and Mixtures Thereof. (2017).
35. Kashchiev, D. *Nucleation*. (Butterworth-Heinemann, 2000).

Chapter 7 Conclusions & Future Work

Summary: This chapter draws together conclusions from the research studies presented and relates the outcomes to the aims & objectives of this project. Suggestions of future work that could be undertaken to further develop this work are presented.

7.1 Conclusions of this Work

This work has aimed to advance the current knowledge surrounding unwanted nucleation events within formulated products, specifically focussed towards the potential to predict when unwanted nucleation might occur across long timescales, how nucleation can be influenced by solution structure and how nucleation can be suppressed through the use of crystallisation additives.

In this, Chapters 2 and 3 have focussed upon how nucleation can be accelerated through the generation of high solution supersaturation conditions, such that the induction time to nucleation is reduced by orders of magnitude. The accelerated method utilised an antisolvent crystallisation mixed solvent system and the work presented in Chapter 4 focussed upon how a mixed solvent system can influence the nucleation process directly, through changes in the solution chemistry, to alter the crystallisability, solution thermodynamics and the nucleation mechanism and kinetics. Chapters 5 and 6 took this concept and applied it towards crystallising systems in the presence of two types of additives that have the potential to inhibit unwanted nucleation, again focussing on how the crystallisability, solution thermodynamics and the nucleation mechanism and kinetics can be affected. As outlined in Section 1.2 of this thesis, Chapters 2 to 6 represent the possibility for a cyclic research and development system encompassing accelerated nucleation testing in product development to assess stability, with alterations in stability being made through changes in the product composition and/or the use of additives, with their effectiveness then assessed through accelerated nucleation testing, etc.

Nevertheless, it should be noted that the research presented in this thesis has focussed on crystallising systems under the effect of agitation, due to the requirements for good mixing in these studies. In reality, a large proportion of formulated products are stored and/or used under quiescent conditions, which would affect the nucleation behaviour in comparison to if they were under agitation. In this, changes in agitation rate have been found to alter the size of the MSZW and the rate of nucleation[1,2] in crystallising systems. However, trends in these effects have been found over ranges of agitation rates, suggesting that it may be possible to extrapolate key nucleation information from agitated to quiescent conditions. More work is needed to fully understand this behaviour.

7.1.1 Accelerated Nucleation Testing

Chapters 2 and 3 presented work relating to the accelerated nucleation of p-aminobenzoic acid, introducing a newly developed methodology for achieving high supersaturation solution

conditions. This method, termed Isothermal by Design (IbD), utilised the concept of antisolvent crystallisation, whereby supersaturation was be generated through the addition of a solvent (antisolvent), in which the solute has low solubility, to an already formed solution. In this, pABA was crystallised from mixed EtOH/H_2O solutions with additional H_2O used as an antisolvent. Taking account of the enthalpy of mixing associated with this procedure by offsetting the temperature of the antisolvent to be added, enabled isothermal conditions to be maintained and an isothermal crystallisation analysis route to be taken for assessing nucleation kinetics.

The exothermic enthalpy of mixing associated with the addition of H_2O to pABA in EtOH/H_2O mixed solvent solutions was found to be substantial, requiring large offsets in antisolvent temperatures in order to maintain solution temperatures after addition. This mixing effect followed a linear relationship as a function of antisolvent temperature, enabling total antisolvent temperature calibrations to be determined by linear extrapolation of results to required solution temperatures and varying initial solution volumes used.

Induction time results obtained through IbD were found to be more controlled, reproducible and reliable than results obtained when the enthalpy of mixing was not accounted for and the antisolvent temperature was not offset to maintain solution temperature. Furthermore, high levels of solution supersaturation were generated, much higher than could be achieved through conventional crystallisation methods, enabling a wide range of induction times for pABA crystallisation. These ranged from around 10,000 seconds at low supersaturation to less than a second at the higher supersaturations generated. At the higher supersaturations the reproducibility of induction time results was found to increase, which is attributed to the much higher driving force to nucleation somewhat overcoming the stochastic nature of nucleation. This substantial change in induction times and increased reproducibility of results at higher supersaturations demonstrates the promising nature of IbD to be used for accelerated nucleation testing, in the hope of predicting unwanted nucleation events over long time scales. Furthermore, due to the large range of supersaturations studied through IbD, a mechanism change from heterogeneous to homogeneous nucleation was observed at a supersaturation of around $S \approx 1.5$, providing key insight into the fundamental crystallisation behaviour of pABA over the supersaturations studied.

Results obtained via IbD for pABA crystallising from mixed EtOH/H_2O solutions were also compared with those obtained for pABA crystallising from pure EtOH and H_2O solutions using a common experimental isothermal crystallisation method, temperature jump isothermal method (TJM). The range of supersaturations studied through TJM was much lower than those

through IbD, due to the limited levels achievable through this method. However, a comparison of results obtained over a similar supersaturation range demonstrated that the induction time versus supersaturation behaviour of the crystallising solutions was similar for pABA crystallising from mixed EtOH/H_2O solutions through IbD and pABA crystallising from EtOH solutions using TJM. In contrast, induction times determined for pABA crystallising from H_2O solutions through TJM demonstrated that a much higher driving force was required to nucleate pABA for a given induction time. This suggests that the local solvation environment in a crystallising solution could be dominated by the highly solvating solvent, in this case EtOH, and as such, could dominate the nucleation behaviour. Thorough analysis of the calculated nucleation parameters demonstrated that although the effective interfacial tension increased the driving force to nucleation required pABA to crystallise from mixed EtOH/H_2O solutions with higher H_2O content, kinetic parameters offset this behaviour due to changes in solution concentrations, supersaturations and compositions, resulting in lower induction times at higher H_2O content.

7.1.2 Influence of Solution Structure on Nucleation from Solution

Chapter 4 followed on from the mixed solvent crystallisation behaviour investigated in the presented IbD studies, with an investigation into the impact of solution chemistry and structure on the nucleation behaviour of a mixed solvent crystallising system. Here, eicosane crystallising from mixed toluene/acetone solutions was studied through a combination of experimental and computational techniques.

Eicosane was found to be more soluble in toluene than in acetone, with, in general, a decrease in eicosane solubility with increasing acetone content within the mixed toluene/acetone solutions at solution temperatures below 25 °C. However, at 25 °C small additions of acetone to eicosane in toluene solution were found to increase eicosane solubility, in line with results obtained for pABA in mixed EtOH/H_2O solutions with additions of H_2O to pABA in EtOH solution. This behaviour is suggested to occur due to the lower solubility solvent interacting with empty solvation sites to the solute molecules that the higher solubility solvent may not be able to solvate. A temperature dependency of this behaviour would suggest that a certain level of molecular mobility would be required for this to occur however.

Over the full range of solution compositions studied, the MSZWs, enthalpies of dissolution/mixing, interfacial tensions and the values of slopes for the calculation of IN/PN mechanism, providing an indication of the relative impact of thermodynamic and kinetic factors on the nucleation process, were found to follow a similar trend. In this, these metrics were found

to increase for solutions up to an acetone mol fraction (y) of 0.85, followed by a decrease at higher acetone content, reflecting likely changes in the solution chemistry as a function of composition.

Grid-based molecular modelling studies provided elucidation towards this behaviour, demonstrating that the local solvation environment of an eicosane molecule within the mixed solvent solution would be structured differently depending upon the solvent composition. Solutions with an excess of toluene and those of the pure solvents would be dominated by homogeneous solvent:solvent interactions that would allow for the stabilising of eicosane prenucleation clusters prior to nucleation, leading to an IN mechanism. In contrast, for solutions containing an excess of acetone, a more complicated local solvation environment was suggested, whereby acetone would form a 'cage' around toluene molecules that could be solvating an eicosane molecule, practically solvating the toluene molecules and withdrawing some of the solvation propensity towards eicosane. This behaviour could lead to less stable prenucleation cluster formation and direct the nucleation towards a PN mechanism, as was observed for these solutions. This solution chemistry behaviour was found to be responsible for the trends observed for all the aforementioned solution property and crystallisation metrics.

7.1.3 Effect of Tailor-Made Additives on Nucleation

Chapter 5 focussed upon the ability to disrupt the process of nucleation through the use of 'imposter' molecules that have a similar molecular structure to the solute that is to be crystallised, which are referred to as tailor-made additives (TMAs). Here, 7 TMAs were studied for their potential effect upon the crystallisation of pABA from ethanolic solutions, using a combination of grid-based molecular modelling and experimental techniques. The TMAs were selected based upon their potential to interrupt the synthons important for the nucleation of pABA from ethanolic solution, mainly: synthons A, B and C, with synthon A being the most important with regards to initiating pABA nucleation.

Out of the 7 TMAs studied, 3 were found to form stronger synthonic interactions with pABA in comparison to pABA with itself, with the strongest interaction type being synthon A; the 4 remaining TMAs interacted more weakly and so were assumed to have negligible effects upon pABA nucleation. These strongly interacting pABA:TMA heterodimers were found to be more stable in solution than pABA:pABA homodimers and one of the TMAs, 4-amino-3-nitrobenzoic acid (ANBA3), was found to be able to direct non-crystallographic synthons with subsequent pABA molecules interacting with the heterodimer. Substituting the heterodimers into the pABA crystal structure demonstrated that the TMAs would sterically hinder the

required structural formation and assessment of atomic charges demonstrated that they would also cause electrostatic interactions that would further disrupt pABA nucleation.

Experimental results corroborated these findings, with only the 3 strongly interacting TMAs being found to lower the temperature of pABA crystallisation from ethanol solution, with ANBA3 being the most effective. Further analysis of the impact of ANBA3 demonstrated that it induced a nucleation mechanism change from IN for pABA crystallising in the absence of ANBA3 to PN with it present in solution. This mechanism change is suggested to occur due to ANBA3 disrupting the ability of pABA to form into its crystal structure, which is a requirement for the nucleation process.

7.1.4 Effect of a Polymeric Additive on Nucleation

A study focussing upon the impact of a polymeric commercially available cold-flow improver additive (IA) on the nucleation of eicosane from toluene solutions was presented in Chapter 6. Various solution IA treat rates, ranging from 0 to 10 wt% IA, were used in this study. For a treat rate of 2 wt% IA and above phase separation was found to occur, whereby IA crystallised prior to the nucleation of eicosane upon cooling, whereas upon heating, eicosane dissolved prior to the dissolution of IA. This phase separation was identified by turbidity measurements and an analysis route, termed RRT, was proposed to distinguish between the phase transformation processes of eicosane and IA, respectively.

IA was found to have negligible impact upon the solubility of eicosane, but reduced the crystallisation temperature, increasing the MSZW, with a higher treat rate lowering the crystallisation temperature in a linear manner. Nucleation kinetics and mechanism analysis demonstrated that in the absence of IA, eicosane nucleated via an IN mechanism, whereas in the presence of IA all solutions nucleated via a PN mechanism. This behaviour is suggested to be caused due to the interaction of IA with growing eicosane prenucleation clusters, limiting the ability of stable prenucleation clusters to form and inhibiting the nucleation of eicosane. Assessment of nucleation parameters for a given solution undercooling demonstrated that a higher IA treat rate resulted in a higher effective interfacial tension and, as such, a lower rate of nucleation.

7.2 Review of the Aims & Objectives

In order to determine the success of this work in meeting the originally targeted project aims and objectives, an assessment of the progress made towards completing each objective must be made.

Objective #1. Design and develop experiments to generate high supersaturation conditions within solutions and, as such, drastically increase the rate of nucleation.

This objective was met through the development of the isothermal by design (IbD) method, which enabled the generation of much higher levels of solution supersaturations than might be attained through conventional crystallisation methods, such as cooling, isothermal or evaporative crystallisation. Furthermore, IbD created almost instantaneous generation of high supersaturation conditions, enabling very high rates of nucleation to be probed. However, there are drawbacks to the developed procedure that should be noted, such as the IbD method being limited to an antisolvent crystallisation procedure, which generates the requirement for a large amount of experimental data to be obtained prior to the collection of any nucleation data at high supersaturation conditions. Further experimental effort is also required to produce antisolvent calorimetry calibrations to ensure isothermal conditions are maintained. As stated in Chapter 2, difficulties might also arise when trying to perform IbD on larger scale crystallisation vessels, due to inefficiencies of mixing.

Objective #2. Develop a procedural workflow to aid in standardised accelerated nucleation testing and extrapolation of kinetics from high to low supersaturation conditions.

This objective has not been fully met by the work outlined in this thesis. A procedural workflow was devised for standard accelerated nucleation testing through IbD, but a statistical model enabling the extrapolation of kinetic information from high to low supersaturation conditions has not been developed. Furthermore, results presented under the IbD method pertain to a model aqueous system, but in order to generate standardised testing non-aqueous as well as more complex systems need to be studied. However, steps have been taken to progress these aspects and will be discussed in Section 7.3.

Objective #3. Determine how the types and relative strengths of intermolecular interactions within solutions can influence the nucleation process by altering solution structure.

This objective was mostly met through the work presented in Chapter 4, whereby through a combination of experimental and modelling techniques, alterations of solution structure caused by changes in solution environment were assessed, with the effects on nucleation identified. However, it should be noted that the system studied constituted a hydrophobic crystallisation system, therefore in order to fully realise this objective, information relating to a hydrophilic crystallisation system should be gained, with particular focus towards the impact of hydrogen bonding upon solution structure and subsequent nucleation. Nevertheless, a workflow was developed to aid in this and any future studies relating to understanding the influence of solution chemistry and structure on nucleation.

Objective #4. Develop a procedure to aid in the understanding of how additives can inhibit nucleation on a molecular/atomic level.

This objective was mostly met through the work presented in Chapter 5, which focussed upon the impact of TMAs on nucleation. Through the use of grid-based molecular modelling an understanding of the impact of these additives on the nucleation of pABA from ethanolic solution at a fundamental molecular and atomic level was gained. A procedural workflow was developed to aid future studies focussing upon the mechanistic and fundamental understanding of how these types of additives can inhibit nucleation of other crystallising systems. However, this currently is limited towards the study of TMAs and to be universally applicable to all types of crystallisation additives, further work and potentially different techniques are needed. Furthermore, the systems studied represent relatively simple aqueous crystallising solutions, but in order for the developed procedure to be deemed ‘effective’ a range of varying systems need to be studied.

Objective #5. Perform a case study on a commercially available cold-flow improver additive to determine its potential nucleation inhibition effect on a model compound.

This objective was met through the work presented in Chapter 6, which focussed on the crystallisation of eicosane from toluene solution in the absence and presence of a commercially available cold-flow improver additive (IA) at different additive treat rates. Insight was gained into characterising nucleation kinetics and mechanism through turbidometric analysis and IA’s nucleation inhibition effect was assessed.

Objective #6. Generate a numerical solution to the Kashchiev-Borissova-Hammond-Roberts kinetic analysis approach and link to the developed accelerated nucleation testing procedure.

This objective was not met by the work presented in this thesis. However, a numerical solution to the KBHR approach has been initiated through its incorporation into the commercially available process simulation software: gPROMS FormulatedProducts, produced by Siemens Process Systems Enterprise. This will discussed in more detail in Section 7.3.

Although there has been a large amount of success in meeting the majority of aims and objectives set out under this work, there are limitations to the scope of this work that should be addressed. One limitation is the lack of focus upon whether crystallisation in the systems studied proceeded via classical nucleation theory or a non-classical nucleation theory, such as two-step nucleation. This is a key focus in nucleation research currently and demonstrates one of the exciting and challenging areas in which the scope of this work could have focussed. In understanding whether classical or non-classical nucleation routes occurred, a greater understanding of how to control the nucleation process could have been gained. Suggestions in the presented work, however, demonstrate that some of the systems studied nucleate through the existence of prenucleation clusters, which is somewhat suggestive of a non-classical nucleation process. With a greater focus upon this aspect, more fundamental information could have been elucidated with respect to the nucleation route.

Furthermore, unwanted nucleation events occur across a range of products that are stored/used over highly varied volumes, such as agrochemical products being stored in large vessels in the m^3 range and pharmaceutical drugs held in capsules in the μL range. However, the scope of this work did not encompass studies focussing upon the impact of solution volumes on the nucleation behaviour concepts outlined, such as on the effectiveness of additives or changes in induction time variability.

Overall, a myriad of potential research areas concentrating on unwanted nucleation events could be proposed that are beyond the scope of this work. Nevertheless, given the extensive possibilities available when studying fundamental unwanted nucleation behaviour, although many options exist for potential research avenues, the work presented in this thesis constitutes an extensive investigation into areas surrounding unwanted nucleation events. Future studies would therefore be required to expand the research presented in this thesis.

7.3 Suggested Future Work

The work presented in this thesis not only provides newly developed procedures and insights towards the assessment of various aspects of the crystallisation process, but provides an excellent foundation for future studies to use and further develop these concepts. From this foundation, future studies could explore a wide range of areas relating to unwanted nucleation events and beyond, however, suggestions can be made regarding studies that could go further towards meeting all of the aims and objectives set out under this project.

7.3.1 IbD Non-aqueous System

Firstly, the IbD methodology has been shown to be successful at generating high levels of solution supersaturation when utilised for a model aqueous system with a relatively large metastable zone. However, in order to be developed as a standardised accelerated nucleation procedure, it is important that IbD be tested on a non-aqueous system, a more complex system and on a system with a varied metastable zone. This could take the form of a combined crystallisation system from Chapters 5 and 6, whereby eicosane in the presence of the cold flow improver additive (IA) is crystallised from mixed toluene/acetone solutions, with acetone acting as an antisolvent. Given that results from Chapters 5 and 6 demonstrate that eicosane is much less soluble in acetone than in toluene and these solvents are miscible across the full compositional range and that IA is able to increase the relatively small MSZW of eicosane, this system would provide a strong basis for further IbD testing. The size of the MSZW, and as such the range of supersaturations attainable, could be controlled by the IA treat rate, however, care should be taken with regards to the phase separation behaviour observed at IA treat rates of 2 wt% and above. Also, it would be necessary to determine the solubility of eicosane over the range of toluene/acetone compositions used for the experiments.

Initial testing of the enthalpy of mixing effect when acetone is added to toluene in different ratios has already been performed to determine the possible thermal mixing behaviour of this system. The same procedure as outlined in Chapter 2 Section 1.3.2 was followed and a linear relationship was found between the initial temperature of the antisolvent and the final solution temperature, as shown in Figure 7.1a). This result demonstrates that, as for the pABA EtOH/H_2O system, when using toluene and acetone as a solvent and antisolvent, respectively, the required acetone temperature to maintain solution temperature after addition can be determined through the simple calibration procedure outlined by IbD. This provides some confidence that IbD is applicable towards a non-aqueous crystallising system, however, further difficulties were found when assessing the mixing behaviour. As shown in Figure 7.1b), when

mixing calibrations were performed for toluene held at temperatures below 13 °C, exothermic mixing occurred, whereby in order to maintain solution temperature the acetone had to be at a lower temperature than the toluene. However, at toluene temperatures above 13 °C the opposite behaviour was observed and acetone was required to be at a higher temperature than toluene in order to maintain the set temperatures. This behaviour was found to follow a linear relationship, with the offset in required acetone temperature changing linearly with the temperature at which toluene was held. Nevertheless, a region of relatively constant endothermic mixing behaviour was observed between temperatures in the range of around 20 to 30 °C. This variable enthalpic mixing behaviour demonstrates added challenges to the IbD method and further work is clearly required to fully test this.

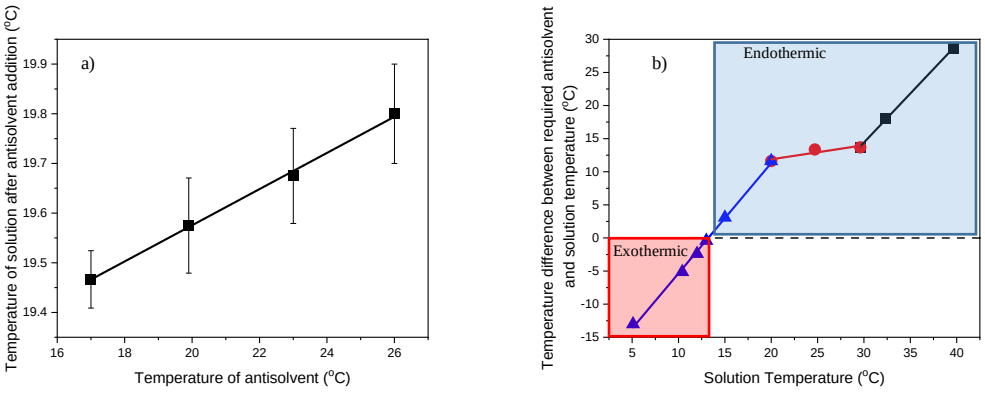


Figure 7.1. Effect that the antisolvent (acetone) temperature had upon the final solution temperature. a) acetone added to different volumes of toluene that were held at 20 °C. b) Exothermic and endothermic mixing behaviour observed when toluene was held at different temperatures. Coloured points and linear regressions represent different thermal mixing trends. Coloured regions represent different enthalpic mixing behaviour (red – exothermic, blue- endothermic).

7.3.2 Extrapolation of Induction Time Data

Furthermore, a route to extrapolating nucleation kinetic data from high to low supersaturation conditions needs to be determined in order for the predictive nature of unwanted nucleation testing to be realised. Given the induction time vs. supersaturation relationship for the pABA in mixed EtOH/H_2O system studied through IbD followed a curve, as observed in Figure 2.7, a statistical model fitted through the data could provide a way to extrapolate induction time data. This would then enable induction time measurements made at the high supersaturation conditions to be used to predict induction times at low supersaturation conditions, nullifying the need for experiments at low supersaturations. This is extremely important for predicting unwanted nucleation events, given that the timeframe for nucleation at low supersaturations

can be extensive and beyond what is reasonable for experimental testing. A statistical model is therefore necessary to make this testing applicable to a multitude of crystallisation systems.

The statistical model used would need to incorporate the key parameters effecting the rate of nucleation that IbD utilises to achieve high rates of nucleation, including the level of supersaturation, the solution composition, the concentration of solute within solution and the solution temperature. These parameters relate strongly to the nucleation rate expression outlined by classical nucleation theory, whereby the rate is dominated by the supersaturation, temperature and the interfacial tension (which is altered by solution compositional changes). Initial statistical analysis has been performed with the help of Dr Alan Brown at Syngenta UK Ltd., to determine the influence of these parameters on the induction time vs. supersaturation results. From this, it was found that the solute concentration and solution temperature, for the ranges studied in the IbD experiments, had negligible effect on the induction time vs. supersaturation relationship, in comparison to both the solution composition and the level of supersaturation. However, these parameters were not found to be independent of each other, given the intrinsic link between, for example, the supersaturation, amount of antisolvent and the solution temperature, making it difficult to uncouple the effect of these parameters on the overall relationship. Furthermore, given the change observed from heterogeneous to homogeneous nucleation at a supersaturation of around $S \approx 1.5$, a single model may not be a viable route for predicting induction times for the pABA EtOH/H_2O system studied. Instead, multiple models may be necessary, one related to heterogeneous nucleation and another to homogenous nucleation. However, this may not be necessary for all systems studied through IbD, as this transition may not occur over the supersaturation ranges assessed. Examples of predicted induction times in comparison to experimentally collected induction times for potential statistical models are shown in Figure 7.2. Future work in this area should probe both the effect of the dependency of the variables and any mechanistic changes in the nucleation process towards a robust statistical model that can be used for extrapolation purposes. In this, it may be found that additional experimental data is required to de-couple the variables and provide independent data and that multiple models are required to fit the data.

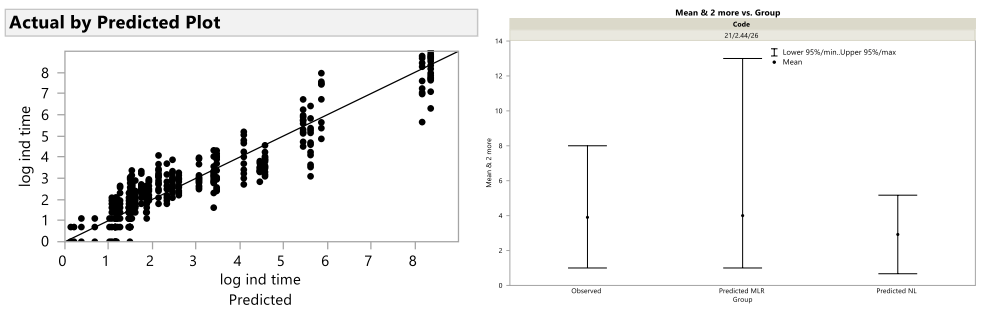


Figure 7.2. Induction time predictions from statistical models. a) Actual vs. predicted log induction times for all data using a non-linear regression model. b) Actual (observed) vs. predicted induction time using a multiple linear regression (MLR) model and a non-linear regression model (NL) for S = 2.44 and T = 26 °C.

7.3.3 IbD Variable Flow

The IbD method developed as part of this project, although successfully implemented for controlled generation of high supersaturation conditions, has some drawbacks that can be improved upon with further development. For example, the current procedure of using a needle and syringe to withdraw and inject antisolvent is not only user intensive but also creates opportunities for errors that can influence the final induction time results, such as not withdrawing the full amount of antisolvent and, as such, altering the final solution supersaturation. This also limits the solution volumes that can be studied through IbD, as only small volumes can be used to enable the rapid mixing required for accurate induction time measurements. In order for IbD to become a robust and routinely used technique, a new procedure could be developed that could also tackle the difficulties faced by the intrinsic stochasticity of nucleation measurements when studying induction times, which provides uncertainty in results. In this, IbD could be tailored towards a procedure akin to polythermal crystallisation, whereby nucleation is driven to occur as opposed to waiting for it to occur, lowering the level of standard deviation within results. This could take the form of a variable flow setup, whereby instead of the current 'instant addition' procedure, antisolvent is added at a rapid rate under controlled pumping, with different levels of supersaturation achieved via alteration of the antisolvent flow rate.

However, this provides added difficulties in controlling the solution temperature upon antisolvent addition given that the antisolvent would be continually added to the solution at different rates and so there would need to be dynamic control of the solution temperature. This is demonstrated in Figure 7.3a), whereby solution temperature increased at different rates and by different amounts depending upon addition flow rate. This could be overcome, however, by utilising separate control systems, such as a power compensation coil, which would use the concept of reaction calorimetry to maintain solution temperature. In this, the coil would provide some of the heat to maintain solution temperature prior to antisolvent addition and upon addition the power to the coil would be reduced/increased in order to offset the changes in temperature caused due to the enthalpy of mixing. This behaviour is demonstrated in Figure 7.3b), whereby the change in solution temperature with exothermic mixing of water and propanol was reduced by the action of a power compensation coil. Future work would take

these concepts and develop a robust IbD procedure that could maintain solution temperature, generate high supersaturation conditions and enable the collection of nucleation data.

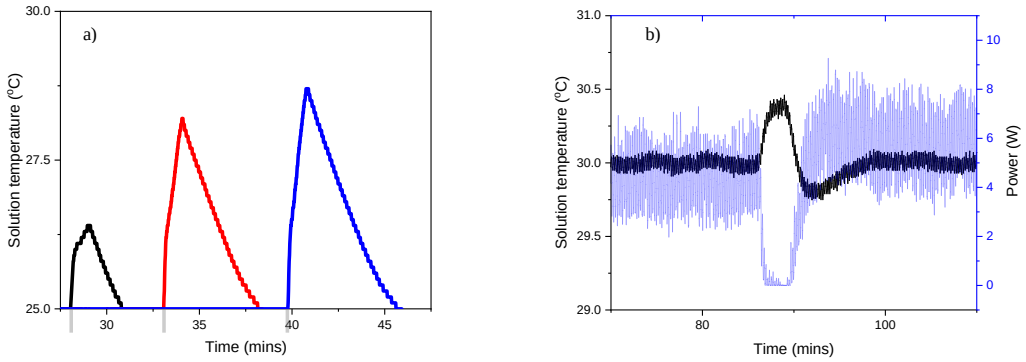


Figure 7.3. Effect upon solution temperature of adding a second solvent at controlled rates to a solution maintained at a set temperature. a) Water at room temperature added to 40 ml ethanol held at 25 °C at varying addition rates of 10 (black line), 17.5 (red line) and 31 (blue line) ml min^{-1}. Grey lines on x-axis show the start of water addition. b) Propanol at room temperature added at a rate of 50 ml min^{-1} to 300 ml of water held at 30 °C, with a power compensation coil set at a 5 °C compensation.

7.3.4 Numerical Solution of Crystallisation Kinetics Approach

The Kashchiev-Borissova-Hammond-Roberts (KBHR) approach to assessing nucleation kinetics through polythermal crystallisation studies is currently limited to a range of relatively low supersaturation conditions, in order to generate the current analytical solution to the model. Therefore, to make it universally applicable for all polythermal crystallisation studies a numerical solution that is not subject to this limitation is required. Furthermore, the suggested IbD variable flow rate methodology would produce data that is akin to polythermal crystallisation data, in that the solution supersaturation conditions are continually changed until nucleation occurs. Therefore, the data would be required to be analysed through a similar assessment method, which could take the form of the KBHR approach. Given that high supersaturation conditions are likely to be generated outside the range currently applicable to KBHR, it is important that a numerical solution be developed. To generate a numerical solution a robust computer modelling/simulation software should be used that enables the estimation of nucleation kinetic parameters from experimentally collected data, whilst allowing for the overarching KBHR equations to be inputted into the system to enable the execution of the numerical solution. Two such simulation packages that could be utilised are MATLAB and gPROMS FormulatedProducts, which would both enable the KBHR models to be inputted into the system and kinetic parameters to be determined from experimental data. The latter software, gPROMS FormulatedProducts is a commercially available process simulation modelling

platform that could provide an environment in which to not only generate a numerical solution to KBHR, but to run separate crystallisation process simulations to generate initial data that could be used as part of the inputted data. This modelling platform also has an extensive parameter estimation tool set that could provide the rigorous modelling criteria for calculating the kinetic parameters of KBHR.

An initial study was performed to determine the ability of gPROMS FormulatedProducts to generate a rigorous numerical solution to the KBHR approach. In this, with the help of Dr Niall Mitchell from Siemens Process Systems Enterprise Ltd., the base KBHR equations, Equations A.40, A.41 and A.42 given in Appendix A, were inputted into the modelling platform environment in the gPROMS language. Experimental data from Camacho Corzo et al.[3] was used to test the model, with crystallisation temperatures at given cooling rates inputted into the process model, alongside calculated crystal mass and an estimates of the average crystal size at the points of detection. The nucleation and growth rate models from the KBHR approach were used with values of parameters taken from the literature data and initial estimates of the nucleation rate constant, the growth rate constant and the thermodynamic parameter b, all three of which were to be determined through the parameter estimation tool in gPROMS FormulatedProducts. It was found that when the value of the thermodynamic parameter b was fixed at the value calculated by Camacho Corzo et al., the rate constants were estimated to be close to those calculated in the study. However, when none of the three parameters were fixed, the software was not able to accurately estimate parameters. This was attributed to the lack of crystal size distribution and evolving crystal mass data necessary for the population balance model based gPROMS FormulatedProducts to accurately estimate nucleation parameters. An example of the process flowsheet used and outputs from a process execution for the crystallisation of methyl stearate from kerosene solution using KBHR nucleation and growth models with the estimated nucleation and growth constants from parameter estimations, setting b as a fixed value, is given in Figure 7.4. Therefore, in order for this software to be used for a KBHR numerical solution, more extensive experimental data is required than measurements of crystallisation and dissolution temperatures. Future work is needed to determine whether this added experimental data does enable the numerical solution to be accurately determined through gPROMS FormulatedProducts and it is also suggested that the KBHR model be inputted into more simple modelling software, such a MATLAB, to generate the numerical solution in a potentially less restricted manner.

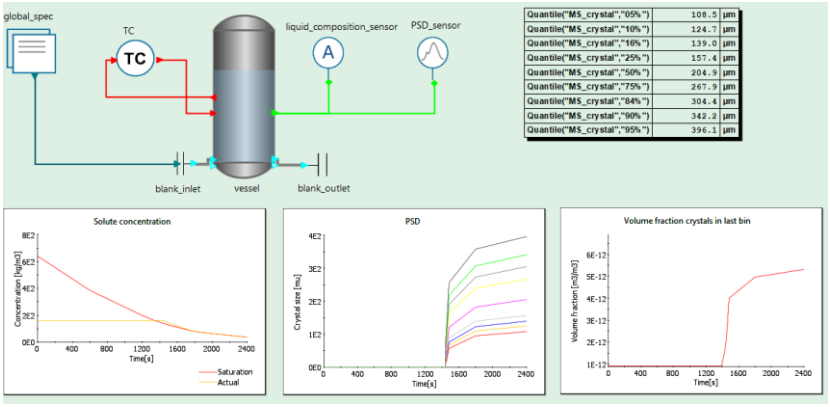


Figure 7.4. Execution output and process flowsheet from gPROMS FormulatedProducts simulation using KBHR kinetic models for methyl stearate crystallisation from kerosene solution.

7.4 Closing Remarks

Overall, this study has provided new insight into accelerating, characterising and controlling crystal nucleation from solution environments, whilst also developing methodologies that can be implemented in future studies to generate the same/similar outcomes in these areas of crystal science and engineering. It is my hope that the foundations developed through this study are further built upon by future researchers, either through the suggested future work packages or through their own insightful studies. As knowledge of crystal nucleation is advanced and a greater understanding of the fundamental processes involved in nucleation are gained, I believe that we will be able to fully control this highly complex phenomenon.

7.5 References

1. Mohd Noor, S. Z., Camacho, D. M., Yun Ma, C. & Mahmud, T. Effect of Crystallization Conditions on the Metastable Zone Width and Nucleation Kinetics of p-Aminobenzoic Acid in Ethanol. Chem. Eng. Technol. 43, 1105–1114 (2020).

2. Liang, K. et al. Examination of the Process Scale Dependence of l -Glutamic Acid Batch Crystallized from Supersaturated Aqueous Solutions in Relation to Reactor Hydrodynamics. Ind. Eng. Chem. Res. 43, 1227–1234 (2004).

3. Camacho Corzo, D. M. et al. Nucleation mechanism and kinetics from the analysis of polythermal crystallisation data: methyl stearate from kerosene solutions. CrystEngComm 16, 974–991 (2014).

Appendix A Crystallography, Crystallisation, Nucleation and Growth

A.1 Crystallography

A crystal, in its most basic terms, is a solid that is made up of a repeating set of elements, which are held in an ordered three-dimensional structure. The arrangement of these repeating sets, whether they be in atomic or molecular form, is an innate property of a crystal and determines the pattern in which it will form[1]. The structural packing of a crystal is anisotropic and exists over what can be deemed an infinite distance, taking into account the entire scale of the solid. It can be described by determining an item that is repeated over the structure, known as a motif. This motif forms an array over the structure of the crystal, known as a crystal lattice, with each point making up the array defined as a lattice point. The environment of every lattice point is identical, therefore it is useful to define only a small section of the entire lattice, in order to show a representative area of how the pattern is repeated, which is known as a unit cell.

As both the components and the geometry of the unit cell are identical in infinite space, it can be described in three dimensions by the length of its sides, a, b and c, and also by the angles between these sides, α, β and γ. These characteristics of a unit cell are termed the lattice parameters, Figure A.1.[2]

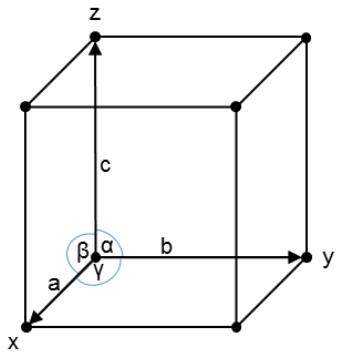


Figure A.1 - A representative unit cell, with unit cell parameters

A.1.1 Crystal Chemistry

The chemistry of a crystal is determined by the forces that act upon and between its atoms, molecules and/or particles and their physical properties, such as size, shape and rotational capacity. All of these factors affect the overall crystal structure. With regards to organic materials the bonds that exist can be defined atomically and molecularly, with atoms in molecules being held together by strong covalent bonds and the molecules that make up the

structure being held together by weaker intermolecular forces. This intermolecular bonding plays a key role in the properties of a crystal and it can be defined by its bond strength and distance. In terms of intermolecular bond strength there is both strong (hydrogen and ionic bonds) and weak (Van der Waals and dipole-dipole interactions), and in terms of intermolecular force distance there is both short (Van der Waals and hydrogen bonds) and long (dipole-dipole and ionic bonds) range interactions between molecules. The range of bonding types present in an organic crystal have a large effect on its mechanical and thermal properties[2].

A.1.2 Polymorphism

Polymorphism is a term used to describe how a crystal can exhibit more than one crystalline structure, with the structures known as polymorphs. These crystalline structures show identical chemical properties, but can have varied physiochemical properties, which can affect its solubility, thermal stability, conductivity, etc.[3] This is due to the different arrangements of molecules in each structure, with a large deviation in properties caused by the changes in bonding at the surface of the crystal.

Polymorphism can result in a different degree of stability between polymorphs. This means that for the same system a resulting crystal can either be stable, or metastable (less stable). The metastable form can exist in an infinitesimal time scale or for a period of years, depending on the particular material and the environment it exists in. A famous example of a polymorphic system where the metastable form converted to the stable form after a time period in the scale of years is ritonavir. Ritonavir is a protease inhibitor used for HIV treatment, which was taken off of the market two years after it was released due to a conformational polymorphic change to its more stable structure, which significantly affected its solubility and hence its bioavailability, meaning it was no longer useful as a HIV treatment drug[4].

A.2 Solution Crystallisation

A homogeneous mixture of at least two substances in a single phase is known as a solution, with components termed solvents and solutes, with respect to a liquid solution. A solution is formed when a solute separates into molecules or ions and the resulting separated components become surrounded by solvent molecules. The interaction between solute and solvent molecules is known as solvation.

Energy changes are associated with the process of forming a solution. The initial enthalpy change (H) of dissolution is related to the energy required to break the intermolecular forces

between the solute-solute and solvent-solvent molecules. In contrast, energy is then released when new bonds are formed between solute-solvent molecules during solvation. The total energy associated with this mechanism is defined as the dissolution enthalpy (ΔH_{diss}). If the solute-solvent interactions are stronger than solute-solute and solvent-solvent interactions ($\Delta H_{diss} < 0$) then dissolution would occur spontaneously. However, if this is not the case ($\Delta H_{diss} > 0$) then dissolution could only occur spontaneously if the entropy of the system (S) was increased by a certain amount. The type and strength of the solute-solvent interactions is very dependent on the solute and solvent chemistry. For non-ionic solutions, such as the solutions being researched for this project, Van der Waals forces and hydrogen bonding dominate the dissolution process[5].

A.2.1 Ideality and Activity

Solutions can be defined as ideal or non-ideal, depending on the interplay between intermolecular interactions. A solution that displays non-ideal behaviour can be described by a factor called activity (a), which gives an indication of its deviation from ideality. The activity shows how active a compound is compared to when it is at its standard state. In real terms it describes the difference in chemical potential when a compound is in a solution and when it is at its standard state[6]. The activity of a component (a_i) can be related to a component mole fraction (x_i) by a value known as the activity coefficient of a component (Υ_i), shown in Equation A.1:

$$a_i = \Upsilon_i x_i \qquad \text{A.1}$$

A general expression relating the activity with solid-liquid equilibrium can be defined as:

$$\ln\left(\frac{\Upsilon_i^L x_i}{\Upsilon_i^S z_i}\right) = \frac{\Delta H_{fus,i}}{RT}\left[\frac{T}{T_{f,i}} - 1\right] + \frac{\Delta C_{p,i}}{R}\left(\frac{T_{f,i} - T}{T}\right) - \frac{\Delta C_{p,i}}{R} ln \frac{T_{f,i}}{T} \qquad \text{A.2}$$

Where: $\Delta H_{fus,i}$ – enthalpy of fusion for component i, R – ideal gas constant, T – temperature, T_f – solute fusion temperature, $\Delta C_{p,i}$ – specific heat capacity of component I, z_i – mole fraction of component in solid phase.

For an ideal solution the solute-solute and the solute-solvent interactions are the same strength, therefore the activity is unity. This means that equation A.2 can be simplified under the assumption that Υ_i^L, Υ_i^S and z_i are all equal to 1. This gives equation A.3.

$$\ln(x_i) = \frac{\Delta H_{fus,i}}{RT}\left[\frac{T}{T_{f,i}} - 1\right] + \frac{\Delta C_{p,i}}{R}\left(\frac{T_{f,i} - T}{T}\right) - \frac{\Delta C_{p,i}}{R} ln \frac{T_{f,i}}{T} \qquad \text{A.3}$$

Assuming that the change in specific heat capacity is negligible over the range of temperatures, this can be simplified further, giving equation A.4:

$$\ln(x_i) = \frac{\Delta H_{fus,i}}{RT}\left[\frac{1}{T} - \frac{T}{T_{f,i}}\right] \quad \text{A.4}$$

At the solute fusion temperature, the enthalpy of fusion (ΔS_{fus}) can be related to the enthalpy of fusion, shown by equation A.5:

$$\Delta S_{fus,i} = \frac{\Delta H_{fus,i}}{T_{f,i}} \quad \text{A.5}$$

Therefore, equation A.3 can be rewritten in the from of the van't Hoff expression:

$$\ln(x_i) = -\frac{\Delta H_{fus,i}}{RT} + \frac{\Delta S_{fus,i}}{R} \quad \text{A.6}$$

In non-ideal solutions there is deviation from ideal behaviour, and as such the activity coefficients are not equal to unity, meaning equation A.6 cannot be used for non-ideal solutions. Instead, by amending the right hand side of the van't Hoff expression the solubility of non-ideal solutions can be determined, leading to equation A.7.

$$\ln(x_i) = -\frac{\Delta H_{diss}}{RT} + \frac{\Delta S_{diss}}{R} \quad \text{A.7}$$

Therefore, a plot of $\ln(x_i)$ vs. $\frac{1}{T}$, determined from experimentally collected solubility data, gives a slope of $\frac{\Delta H_{diss}}{R}$ and a y-axis intercept of $\frac{\Delta S_{diss}}{R}$, allowing the enthalpy of dissolution and the entropy of dissolution to be determined, respectively.

Nevertheless, these equations are based on many assumptions, such as the heat capacity change is negligible over a range of temperatures and that the standard state of two phases are equal. These assumptions create errors in the values calculated from the van't Hoff equations, however they are still very suitable and widely used as expressions for calculating deviations from ideality along with ΔH_{diss} and ΔS_{diss}.

A.2.2 Non-ideal Solutions

Non-ideal solutions can be categorised into two classification, regular or a-thermal, depending on the factors that affect their deviation from ideality. Enthalpy effects are responsible for the deviation from ideality associated with regular solutions, as the total excess Gibbs free energy

(ΔG^E) is equivalent to the enthalpy excess function (ΔH^E). However, an a-thermal solutions deviation from ideal behaviour is due to entropic effects, as the total excess Gibbs free energy (ΔG^E) is equivalent to -$T\Delta S^E$, where ΔS^E is the entropy excess function.

In general, if a solution is formed from similar sized components but with different intermolecular forces, a regular solution is formed. If solution components differ in molecular size but have similar intermolecular forces, then a-thermal solutions are formed.

A.2.3 Solubility

The amount of solute that can be dissolved in a given solvent at a given temperature, in order to form a saturated solution, is termed its solubility. In the majority of cases the solubility of a solute increases with increasing temperature, although there are instances where this is not the case, such as calcium hydroxide in water. No rigorous model exists to allow for an accurate prediction of solubility, although several ways of predicting solubility have been formed. Solubility curves are presented as exponential functions based on the relationship between temperature and concentration[7].

When excess solute is added to a solvent, the solute will dissolve until equilibrium is established within the system. This is subject to the temperature and pressure at which the solution is held and for a given temperature the composition achieved at this equilibrium point is termed the equilibrium solubility. The solubility of a substance is determined by both its physical and chemical properties and those of the solvent in which it is undergoing dissolution in[2].

For crystallisation to take place from a solution, the system must be subjected to a change that affects its solubility and enables solid particles to form.

A.3 Supersaturation

A solution can be classified in one of three ways with regards to how much solute it contains, either undersaturated, saturated or supersaturated. As discussed earlier, at a given temperature there is a maximum amount of solute that can dissolve in a solvent, creating an equilibrium which is equal to the solubility of the solute. At this point the solution is termed *saturated*, and thermodynamic equilibrium exists. If the solution contains less solute than the solubility at a given temperature, then the solution is termed *undersaturated*. However, it is possible for a solution to contain more solute than the solubility suggests and at this point the kinetics of the

system play a vital role in the crystallisation process as opposed to its thermodynamics. In this instance the solution is said to be *supersaturated*[2].

In order for crystallisation from solution to occur it is well known that three stages must take place:

1) The system must become supersaturated
2) Nucleation occurs
3) Growth occurs

Therefore, supersaturation is the driving force for crystallisation from solution. Due to the importance of supersaturation, it is imperative that the level of supersaturation in a system can be quantified. This is achieved through the knowledge of solution concentration, solution temperature and chemical potential.

In terms of concentration, the level of supersaturation can be determined from the absolute solute concentration (c) and the saturation concentration (c^*), which describe the amount of solute in the system and the equilibrium solubility concentration, respectively. Several definitions exist to describe the level of supersaturation in a solution, including the concentration driving force (Δc), the supersaturation ratio (S), and the relative supersaturation (σ). The respective expressions for these quantifying factors are given below:

$$\Delta c = c - c^* \qquad \text{A.8}$$

$$S = \frac{c}{c^*} \qquad \text{A.9}$$

$$\sigma = \frac{\Delta c}{c^*} = S - 1 \qquad \text{A.10}$$

In order to relate the solution temperature with supersaturation the undercooling (ΔT) must be defined:

$$\Delta T = T_e - T \qquad \text{A.11}$$

Where: T_e - equilibrium saturation temperature.

This leads to the relationship:

$$\Delta c = \left(\frac{dc^*}{dT}\right)\Delta T \qquad \text{A.12}$$

With respect to chemical potential (μ), supersaturation is given by:

$$\Delta\mu = \mu_{solution} - \mu_{solid} \quad \text{A.13}$$

This can be related to the activity of the solution by:

$$\mu = \mu^0 + RTln(a) \quad \text{A.14}$$

Therefore, a relationship can be established between the chemical potential and the supersaturation ratio:

$$\frac{\Delta\mu}{RT} = ln\left(\frac{a}{a_e}\right) = \ln(S) \quad \text{A.15}$$

Or,

$$S = e^{\frac{\Delta\mu}{RT}} \quad \text{A.16}$$

Where: a_e - activity of the solution at saturation equilibrium.

For the purpose of this study the supersaturation ratio, S, calculated using knowledge of the solution concentration will be used to describe the level of supersaturation in a solution.

A.3.1 Metastability

A solution can be deemed stable if it is undersaturated or saturated, that is, the solution will stay as it is unless it is acted upon by a mechanism that enables supersaturation to occur, resulting in crystallisation. In contrast, supersaturated solutions, having more solute than thermodynamically favourable, have the ability to crystallise. However, this will not occur as soon as supersaturation is reached, instead spontaneous crystallisation may not occur from a timeframe between infinitesimally small to a period of years. This behaviour is due to the metastability of the supersaturated solution.

In order to describe the conditions in which spontaneous crystallisation may occur the terms *labile* and *metastable* must first be established. As soon as a labile solution is formed crystallisation will occur spontaneously, however, in order to reach a labile state a solution must first pass through its metastable zone. This 'zone' lies between the solubility and supersolubility lines of a solute in a solvent. The solubility line is determined from the equilibrium solubility values at given temperatures, whereas the supersolubility line indicates where a solution passes from being metastable to labile, at a given temperature.

Therefore, regardless of the mechanism by which crystallisation takes place, a supersaturated solution will not become labile until a critical level of supersaturation is reached corresponding to the metastable zone width (MSZW). This quantity depends upon the nucleation and growth kinetics, giving an indication of the kinetic limit of metastability. Due to its dependence on nucleation and growth kinetics the size of the MSZW is related to the crystallisation environment, meaning factors such as cooling rate (q), agitation rate, presence of impurities, among others, have a large effect on the ability of a solution to crystallise. There has been a number of studies that show this parameter can be used in order to analyse nucleation kinetics[2,8–11].

A schematic representation of how a solution passes from undersaturated-to-supersaturated is termed a solubility-supersolubility diagram, which was first proposed by Miers & Isaac in 1906[12]. An example plot is shown in Figure A.2.

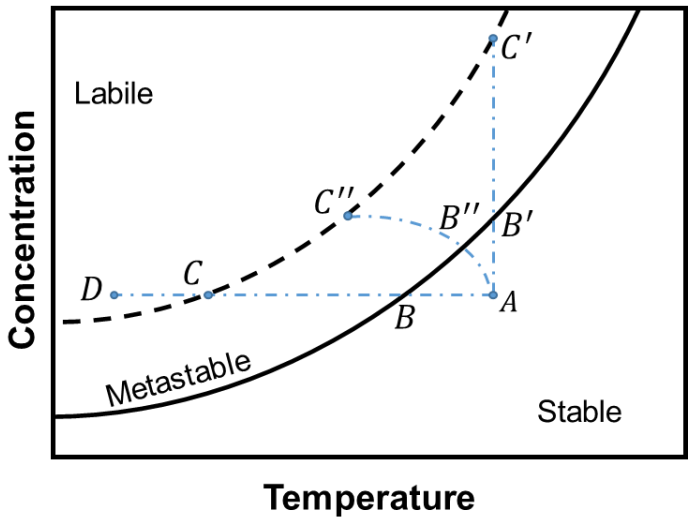


Figure A.2 - A representative solubility-supersolubility diagram. The solid curve separating the stable and metastable zones shows the solubility line, with the dashed curve separating the metastable and labile zones showing the supersolubility line. The line $A-C$ represents increasing supersaturation due to cooling crystallisation. The line $A-C'$ represents an increasing supersaturation due to the removal of solvent (evaporative crystallisation). The line $A-C''$ represents a combination of the two described crystallisation routes. Point D represents a solution that has crystallised.

A.3.2 Producing a Supersaturated Solution

In order to induce supersaturation in a solution, several methods can be used, including: chemical reaction, modifying the solubility of the solution and changing the concentration of solute in solution.

Supersaturation by chemical reaction is achieved if the result of a reaction yields a product that is in a concentration above its solubility. This method is not a commonly used route to crystallisation, much more common is the modification of solubility. This involves the addition of another species to the solution and/or a change in the solution temperature.

A number of research studies have been completed focussing on the introduction of a substrate to a solution[13–17], with a marked increase in supersaturation being attributed to the lowering of free energy by the heterosurface. However, the introduction of a second solvent, known as an antisolvent, is a more commonly used route for modifying the solubility. An antisolvent is a solvent in which the solute has a lower solubility than the solvent it is in solution with. When an antisolvent is added to a solution it lowers the solubility of that solution, inducing/increasing supersolubility. Both of these methods involve adding a new species to the crystallisation system, but it is possible to modify the solubility without any external introductions.

Most solutions have a solubility that is proportional to the temperature of the system, in that, as the temperature of a solution increases so too does the solubility. This means that if an undersaturated solution is created by increasing the solution temperature, when cooled, a supersaturated solution can be created. Cooling crystallisation can also provide very accurate control over the level of supersaturation achieved in a solution. This is by far the most common route taken to induce crystallisation and its process can be seen schematically in Figure A.2, following the line $A - C$.

Supersaturation may also be produced by increasing the concentration of solute in a solution. This can be achieved through evaporative crystallisation, where the solvent in an undersaturated solution evaporates, increasing the supersaturation until crystals form. This is represented in Figure A.2, following the line $A - C'$. Unlike anti-solvent crystallisation and cooling crystallisation, the level of supersaturation is difficult to control by this method.

A.4 Nucleation

Nucleation is the process in which the birth of an undetectably small body occurs from a supersaturated homogeneous phase. In solution crystallisation it signifies the time at which solute molecules cluster together to form nuclei that reach a certain size, allowing them to persist and grow from solution, forming a heterogeneous mixture[2]. Nucleation has an enormous effect on the overall outcome of crystallisation and is responsible for a number of crystal properties, such as particle size, polymorphism and number of crystals, among others. The

study of nucleation is extremely difficult, which means that although an innumerable number of research studies have been conducted on this subject for many decades, there is still no concrete understanding of its mechanism and as such no full description of the nucleation process. This is due to the stochastic nature of nucleation and the extremely small length scales associated with the process.

However, it is known that it takes place by either one of two mechanisms: mononuclear or polynuclear nucleation. Polynuclear nucleation occurs when the formation of many nuclei is favourable and can itself be expressed in two different ways, referred to as instantaneous nucleation (IN) and progressive nucleation (PN)[18]. IN is the process by which all crystal nuclei emerge simultaneously and subsequently grow to form crystals[18,19]. In contrast, in PN crystal nuclei continuously form from solution and subsequently grow in the presence of newly forming nuclei[8,18]. A schematic representation of the two processes is shown in Figure A.3.

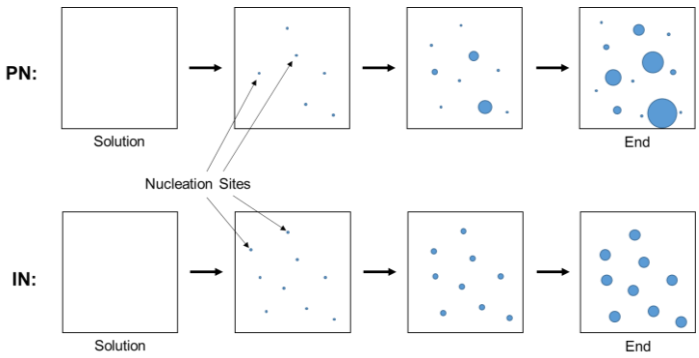


Figure A.3 - Schematic diagram showing the mechanisms of progressive and instantaneous nucleation.

Nucleation can be further characterised into two more categories, primary and secondary nucleation. Primary nucleation describes the process by which nucleation occurs in the absence of any crystalline matter in the solution, whereas secondary nucleation describes the process of nucleation when 'seed' crystals are present in the system. Primary nucleation can be further divided into two categories: heterogeneous and homogeneous nucleation. Heterogeneous nucleation (HEN) is caused when sites, usually suspended particles or impurities in the solution, provide a surface for nucleation to occur and is usually associated with both IN and PN, when it is favoured by relatively strong nucleation active sites and relatively weak nucleation active sites, respectively. Homogeneous nucleation describes spontaneous nucleation and is associated with PN[8,18,19]. A schematic diagram illustrating the classification of the various nucleation mechanisms is shown in Figure A.4.

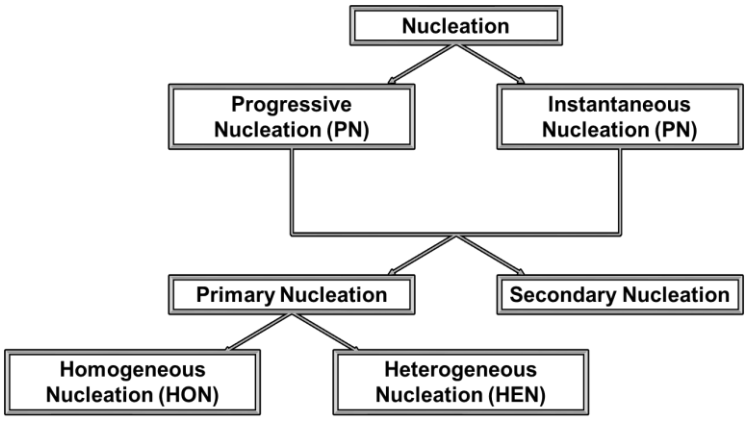


Figure A.4 - Nucleation mechanism classification.

Furthermore, although no accurate description of the nucleation process exists to date, a theory that has been commonly used for over half a century in the majority of nucleation studies is the classical nucleation theory (CNT). CNT is an approximate theory that gives reasonable estimations of nucleation parameters, in the majority of cases and it stems from the early work of Gibbs[20], Volmer and Weber[21], Becker and Döring[22], and Frenkel[23]. Originally, this theory was based on the condensation of vapour into a liquid, but it was subsequently extended to liquid-solid applications, such as solution and melt crystallisation.

Although CNT is based on numerous assumptions, primary-homogeneous nucleation can be described by it.

A.4.1 Homogeneous Nucleation

Homogeneous nucleation occurs, like all nucleation processes, due to the formation of clusters in solution that are made up of solute molecules. Unlike other nucleation processes, HON occurs when the cluster of the new phase is only in contact with the old phase and no other phase and/or molecular species[18]. This is depicted schematically in Figure A.5.[18] The formation of these clusters is caused by the random motion of particles within a solution causing collisions within the system. The way in which clusters form and the structure of the clusters is not understood, nevertheless it is known that if a cluster is formed it will not necessarily grow into a macroscopic crystal, but instead may re-dissolve back into solution. However, If a cluster is able to grow to a critical size, the critical radius (r^*), it forms a nucleus, which is the smallest solid structure that will not re-dissolve and will instead grow into a larger crystal[2].

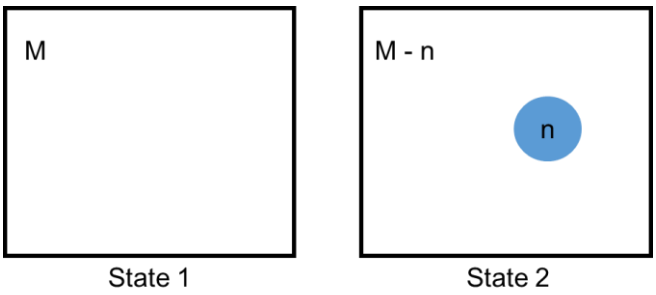


Figure A.5 - Schematic of cluster formation in HON. State 1 shows the old phase of M molecules before HON, whereas state 2 shows the formation of a cluster of n molecules within the old phase. Adapted from Kashchiev 2000.[18]

Furthermore, it is possible for a small crystal to be in an unstable equilibrium with a supersaturated solution. This process occurs due to a size difference of growing crystals, where a small particle may re-dissolve back into solution in the presence of a larger crystal, which continues to grow larger as the small particle disappears. This process is known as Ostwald ripening.

In order for a nucleus to grow to a critical size it must gain additional solute molecules. The number of molecules that form a stable nucleus varies from system to system and can be anywhere in the range from around ten to several thousand. However, the formation of a stable nucleus could not occur due to a single event of simultaneous collisions of the required number of molecules, as this event would be far too rare. Therefore, it is more easily envisaged that the addition process could occur through a series of bimolecular additions, according to the scheme:

$$A + A \leftrightarrow A_2$$
$$A_2 + A \leftrightarrow A_3$$
$$A_{n-1} + A \leftrightarrow A_n$$

Where: A_n - represents a critical cluster.

Further additions to A_n result in crystal growth. However, the structure of the critical nucleus is not known and due to the very small size of stable critical clusters it is not possible, with current technology, to observe them in order to determine the structure.

A.4.1.1 Classical Nucleation Theory of Homogeneous Nucleation

For homogeneous nucleation CNT describes the change in Gibbs free energy (ΔG) associated with the formation of a spherical crystalline nucleus of radius (r) from a supersaturated solution. The overall change in Gibbs free energy due to the formation of a new solid phase from an old

phase is a function of the change in surface free energy (ΔG_S) and volume free energy (ΔG_V), shown in Equations A.17 and A.18.

$$\Delta G = \Delta G_S + \Delta G_V \quad \text{A.17}$$

$$\Delta G = 4\pi r^2 \gamma + \frac{4}{3}\pi r^3 \Delta G_v \quad \text{A.18}$$

Where: γ - interfacial tension between the crystal and the surrounding supersaturated fluid and ΔG_v - free energy per unit volume associated with the phase change.

Equation 2.19 is derived from the assumption that the clusters that form from a supersaturated solution are spherical in shape. This lead to proportional relationships for the surface and volume contribution terms, where the ΔG_S and ΔG_V are proportional to r^2 and r^3, respectively. The surface term provides a positive free energy increase, whereas the volume term creates a decrease in free energy, meaning that the total free energy is associated with a competition between the two terms, as a function of radius, shown schematically in Figure A.6.

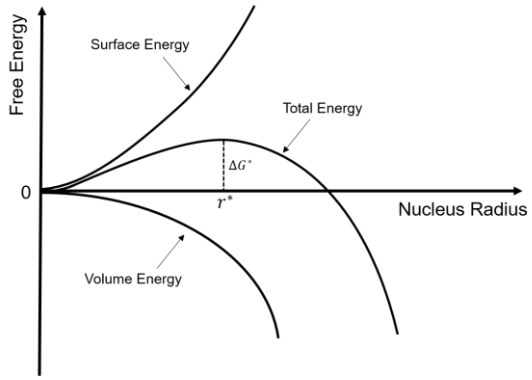


Figure A.6 - Free energy schematic for nucleation.

If a nucleus forms that is smaller the r^* it can reduce its free energy by reducing its size, meaning that it will dissolve back into the solution. However, if a nucleus grows to a size above r^*, a decrease in free energy is favoured by growth, therefore it will continue to grow into a macroscopic crystal. In order for this to occur, a free energy barrier must be overcome, known as the critical free energy (ΔG^*), shown in Figure A.6.

An expression for the critical radius and the critical free energy can be derived from Equation A.18, giving Equations A.19 and A.20, respectively.

$$r^* = \frac{-2}{\Delta G_v} \quad \text{A.19}$$

$$\Delta G^* = \frac{16\pi\gamma^3}{3(\Delta G_v)^2} = \frac{4\pi\gamma {r^*}^2}{3} \quad \text{A.20}$$

The critical free energy provides an indication of how much energy is required to form a stable nucleus. The amount of energy associated with ΔG^* is due to the fluctuations in energy in a fluid system at constant temperature and pressure. This means that there is a statistical distribution of energy in the molecules that constitute the solution, with temporary rises in energy levels in supersaturated regions favouring nucleation and critical cluster size formation.

It is possible to express ΔG^* in terms of supersaturation using the relationship between particle size and solubility with a basic Gibbs-Thompson relationship:

$$\ln S = \frac{2\gamma v_0}{kTr} \quad \text{A.21}$$

Where: v_0 - is the volume occupied by a solute molecule in a crystal and k - Boltzmann constant.

From equation A.21 ΔG_v can be expressed as:

$$-\Delta G_v = \frac{2\gamma}{r} = \frac{kTln\ S}{v_0} \quad \text{A.22}$$

Hence, from Equation A.20 it follows that ΔG^* may be expressed as:

$$\Delta G^* = \frac{16\pi\gamma^3 {v_0}^2}{3(kTln\ S)^2} \quad \text{A.23}$$

The rate at which nucleation occurs (J) can be expressed as an Arrhenius reaction rate equation:

$$J = A \exp\left(-\frac{\Delta G^*}{kT}\right) \quad \text{A.24}$$

Where: A - pre-exponential parameter, which is related to the Zeldovich factor (z), the frequency of monomer attachment to the nucleus (f^*) and the concentration of nucleation sites (c_o).

Therefore, from Equations A.23 and A.24 the rate of nucleation may be expressed as:

$$J = A \exp\left[-\frac{16\pi\gamma^3 {v_0}^2}{3k^3T^3(ln\ S)^2}\right] \quad \text{A.25}$$

Equation A.25 indicates that there are three main contributors to the rate of nucleation: temperature, degree of supersaturation and interfacial tension.

A.4.2 Heterogeneous Nucleation

Primary nucleation may take a different form than HON, where it can occur as a result of impurities or suspended particles within a system, and this process is known as heterogeneous nucleation (HEN)[2]. HEN occurs due to a substrate providing a surface for nucleation, which decreases the interfacial tension that must be overcome in order for nucleation to occur. A schematic of HEN is shown in Figure A.7.[18] The decrease in interfacial tension as a result of a nucleation surface increases the rate of nucleation, as can be seen by Equation A.25. The HON interfacial tension is related to the HEN effective interfacial tension (γ_{eff}), by the activity factor (φ), shown in Equation A.26.

$$\gamma_{eff} = \varphi\gamma \qquad \text{A.26}$$

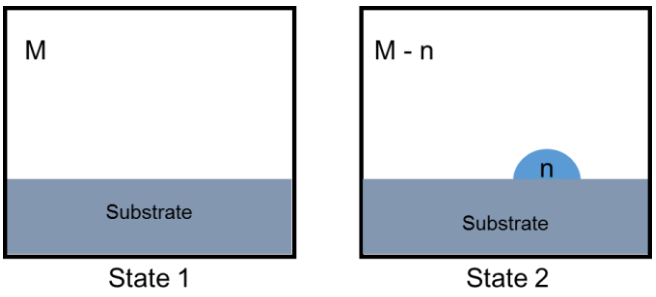


Figure A.7 - Schematic of cluster formation in HEN. State 1 shows the old phase of M molecules before HEN, whereas state 2 shows the formation of a cluster of n molecules within the old phase, on a surface of a substrate. Adapted from Kashchiev 2000.[18]

A.4.3 Limitations of CNT

CNT is an attractive theory to employ with regards to the complex process of nucleation due to its relative simplicity and ease of use, however, it is widely accepted that CNT cannot provide an accurate description of the process of nucleation[24–26].

This is somewhat due to a number of assumptions that CNT is based upon. For instance, the clusters are determined to be spherical in shape with a uniform density and a defined interface, which suggests that the arrangement of solute molecules in a cluster is identical to the macroscopic crystal structure. Also, the addition of monomers occurs one by one, without any collisions between a number of molecules and/or clusters, etc., which would make clusters

immobile and in contact with only the solution. Furthermore, there is no size dependence for surface tension as well as no temperature dependence towards surface energy. These assumptions, amongst others, as well as the described mechanism of nucleation under CNT could help explain the high deviations between predicted and measured nucleation rates in a number of studies.

Condensation reactions provide a good basis for the comparison of predicted and measured nucleation rates using CNT because the input parameters of CNT are known with high accuracy. Therefore, any significant deviation in predicted and measured values would indicate the applicability of CNT to certain applications. Research into the condensation of water vapour, using expansion cloud chamber experiments, showed CNT predicts nucleation rates that are 1-2 orders magnitude higher than experimental results[25,27]. Furthermore, studies have shown that temperature-dependent correction factors must be applied to CNT to make the predicted results agree with experiments, with over-predictions at high temperatures and under-predictions and low temperatures. In the case of experiments with heptane and nonane, correction factors of four orders of magnitude were required[28–32].

There are a number of studies that show the inconsistency of CNT with regards to experimentally obtained results, which has led to the growing opinion that a new theory underpinning the process of nucleation is required in order to better understand this high complexity process.

A.4.4 Two-Step Nucleation Theory

In recent decades, both experimental and modelling studies have suggested that nucleation of solid crystalline material from solution may not occur via the traditional route explained by CNT[25,27,33–36]. These studies have mainly focused on proteins and calcium carbonate ($CaCO_3$), the latter being extensively researched due to its importance in many biomineralisation processes[37]. The research findings have resulted in new theories of nucleation, termed non-classical nucleation theories, which include two-step nucleation that is used to describe a number of different mechanisms.

The general findings of two-step nucleation state that nucleation does not occur via a one-step process, where the clusters that form are spherical in shape and directly relate to the structure of the macroscopic crystalline form. Instead, it is proposed that there is an initial stage of prenucleation clustering, made up of either liquid, amorphous or even crystal-like configurations, followed by a re-ordering of the molecules within the dense clusters to form the

crystal structure. This transformation process lowers the energy barrier associated with nucleation as instead of one major step of solute molecules forming a cluster akin to the macroscopic crystal structure, two smaller energy barriers are present; the first being associated with a dense cluster that has a structure more similar to that of the bulk solution and a second smaller barrier associated with the transformation of the already formed cluster into a stable nucleus[25]. This is illustrated in Figure A.8.

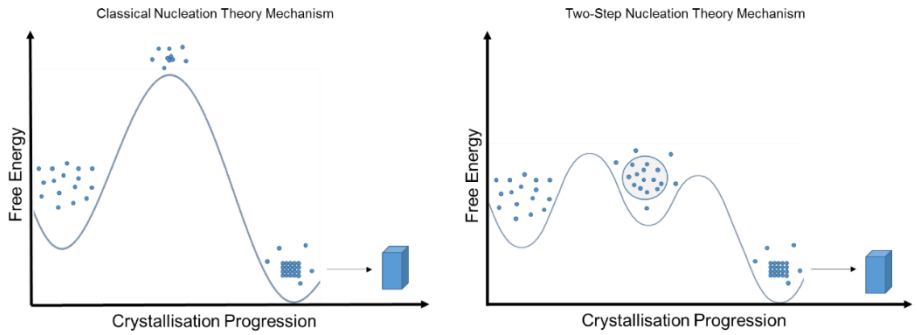


Figure A.8 - Free energy barriers to CNT and two-step nucleation.

There have been a number of studies that have focussed on and furthered the evidence for the existence of two-step nucleation. One of the first reports supporting the two-step mechanism was performed by computational simulations of homogeneous nucleation by ten Wolde and Frenkel[38]. Furthermore, a set of studies that has been important to the development of two-step nucleation were those completed by Vekilov and coworkers[39]. From the work, studying three haemoglobin variants and the proteins lumazine synthase and lysozyme, it was demonstrated that metastable dense liquid clusters facilitate nucleation. It was concluded that density fluctuations occurred within the solutions and those that reached an optimum size and density provided the best probability for nucleation to occur. Therefore, it was shown that only small density fluctuations and lifetimes are required for the nucleation process to take place.

Research undertaken by Myerson and coworkers[25,37,40] has also proved to be invaluable in the development of two-step nucleation theory. They have shown its existence through comparison of lysozyme induction times with CNT and more importantly through their use of nonphotochemical laser-induced nucleation (NPLIN) on small organic molecules, increasing the nucleation rate compared to a standard nucleation pathway. Their evidence stems from the electric-field alignment effect cause by NPLIN, which if aggregated clusters of solute molecules were in a structured form, as described by CNT, this would have no effect on the nucleation rate, and hence the observed change in rate was a result of the second stage of two-step nucleation. Furthermore, it was found that supersaturated solutions required aging being

NPLIN initiated nucleation, suggesting that a dense cluster required to be a certain size before nucleation could take place, further supporting two-step nucleation.

Although there are many experimental results that favour two-step nucleation theory, difficulty is faced in the ability to separate nucleation and growth processes during the experiments. Modelling these systems through computer simulations could provide the best possibility for studying these complex processes, as they can provide detail unfeasible in experimental studies. However, molecular simulations face two major obstacles, the longer time scales that molecular simulations cannot access and ensuring the models are accurate enough for such a complex process. Currently, several methods are being employed in order to try and overcome these obstacles, such as replica-exchange molecular dynamics[41] and metadynamics[42], but these are thwart with their own challenges, such as ensuring proposed parameters are correct, in the case of biased models, and limited complexity, in the case of unbiased models.

Due to the complexity of the nucleation process and the limited areas in which experimental and modelling studies have focussed, two-step nucleation is currently an emerging theory and not a fully adopted theory. As such, CNT still provides the best estimate of nucleation thermodynamics and kinetics for a large majority of applications.

A.5 Assessment of Nucleation Kinetics

A.5.1 Induction Time

When supersaturation is achieved in a solution, a certain period of time elapses before crystals begin to appear. This 'time lag' between the two described events is termed the induction time (or induction period), τ.

The existence of an induction time in a supersaturated solution is contradictory to the process described through CNT, which makes the assumption of ideal stead-state conditions as well as a prediction of immediate nucleation once supersaturation is achieved. Therefore, it is possible to state that the induction time is a function of more than one time period that is related to the nucleation process. Overall, the induction time can be affected by three time periods: the first being a relaxation time, which is related to the time it takes for the system to distribute the clusters present due to supersaturation, t_r, the second being the time it takes to form a stable nucleus, t_n, and finally, the time it takes for the nucleus to grow to a detectable size, t_g. Given these three periods, it is possible to write the induction time in the following form[2].

$$\tau = t_r + t_n + t_g \qquad \text{A.27}$$

Although it is theorised that these three time periods contribute to the induction time, it is nearly impossible to distinguish between and isolate them. Furthermore, each time period varies depending on the system studied and the way that crystallisation is induced.

The relaxation time is greatly dependent on the viscosity of the system and as such the diffusivity, D, with Nielsen[43] suggesting:

$$t_r = 10^{-17} D^{-1} \qquad \text{A.28}$$

The time required to form a stable nucleus is dependent upon the level of supersaturation achieved during the crystallisation process and estimations of its value are widely disregarded. The time required for a nucleus to grow to a detectable size varies extensively from system to system and is highly subjective upon the instrumentation used to detect crystals. This makes estimations of t_g difficult, with a measurable growth rate at a macroscopic level being very different to that of a nucleus[2].

Furthermore, due to the stochastic nature of nucleation, caused due to energy and molecular distributions within solutions, induction times can vary dramatically for the same system crystallised by the same method. This makes taking a representative value of an induction time for a crystallising system at a given level of supersaturation from measurements of induction times extremely challenging. A number of other factors can also affect induction times, such as, impurities within the solution, the level of agitation applied to the solution and the presence of seed crystals, etc. It is a quantity that is most often determined through the use of the isothermal method of crystallisation.

A.5.2 Isothermal Method

The isothermal method of crystallisation is performed under a generalised procedure that enables crystals to form from solution. Thermally, this consists of heating a saturated solution past its saturation temperature, holding at that temperature to ensure all solid undergoes dissolution, and then cooling rapidly to a temperature below the saturation temperature. This temperature is held until crystallisation takes place, and the time for that to happen is the previously described induction time. In general terms it is taken as the time elapsed between the moment supersaturation is created and the moment crystals are detected, meaning it can also be calculated through other crystallisation routes, such as antisolvent addition. Here, an

antisolvent is added to a solution to create a lower solubility of the solute, suddenly increasing the level of supersaturation in solution.

The isothermal method relates the induction time with supersaturation, in order to calculate nucleation kinetic parameters. This can initially be determined through the expression for supersaturation relating to the chemical potentials of solute molecules in the solution and in the crystal[18]:

$$\tau = k_{md}\left[exp\left(\frac{-\Delta\mu}{kT}\right)\right]\left[1 - exp\left(\frac{-\Delta\mu}{kT}\right)\right]^{\frac{-md}{(1+md)}}\left[exp\left(\frac{B}{(1+md)\Delta\mu^2}\right)\right] \qquad \text{A.29}$$

Where: m - crystallite growth exponent. d - related to the dimensionality of crystal growth.

From Equation A.29, k_{md}, B and $\Delta\mu$ are given by:

$$k_{md} = \left[\frac{(1+md)\alpha_{det}}{k_v z f_e^* c_s d_0^d f_{e,s}^{md}}\right]^{\frac{1}{(1+md)}} \qquad \text{A.30}$$

$$B = \frac{16\pi v_0^2 \gamma_{eff}^3}{3kT} \qquad \text{A.31}$$

$$\Delta\mu = kT ln\, S \qquad \text{A.32}$$

Where: α_{det} - fraction of detectable crystallised volume. k_v - crystallite growth shape factor. z - Zeldovich factor. f_e^* - frequency of monomer attachment to the nucleus at $\Delta\mu = 0$. c_s - solution concentration at crystal solution interface. d_0- molecular diameter $\approx \left(\frac{6v_o}{\pi}\right)^{1/3}$. $f_{e,s}$ - frequency of molecular attachment per growth site at $\Delta\mu = 0$.

Combining Equations A.29 and A.32 enables an expression relating τ and S to be determined:

$$ln\left\{\tau[S(S-1)^{md}]^{\frac{1}{1+md}}\right\} = \ln k_{md} + \frac{B}{[(1+md)(kT\ln S)^2]} \qquad \text{A.33}$$

From this expression, a plot of $ln\left\{\tau[S(S-1)^{md}]^{\frac{1}{1+md}}\right\}$ vs. $\frac{1}{T^3(\ln S)^2}$ gives a straight line with the slope equal to $\frac{16\pi v_0^2 \gamma_{eff}^3}{3(1+md)k^3}$, which enables the interfacial tension to be calculated.

It is also possible to calculate the critical nucleus radius, r^*, and the number of molecules within the critical nucleus, i^*, assuming that the nucleus is spherical in shape, through Equations A.34 and A.35, respectively.

$$r^* = \frac{2\gamma_{eff} v_0}{kT ln\, S} \quad \text{A.34}$$

$$i^* = \frac{4\pi r^{*3}}{3v_0} \quad \text{A.35}$$

A.5.3 Polythermal Method

Much like the isothermal method, the polythermal method of crystallisation is performed under a generalised procedure that enable crystals to form from solution. Again, like for the isothermal method, this consists of initially heating a saturated solution past its saturation temperature and holding at that temperature to ensure all solid undergoes dissolution. However, unlike for the previously described method, the solution is cooled at a constant rate and cooling continues to occur past the onset of crystallisation and is then subsequently heated at the same rate past the point dissolution occurs.

The polythermal method uses the concept of the MSZW and relates the critical undercooling, ΔT_c, to the cooling rate, q, in order to calculate nucleation kinetic parameters. The most commonly used approach to interpreting $\Delta T_c(q)$ data is by using Nyvlt expressions[44]. This method is based on a semi-empirical formula for the nucleation rate and predicts a linear relationship between ln ΔT_c and ln q, under the assumption that the decrease in supersaturation of a solution is solely based upon the solute molecules forming the nuclei. This assumption oversimplifies the crystallising system and takes no account of the effect on supersaturation of the growing crystallites, due to its modelling of the early stage of crystallisation. At this point, the limit of metastability corresponds to the point at which the first nuclei form and as such their surface areas are deemed to be negligible. Therefore, it is possible to express the rate of supersaturation change by cooling to the nucleation rate:

$$J = k_j(\Delta c_{max})^{m_0} = \frac{dc^*}{dT} q \quad \text{A.36}$$

Where: J - nucleation rate. k_j - empirical parameter. Δc_{max} - $\frac{dc^*}{dT}\Delta T_c$. m_0 - empirical order of nucleation. $\frac{dc^*}{dT} q$ - number of solute molecules precipitated per unit time and unit volume.

Although the Nyvlt approach has been used extensively, it is widely accepted that it cannot contribute towards a deeper understanding of both nucleation and growth mechanisms[8]. This is due to the two empirical parameters present in Equation A.36, which were noted to have no concrete physical meaning by Nyvlt himself[44]. Due to these inaccuracies, other methodologies have since been devised that try to avoid the limitations and approximations associated with the Nyvlt approach.

Kubota[45] proposed a new interpretation of $\Delta T_c(q)$ data, still using the semi-empirical equation used by Nyvlt, but utilised the concept that the method of detection affects the calculated value of the MSZW. Through this, Kubota arrived at the Nyvlt $\Delta T_c(q)$ expression, but with redefined semi-empirical parameters under the assumption that the value of the MSZW relates to the undercooling when the number density of nuclei reach a detectable fixed, but unknown, value. More recently, Sangwal[10] derived an expression from re-deriving Nyvlt's equation and ended up with the Nyvlt $\Delta T_c(q)$ expression, but with redefined parameters. Later, Sangwal[9,46] utilised CNT to derive a $\Delta T_c(q)$ expression, which provided an insight into parameters associated with it and unlike Nyvlt's expression, it predicted a linear relationship between $\ln \frac{1}{\Delta T_c{}^2}$ and $\ln q$.

Unfortunately, although these new interpretations advance Nyvlt's expression for interpreting $\Delta T_c(q)$ data, they disregard the growth of nuclei to sizes that correspond to the limit of detectability. Therefore, an expression that can resolve the $\Delta T_c(q)$ dependence is still required. One such expression is given by the Kashchiev-Borissova-Hammond-Roberts (KBHR) approach[8,19].

A.5.4 KBHR Approach

Unlike the previously described approaches, the KBHR approach does not interpret $\Delta T_c(q)$ data with a linear relationship, instead, the dependency of $\ln \Delta T_c$ and $\ln q$ is dependent upon the nucleation mechanism involved.

KBHR is based upon the assumption that the crystallites that form do not contact one another, and as such this approach relates to the early stages of crystallisation. It makes use of the classical theory for stationary three-dimensional HON and HEN nucleation. Due to the limitations of modern analytical techniques, the limit of metastability can only be registered when nuclei have grown to a detectable size, and as such a detectable number of molecules. Therefore KBHR relates the limit of metastability to the fraction (α_{det}) of crystallites in the volume of solution or the number (N_{det}) of nucleated crystallites at the detection point. At this point the nucleation and growth rates will both have an influence on the crystallites that have formed. It enables the calculation of key kinetic parameters and also allows for the mechanism of nucleation, either PN or IN, to be determined, under the 'rule of three'.

The KBHR approach is based upon the Kolmogorov-Johnson-Mehl-Avrami (KJMA) formula. This formula enables a description of phase transformation kinetics, with focus on the time dependency of the fraction (α) of crystallised volume, given by:

$$\alpha = \frac{V_c}{V} \qquad \text{A.37}$$

Where: V_c - total crystallised volume. V - solution volume.

It follows the assumption that nucleation occurs at a rate, $J(t)$, and grows irreversibly at a rate, $G(t)$, in the radial direction only. This enables a relatively easy expression for α, expressing it in terms of $J(t)$ and $G(t)$, with the resulting formula revealing basic kinetic parameters of nucleation and growth rates.

Using the KBHR approach, determination of the average values of dissolution temperature, T_{diss}, and crystallisation temperature, T_c, enable the calculation of the critical undercooling, ΔT_c, under the expression shown in Equation A.11. A dimensionless quantity associated with ΔT_c is the relative critical undercooling, u_c, and is calculated through the expression:

$$u_c = \frac{\Delta T_c}{T_e} \qquad \text{A.38}$$

With regards to the mechanism by which nucleation proceeds, it is necessary to distinguish between PN and IN when determining the critical undercooling. This was firstly recognised by Hulburt[47] and by Söhnel & Nyvlt[48], with the studies showing that for PN, ΔT_c is dependent on both the nucleation and grow rates, whilst for IN, ΔT_c is dependent on the growth rate alone. This result is applied to KBHR, with different derivations based upon the mechanism of nucleation.

A.5.4.1 Progressive Nucleation Case

For the case of PN, the KJMA formula in the limit of $\alpha < 0.1$ is given by:

$$\alpha(t) = k_v \int_0^t J(t') \left[\int_0^{t-t'} G(t'')dt'' \right]^d dt' \qquad \text{A.39}$$

Where: k_v - growth shape factor. t' and t'' are integration variables with the physical significance of time. G - radial crystallite growth rate

From the classical theory for stationary three-dimensional nucleation, the time-dependent rate of nucleation, $J(t)$, can be expressed as:

$$J(t) = k_J exp\left[\frac{-b}{(1-u_c){u_c}^2}\right] \quad \text{A.40}$$

Where: k_J - kinetic factor. b - dimensionless thermodynamic parameter, and is given by:

$$b = \frac{k_n v_0^2 \gamma_{eff}^3}{kT_e \lambda^2} \quad \text{A.41}$$

Where: k_n - nucleus numerical shape factor.

It also follows that the dependence of radial crystallite growth rate on time is given by:

$$G(t) = m\left(\frac{T_e}{q}\right)^{m-1} k_G^m \left[1 - exp\left(\frac{-au}{1-u}\right)\right]^{nm} u^{m-1} \quad \text{A.42}$$

Where: k_G - crystal growth rate constant. n and m - crystallite growth exponents (> 0). a - dimensionless molecular latent heat of crystallisation, given by:

$$a = \frac{\lambda}{kT_e} \quad \text{A.43}$$

From these equations it is possible to express α in terms of u, by inserting Equations A.40 and A.42 into equation A.39 and defining:

$$t' = \left(\frac{T_e}{q}\right)x \quad \text{A.44}$$

$$t'' = \left(\frac{T_e}{q}\right)z \quad \text{A.45}$$

This gives:

$$\alpha(u) = C_{m,d} \int_0^u exp\left[\frac{-b}{(1-x)x^2}\right]\left\{\int_0^{u-x} z^{m-1}\left[1 - exp\left(\frac{-az}{1-z}\right)\right]^{nm} dz\right\}^d dx \quad \text{A.46}$$

Where: the dimensionless parameter $C_{m,d}$ is given by:

$$C_{m,d} = k_v m^d k_J k_G^{md} \left(\frac{T_e}{q}\right)^{md+1} \quad \text{A.47}$$

As performing the integrals in Equation A.46 in closed form is generally impossible, an analytical solution can be determined, under the inequalities:

$$u < 0.1, au < 1 \quad \text{A.48}$$

Then,

$$1 - u \approx 1, 1 - exp\left[\left(\frac{-au}{1-u}\right)\right] \approx au \qquad \text{A.49}$$

Therefore, Equation A.46 can be simplified to:

$$\alpha(u) = C_{m,d} a^{nmd} \int_0^u exp\left(\frac{-b}{x^2}\right)\left[\int_0^{u-x} z^{(n+1)m-1} dz\right]^d dx \qquad \text{A.50}$$

After performing the inner integral in Equation A.50, this leads to:

$$\alpha(u) = C_{m,d}\left[\frac{a^{nm}}{(n+1)m}\right]^d \int_0^u (u-x)^{(n+1)md} exp\left(\frac{-b}{x^2}\right) dx \qquad \text{A.51}$$

It has been shown by Kashchiev and Firoozabadi[49] that the integration in Equation A.51 can be carried out analytically, when $(n+1)md = 0,1,2,3$ ... This enables $\alpha(u)$ to be expressed exactly by a special mathematical function, however it takes a much more simple form when the values of u are sufficiently small, fulfilling the condition:

$$u < \left(\frac{2b}{3}\right)^{\frac{1}{2}} \qquad \text{A.52}$$

From this, $\alpha(u)$ can be presented as:

$$\alpha(u) = k_{m,d}\left(\frac{u^3}{2b}\right)^{(n+1)md+1} exp\left(\frac{-b}{u^2}\right) \qquad \text{A.53}$$

This equation can be used as an approximation for $\alpha(u)$ dependence for non-integer values of $(n+1)md$. It was found that the accuracy of the $\alpha(u)$ dependence is higher when the exponential factor $exp\left(\frac{-b}{u^2}\right)$ is replaced with $exp\left(\frac{-b}{(1-u)u^2}\right)$. This yields the basic approximate $\alpha(u)$ expression of the KBHR theory:

$$\alpha(u) = k_{m,d}\left(\frac{u^3}{2b}\right)^{(n+1)md+1} exp\left(\frac{-b}{(1-u)u^2}\right) \qquad \text{A.54}$$

The dimensionless parameter $k_{m,d}$ is given by:

$$k_{m,d} = \frac{\Gamma[(n+1)md+1]}{(n+1)^d} k_v a^{nmd} k_J k_G^{md} \left(\frac{T_e}{q}\right)^{md+1} \qquad \text{A.55}$$

Where: Γ - complete gamma function.

The approximate $N(u)$ expression of the KBHR approach can be gained by replacing α with N and setting $d = 0$ in Equation A.54, yielding:

$$N(u) = k_N \left(\frac{u^3}{2b}\right) exp\left[\frac{-b}{(1-u)u^2}\right] \quad \text{A.56}$$

Where k_N is given by:

$$k_N = \frac{V k_J T_e}{q} \quad \text{A.57}$$

Expressing Equation A.56 in terms of u_c as opposed to u, taking logarithms of both sides and rearranging gives an expression relating u_c and q:

$$\ln q = \ln q_o + a_1 \ln u_c - \frac{a_2}{(1-u_c)u_c^2} \quad \text{A.58}$$

Where: q_0, a_1 and a_2 are given by:

$$q_0 = \frac{V k_J T_e}{N_{det} 2b} \quad \text{A.59}$$

$$a_1 = 3 \quad \text{A.60}$$

$$a_2 = b \quad \text{A.61}$$

When Equation A.58 is derived in terms of α_{det}, then q_0, a_1 and a_2 become:

$$q_0 = T_e \left\{\frac{\Gamma[(n+1)md+1] k_v a^{nmd} k_J k_G^{md}}{(n+1)^d (2b)^{(n+1)md+1} \alpha_{det}}\right\}^{\frac{1}{md+1}} \quad \text{A.62}$$

$$a_1 = 3 + \frac{3nmd}{md+1} \quad \text{A.63}$$

$$a_2 = \frac{b}{md+1} \quad \text{A.64}$$

The parameters, q_0, a_1 and a_2, have distinct physical meanings. q_0 is controlled by both the nucleation and growth processes, a_1 relates to the crystallite growth law, and a_2 is equal to, or a fraction of, the thermodynamic parameter b.

From these equations the critical radius us, r^*, and the number of molecules within the critical radius, i^*, can be determined by:

$$r^* = \frac{2\gamma_{eff} v_0}{\lambda u} \quad \text{A.65}$$

$$i^* = \frac{2bkT_e}{\lambda u^3} \quad \text{A.66}$$

A.5.4.2 Instantaneous Nucleation Case

For the case of IN, $\alpha(u)$ dependence is controlled solely by the growth rate, as such, it can take the form of:

$$\alpha(t) = k_v C_0 \left[\int_{t_0}^{t} G(t')dt'\right]^d \quad \text{A.67}$$

From Equations A.42 and A.44 α can be related to u by:

$$\alpha(u) = C_{m,d}\left\{\int_{u_0}^{u} x^{m-1}\left[1 - exp\left(\frac{-ax}{1-x}\right)\right]^{nm} dx\right\}^d \quad \text{A.68}$$

Where: the dimensionless parameter $C_{m,d}$ is given by:

$$C_{m,d} = k_v m^d C_0 \left(\frac{k_G T_e}{q}\right)^{md} \quad \text{A.69}$$

If the inequalities and approximations in Equations A.48 and A.49, respectively, are met then Equation A.68 can be simplified to:

$$\alpha(u) = k_{m,d}\left[u^{(n+1)m} - {u_0}^{(n+1)m}\right]^d \quad \text{A.70}$$

Given the nature of IN, all crystal nuclei form simultaneously with a concentration, c_0, at one instance in time, t_0, corresponding to u_0. Where, u_0 is the relative critical undercooling at time t_0, expressed as:

$$u_0 = \frac{\Delta T_0}{T_e} \quad \text{A.71}$$

Where: ΔT_0 is given by:

$$\Delta T_0 = T_e - T_0 \quad \text{A.72}$$

Where: T_0 - solution temperature at time t_0

The dimensionless parameter, $k_{m,d}$, in Equation A.70 is given by:

$$k_{m,d} = \frac{k_v C_0 \left(\frac{a^n k_G T_e}{q}\right)^{md}}{(n+1)^d} \quad \text{A.73}$$

Expressing Equation A.70 in terms of u_c as opposed to u, taking logarithms of both sides and rearranging gives an expression relating u_c and q:

$$\ln q = \ln q_0 + \left(\frac{1}{m}\right)\ln\left[u_c^{(n+1)m} - u_0^{(n+1)m}\right] \quad \text{A.74}$$

Here, $u_0 \geq 0$, $u_c > u_0$, and q_0 is given by:

$$q_0 = \left[\frac{k_v C_0}{(n+1)^d \alpha_{det}}\right]^{\frac{1}{md}} a^n k_G T_e \quad \text{A.75}$$

Also, meeting the inequality:

$$u_0^{(n+1)m} \ll u_c^{(n+1)m} \quad \text{A.76}$$

Equation A.74 takes a simple Nyvlt-like form:

$$\ln q = \ln q_0 + (n+1) \ln u_c \quad \text{A.77}$$

Additionally, for a small range of q values, Equation A.58, can also be expressed in a Nyvlt-like form:

$$\ln q = \ln Q + \left(3 + \frac{3nmd}{md+1} + \omega a_2\right) \ln u_c \quad \text{A.78}$$

Where: Q - parameter related to q_0. ω - a positive number.

In Equation A.77 the term $(n+1)$ is always usually ≤ 3, as typically $n \leq 2$, whereas in Equation A.78 the term behind $\ln u_c$ is always > 3. This 'rule of three' provides a way in which the mechanism of nucleation can be determined from a plot of $\ln q$ vs. $\ln u_c$ and fitting a linear regression through the data. This gives a slope that indicates whether PN or IN has taken place, if the gradient of the slope is > 3 or < 3, respectively.

The KBHR approach provides substantial benefits in its use, providing a theoretical interpretation of $\Delta T_c(q)$ data, as well as providing parameters with a distinct physical meaning and enables the mechanism by which nucleation takes place to be determined. However, although it has been used successfully on a number of occasions[11,50,51] the inequalities that the derivation is subject to makes it unusable in a number of cases, such as at very high undercoolings. Therefore, in order to be universally applicable, a numerical solution must be found that does not limit the theory certain situations.

A flow chart showing the procedure undertaken when using the KBHR approach is shown in Figure A.9.[11]

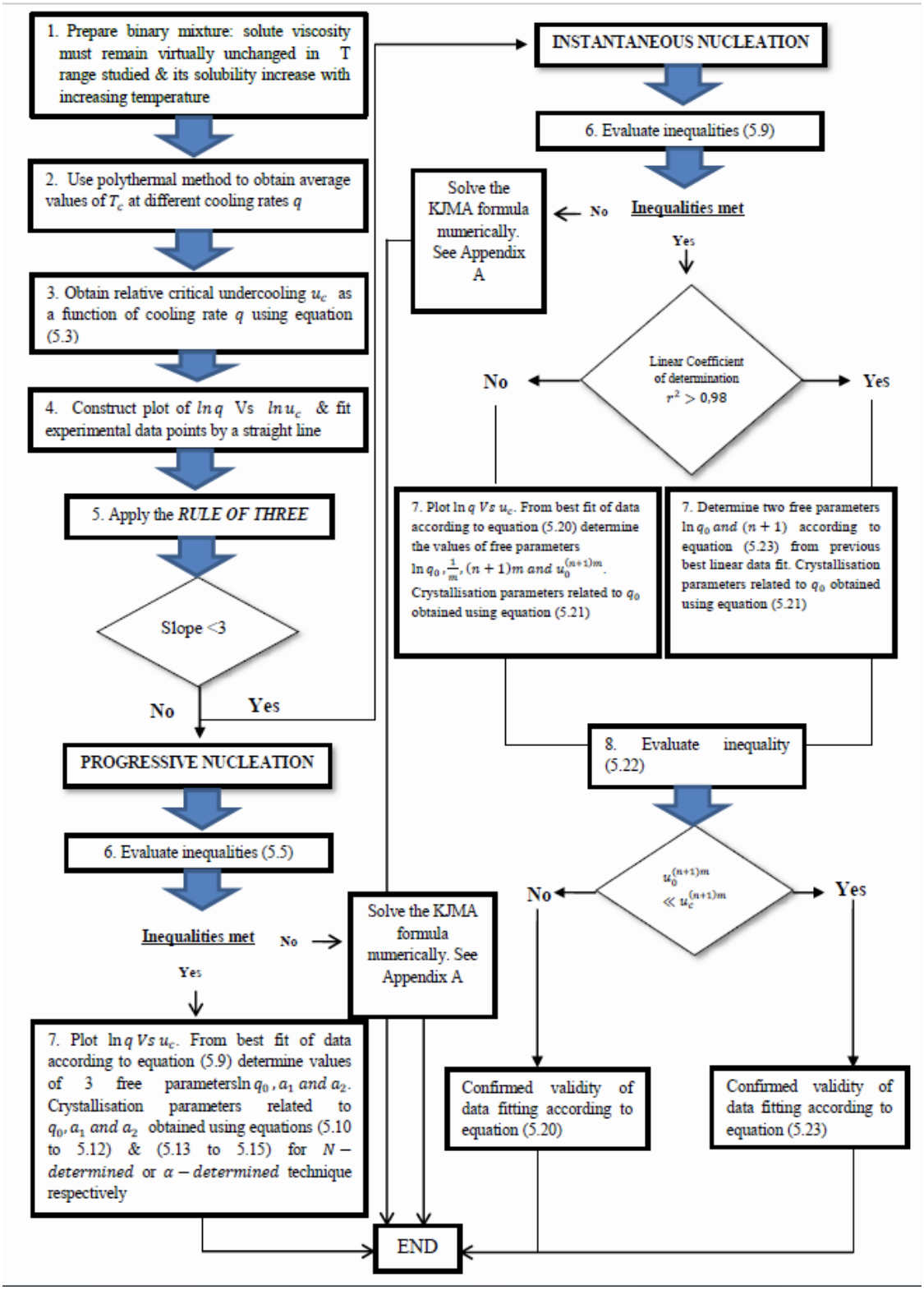


Figure A.9 – Flowchart summarising the procedure undertaken to apply KBHR theory from results obtained using the polythermal method of crystallisation[11].

A.6 Growth

A.6.1 Crystal Surfaces

On a macroscopic scale, crystals grown from solution generally appear to have regular and smooth facets, however, on a molecular level this may not be the case. The surface topography of a growing crystal exhibits a number of possible growth sites that are closely related to the growth mechanism. These sites include steps, terraces and kinks, according to the Kossel model[2]. Representing molecules as cubes generates a simple way to demonstrate these sites, as shown in Figure A.10. Through this model, the likelihood of molecular attachment to a growing crystal face can be determined, with a single bond formed when a molecule attaches to a terrace, two bonds formed with attachment to a step and three bond formed when a molecule attaches at a kink site.

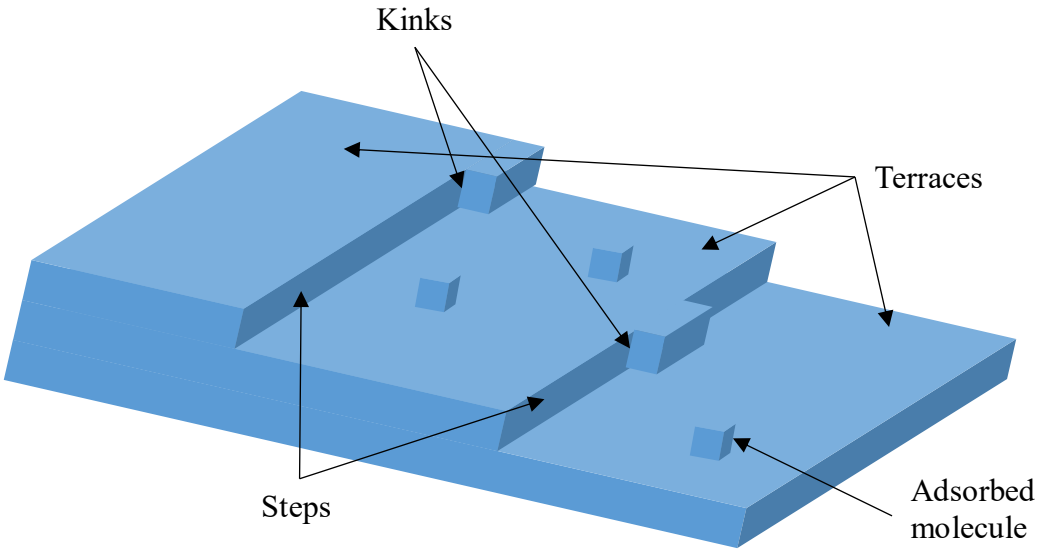


Figure A.10 – Kossel model of a crystal surface, showing terraces, step and kink sites as well as adsorbed molecules.

A.6.2 Crystal Habit

The external shape of a crystal, relating to the relative size of its faces, is known as the modification of habit, or the crystal habit. Certain faces may grow more rapidly or be stunted, giving rise to different crystal shapes. The speed at which a crystal face grows is subject to the functional groups on its surface, leading to different attachment energies, which is related to anisotropic intermolecular interaction strengths[52–54]. The slowest growing faces determine the

crystal habit as they dominate the observed shape[2]. For example, needle-like crystals have rapid growth along one crystallographic axes and slow growth in the remaining axes, resulting in a long and thin morphology that looks like a needle, hence the name. This has a large effect on surface chemistry because different faces contain different functional groups, due to the arrangement of molecules within a crystal.

One of the most common ways to alter crystal habit is the incorporation of impurities into a system, which can interact with the functional groups on the growing faces and alter the growth rate, and as such the overall morphology. The growth rates are also affected by the level of supersaturation and the solvent type[55].

A.6.3 Crystal Growth Models

Crystal growth from solution encompasses two processes pertaining to the transport of growth units from the bulk solution to the crystal-solution interface and incorporation of growth units onto a crystal face, termed volume and surface diffusion, respectively. The growth rate is determined by the slowest (rate-limiting) process. Crystal growth can be described by three mechanisms: Burton-Cabrera-Frank (BCF), birth and spread (B&S) and rough interface growth (RIG), which are dependent upon the crystallising system and the level of supersaturation within solution.

A.6.3.1 Spiral Growth Mechanism

The BCF model[56] of crystal growth occurs when screw dislocations are formed through a crystal, which form spiral steps upon a crystal face. Adsorbed growth units can migrate to these steps and growth occurs in a spiral rotating around the dislocation emergence point, essentially generating a 'spiral staircase'. This mechanism can be described through the BCF model given in Equation A.79:

$$R = k_G \sigma_S^2 \tanh(\frac{A_1}{\sigma_S}) \qquad \text{A.79}$$

Where R is the growth rate, k_G is the growth rate constant and A_1 is a temperature-dependent constant.

A.6.3.2 2D Nucleation Growth Mechanism

Crystal growth upon 'smooth' faces takes place via 2D nucleation as described through the B&S model, whereby, much like in 3D nucleation, a critical nucleus size must be reached in

order to form a stable nucleus and enable growth units to incorporate and growth to occur. Through this mechanism the 2D nucleus spreads across the crystal face and results in monolayer formation, upon which further 2D nucleation events can occur. B&S can progress via a mononuclear or polynuclear mechanism, whereby the former describes a single nuclei spreading across a crystal face and the latter describes a number of nuclei spreading across a single crystal face at one instance until they encounter each other or the face edges. The B&S model can be described through Equation A.80:

$$R = k_G \sigma_S^{\frac{5}{6}} \exp\left(\frac{A_2}{\sigma_S}\right) \quad \text{A.80}$$

Where A_2 is a system related constant.

$$A_2 = -\frac{\pi \gamma_{2D}^2}{3(kT)^2 \sigma_S} \quad \text{A.81}$$

Where γ_{2D}^2 is the interfacial tension of the 2D nucleus.

A.6.3.3 Rough Surface Growth Mechanism

When a crystal face is molecular rough, a large number of kink sites exist on the surface and growth units can readily be incorporated into the sites, generating high growth rates. Here the growth is continuous and is described through the RIG model by Equation A.82.

$$R = k_G \sigma_S \quad \text{A.82}$$

The type of crystal growth mechanism that occurs within solution is dependent upon the surface structure of the growing crystal and the level of supersaturation. The mechanism can be estimated through a quantity known as the alpha factor (α_f), which is given by:

$$\alpha_f = \frac{\xi \Delta H}{kT} \quad \text{A.83}$$

Where ξ is an anisotropy factor related to the crystal surface layer bonding energy.

Values of α provide an indication as to the growth mechanism, such that $\alpha_f < 2$ is indicative of RIG, $2 < \alpha_f < 5$ demonstrates B&S and $\alpha_f > 5$ indicates a BCF mechanism.

A.7 Conclusions

This chapter has provided a comprehensive overview of the scientific principles of crystallography, solution crystallisation and nucleation, beginning with an introduction to crystal structure and characteristics, through to describing crystallisation behaviour and ways in which it can be assessed.

Initially, the basic concepts of crystallography were presented, starting with a description of basic building blocks, unit cells, and the seven possible crystal systems. Crystal chemistry, which is responsible for the properties of a crystal was discussed. This section ended with discussions of both polymorphism.

The next section discussed the concepts that are present in solution crystallisation, beginning with a description of a solution and how one is formed. The concept of solubility was introduced, giving an idea of how each solution varies with respect to equilibrium conditions. Ideality and activity were then discussed, with the derivation of the van't Hoff equation displayed.

Following this, supersaturation and metastability were discussed, with an idea of how a solution crystallises and how it can maintain in a metastable state due to the kinetics of the system. Ways in which supersaturation can be achieved were highlighted.

The next section focussed on the nucleation step of crystallisation. Initial discussion focussed on possible nucleation routes and provided explanations of how each one proceeds. Homogeneous nucleation and classical nucleation theory were discussed, with the basic concepts and overarching equations presented. Heterogeneous nucleation was introduced, followed by a description of how CNT is limited in its applicability and the assumptions it makes. The concept of two-step nucleation theory was presented, with a discussion of how it was developed and current advances in its study.

Furthermore, a section focussing on the assessment of nucleation kinetics was presented. Induction time was discussed along with the contributing factors associated with this phenomenon and the isothermal method of crystallisation, with equations based upon this method presented. Next, the polythermal method of crystallisation was described, giving an overview of the basic ideas that brought about this crystallisation process, as well as the ways in which results obtained via this route can be analysed. An in-depth discussion of one of these concepts, the KBHR approach, was presented. The derived equations associated with both progressive nucleation and instantaneous nucleation were displayed and explained. A description of the benefits of the KBHR approach and the current limitations with it were outlined, with a route map showing how analysis by this approach is performed.

Finally, basic concepts of crystal growth were introduced, focussing upon the structure of crystal surfaces and the crystal habit. Three crystal growth mechanisms were introduced,

described through Burton-Cabrera-Frank, birth and spread and rough interface growth mechanisms. The alpha factor, which provides an indication as to the growth mechanism occurring for a given crystallising system, was discussed.

A.8 References

1. Davey, R. & Garside, J. *From Molecules to Crystallizers. An Introduction to Crystallization*. (Oxford University Press, 2000).
2. Mullin, J. W. *Crystallization*. (Butterworth-Heinemann, 2001).
3. Bernstein, J. *Polymorphism in Molecular Crystals*. (Oxford University Press, 2002).
4. Bauer, J. *et al*. Ritonavir: An Extraordinary Case of Conformational Polymorphism. *Pharm. Res.* **18**, 859–866 (2001).
5. Elwell, D. & J, S. H. *Crystal Growth from High-Temperature Solutions*. (Academic Press Inc, 1975).
6. Dickerson, R. E. *Molecular Thermodynamics*. (W.A.Benjamin, 1969).
7. Broul, M., Nývlt, J. & Söhnel, O. *Solubility in Inorganic Two-component Systems*. (Elsevier Scientific Pub. Co., 1981).
8. Kashchiev, D., Borissova, A., Hammond, R. B. & Roberts, K. J. Effect of cooling rate on the critical undercooling for crystallization. *J. Cryst. Growth* **312**, 698–704 (2010).
9. Sangwal, K. Novel Approach to Analyze Metastable Zone Width Determined by the Polythermal Method : Physical Interpretation of Various Parameters. *Cryst. Growth Des.* **9**, 942–950 (2009).
10. Sangwal, K. A novel self-consistent Nývlt-like equation for metastable zone width determined by the polythermal method. *Cryst. Res. Technol.* **44**, 231–247 (2009).
11. Camacho Corzo, D. M. *et al.* Nucleation mechanism and kinetics from the analysis of polythermal crystallisation data: methyl stearate from kerosene solutions. *CrystEngComm* **16**, 974–991 (2014).
12. Miers, H. & Isaac, F. XLVII.-The refractive indices of crystallising solutions, with especial reference to the passage from the metastable to the labile condition. *J. Chem. Soc. Trans.* **89**, 413–454 (1906).
13. Lopez-Mejías, V., Knight, J. L., Brooks, C. L. & Matzger, A. J. On the mechanism of crystalline polymorph selection by polymer heteronuclei. *Langmuir* **27**, 7575–7579 (2011).
14. Sharma, M. & Trout, B. L. Effect of Pore Size and Interactions on Paracetamol Aggregation in Porous Polyethylene Glycol Diacrylate Polymers. *J. Phys. Chem. B* **119**, 8135–8145 (2015).
15. Yazdanpanah, N. *et al.* Continuous Heterogeneous Crystallization on Excipient

Surfaces. *Cryst. Growth Des.* **17**, 3321–3330 (2017).

16. Chunsrivirot, S., Diao, Y. & Trout, B. L. Binding affinity of a small molecule to an amorphous polymer in a solvent. Part 1: Free energy of binding to a binding site. *Langmuir* **27**, 12381–12395 (2011).
17. Chadwick, K., Chen, J., Myerson, A. S. & Trout, B. L. Toward the rational design of crystalline surfaces for heteroepitaxy: Role of molecular functionality. *Cryst. Growth Des.* **12**, 1159–1166 (2012).
18. Kashchiev, D. *Nucleation*. (Butterworth-Heinemann, 2000).
19. Kashchiev, D., Borissova, A., Hammond, R. B. & Roberts, K. J. Dependence of the critical undercooling for crystallization on the cooling rate. *J. Phys. Chem. B* **114**, 5441–5446 (2010).
20. Gibbs, W. J. On the Equilibrium of Heterogeneous Substances. *Trans. Conneticut Acad.* **3**, 108–248 (1876).
21. Volmer, M. & Weber, A. Keimbildung in übersättigten Gebilden. *Zeitschrift für Phys. Chemie* **119**, 277–301 (1926).
22. Becker, R. & Döring, W. Kinetische Behandlung der Keimbildung in übersättigten Dämpfen. *Ann. Phys.* **416**, 719–752 (1935).
23. Frenkel, J. A General Theory of Heterophase Fluctuations and Pretransition Phenomena. *J. Chem. Phys.* **7**, 538–547 (1939).
24. Merikanto, J., Zapadinsky, E., Lauri, A. & Vehkam??ki, H. Origin of the failure of classical nucleation theory: Incorrect description of the smallest clusters. *Phys. Rev. Lett.* **98**, 1–4 (2007).
25. Erdemir, D., Lee, A. Y. & Myerson, A. S. Nucleation of Crystals from Solution : Classical and Two-Step Models. *Acc. Chem. Res.* **42**, (2009).
26. Karthika, S., Radhakrishnan, T. K. & Kalaichelvi, P. A Review of Classical and Nonclassical Nucleation Theories. *Cryst. Growth Des.* **16**, 6663–6681 (2016).
27. Sharaf, M. A. & Dobbins, R. A. A comparison of measured nucleation rates with the predictions of several theories of homogeneous nucleation. *J. Chem. Phys.* **77**, 1517–1526 (1982).
28. Strey, R., Viisanen, Y. & Wagner, P. E. Measurement of the molecular content of binary nuclei. III. Use of the nucleation rate surfaces for the water-n-alcohol series. *J. Chem. Phys.* **103**, 4333–4345 (1995).
29. Hruby, J., Viisanen, Y. & Strey, R. Homogeneous nucleation rates for n -pentanol in argon : Determination of the critical cluster size. *J. Chem. Phys.* **104**, 5181–5187 (1996).
30. Rudek, M. M., Katz, J. L., Vidensky, I. V., Ždímal, V. & Smolík, J. Homogeneous nucleation rates of *n* -pentanol measured in an upward thermal diffusion cloud chamber. *J. Chem. Phys.* **111**, 3623–3629 (1999).

31. Iland, K., Wedekind, J., Wölk, J., Wagner, P. E. & Strey, R. Homogeneous nucleation rates of 1-pentanol. *J. Chem. Phys.* **121**, 12259–12264 (2004).
32. Gharibeh, M. *et al.* Homogeneous nucleation of n-propanol, n-butanol, and n-pentanol in a supersonic nozzle. *J. Chem. Phys.* **122**, (2005).
33. Vekilov, P. G. Nucleation. *Cryst. Growth Des.* **10**, 5007–5019 (2010).
34. Vekilov, P. G. The two-step mechanism of nucleation of crystals in solution. (2010). doi:10.1039/c0nr00628a
35. Gebauer, D., Kellermeier, M., Gale, J. D. & Bergstro, L. Pre-nucleation clusters as solute precursors in crystallisation. *Chem. Soc. Rev.* **43**, 2348–2371 (2014).
36. Zahn, D. Thermodynamics and Kinetics of Prenucleation Clusters, Classical and Non-Classical Nucleation. *ChemPhysChem* **16**, 2069–2075 (2015).
37. Myerson, A. S. & Trout, B. L. Nucleation from Solution. *Science (80-.).* **341**, 855–856 (2013).
38. ten Wolde, P. R. & Frenkel, D. Enhancement of protein crystal nucleation by critical density fluctuations. *Science (80-.).* **277**, 1975–1978 (1997).
39. Vekilov, P. G. Dense liquid precursor for the nucleation of ordered solid phases from solution. *Cryst. Growth Des.* **4**, 671–685 (2004).
40. Zaccaro, J., Matic, J., Myerson, A. S. & Garetz, B. A. Nonphotochemical, laser-induced nucleation of supersaturated aqueous glycine produces unexpected γ-polymorph. *Cryst. Growth Des.* **1**, 5–8 (2001).
41. Wallace, A. F. *et al.* Microscopic Evidence for Liquid-Liquid Separation in Supersaturated CaCO3 Solutions. *Science (80-.).* **341**, 885–889 (2013).
42. Giberti, F., Tribello, G. A. & Parrinello, M. Transient polymorphism in NaCl. *J. Chem. Theory Comput.* **9**, 2526–2530 (2013).
43. Nielsen, A. E. *Kinetics of Precipitation*. (Pergamon Press, 1964).
44. Nyvlt, J. Kinetics of Nucleation in Solutions. *J. Cryst. Growth* **3/4**, 377–383 (1968).
45. Kubota, N. A new interpretation of metastable zone widths measured for unseeded solutions. *J. Cryst. Growth* **310**, 629–634 (2008).
46. Sangwal, K. Effect of impurities on the metastable zone width of solute – solvent systems. *J. Cryst. Growth* **311**, 4050–4061 (2009).
47. Hulburt, H. M. Die Induktionsperiode bei der Chargenkristallisation und beim Ausfällen. *Chemie Ing. Tech.* **47**, 373–375 (1975).
48. Söhnel, O. & Nyvlt, J. Induction time in batch crystallisation. *Krist. und Tech.* **11**, 239–244 (1976).
49. Kashchiev, D. & Firoozabadi, A. Kinetics of the initial stage of isothermal gas phase formation Kinetics of the initial stage of isothermal gas phase formation. *J. Chem. Phys.* **98**, 4690–4699 (1993).

50. Tang, X. Crystal Structure, Phase Behaviour and Kinetics Associated with the Crystallisation of Octadecane, Hexadecane, and Mixtures Thereof. (2017).
51. Turner, T. D. Molecular Self-Assembly, Nucleation Kinetics and Cluster Formation Associated with Solution Crystallisation. (University of Leeds, 2015).
52. Hartman, P. & Perdok, W. G. On the relations between structure and morphology of crystals. I. *Acta Crystallogr.* **8**, 49–52 (1955).
53. Hartman, P. & Perdok, W. G. On the relations between structure and morphology of crystals. II. *Acta Crystallogr.* **8**, 521–524 (1955).
54. Hartman, P. & G, P. W. On the relations between structure and morphology of crystals. III. *Acta Crystallogr.* **8**, 525–529 (1955).
55. Sangwal, Mk. *Additives and Crystallization Processes: From Fundamentals to Applications*. (John Wiley & Sons Ltd., 2007).
56. Burton, W. K., Cabrera, N., Frank, F. C. & Jun, N. The Growth of Crystals and the Equilibrium Structure of their Surfaces Philosophical Transactions of the Royal Society of London . Series A , Mathematical and Physical The Growth of Crystals and the Equilibrium Structure of their Surfaces. **243**, 299–358 (1951).

Appendix B Nucleation Studies

B.1 Accelerated Nucleation

The terminology used in this section 'accelerated nucleation' is proposed in such a way as to encompass a wide variety of research studies that have focussed/inadvertently found ways in which the supersaturation of a system can be increased when compared to a standard crystallisation study. From an increased supersaturation the rate of nucleation has been found to increase (been accelerated) and crystals have been detected at shorter induction times than under 'normal' conditions. There are many ways in which to achieve this and the most prominent of them are reviewed in section.

B.1.1 Antisolvent Crystallisation

Antisolvent crystallisation is widely used in industrial applications in order to generate a number of different materials[1]. In antisolvent crystallisation a solution is made with a solute and fixed solvent, with a solvent that the solute is less soluble in is added to the solution, with the difference in solubility increasing the solution supersaturation and as such driving the crystallisation process[2].

Antisolvent crystallisation has been studied extensively with different research focus on the effect antisolvents have upon certain crystallisation systems. This has taken the form of studies of different flow rates[1], solvent composition[3], polymorphism[2], crystal size distribution (CSD)[4], antisolvent control[5], combined antisolvent and cooling[6], antisolvent in continuous crystallisers[7], and much more.

Kim & Kim[8] studied nucleation and supersaturation of antisolvent crystallisation in a T-mixer. A solution of sodium chloride (NaCl) in water was mixed with methanol (the antisolvent) at a junction in the reactor, inducing high micromixing, whilst varying the feed rates and ratio of solution to antisolvent. Using the unconventional crystalliser reactor geometry supersaturations as high as 50 were achievable and an increase in supersaturation was created by an increase in the amount of antisolvent used, leading to the observation that antisolvent fraction and not concentration of solute, had a key effect on the supersaturation. An unexpected finding of the study was that a change in nucleation mechanism from heterogeneous and homogeneous nucleation was found at a relatively low supersaturation ($S = 1.7$). This is in contrast to a reaction crystallisation, where this result is observed for supersaturation ratios in the region of $S = 20 - 50$[8]. Another finding was that the mean crystal size was dependent upon the supersaturation, with higher supersaturations leading to higher nucleation rates and smaller

crystals. This was the result of increased methanol feed rates and not the ratio of solution to antisolvent or the solute concentration.

Zhu et al.[9] studied solubility and MSZWs of 1,3-dihydroxyacetone (DHA) in water and ethanol (antisolvent) mixtures. The very high solubility of DHA in water meant that an antisolvent system could be beneficial to controlling viscosity of a DHA solution and for crystallisation design, due to the very high metastable zone widths associated with DHA crystallisation from aqueous solution. However, regardless of the amount of ethanol antisolvent used, the solubility and the MSZW remained very large. This result shows that choice of solvent is imperative when completing antisolvent studies.

As well as introducing an antisolvent to a binary solution, like those previously described, antisolvent crystallisation studies have also been completed on ternary solutions, with antisolvent being introduced to a solution containing two solutes and a solvent. Pina et al.[10] studied M_2SO_4-$LiSO_4$ (M = Na, Rb) in water solutions, with methanol being added as an antisolvent. In the study equations were derived for evaluating supersaturation, S, and supersaturation rate, R_S. The nucleation behaviour of the systems was evaluated through measurement of induction times and the volume of methanol added to the system. From this data, plots of $\ln R_S \ vs. \ln S$ were created and the parameters were found to have a generally linear relationship, which suggests that metastability can be described through these parameters. The metastability was also found to be controlled through the dehydration energies calculated, which were associated with the ionic pairs formed from the sulphate aqueous solutions.

Although conventional antisolvent routes were taken in the described studies, it is also possible to perform reverse-antisolvent crystallisation and to couple antisolvent addition with other crystallisation routes, such as cooling.

Chang et al.[11] studied the agglomeration of *L*-ornithine aspartate (LOA) in water solution with a methanol antisolvent, using reverse-antisolvent crystallisation. This was performed by holding methanol in an agitated reactor and adding in a solution of LOA and water into the reactor. The rate of agitation, feed rate, feed concentration and ratio of antisolvent to feed solution, were all varied in this study to evaluate the effects they have upon crystal agglomeration. Mean particle size was found to increase with a higher feed concentration, a longer feeding time and a higher ratio of methanol to the feed solution, but was reduced as agitation rate was increased, due to mechanical breakage of agglomerates. Supersaturation was

also studied and it was found that a higher ratio of antisolvent to feed solution, as well as a higher feed concentration increased the level of supersaturation. This increased the rate of nucleation, creating more nuclei formation events and increased the mean particle size. A similar study, using conventional antisolvent crystallisation, by Plasari et al.[12] also found that the rate of agitation, agitator type, solvent to antisolvent ratio and solute concentration were all factors that affected the overall particle shape and size, with solute concentration having the largest effect on CSD.

The combination of antisolvent addition and cooling brings a polythermal methodology to the crystallisation process, unlike the isothermal crystallisations described previously. This introduces an added complexity to the system as there is another variable to take into consideration and as such it is important to try and optimise the combined process. Lindenberg et al.[6] used experimental and population balance modelling of acetylsalicylic acid (ASA) in ethanol and water mixtures, to design and optimise a combined cooling and antisolvent crystallisation (CCAC). This comprehensive study showed that it is possible to optimise CCAC operations and achieve an improved product performance, compared to the conventional and commonly applied industrial routes of adding antisolvent at the beginning or at the end of the cooling process. It was found that a constant cooling and constant antisolvent feed rate, where cooling and feeding time were equal, was a simple and more effective crystallisation route and through the multiobjective optimisations performed, the nucleation and growth kinetics could be determined as a function of temperature and solvent composition. Furthermore, Knox et al.[13] used CCAC for paracetamol in isopropanol (IPA) and water (antisolvent) solution mixtures using seeded and non-seeded runs. Linear cooling and antisolvent rates were used for the study as well as three different models for the interpretation of experimental MSZW data of unseeded runs. These were based on equations given by: Nagy et al.[14], Mersmann & Bartosch[15], and Nyvlt[16]. These models were used to predict the induction times and maximum supersaturations. It was found that both the MSZW and the induction times decreased as the cooling rate was increased and as the time-averaged mass fraction of water in solution increased, which could be due to an increased water mass fraction creating a decrease in interfacial energy between paracetamol and the solution. Also, the introduction of antisolvent was found to affect the product yield. A yield of 78% was gained when antisolvent was added after cooling had taken place, whereas a yield of 93% was achieved when antisolvent addition occurred first.

Overall, there are numerous studies related towards antisolvent crystallisation and the effect it has upon the crystallisation process. Its ability to accelerate nucleation has been well established and its use as a common crystallisation route is wide spread. One major issue with it however is the introduction of another material into the crystallising system which creates an added order

of complexity and has the potential to effect numerous crystallisation parameters, such as crystal morphology and size, CSD, polymorph and more.

B.1.2 Crash Cooling

Crash cooling describes the process by which a solution at an elevated temperature is subjected to a drastic change in temperature, which cools the solution down much further than its saturation temperature, creating a rapid, very high, supersaturation. Due to the wide effect temperature change has on metallic structures, studies on crash cooling and its effects have mainly focussed on this avenue of research[17,18], with the terminology used as 'quenching'. Nevertheless, there are studies that have incorporated crash cooling methodologies to investigate different aspects of the crystallisation process.

Croker et al.[19] studied the effect of solvent choice and crystallisation conditions on crystal habit and CSD of the pharmaceutical compound, phenacetin. This study incorporated both antisolvent and crash cooling crystallisation, amongst others. Much like the previously described studies, the antisolvent experiments yielded results showing that a higher antisolvent addition rate increased the supersaturation of the solution, increasing the rate of nucleation and producing crystal with a small needle-like habit. The kinetically controlled crash cooling experiments were performed with 15 different solvents. A variety of morphologies were gained from these experiments, which were performed by transferring a vial containing a relatively hot solution to a water bath set at 5°C. A variety of morphologies was gained for the different solvents used, with the habit being effected by the level of supersaturation, which determines the nucleation and growth rates. Crystal habit is determined by the crystallographic faces and their growth rates, which are highly dependent upon supersaturation, with different faces having different dependencies on the mechanism of growth. The high supersaturations achieved from the crash cooling experiments also had an effect on the mechanism of growth, which can change depending on the supersaturation level. This study also showed that solvent choice is very important with regards to crystal morphology as it can influence the thermodynamics of crystal faces as well as the growth rate dependency of supersaturation of a solution.

Musumeci et al.[20] also studied the effect of solvents on crystallisation, however this study focussed on the polymorphism of arcidine in four different solvents, whilst utilising crash cooling and evaporative crystallisation methodologies. These two techniques constitute a rapid and a slow crystallisation comparison, with the former being controlled by kinetics and the latter being controlled by thermodynamics[19]. The crash cooling experiments were performed creating saturated solutions at 50°C, which were plunged into an ice bath, reducing the

temperature rapidly to 0°C. Comparison of the results obtained from both slow and fast evaporative experiments at the same temperature were made. The same polymorphs were obtained for the majority of solutions, except for the crash cool experiment using acetone. This result shows that crash cooling may have affected the hydrogen bonding of the crystal in some way, enabling a different polymorph to form.

Polymorphism was also studied by Ni et al.[21]. The effect of agitation rate, temperature and cooling rate on the formation of L-glutamic acid polymorphs were investigated. L-glutamic acid is known to form either a metastable α-form or a stable β-form, giving prismatic and needle shaped crystals, respectively. The crash cooling experiments as part of this study were performed by heating an L-glutamic acid solution to 80°C in a water bath, quickly emptying the contents of the bath and filling it with cold water, with the set-point temperature set at 15°C, and placing the solution back into the bath, ensuring raid cooling. This was not found to have any effect on the polymorph of L-glutamic acid crystals formed, resulting in the stable β-form. However, a previous study by Kitamura[22] found the opposite result, with the metastable α-form being formed through the use of rapid cooling.

Although it is widely understood that crash cooling can accelerate nucleation by producing high levels of supersaturation in solutions, not all systems can successfully crystallise using this methodology. Instead, problems can occur in then systems, resulting in 'oiling-out'.

Oiling-out can occur if a solution system has a poor nucleation ability, leading to a heavily supersaturated system, which may fail to crystallise and result in the formation of an emulsion phase. This phenomenon occurs because if nucleation does not occur in a supersaturated system and the supersaturation continues to increase, the solution is unable to thermodynamically exist in one phase and so separates into two separate liquid phases.[23] A vast number of studies has been performed on oiling-out[24–28] due to its presence in a number of common industrial crystallisations of products that poorly nucleate, such as pharmaceuticals and polymers. For example, Groen et al.[27] studied the crystallisation behaviour of citric acid in aqueous solution using an on-line attenuated total reflection-Fourier transform infrared (ATR-FTIR) and found that this system underwent oiling-out due to the citric acid solute molecules poorly nucleating, resulting in a two liquid phases being formed.

Due to oiling out being related to the kinetics of crystallisation for certain compounds, crash cooling can induce this behaviour. This is due to the supersaturation being raised at a substantial

rate, which may not enable the solute to nucleate, and the thermodynamics of the system may mean that a second liquid phase is created.

B.1.3 Sono and Gassing Crystallisation

Sonocrystallisation describes the process in which ultrasound is used during a crystallisation process, whether it is before crystals have formed or when crystals are present within the system. Although its influence on crystallisation was recognised in the early 20th Century, its impact upon the nucleation process and the mechanism by which it achieves this has been the topic of discussion since its discovery. In 1967, Hem[29] proposed a series of mechanisms by which ultrasound affects the crystallisation process. This included agitation effect, with ultrasound increasing the collisions of solute molecules, leading to a higher probability of stable cluster formation; the cooling effect, where solvent evaporates into bubbles formed due to sonication, producing locally higher supersaturations around the bubble surface; heterogeneous nucleation, where the bubbles formed act as a surface for crystal nuclei to from, reducing the Gibbs free energy required; and the cavitation effect, where bubbles collapse producing areas of high pressure, which can increase the melting point of a liquid and thus induce nucleation. The latter effect is widely accepted as the most important of the sonocrystallisation process.

Cavitation is the process of forming, growing and collapsing voids that occur in solution due to the application of ultrasound, shown in Figure B.1.

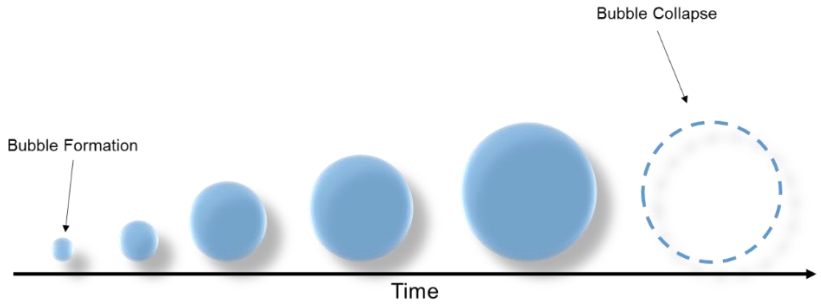


Figure B.1 - The process of cavitation. From bubble formation, bubble growth and eventual bubble collapse.

The cavitation bubbles that form through this process can either be empty, filled with gas or fluid with vapour, depending on the intensity of ultrasound used. The conditions used also dictate how the bubbles that form will eventually undergo cavitation, stable or transient cavitation will cause the bubble to either ascend, decay or implode violently under very high local temperatures and pressures of around 5000 K and 1000 bar, respectively[30,31]. Cavitation is affected by a number of parameters, including: viscosity, surface tension, impurities, frequency of ultrasound, and more[32,33].

Research studies into sonocrystallisation have been extensive due to its ability to induce and accelerate crystallisation, creating a highly supersaturated solution that can be controlled relatively well[34]. The majority of studies undertaken focus on the feasibility of sonocrystallisation to certain systems, but there are still numerous studies that concentrate on the effect it has upon crystallisation itself.

Miyasaka et al.[35] investigated the effect of ultrasound on the number of acetylsalicylic acid crystals formed from an acetic acid solution, using an ultrasonic probe. It was found that, like other studies, the number of crystals was increased at higher level of ultrasonic energy, but more importantly it was found that at low levels of ultrasonic energy the average number decreased. These findings suggest that when employing ultrasound in crystallisation processes there is an ultrasonic energy region where nucleation is actually inhibited and as such a specific level of ultrasonic energy is required to induce nucleation. Other research studies have found interesting results, such as that by Kordylla et al.[36] which found that under sonocrystallisation solvent properties, such as surface tension and vapour pressure, do not affect the induction of nucleation and instead it is determined by the ultrasonic parameters and the initial supersaturation level at which ultrasonic energy is applied.

Most importantly, there have been a number of research studies related to the effect sonocrystallisation has on the MSZW and the rate of nucleation. Lyczko et al.[37] studied the effect of applying ultrasound to a system of potassium sulphate in water. The results of the study showed that by applying ultrasonic energy the MSZW and the induction times were reduced. This result was also found by Bari et al.[38] which also studied sonocrystallisation of potassium sulphate in water. This research also showed that the CSD was reduced through the use of ultrasound and the kinetic parameters obtained as part of the study showed an increase in the rate of nucleation of the potassium sulphate. Most studies relating to a reduction in the induction time and an increased rate of nucleation have found this to be the case[39–41].

Although sonocrystallisation has yielded positive experimental results, in practice at larger scales it is not adopted, due to the large amounts of energy that would be required for its use and the difficulty in maintaining control of the system[39]. Furthermore, the mechanism by which nucleation is induced is not clear. Due to this, Wohlgemuth et al.[42] proposed a technique of gassing crystallisation that would enable the mechanism to be understood. This enabled a comparison of the two processes as for sonocrystallisation bubbles grew and collapsed, whereas for gassing crystallisation the bubbles only grew. Therefore, the study could show whether crystallisation was induced due to the collapsing phenomena or via a heterogeneous mechanism

on the surface of the bubbles. The results of this study showed that gassing crystallisation can also reduce the MSZW when applied within the MSZ. Also, the effect of solvent evaporation into bubbles was shown to have no effect on nucleation. This suggested a heterogeneous nucleation mechanism was occurring. A further study by Wohlgemuth et al.[43] compared the two crystallisation processes with adipic acid in different solvents, which showed that the MZSW and the CSD could be reduced by gassing crystallisation. It was concluded that gassing can be used as an alternative to ultrasound in order to accelerate nucleation.

Since the introduction of gassing crystallisation, numerous studies have focussed on its ability to accelerate and control nucleation. Kleetz et al.[44] studied the effect gassing crystallisation has on the median crystal diameter using a succinic acid in water solution. The results of this study showed that, much like for sonocrystallisation, the supersaturation level when gassing is introduced is a key parameter in nucleation control and that by carefully selecting a cooling profile and gassing supersaturation, the median crystal diameter can be controlled. It was also found that this technique has an enlarging effect on product crystals, which could make it possible to reduce required batch times of crystallisation processes. Later, Kleetz et al.[45] studied its effect on induction times and CSD. Using a succinic acid in water system, it was found that the induction time could be reduced relatively significantly when gassing supersaturation was increased, accelerating the nucleation process. It was also found that the CSD became narrower as the supersaturation was increased and that varying gassing duration had no effect on induction time, suggesting that nuclei formed at the beginning of the gassing period only. Another study by Kleetz et al.[46] varied process parameters and crystalliser geometry to study the success of gassing crystallisation when compared to standard cooling crystallisation. It was found that after the application of gassing, MZSWs were narrowed, crystal median diameters were enlarged and reproducibility was improved. Terdenge et al.[47] studied its effect on agglomeration and found that it possesses an ability to produce crystal products with lower agglomeration when compared to standard cooling crystallisation and the reproducibility of results was improved.

Overall, although gassing crystallisation is a relatively new concept, it has potential to enable an accelerated nucleation methodology and affords great control over the nucleation process itself, however, it does limit the nucleation mechanism to one of HEN.

B.1.4 Substrate

Substrate crystallisation refers to the process by which a substance is added to a solution which enables nucleation on its surface. This creates a surface for crystals to grow from and as such creates a heterogeneous nucleation mechanism that, much like with sono and gassing crystallisation, reduces the free energy required to nucleate. However, not only is there a lack of knowledge over the mechanistic understanding of the process of heterogeneous nucleation[48], the effect of surfaces on this mechanism is also not understood and is not generally systematically researched[49].

Curcio et al.[49] performed a comprehensive study on the effect six commercially available polymers played on regulation nucleation kinetics of acetaminophen (ACM) in deionised water solution. Induction times were measured for the six polymers with the ACM-H_2O solutions, with the systems held at constant supersaturation, to compare the effect each one had on the crystallisation process. No crystals were formed in the solutions containing no polymers and the range of induction times for the solutions containing the six chosen polymers ranged from an average of 1310 hours for polydimethylsiloxane (PDMS) to 11.5 hours for ethylene/acrylic acid (15%) copolymer (EAA). Subsequent tests were performed to determine the influence of specific intermolecular interactions between ACM and polymer surfaces during nucleation, by studying the preferred orientation (PO) of crystal facets on the solid surfaces. It was found that a higher PO enhanced nucleation activity and the level of PO is dependent on the intermolecular interaction strength at the crystal/polymer interface, suggesting surface chemistry plays a key role in substrate heterogeneous nucleation kinetics. This study provides evidence that a substrates ability to promote specific intermolecular interactions improves nucleation behaviour, whereas nucleation is retarded when specific directional interactions are not promoted. This could be due to the two-step nucleation theory that suggests molecules in a cluster require a reorganisation to resemble the macroscopic crystal structure[49,50].

A similar study by Diao et al.[51] investigated the surface chemistry and morphology effects of polymeric substrates on the induction times of aspirin. It was found that some polymers significantly enhanced nucleation rates and reduced the induction times, whereas the polymers used that were less polar were ineffective in enhancing nucleation kinetics. This result illustrates the importance of substrate surface chemistry and selectivity in accelerating nucleation. Furthermore, it was found that polymers containing nanoscopic pores drastically increased the rate of nucleation by orders-of-magnitude more than those without pores, although the effect of pore structure on nucleation kinetics was not determined. Preferred orientation (PO) was also investigated, and it was found that hydrogen bonding between the polymers and crystals plays a key role in orientation and polymers that enabled these interactions preferentially nucleated polar facets of aspirin. Later, Diao et al.[52] investigated the

effect of nanoscopic pore shape on enhancing the nucleation kinetics of aspirin using lithographic methods. It was found that a spherical pore of 15-120 nm retarded nucleation, whereas angular pores of the same size enhanced it and that favourable surface-solute interactions are required if angular pores are to enhance nucleation. It was proposed that the orientation order of aspirin near the pores was altered by the angle of the pore.

Due to the potential of substrate crystallisation to enhance nucleation kinetics, there are numerous studies that focus on this area of research[48,53–56]. Although the previously described research studies focussed on enhancing nucleation kinetics, research on substrate crystallisation has been performed on a number of different research avenues. For example, Chadwick et al.[57] investigated the effect substrates have on polymorphic transformations.

B.2 Predicting Nucleation

The high complexity associated with the crystallisation process and the long length of time required to undertake research studies in this area means that accurate predictions of various aspects of the process have been desired for a long period of time. Unfortunately, this complex nature has made accurate predictions very difficult to achieve, although a number of studies have been undertaken in order to formulate accurate predictions.

Recently, Patel et al.[58] used a predictive methodology to determine how polymer substrates affect induction times. A novel approach known as PETI (Predicting Efficacy Through Intermolecular Interactions) was developed in order to advance the previously empirical based research into substrate crystallisation. PETI was devised in order to predict the ability of different polymer surfaces in enhancing heterogeneous nucleation kinetics and it is based on the concept that the more likely a substrate and a solute are to form an intermolecular bond, the faster the rate of heterogeneous nucleation. Two major assumptions are made under PETI: a polymer surface contains only one strongly directional functional group which interacts with solute molecules to form heteronucleation sites, and only the most favourable interaction is taken into account. For this study benzocaine (BZC) and 1,1'-bi-2-naphthol (BINOL) were used and tested with a variety of polymers. PETI works by splitting the compounds into functional moieties, which are able to form intermolecular interactions such as hydrogen bonds, and the Cambridge Structural Database (C.S.D.) is searched to determine the number of occurrences an intermolecular interaction between each moiety and the functional group of a polymer. The greater this value, the greater the enhancement of nucleation rate. For the experimental investigation using BZC induction time measurements were made and were compared with predicted nucleation kinetic enhancements. Out of the six systems investigates, two didn't

follow the prediction, although this was found to be due to other interactions occurring between the polymers and BZC. Under the BINOL experimental study, polystyrene (PS) and poly-(N,N-dimethylacrylamide) (PDMA) were used as competing surfaces for crystallisation. From PETI it was predicated that crystallisation would be favoured on PS and from the investigation this was found to be the case. Overall, PETI's use for predicting heterosurface impact on nucleation kinetics has a high potential for further predictive studies, although some issues with oversimplification occurred in this study, meaning a potential improvement of the predictive model may be required for improved accuracy.

Gu et al.[59] also proposed a way in which to predict aspects of nucleation, but focussed on the polymorphism of pharmaceutical compounds. In this study, solvent-mediated polymorphic transformation was implemented, where a less stable crystal form was suspended in a saturated solution and the more stable form crystallised at the expense of the dissolution of the less stable form. This technique enables a polymorphic screening ability, in that, it can be used to predict whether a crystal form will remain stable or will transform into another polymorph at some time. It was found that the solubility and also solvent-solute interaction had a very strong effect on whether polymorphic transformation would occur in solution, along with temperature and degree of agitation influencing the nucleation kinetics of the stable polymorph. Miller et al.[60] built upon this work to study solvent-mediated polymorphic transformation of Ritonavir and a drug compound in early stages of development. The stable form of Ritonavir was produced from the screen and more interestingly, the study resulted in a more stable polymorphic form of the early stage development drug being discovered. Without this test, the compound may have progressed as a metastable form through development, and later be recalled. This study showed the importance of predicting nucleation events and provided evidence of the ability of solvent-mediated polymorphic transformation screening to do this. However, this technique is limited, as it is subject to solubility of compounds, the type of solute-solvent interactions and it does not provide a way in which to predict when a nucleation event may occur over time.

Limited success has been gained in attempts to predict the nucleation process, as such any progression within this area of research could prove substantial and beneficial to the wider crystal community.

B.3 Controlling Nucleation

B.3.1 Growth Inhibition

The terminology used to describe this section has been chosen due to the fact that if a solution crystallisation process is going to happen there is nothing, currently, that can stop it from happening, other than changing the conditions of the solution, i.e. temperature, concentration, etc. Although 'controlling' could be used to described the ability to accelerate nucleation, the ability to control whether a crystallisation process will or won't occur without changing the conditions of the process is deemed to be a more substantial view of control. Therefore, this section will review the work of research studies that have attempted to inhibit crystallisation in some way.

Ilevbare et al.[61] studied the inhibition of crystallisation of ritonavir, in an attempt to understand how supersaturating dosage forms, such as amorphous suspensions, can be effective in delivering poorly water-soluble drugs. A number of commercially available polymers as well as a number of non-commercial cellulose derivatives were studied in order to understand the effectiveness of polymers for this purpose. Particularly, the study focussed on the inhibition of ritonavir crystal growth from solution. The cellulose derivatives, in general, were found to be more effective at inhibiting growth than the synthetic polymers, due to their semi-rigid structure, amphiiphilicity and hydrophobicity, with the latter being found to be an important factor under orthogonal partial-least squares analysis. The results suggested that these properties enhanced the adsorption of the cellulose-based polymers to ritonavir's crystallising surface, inhibiting growth.

Ilevbare et al.[62] further built upon this work and studied the effect of binary additive combinations on crystal growth. Polymer/polymer additives were seen to reduce the crystal growth rate of the case study drug Ritonavir, by more than the individual polymers themselves. This finding was attributed to the formation of polymer-polymer hydrophobic interactions. However, polymer/surfactant combinations that were investigated in this study actually increased the crystal growth rate. This was due to a decrease in interactions between the solute and the polymers, caused by the presence of surfactant molecules. This study showed the importance of additive selection for crystal growth inhibition.

More recently, Schram et al.[63] studied the crystal growth rates of felodipine, a poorly water soluble drug, in the absence and presence of a polymer. This research was undertaken in a rotating disk apparatus that enabled the isolation of the mass transfer and integration steps,

enabling kinetic rate constants of each step to be determined. The study concluded that felodipine crystal growth rate was slowed due to absorption of polymers on the crystal surface, causing a decrease in integration rate.

B.3.2 Nucleation Inhibition

The inhibition of crystal nucleation is an avenue of research that has been limited, in large part, due to a lack of fundamental understanding as to the mechanism by which solutes in solution come together to form critical nuclei. It is only recently, in a study by Siepermann et al.[64], which focussed upon inhibiting the nucleation of benzoic acid through chemical complexation with 1,3-di-o-tolylguanidine. This complex pair was chosen as it was known to have strong intermolecular interactions and the effect of complexing on nucleation was studied using statistical measurements of induction time. The results showed that even a small amount of complexing agent (≤ 0.05 mg/ml) was able to retard the onset of nucleation, with an increase in measured induction times of above 150%, when compared to uncomplexed solutions. The effect of nucleation inhibition was shown to increase monotonically with increasing complexing agent concentration. It was concluded that a complex set of molecular interactions was responsible for kinetically impeding crystal nuclei formation, although no mechanism was postulated.

More recently, Siepermann & Myerson[65] built upon this work to study the effect of weakly interacting dilute complexing agent, 3-aminobenzoic acid, on the nucleation rate inhibition of 3-nitrophenol. The effect of the presence of a complexing agent was seen to effect nucleation in the same manner as in the previously described study. In this work, a concentration of 0.25% molar complexing agent, with respect to solute, increased induction times by 233%, when compared to uncomplexed solutions. The strength of intermolecular interaction was shown to not have an effect on nucleation inhibition, as a comparable degree of inhibition was seen in the weakly interacting pair in this study, and the strongly interacting pair, in the previous study. This was attributed to the low concentration of complexing agent creating favourable binding interactions, explained by Le Chatelier's principle. This study also examined the calculated nucleation rates through CNT, a two-step nucleation model and a new functional form of the nucleation rate equation. From the analysis it was concluded that the inclusion of a complexing agent form an obstacle in the prenucleus high-density clusters, suppressing the ordering kinetic constant for the transition from a prenucleation cluster to a stable nucleus, in the proposed two-step nucleation mechanism. A mechanistic proposal was put forward, stating that the formation of complexes hinders the rearrangement of molecules within prenucleation clusters.

These studies show promising results in an endeavour to retard the nucleation process and inhibit crystal formation, however, they currently only provide a way in which to increase induction times and not to stop nucleation entirely. The work described in these two studies provides a foundation for further studies into the inhibition of nucleation.

B.4 Modelling Nucleation

The terminology used to describe this section refers to the modelling of crystallisation through the use of computer simulations. Although there are a vast number of mathematical models and solution methods, the focus of this section has been chosen as it relates to the work presented in this thesis.

The complex nature of nucleation, from its stochastic nature to its very small length scale means that it is not possible to understand its characteristics or even detect its onset accurately, through the use of experimental investigations. The advancement of computer technology has enabled aspects of these difficulties to be overcome, with computer simulations allowing the process of nucleation to be modelled. The introduction of modelling in the field of crystallisation has created more understanding in how the, still not fully understood, process occurs, although it is limited by the current models that exist to describe the complexities of nucleation and growth, as well as the software available in which to model the processes. Nevertheless, advancements have been made in more recent years from modelling studies, for example, as eluded to in Section A.5.4, it was a study performed by ten Wolde and Frenkel[66], using computational simulation software, that was one of the first studies supporting the concept of two-step nucleation. This study focussed on the HON crystallisation of a model globular protein using a biased Monte Carlo approach. From this modelling methodology, it was possible to identify the structure of the surroundings of each protein particle as well as the local density. Large density fluctuations were observed around T_c, where the first step in nucleation was the formation of a liquid-like droplet, followed by a crystalline nucleus forming inside the droplet.

A number of other studies have focussed upon modelling aspects of crystallisation, such as combined cooling and antisolvent crystallisation[67], alkane crystalisation[68,69], polymorphism[70], and more.

Zerze et al.[69] used molecular dynamics simulations to study the melt crystallisation of eicosane, with a view to further model expansion to the more computationally demanding modelling of polymers, such as polyethylene. A wide range of nucleation phenomena was modelled and compared to experimentally gained results from previous studies. It was found that the proposed

model was capable of predicting crystal domains of eicosane, including the density and crystal lattice parameters, as well as crystallisation kinetics, cluster analysis and nuclei formation. It was concluded that the methodology undertaken through molecular dynamics simulations enables a relatively comprehensive study of nucleation in more complex systems. Yi and Rutledge[68] also modelled the melt crystallisation of eicosane, but combined molecular dynamic simulations with a Monte Carlo method to establish key parameters of the nucleation process. Induction times, nucleation rates, free energies and interfacial energies were calculated. The simulations undertaken also showed that the critical nucleus consisted of a bundle of stretched segments, in a cylindrical shape.

Synthonic simulations of para-aminobenzoic acid (pABA) were undertaken by Rosbottom et al.[71] to reveal its solid state, surface and morphological properties. An array of software packages was used in this investigation, with Materials Studio, Mercury 3.3, HABIT and C.S.D all being used to gain a holistic view of how the intermolecular interactions (synthons) affect the molecular properties of both α-pABA and β-pABA, ranging from their morphologies, lattice energies, crystal chemistries, monomer attachment processes, etc, enabling a more in-depth understanding of the crystallisation of pABA. Toroz et al.[72] also performed a comprehensive study of pABA and used modelling methods, alongside a variety of experimental procedures to create a detailed overview of its crystallisation from ethanolic solutions. Computational simulations were performed in order to understand why the α-form was favoured in crystallisation from ethanol. From combined ab initio with molecular dynamics simulations it was found that carboxylic-acid dimers present in the α-structure were responsible for the stability of small clusters in solution, favouring the crystallisation of the α-form.

A recent study by Bobrovs et al.[73] used a combination of NMR spectroscopy and MD simulations to probe the structural pathways to the formation of the α-pABA and β-pABA polymorphs in water, ethanol and acetone. This study suggested that the self-assembly of pABA is highly dependent upon solution environment, with π-π stacking intermolecular interactions being dominant in water solutions and hydrogen bonding intermolecular interactions being dominant in the organic solvent studied. The findings provide strong insight into how the nucleation pathway can be controlled through controlling solution environment and how computational modelling can provide molecular scale insights into the complex processes of nucleation.

The number of studies that have been undertaken in order to model the crystallisation of a wide range of molecular species is vast and is increasing rapidly as computing power, modelling software and an understanding of how nucleation actually occurs in certain systems improves.

One set of crystallisation modelling studies that is relevant to the future work suggested to continue from the work presented in this thesis are those performed using Process Systems Enterprise gPROMS FormulatedProducts software's[74], mainly the gCRYSTAL functionality.

Su et al.[75] used gCRYSTAL's extensive software capabilities to validate a mathematical model that was developed for crystallisation processes under continuous mixed-suspension mixed-product removal operation. Good agreement between the implemented model in MATLAB and in gCRYSTAL was seen for a number of parameters. Parisi et al.[76] investigated the scale up of dextrose cooling crystallisation, from lab scale to pilot scale (200 litre reactor), whilst implementing gPROMS Formulated Products to interpret experimental results and to perform parameter estimations on three kinetic growth and nucleation rate parameters. Concentration and crystal size distribution (CSD) from experimental investigation was in good agreement with the simulated results. The parameter estimations suggested that the kinetic parameter estimations were robust. Overall, the use of gPROMS coupled with the experimental procedure in this study was deemed to obtain robust kinetic data that could be applied on an industrial scale. Recently, Bari and Pandit[77] used gPROMS parameter estimation tools to determine crystallisation nucleation, growth, breakage and agglomeration kinetics of the crystallisation of potassium sulfate in water. They devised a sequential procedure in which to estimate parameters in three steps, first determining the primary nucleation and growth parameters, followed by secondary nucleation parameters and finally the breakage and agglomeration parameters. It was found that the sequential procedure was effective in estimating parameters, saving on the much larger computational effort that would be required to perform the same task simultaneously. The methodology worked due to the sequential process of crystallisation itself, with primary nucleation being first, followed by growth, etc. This result showed that both primary nucleation and growth parameters could be estimated from both MSZW and induction time measurements, and then be subsequently used in further crystallisation phenomena parameter estimations.

Overall, the studies described, although only being a small collection in a much larger research article area, demonstrate the ability to model the processes of crystallisation. More importantly, the described research provides evidence that the methodology undertaken as part of this PhD project is feasible.

B.5 Conclusions

This chapter has provided a review of literature that focusses upon the nucleation aspect of crystallisation. Ways in which nucleation has been accelerated and research studies in the described areas are discussed. This was initially described through antisolvent crystallisation

studies, followed by crash cooling studies. Both these techniques are similar in the sense they both change the supersaturation in a system rapidly. Sono and gassing crystallisation studies were reviewed, followed by substrate crystallisation studies. These techniques are similar as they both induce heterogeneous nucleation in order to accelerate nucleation. Studies related towards predicting nucleation were then discussed, with an effort to show how attempts have been made to aid in the accuracy and development of different crystallisation concept approaches. Next, research relating towards the inhibition of crystallisation processes was reported and discussed, giving promising details as to the ability of foreign molecules in a solution to hinder either the growth stage and/or the nucleation stage of crystallisation. Finally, the modelling of nucleation was discussed, with respect to numerous research studies, giving evidence of the ability to model and estimate aspects of the complex process that is crystallisation.

B.6 References

1. Sangwal, K. & Mielniczek-Brzóska, E. Antisolvent crystallization of aqueous ammonium dihydrogen phosphate solutions by addition of methanol. *J. Cryst. Growth* **451**, 139–149 (2016).
2. Roelands, C. P. M. *et al.* Antisolvent crystallization of the polymorphs of L-histidine as a function of supersaturation ratio and of solvent composition. *Cryst. Growth Des.* **6**, 955–963 (2006).
3. Granberg, R. A., Bloch, D. G. & Rasmuson, C. Crystallization of paracetamol in acetone — water mixtures. *J. Cryst. Growth* **198/199**, 1287–1293 (1999).
4. Hermanto, M. W., Chow, P. S. & Tan, R. B. H. Operating strategy to produce consistent CSD in combined antisolvent-cooling crystallization using FBRM. *Ind. Eng. Chem. Res.* **51**, 13773–13783 (2012).
5. Sheikhzadeh, M., Trifkovic, M. & Rohani, S. Adaptive MIMO neuro-fuzzy logic control of a seeded and an unseeded anti-solvent semi-batch crystallizer. *Chem. Eng. Sci.* **63**, 1261–1272 (2008).
6. Lindenberg, C., Kra, M., Cornel, J. & Mazzotti, M. Design and Optimization of a Combined Cooling / Antisolvent Crystallization Process. *Cryst. Growth Des.* **9**, 1124–1136 (2009).
7. Yang, Y. & Nagy, Z. K. Combined Cooling and Antisolvent Crystallization in Continuous Mixed Suspension, Mixed Product Removal Cascade Crystallizers: Steady-State and Startup Optimization. *Ind. Eng. Chem. Res.* **54**, 5673–5682 (2015).
8. Kim, K. J. & Kim, J. K. Nucleation and supersaturation in drowning-out crystallization using a T-mixer. *Chem. Eng. Technol.* **29**, 951–956 (2006).

9. Zhu, Y. *et al.* Study of the solubility and the metastable zone of 1,3-dihydroxyacetone for the drowning-out process. *J. Cryst. Growth* **257**, 370–377 (2003).
10. Pina, C. M., Fernández-Díaz, L., Prieto, M. & Veintemillas-Verdaguer, S. Metastability in drowning-out crystallization: Precipitation of highly soluble sulphates. *J. Cryst. Growth* **222**, 317–327 (2001).
11. Chang, S. M., Kim, J. M., Kim, I. H., Shin, D. M. & Kim, W. S. Agglomeration control of L-ornithine aspartate crystals by operating variables in drowning-out crystallization. *Ind. Eng. Chem. Res.* **45**, 1631–1635 (2006).
12. Plasari, E., Grisoni, P. H. & Villermaux, J. Influence of process parameters on the precipitation of organic nanoparticles by drowning-out. *Chem. Eng. Res. Des.* **75**, 237–244 (1997).
13. Knox, M., Trifkovic, M. & Rohani, S. Combining anti-solvent and cooling crystallization: Effect of solvent composition on yield and meta stable zone width. *Chem. Eng. Sci.* **64**, 3555–3563 (2009).
14. Nagy, Z. K., Fujiwara, M., Woo, X. Y. & Braatz, R. D. Determination of the kinetic parameters for the crystallization of paracetamol from water using metastable zone width experiments. *Ind. Eng. Chem. Res.* **47**, 1245–1252 (2008).
15. Mersmann, A. & Bartosch, K. How to predict the metastable zone width. *J. Cryst. Growth* **183**, 240–250 (1998).
16. Nyvlt, J. Kinetics of Nucleation in Solutions. *J. Cryst. Growth* **3/4**, 377–383 (1968).
17. Stepanova, M. G., Valyaeva, V. I. & Garbus, A. V. Effect of Rapid Cooling in Crystallization on the Structureand Properties of Sintered Alloy 1201. *Met. Sci. Heat Treat.* **24**, 201 (1982).
18. Bar, M. D., Surifiach, S., Diego, J. A. & Clavaguera-Mora, M. T. Effect of the quenching conditions on the crystallization kinetics and morphology of Fe65Co18B16Si1. *Mater. Sci. Eng.* **133**, 807–810 (1991).
19. Croker, D. M. *et al.* Demonstrating the Influence of Solvent Choice and Crystallization Conditions on Phenacetin Crystal Habit and Particle Size Distribution. *Org. Process Res. Dev.* **19**, 1826–1836 (2015).
20. Musumeci, D., Hunter, C. A. & McCabe, J. F. Solvent effects on acridine polymorphism. *Cryst. Growth Des.* **10**, 1661–1664 (2010).
21. Ni, X. W. *et al.* On the crystal polymorphic forms of L-glutamic acid following temperature programmed crystallization in a batch oscillatory baffled crystallizer. *Cryst. Growth Des.* **4**, 1129–1135 (2004).
22. Kitamura, M. Polymorphism in the crystallization of L-glutamic acid. *J. Cryst. Growth* **96**, 541–546 (1989).
23. Groen, H. On-Line Monitoring and Control of Supersatuartion in Batch Crystallisers for

Organic Fine Chemical Products using ATR FTIR Spectroscopy. (2001).

24. Deneau, E. & Steele, G. An in-line study of oiling out and crystallization. *Org. Process Res. Dev.* **9**, 943–950 (2005).
25. Lu, J., Carpenter, K., Li, R. J., Wang, X. J. & Ching, C. B. Cloud-point temperature and liquid-liquid phase separation of supersaturated lysozyme solution. *Biophys. Chem.* **109**, 105–112 (2004).
26. Kiesow, K., Tumakaka, F. & Sadowski, G. Experimental investigation and prediction of oiling out during crystallization process. *J. Cryst. Growth* **310**, 4163–4168 (2008).
27. Groen, H. & Roberts, K. J. Nucleation, growth, and pseudo-polymorphic behavior of citric acid as monitored in situ by attenuated total reflection fourier transform infrared spectroscopy. *J. Phys. Chem. B* **105**, 10723–10730 (2001).
28. Bonnett, P. E., Carpenter, K. J., Dawson, S. & Davey, R. J. Solution crystallisation via a submerged liquid–liquid phase boundary: oiling out. *Chem. Commun.* 698–699 (2003). doi:10.1039/b212062c
29. Hem, S. L. The effect of ultrasonic vibrations on crystallization processes. *Ultrasonics* **5**, 202–207 (1967).
30. Neppiras, E. a. Acoustic cavitation. *Phys. Rep.* **61**, 159–251 (1980).
31. McNamara, W. B., Didenko, Y. T. & Suslick, K. S. Sonoluminescence temperatures during multi-bubble cavitation. *Nature* **401**, 772–775 (1999).
32. Wohlgemuth, K. Induced Nucleation Processes during Batch Cooling Crystallization. (2012).
33. Apfel, R. E. Acoustic Cavitation. in *Methods in Experimental Physics* **19**, 355–411 (Academic Press, 1981).
34. Ratsimba, B., Biscans, B., Delmas, H. & Jean, J. Sonocrystallization: The End of Empiricism? *Kona* **17**, 38–48 (1999).
35. Miyasaka, E., Kato, Y., Hagisawa, M. & Hirasawa, I. Effect of ultrasonic irradiation on the number of acetylsalicylic acid crystals produced under the supersaturated condition and the ability of controlling the final crystal size via primary nucleation. *J. Cryst. Growth* **289**, 324–330 (2006).
36. Kordylla, A., Koch, S., Tumakaka, F. & Schembecker, G. Towards an optimized crystallization with ultrasound: Effect of solvent properties and ultrasonic process parameters. *J. Cryst. Growth* **310**, 4177–4184 (2008).
37. Lyczko, N., Espitalier, F., Louisnard, O. & Schwartzentruber, J. Effect of ultrasound on the induction time and the metastable zone widths of potassium sulphate. *Chem. Eng. J.* **86**, 233–241 (2002).
38. Bari, A. H., Chawla, A. & Pandit, A. B. Sono-crystallization kinetics of K2SO4: Estimation of nucleation, growth, breakage and agglomeration kinetics. *Ultrason.*

Sonochem. **35**, 196–203 (2017).

39. Amara, N., Ratsimba, B., Wilhelm, A. M. & Delmas, H. Crystallization of potash alum: Effect of power ultrasound. *Ultrason. Sonochem.* **8**, 265–270 (2001).
40. Luque de Castro, M. D. & Priego-Capote, F. Ultrasound-assisted crystallization (sonocrystallization). *Ultrason. Sonochem.* **14**, 717–724 (2007).
41. Virone, C., Kramer, H. J. M., van Rosmalen, G. M., Stoop, A. H. & Bakker, T. W. Primary nucleation induced by ultrasonic cavitation. *J. Cryst. Growth* **294**, 9–15 (2006).
42. Wohlgemuth, K., Kordylla, A., Ruether, F. & Schembecker, G. Experimental study of the effect of bubbles on nucleation during batch cooling crystallization. *Chem. Eng. Sci.* **64**, 4155–4163 (2009).
43. Wohlgemuth, K., Ruether, F. & Schembecker, G. Sonocrystallization and crystallization with gassing of adipic acid. *Chem. Eng. Sci.* **65**, 1016–1027 (2010).
44. Kleetz, T., Braak, F., Wehenkel, N., Schembecker, G. & Wohlgemuth, K. Design of Median Crystal Diameter Using Gassing Crystallization and Different Process Concepts. *Cryst. Growth Des.* **16**, 1320–1328 (2016).
45. Kleetz, T., Funke, F., Sunderhaus, A., Schembecker, G. & Wohlgemuth, K. Influence of Gassing Crystallization Parameters on Induction Time and Crystal Size Distribution. *Cryst. Growth Des.* **16**, 6797–6803 (2016).
46. Kleetz, T., Pätzold, G., Schembecker, G. & Wohlgemuth, K. Gassing Crystallization at Different Scales: Potential to Control Nucleation and Product Properties. *Cryst. Growth Des.* **17**, 1028–1035 (2017).
47. Terdenge, L. M., Kossuch, J. A., Schembecker, G. & Wohlgemuth, K. Potential of gassing crystallization to control the agglomeration degree of crystalline products. *Powder Technol.* **320**, 386–396 (2017).
48. Wijethunga, T. K., Baftizadeh, F., Stojaković, J., Myerson, A. S. & Trout, B. L. Experimental and Mechanistic Study of the Heterogeneous Nucleation and Epitaxy of Acetaminophen with Biocompatible Crystalline Substrates. *Cryst. Growth Des.* **17**, 3783–3795 (2017).
49. Curcio, E. *et al.* Regulating nucleation kinetics through molecular interactions at the polymer-solute interface. *Cryst. Growth Des.* **14**, 678–686 (2014).
50. Erdemir, D., Lee, A. Y. & Myerson, A. S. Nucleation of Crystals from Solution : Classical and Two-Step Models. *Acc. Chem. Res.* **42**, (2009).
51. Diao, Y., Myerson, A. S., Hatton, T. A. & Trout, B. L. Surface design for controlled crystallization: The role of surface chemistry and nanoscale pores in heterogeneous nucleation. *Langmuir* **27**, 5324–5334 (2011).
52. Diao, Y., Harada, T., Myerson, A. S., Alan Hatton, T. & Trout, B. L. The role of nanopore shape in surface-induced crystallization. *Nat. Mater.* **10**, 867–871 (2011).

53. Yazdanpanah, N. *et al.* Continuous Heterogeneous Crystallization on Excipient Surfaces. *Cryst. Growth Des.* **17**, 3321–3330 (2017).
54. Lopez-Mejías, V., Knight, J. L., Brooks, C. L. & Matzger, A. J. On the mechanism of crystalline polymorph selection by polymer heteronuclei. *Langmuir* **27**, 7575–7579 (2011).
55. Quon, J. L. *et al.* Templated nucleation of acetaminophen on spherical excipient agglomerates. *Langmuir* **29**, 3292–3300 (2013).
56. Chadwick, K., Chen, J., Myerson, A. S. & Trout, B. L. Toward the rational design of crystalline surfaces for heteroepitaxy: Role of molecular functionality. *Cryst. Growth Des.* **12**, 1159–1166 (2012).
57. Chadwick, K., Myerson, A. & Trout, B. Polymorphic control by heterogeneous nucleation - A new method for selecting crystalline substrates. *CrystEngComm* **13**, 6625 (2011).
58. Patel, M. A., Nguyen, B. & Chadwick, K. Predicting the Nucleation Induction Time Based on Preferred Intermolecular Interactions. *Cryst. Growth Des.* **17**, 4613–4621 (2017).
59. Gu, C. H., Young, V. & Grant, D. J. W. Polymorph screening: Influence of solvents on the rate of solvent-mediated polymorphic transformation. *J. Pharm. Sci.* **90**, 1878–1890 (2001).
60. Miller, J. M., Collman, B. M., Greene, L. R., Grant, D. J. W. & Blackburn, A. C. Identifying the stable polymorph early in the drug discovery-development process. *Pharm. Dev. Technol.* **10**, 291–297 (2005).
61. Ilevbare, G. A., Liu, H., Edgar, K. J. & Taylor, L. S. Understanding polymer properties important for crystal growth inhibition-impact of chemically diverse polymers on solution crystal growth of ritonavir. *Cryst. Growth Des.* **12**, 3133–3143 (2012).
62. Ilevbare, G. A., Liu, H., Edgar, K. J. & Taylor, L. S. Effect of binary additive combinations on solution crystal growth of the poorly water-soluble drug, ritonavir. *Cryst. Growth Des.* **12**, 6050–6060 (2012).
63. Schram, C. J., Smyth, R. J., Taylor, L. S. & Beaudoin, S. P. Understanding Crystal Growth Kinetics in the Absence and Presence of a Polymer Using a Rotating Disk Apparatus. *Cryst. Growth Des.* **16**, 2640–2645 (2016).
64. Pons Siepermann, C. A., Huang, S. & Myerson, A. S. Nucleation Inhibition of Benzoic Acid through Solution Complexation. *Cryst. Growth Des.* **17**, 2646–2653 (2017).
65. Pons Siepermann, C. A. & Myerson, A. S. Inhibition of Nucleation Using a Dilute, Weakly Hydrogen-Bonding Molecular Additive. *Cryst. Growth Des.* **18**, acs.cgd.8b00367 (2018).
66. ten Wolde, P. R. & Frenkel, D. Enhancement of protein crystal nucleation by critical

density fluctuations. *Science (80-.).* **277**, 1975–1978 (1997).

67. Nagy, Z. K., Fujiwara, M. & Braatz, R. D. Modelling and control of combined cooling and antisolvent crystallization processes. *J. Process Control* **18**, 856–864 (2008).
68. Yi, P. & Rutledge, G. C. Molecular simulation of bundle-like crystal nucleation from n-eicosane melts. *J. Chem. Phys.* **135**, (2011).
69. Zerze, H., Mittal, J. & Mchugh, A. J. Ab initio crystallization of alkanes: Structure and kinetics of nuclei formation. *Macromolecules* **46**, 9151–9157 (2013).
70. Zhang, H. J., Peng, S. M., Zhou, X. S. & Ju, X. Polymorphic crystals selected in the nucleation stage. *Epl* **107**, (2014).
71. Rosbottom, I., Roberts, K. J. & Docherty, R. The solid state, surface and morphological properties of p-aminobenzoic acid in terms of the strength and directionality of its intermolecular synthons. *CrystEngComm* **17**, 5768–5788 (2015).
72. Toroz, D. *et al.* Towards an understanding of the nucleation of alpha-para amino benzoic acid from ethanolic solutions: a multi-scale approach. *Faraday Discuss.* **179**, 79–114 (2015).
73. Bobrovs, R., Drunka, L., Auzins, A. A., Jaudzems, K. & Salvalaglio, M. Polymorph-Selective Role of Hydrogen Bonding and π-πStacking in p-Aminobenzoic Acid Solutions. *Cryst. Growth Des.* **21**, 436–448 (2021).
74. Process Systems Enterprise Limited. PSE. (2018). Available at: https://www.psenterprise.com/.
75. Su, Q., Nagy, Z. K. & Rielly, C. D. Pharmaceutical crystallisation processes from batch to continuous operation using MSMPR stages: Modelling, design, and control. *Chem. Eng. Process. Process Intensif.* **89**, 41–53 (2015).
76. Parisi, M., Terranova, A. & Chianese, A. Pilot plant investigation on the kinetics of dextrose cooling crystallization. *Ind. Eng. Chem. Res.* **46**, 1277–1285 (2007).
77. Bari, A. H. & Pandit, A. B. Sequential Crystallization Parameter Estimation Method for Determination of Nucleation, Growth, Breakage, and Agglomeration Kinetics. *Ind. Eng. Chem. Res.* **57**, 1370–1379 (2018).

Appendix C Supplementary Information - Isothermal by design: An accelerated approach to the prediction of the crystallisability of slowly nucleating systems

C.1 Crystallisation

Crystallisation occurs in two distinct stages - nucleation and growth. These stages have a large impact on physical and chemical properties of crystals. The crystallisation process route map is given in Figure C.1, highlighting the impact of nucleation and growth on these properties.

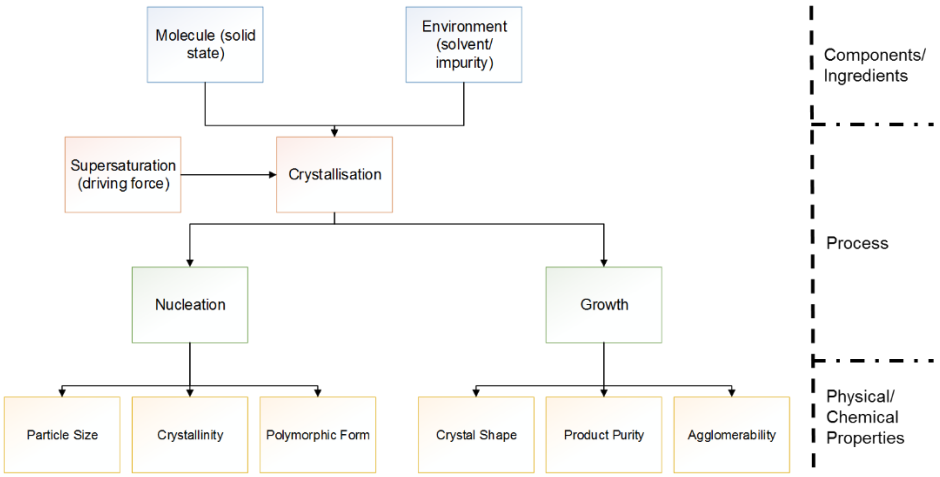


Figure C.1. Crystallisation route map schematic. Adapted with permission from Camacho Corzo et al.[1] Copyright 2017, Springer Science+Business Media B.V.

Nucleation proceeds by either one of two mechanisms: mononuclear or polynuclear nucleation. Polynuclear nucleation occurs when the formation of many nuclei is favourable and can itself be expressed in two different ways, referred to as instantaneous nucleation (IN) and progressive nucleation (PN)[2]. IN is the process in which all crystal nuclei emerge simultaneously and subsequently grow to form crystals[2,3]. In contrast, in PN crystal nuclei continuously form from solution and subsequently grow in the presence of newly forming nuclei[2,4] Nucleation can be further characterised by two more categories, primary and secondary nucleation. Primary nucleation describes the process in which nucleation occurs in the absence of any crystalline matter in the solution, whereas secondary nucleation describes the process of nucleation when seed crystals are introduced into the system. Primary nucleation can be further divided into two categories: heterogeneous and homogeneous nucleation. Heterogeneous nucleation (HEN) is caused when sites, usually suspended particles or impurities in the solution, provide a surface for nucleation and is usually associated with both instantaneous (IN) and progressive (PN)

nucleation, when it is favoured by relatively strong nucleation active sites and relatively weak nucleation active sites, respectively. Homogeneous nucleation (HON) describes spontaneous nucleation and is associated with PN^2.

For over half a century nucleation has been described through classical nucleation theory (CNT). This theory proposes a mechanism whereby, in solution, solute molecules come together to form a spherical nucleus and grow to form a macroscopic crystalline structure. It describes the change in Gibbs free energy (ΔG) associated with the formation of a spherical crystalline nucleus of radius (r) from a supersaturated solution. The overall change in Gibbs free energy due to the formation of a new solid phase from an old phase is a function of the change in surface free energy (ΔG_S) and volume free energy (ΔG_V)[5] and this relationship is expressed as follows:

$$\Delta G = \Delta G_S + \Delta G_V \qquad \text{C.1}$$

$$\Delta G = 4\pi r^2 \gamma + \frac{4}{3}\pi r^3 \Delta G_v \qquad \text{C.2}$$

Where γ is the interfacial tension between the crystal and the surrounding supersaturated fluid and ΔG_v is the free energy per unit volume associated with the phase change.

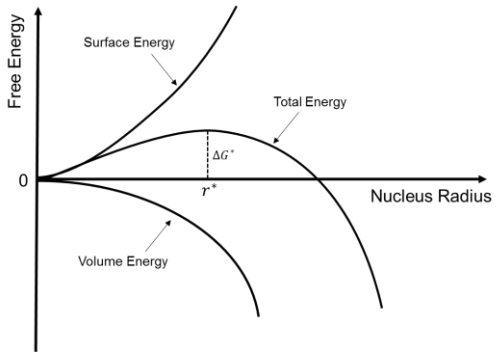


Figure C.2. Free energy schematic for nucleation.

Figure C.2 demonstrates the relationship between surface and volume terms and illustrates that a critical cluster size must be met before growth is favoured, termed the critical nucleus radius (r^*), with a defined number of molecules in the critical nucleus (i^*). The critical free energy required for this to occur can be described by the equation[5]:

$$\Delta G^* = \frac{16\pi\gamma^3 {v_0}^2}{3(kTln\,S)^2} \qquad \text{C.3}$$

Where v_0 is the volume occupied by a solute molecule in a crystal, k is the Boltzmann constant, T is temperature and S is supersaturation.

Furthermore, it is possible to express the rate at which nucleation occurs (J) in an Arrhenius reaction rate equation, as a function of ΔG^*:[5]

$$J = A \exp\left[-\frac{16\pi\gamma^3 {v_0}^2}{3k^3T^3(ln\,S)^2}\right] \quad \text{C.4}$$

Equation S4 indicates that there are three main contributors to the rate of nucleation: temperature, degree of supersaturation and interfacial tension.

C.2 Experimental apparatus

The Technobis Crystal 16® system[6], Figure C.3, was used for all experimental studies. It is made up of sixteen wells, which can hold 1.5 ml disposable glass vials. These are split into four blocks (each has four wells) that are independently temperature controlled to allow different temperature profiles to be set simultaneously, with the use of Peltier elements and an external Julabo bath. The system can be run between -15 °C to 150 °C and condensation at cooler temperatures is stopped by a dry air purge system. Transmission data is collected by a laser passing through the vials, providing information about the cloud and clear points of up to 16 solutions simultaneously.

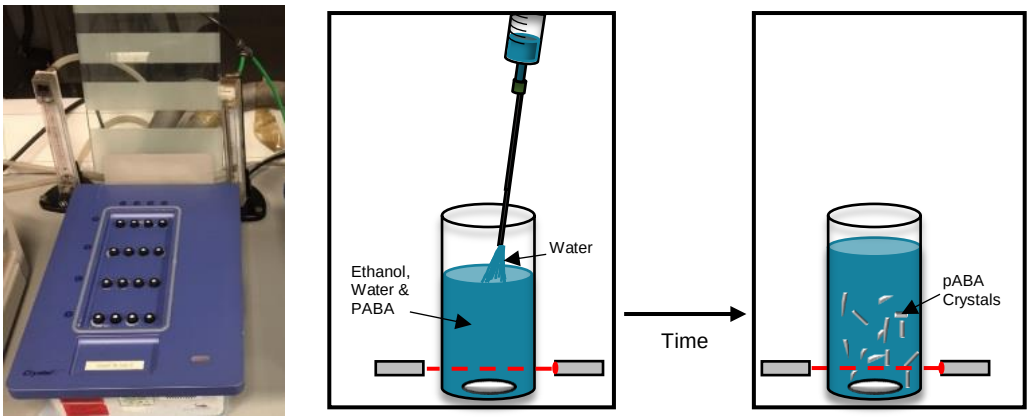


Figure C.3. Technobis Crystal 16 system with vials inserted into each well and a schematic of the process undertaken for the IbD experiments with antisolvent addition to solution vials, inducing crystallisation, as well as transmission detection technique.

C.3 Detailed experimental procedure

C.3.1 Solubility determination

All solutions were prepared at a minimum of four solution concentrations, with the concentrations used dependent upon the solvent composition (e.g. 140, 160, 180 and 200 g kg^{-1} for pure EtOH, 60, 90, 120 and 150 g kg^{-1} for 60:40 wt% EtOH:H_2O, and 5, 7, 9 and 11 g kg^{-1} for pure H_2O). Eleven solvent compositions ranging in 10 wt% increments of EtOH from pure EtOH to pure H_2O were used for the solubility analysis. pABA, EtOH and H_2O were weighed into a glass beaker containing a magnetic stirrer bar, on a balance with ±0.1 mg accuracy, with evaporation of solvents limited by covering the beaker with Parafilm. The solutions were subsequently placed on a hot plate and heated to 333 K at 300 rpm for 1 hour to ensure complete dissolution of pABA and ensure total homogenisation of the solution. 1 ml of solution was then transferred to 1.5ml disposable glass vials for use in the experimental apparatus, which contained 7 mm x 2 mm magnetic stirrers, using a Fisherbrand 100-1000 µl micropipette with pre-heated pipette tips (303 K) to prevent unwanted crystallisation. The 1 ml solutions were subject to different cooling and heating cycles between 333 K and 278 K at set rates (q; where q = 0.3, 0.5, 0.7 and 1 K min^{-1}), while stirring at 600 rpm.

C.3.2 Antisolvent experiments and calorimetry

All solutions were prepared to ensure a saturation temperature of 293 K for a mixed solvent solution of 70 wt% EtOH: 30 wt% H_2O EtOH:H_2O and pABA. The solutions were weighed and prepared in the same way previously described. Solution volumes placed into the glass vials ranged from 0.80 ml to 0.20 ml, in 0.05 ml increments. All solution volumes were made up to 1 ml after antisolvent addition, meaning, for example, for a vial containing 0.80 ml of solution, 0.20 ml antisolvent was added.

In order to create an IbD approach, calibrations based upon solution calorimetry were performed. For this, a minimum of 5 initial volumes were selected (0.80 ml, 0.65 ml, 0.50 ml, 0.30 ml and 0.20 ml) for the calibration at a selected temperature (ranging from 293 K to 301 K in 2 K increments), providing enough points for an accurate calibration over the entire range of solution volumes used. Four different antisolvent temperatures were selected, e.g. for a 297 K isothermal solution temperature, antisolvent temperatures of 293 K, 287 K, 281 K and 274 K were used for the calibrations. Solutions were held at constant temperature, stirring at 900 rpm, with the antisolvent held at constant temperature, stirring at 700 rpm. The calibrations were performed by placing a digital thermometer into the solution vials and then withdrawing

the full antisolvent volume with a 1 ml syringe with attached needle, and transferring the contents into the solution vial rapidly, inducing high mixing. The speed of addition meant that the antisolvent was added almost instantaneously, leading to this procedure being described as 'instant addition'. The temperature of the solution was recorded after each addition by taking the value of the highest recorded temperature on the digital thermometer, within 1 second after antisolvent addition. Each calibration was repeated four times. Plots of selected antisolvent temperatures against the temperature of solutions after antisolvent addition were made and linear regressions were plotted with extrapolations to the desired solution temperature indicating the required antisolvent temperature to maintain solution temperature upon addition. This was then used to determine which antisolvent temperature should be used for each induction time experiment at that temperature. This was subsequently tested to ensure that the calibrations were accurate and that the solution temperatures were maintained upon addition of the antisolvent at the determined calibration temperatures. It was observed that deviations in solution temperature upon addition of H2O, over a range of four repeats, were at most ± 0.2 K, with solutions quickly returning to set temperatures in a manner of a few seconds. Therefore, this effect was deemed to be negligible.

C.3.3 Isothermal antisolvent measurements

After the calorimetry calibrations were completed, the IbD experiments were performed. The same procedure was undertaken as described for the calibrations leading to an 'instant addition' methodology, however, all selected solution volumes were used, antisolvent temperatures were selected based upon the calibrations and no digital thermometer was placed in the vials, ensuring no effect on nucleation by introducing another surface on which to crystallise upon. Sixteen repeats were performed for each initial solution volume used at each selected temperature.

The induction time to nucleation was determined from the collected transmission data, which ranged from 100 % for a homogeneous and 0 % for a completely turbid solution. The crystallisation point was taken when the light transmittance dropped from 100 % to just below 95 % for all measurements, to ensure that a stabilisation period for the transmittance of light had taken place and it was crystallisation that had been detected.

The isothermal transmittance data was used to calculate the time between when the antisolvent was added to the vials and when nucleation had occurred, giving the induction time. The point at which antisolvent was added was also determined by the transmission data. For initial solution volumes of 0.5 - 0.8 ml, a sharp decrease in transmission occurred upon

antisolvent addition, followed by a rapid increased transmittance after mixing. For initial solution volumes of between 0.3 ml - 0.45 ml, the opposite occurred and there was an increase in transmittance associated with antisolvent addition. This was due to the low volume initially in the vials, which were too low to get a regular transmission profile. For these solutions the point of antisolvent addition was taken as the point at which transmission drastically increased. Example transmission plots are provided (Figure C.4).

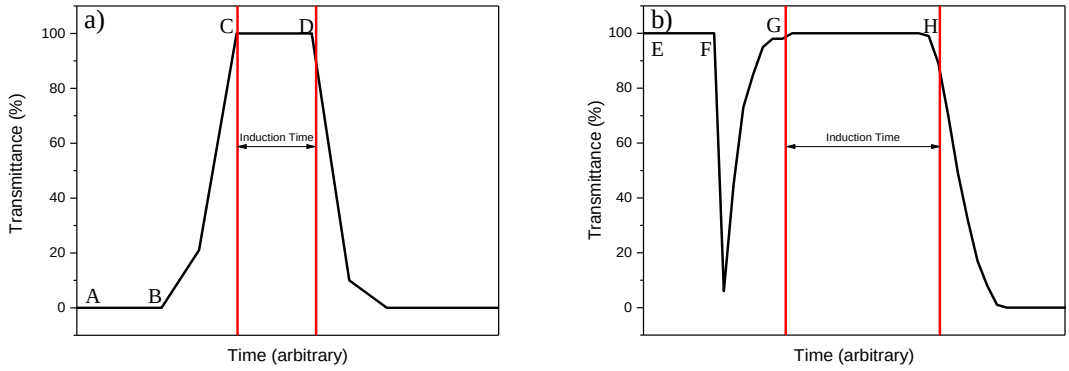


Figure C.4. Transmission profiles as a function of time. a) Vial initially containing 0.35 ml solution. A-B shows transmission profile for undersaturated solution, B indicates time of antisolvent addition, C indicates fully mixed saturated solution, C-D shows transmission profile of supersaturated solution and D indicates onset of crystallisation. b) Vial initially containing 0.55 ml solution. E-F shows transmission profile for undersaturated solution, F indicates time of antisolvent addition, G indicates fully mixed saturated solution, G-H shows transmission profile of supersaturated solution and H indicates onset of crystallisation.

C.4 Equipment Calibration

In order to ensure accurate temperature control during isothermal experiments, calibrations were performed on the Technobis Crystal 16® system. Four vials containing 1 ml of water were placed in each block, which was programmed to a specific temperature in the range of 18 °C to 25 °C and was held at this temperature whilst a thermocouple was used to measure the solvent temperature with ±0.5 °C. The average of the four temperature readings obtained for each block was plotted against the set temperature and fit with a linear regression. The equation of the linear regression was used to ensure that the temperatures of each block could be set to specific values to maintain solutions at desired temperatures. An example calibration performed is shown in Figure C.5.

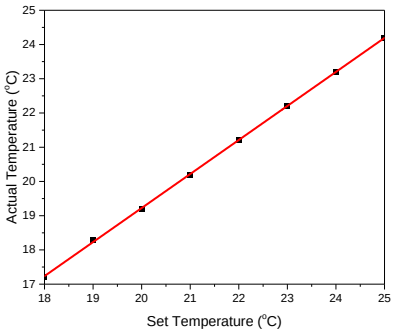


Figure C.5. Temperature calibration for the Technobis Crystal 16® system. Temperature at which the system was programmed is plotted against the actual temperature of the solvent as measured by a calibrated thermocouple.

C.5 Solubility determination and data

Table C.1 displays the full list of average crystallisation (T_c) and dissolution (T_{diss}) temperatures obtained from solubility analysis over the full range of solution concentrations and compositions, alongside the equilibrium saturation temperatures (T_e) calculated from the data. std stands for standard deviation.

EtOH							EtOH: H_2O 9:1						
Conc. (g Solvent / g pABA)	cooling rate (°C/min)	T_c (°C)	std	T_{diss} (°C)	std	T_e (°C)	Conc. (g Solvent / g pABA)	cooling rate (°C/min)	T_c (°C)	std	T_{diss} (°C)	std	T_e (°C)
0.14	0.3	6.5	2.2	20.9	0.1	20.0	0.14	0.3	7.3	2.0	17.5	0.9	16.7
	0.5	5.0	3.6	22.6	0.2			0.5	6.4	0.7	18.0	0.8	
	0.7	2.5	1.8	21.5	0.2			0.7	5.5	0.0	18.1	0.1	
	1.0	0.8	3.5	23.9	0.2			1.0	4.8	0.2	19.2	1.1	
0.16	0.3	15.2	1.7	29.3	0.1	28.4	0.18	0.3	19.6	4.4	30.7	0.7	30.4
	0.5	12.4	4.5	30.9	0.2			0.5	16.5	0.2	30.5	0.7	
	0.7	8.7	2.7	30.1	0.1			0.7	14.4	0.6	30.9	0.8	
	1.0	7.0	4.7	32.1	0.3			1.0	12.1	0.2	31.0	0.8	
0.18	0.3	34.2	0.5	45.8	0.1	45.0	0.22	0.3	30.4	4.3	39.1	2.3	38.7
	0.5	32.0	1.5	47.5	0.2			0.5	27.0	3.3	40.2	1.0	
	0.7	29.7	1.9	46.4	0.4			0.7	25.6	2.5	40.9	0.7	
	1.0	27.7	7.0	48.5	0.2			1.0	21.4	4.6	41.0	0.8	
0.20	0.3	44.3	1.6	51.8	1.4	51.1	0.26	0.3	39.0	3.4	48.8	0.5	48.3
	0.5	39.0	2.3	53.5	0.1			0.5	36.1	2.6	48.8	0.5	
	0.7	35.1	3.2	52.2	0.1			0.7	33.0	3.1	49.5	1.2	
	1.0	31.0	1.4	54.4	0.1			1.0	28.5	9.4	49.6	1.2	

EtOH: H_2O 8:2							EtOH: H_2O 7:3						
Conc. (g Solvent / g pABA)	cooling rate (°C/min)	T_c (°C)	std	T_{diss} (°C)	std	T_e (°C)	Conc. (g Solvent / g pABA)	cooling rate (°C/min)	T_c (°C)	std	T_{diss} (°C)	std	T_e (°C)
0.14	0.3	8.8	1.1	15.2	0.2	15.2	0.16	0.3	16.9	2.7	26.8	0.2	26.0
	0.5	6.6	0.8	16.3	0.1			0.5	15.5	2.2	26.9	0.2	
	0.7	5.6	1.0	16.3	0.2			0.7	13.9	1.9	27.5	0.2	
	1.0	4.9	0.0	16.4	0.1			1.0	12.6	1.6	28.3	0.2	
0.18	0.3	19.4	2.5	27.5	0.2	27.1	0.20	0.3	26.3	1.9	35.7	0.1	35.0
	0.5	16.1	4.3	28.1	0.1			0.5	25.0	1.8	35.8	0.1	
	0.7	13.8	4.1	28.5	0.1			0.7	24.0	1.9	36.2	0.2	
	1.0	10.0	0.9	28.6	0.0			1.0	23.2	2.6	36.9	0.2	
0.22	0.3	28.1	2.8	36.4	0.2	36.2	0.24	0.3	34.8	1.8	42.8	0.2	42.1
	0.5	25.7	4.7	37.0	0.1			0.5	31.3	2.3	42.8	0.2	
	0.7	23.5	2.6	37.5	0.2			0.7	27.5	1.2	44.2	1.4	
	1.0	21.0	3.5	37.5	0.1			1.0	24.0	1.0	44.0	0.1	
0.26	0.3	36.1	1.9	43.9	0.2	43.4	0.28	0.3	41.3	0.3	49.1	0.3	48.5
	0.5	33.5	2.3	43.8	0.3			0.5	40.0	0.2	49.3	0.2	
	0.7	28.3	4.5	45.2	1.3			0.7	39.0	0.1	49.8	0.1	
	1.0	25.5	2.2	44.8	0.0			1.0	38.0	0.1	50.3	0.1	
EtOH: H_2O 6:4							EtOH: H_2O 5:5						
Conc. (g Solvent / g pABA)	cooling rate (°C/min)	T_c (°C)	std	T_{diss} (°C)	std	T_e (°C)	Conc. (g Solvent / g pABA)	cooling rate (°C/min)	T_c (°C)	std	T_{diss} (°C)	std	T_e (°C)
0.12	0.3	20.7	1.5	29.0	0.0	22.0	0.10	0.3	13.3	2.4	28.1	0.1	27.4
	0.5	17.9	2.8	28.9	0.1			0.5	10.4	1.0	28.5	0.1	
	0.7	15.2	4.4	28.7	0.1			0.7	9.3	1.4	28.4	0.2	
	1.0	12.5	1.5	29.9	0.3			1.0	8.3	1.1	29.6	0.2	
0.16	0.3	31.5	4.2	37.4	0.1	32.1	0.14	0.3	29.1	2.4	38.7	0.2	38.1
	0.5	29.0	1.4	37.6	0.2			0.5	27.5	1.1	38.8	0.1	

	0.7	26.8	4.2	36.7	4.3			0.7	26.7	0.2	39.2	0.2	
	1.0	25.5	0.8	38.4	0.1			1.0	25.8	0.4	39.8	0.2	
0.20	0.3	38.7	1.2	45.2	0.1	40.5	0.18	0.3	37.1	1.2	47.5	0.2	48.9
	0.5	36.0	2.6	45.2	0.1			0.5	35.4	3.1	47.4	0.1	
	0.7	34.4	1.7	45.4	0.1			0.7	33.7	2.4	47.9	0.3	
	1.0	31.7	2.2	46.1	0.2			1.0	32.4	4.5	48.4	0.1	
0.24	0.3	43.0	1.5	50.9	0.2	47.5	0.20	0.3	44.2	0.9	54.4	0.1	53.4
	0.5	38.0	2.1	51.1	0.2			0.5	42.1	1.0	54.5	0.2	
	0.7	33.0	4.9	49.6	0.2			0.7	38.7	2.1	54.5	0.3	
	1.0	29.0	4.9	52.0	0.1			1.0	35.3	1.7	56.1	0.0	
EtOH: H_2O 4:6							EtOH: H_2O 3:7						
Conc. (g Solvent / g pABA)	cooling rate (°C/min)	T_c (°C)	std	T_{diss} (°C)	std	T_e (°C)	Conc. (g Solvent / g pABA)	cooling rate (°C/min)	T_c (°C)	std	T_{diss} (°C)	std	T_e (°C)
0.06	0.3	13.2	2.4	23.1	0.1	21.0	0.06	0.3	30.7	1.6	41.2	0.2	40.8
	0.5	9.6	1.5	23.7	4.1			0.5	27.7	1.9	40.5	0.0	
	0.7	8.0	0.0	25.7	0.1			0.7	26.5	0.7	42.2	0.2	
	1.0	5.0	0.1	25.2	0.1			1.0	24.6	0.6	41.4	0.1	
0.09	0.3	27.5	2.4	34.2	0.1	33.1	0.07	0.3	33.7	1.7	44.8	0.1	44.3
	0.5	23.3	3.2	34.4	0.0			0.5	32.0	1.5	44.4	0.1	
	0.7	21.0	1.9	36.6	0.1			0.7	31.0	1.2	45.6	0.1	
	1.0	16.4	2.7	36.3	0.1			1.0	30.3	1.2	45.4	0.2	
0.12	0.3	34.1	2.2	42.4	0.1	41.3	0.08	0.3	38.1	1.7	47.8	0.1	47.4
	0.5	32.5	0.7	42.6	0.1			0.5	35.4	4.4	47.1	0.1	
	0.7	31.0	1.4	45.4	0.3			0.7	33.2	2.5	48.6	0.1	
	1.0	30.6	0.8	44.8	0.1			1.0	31.7	2.1	47.9	0.1	
0.15	0.3	42.8	0.9	51.2	0.1	50.1	0.09	0.3	41.0	1.3	51.1	0.2	50.6
	0.5	38.5	0.4	51.5	0.2			0.5	40.0	0.8	50.9	0.1	
	0.7	36.0	1.6	54.1	0.1			0.7	39.0	0.8	52.0	0.1	

	1.0	33.1	1.4	53.7	0.1	
EtOH: H_2O 2:8						
Conc. (g Solvent / g pABA)	cooling rate (°C/min)	T_c (°C)	std	T_{diss} (°C)	std	T_e (°C)
0.003	0.3	32.5	1.5	42.1	0.1	41.7
	0.5	31.3	1.0	41.7	0.1	
	0.7	31.0	1.5	42.8	0.1	
	1.0	30.0	1.7	42.5	0.1	
0.004	0.3	36.2	1.9	47.0	0.3	46.7
	0.5	34.5	1.4	46.2	0.2	
	0.7	33.4	2.5	47.3	0.1	
	1.0	31.4	1.7	46.8	0.1	
0.005	0.3	49.0	0.6	52.9	0.3	53.0
	0.5	45.4	3.3	53.9	0.2	
	0.7	44.5	2.0	53.2	0.2	
	1.0	40.5	2.7	53.5	0.1	
0.006	0.3	49.1	1.3	56.3	0.2	56.1
	0.5	47.2	0.8	56.0	0.1	
	0.7	46.3	1.9	56.9	0.1	
	1.0	44.4	0.6	56.3	0.3	
H_2O						
Conc. (g Solvent / g pABA)	cooling rate (°C/min)	T_c (°C)	std	T_{diss} (°C)	std	T_e (°C)
0.005	0.3	18.0	0.6	28.3	0.3	27.4
	0.5	17.0	0.7	28.0	0.1	
	0.7	16.5	0.5	29.4	1.0	
	1.0	16.0	0.3	29.5	0.6	
0.007	0.3	27.6	0.7	35.3	0.9	35.1

	1.0	37.8	1.2	51.9	0.1	
EtOH: H_2O 1:9						
Conc. (g Solvent / g pABA)	cooling rate (°C/min)	T_c (°C)	std	T_{diss} (°C)	std	T_e (°C)
0.005	0.3	11.5	1.3	19.0	0.8	19.1
	0.5	10.4	0.9	18.7	0.2	
	0.7	9.6	1.1	18.7	0.2	
	1.0	8.8	0.9	18.5	0.2	
0.01	0.3	27.0	0.3	33.9	0.3	33.8
	0.5	25.5	1.4	33.2	0.2	
	0.7	24.7	0.9	33.2	0.1	
	1.0	23.7	1.2	33.3	0.3	
0.015	0.3	35.4	0.9	42.7	0.1	42.8
	0.5	34.4	1.7	42.1	0.4	
	0.7	33.4	1.2	41.9	0.2	
	1.0	32.5	0.9	41.8	0.1	
0.002	0.3	43.3	0.7	48.8	0.0	49.2
	0.5	40.4	1.1	48.6	0.2	
	0.7	39.4	0.5	48.3	1.0	
	1.0	38.3	0.5	48.0	0.2	

	0.5	27.0	0.9	36.3	0.6	
	0.7	26.4	0.9	36.0	0.4	
	1.0	25.7	0.5	36.7	0.6	
0.009	0.3	34.5	0.8	42.3	0.6	42.0
	0.5	33.4	0.8	42.1	0.4	
	0.7	32.9	0.8	41.5	1.1	
	1.0	32.1	0.7	42.5	1.0	
0.011	0.3	41.4	2.1	48.0	0.5	48.0
	0.5	40.6	1.8	48.1	0.7	
	0.7	39.5	0.7	46.6	0.2	
	1.0	38.5	0.6	47.9	0.3	

C.6 Antisolvent Temperature Calibrations

Figure C.6 display antisolvent addition temperature calibrations performed for different initial solution volumes at different antisolvent addition temperatures. The increased effect antisolvent temperature has when more is added can be seen by the slopes of the linear regressions plotted.

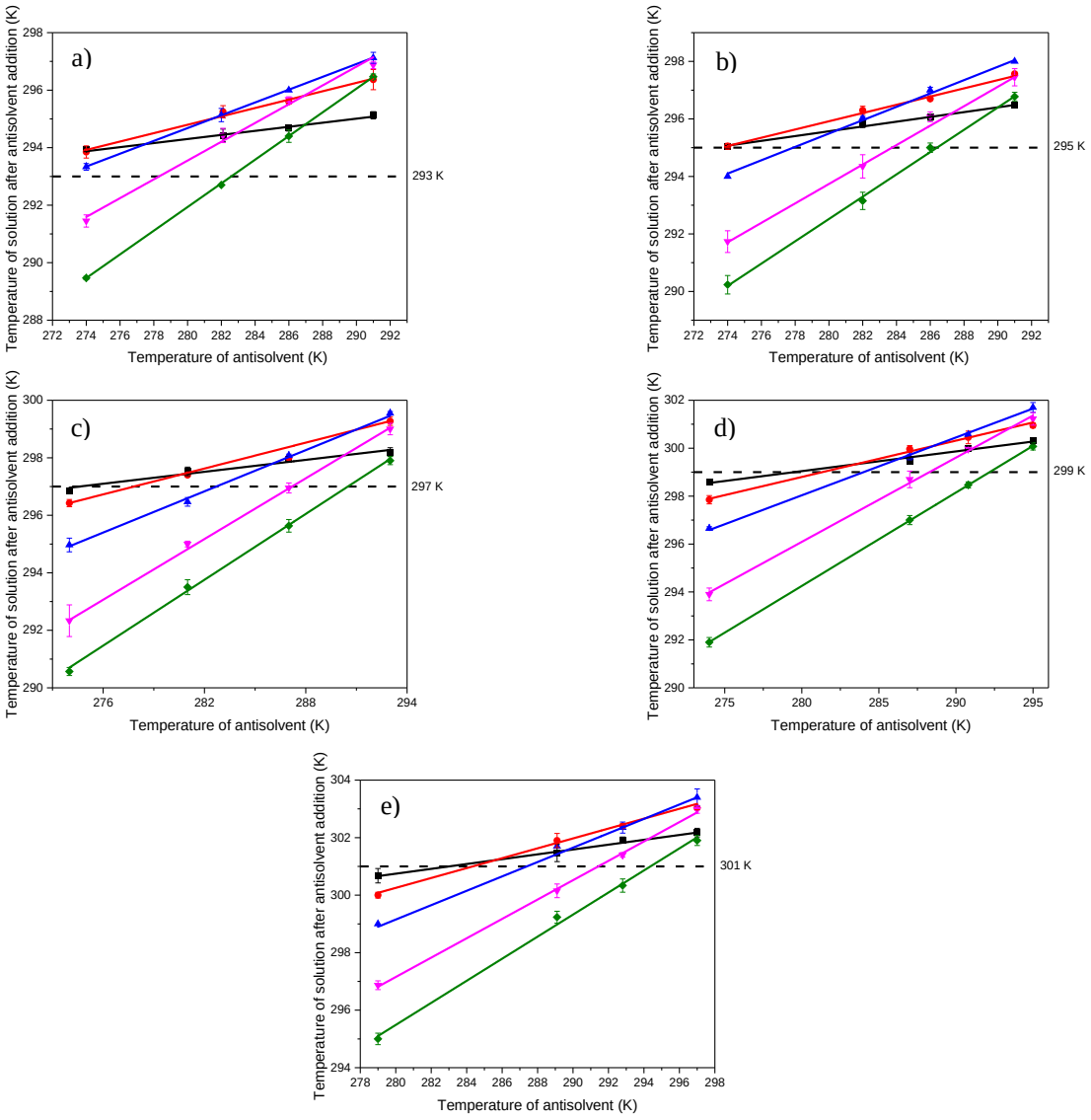
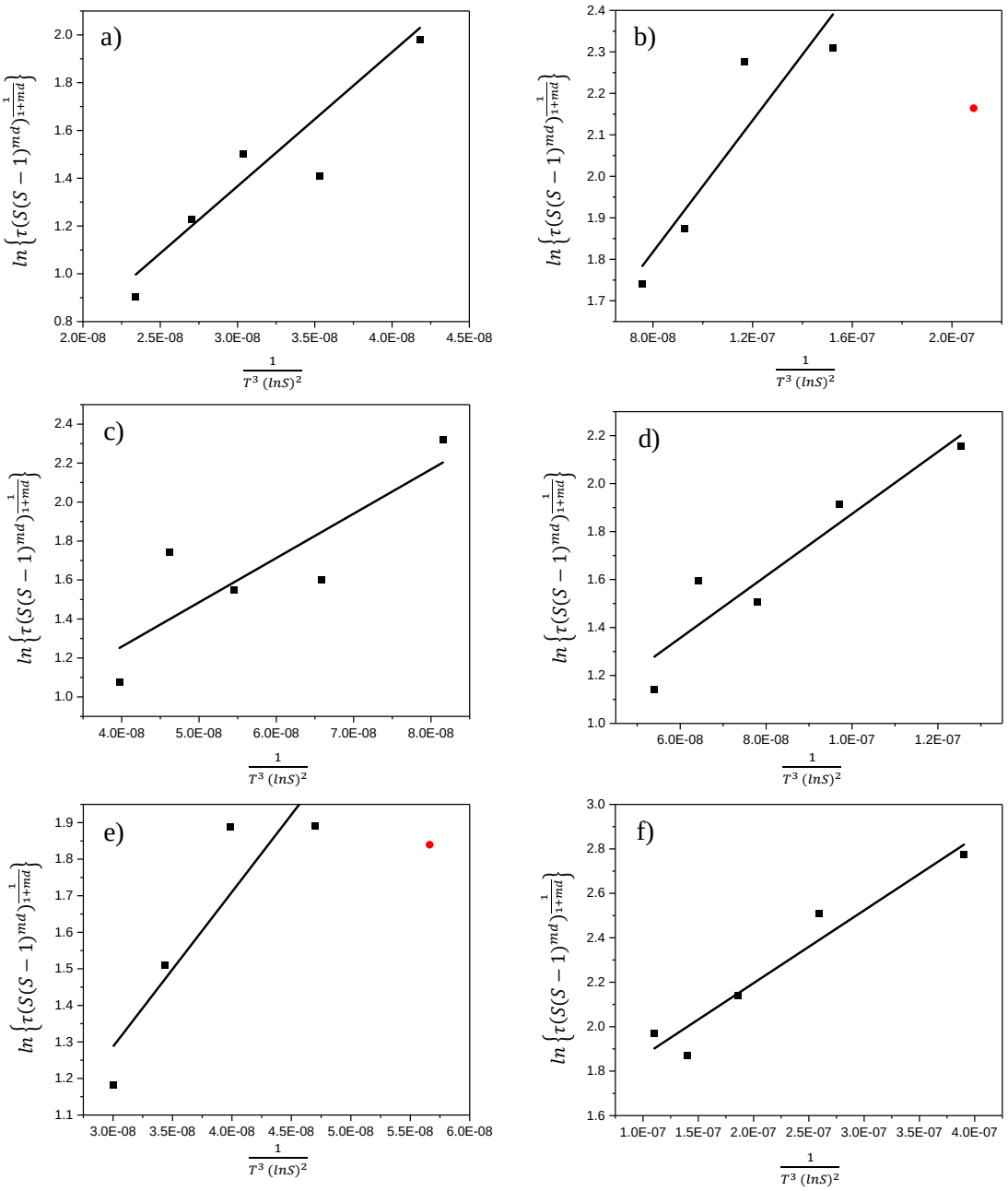


Figure C.6. Effect antisolvent temperature had on solutions of pABA in EtOH:H2O mixed solvent held at constant temperature. Effect of antisolvent temperature on 0.2 ml initial solution (♦), 0.3 ml initial solution (▼), 0.5 ml initial solution (▲), 0.65 ml initial solution (●) and 0.8 ml initial solution (■) shown by the gradients of the linear relationships. a) 293 K, b) 295 K, c) 297 K, d) 299 K, e) 301 K.

C.7 Isothermal analysis

Figure C.7 displays plots used to determine γ_{eff} at each individual composition used, over the entire range of experimental temperatures. The slopes of the linear regressions, equal to $\frac{16\pi v_0^2 \gamma_{eff}^3}{3(1+md)k^3}$, were used to calculate γ_{eff}.



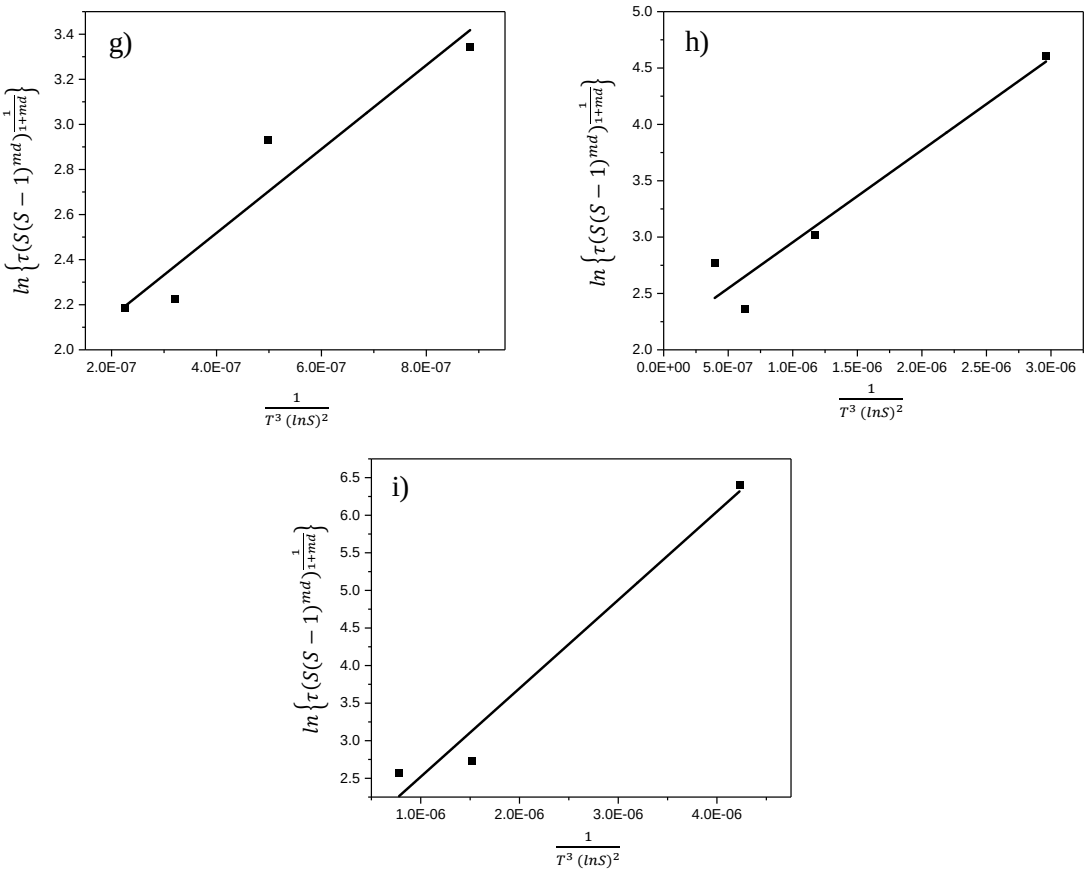


Figure C.7. Induction time data to determine linear slope values for calculation of $\boldsymbol{\gamma_{eff}}$ from data obtained. a) 34.4 g pABA kg^{-1} solvent mixture, b) 40.7 g pABA kg^{-1} solvent mixture, c) 47.0 g pABA kg^{-1} solvent mixture, d) 53.6 g pABA kg^{-1} solvent mixture, e) 60.3 g pABA kg^{-1} solvent mixture, f) 67.2 g pABA kg^{-1} solvent mixture, g) 74.2 g pABA kg^{-1} solvent mixture, h) 81.4 g pABA kg^{-1} solvent mixture, i) 88.9 g pABA kg^{-1} solvent mixture. Red circles in a) and d) represent outlier data not used in $\boldsymbol{\gamma_{eff}}$ calculation.

C.8 Nucleation mechanism change

Plots to determine whether a mechanistic change from HEN to HON over the supersaturation range used for each experimental temperature used are displayed in Figure C.8.

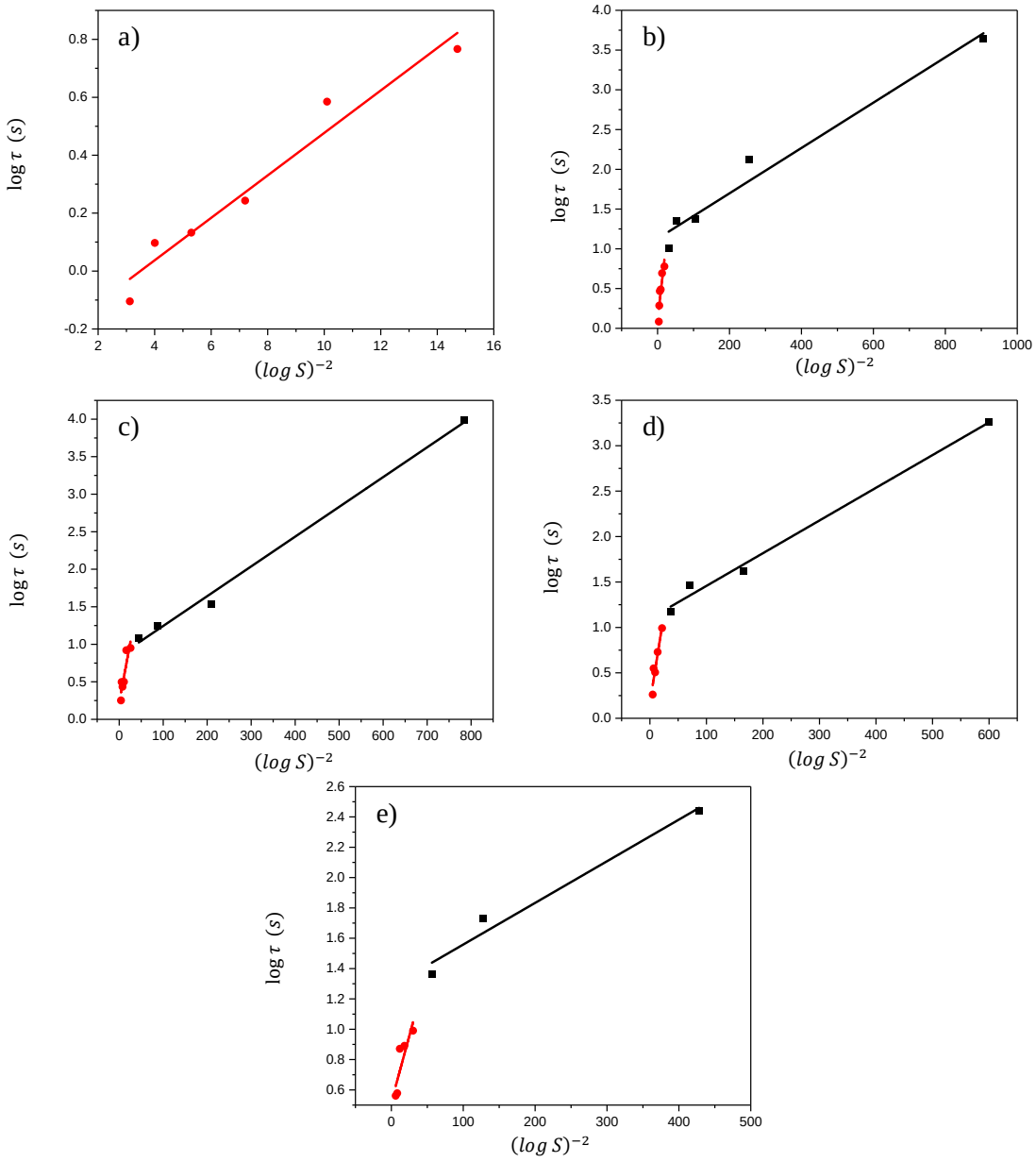


Figure C.8. Induction time vs. supersaturation for single temperature and multiple composition solutions of pABA in EtOH:H_2O mixtures. a) 293 K, b) 295 K, c) 297 K, d) 299 K, e) 301 K. (●) region of homogeneous nucleation. (■) region of heterogeneous nucleation.

The finding of a nucleation mechanism change is of significant importance, especially in industry, as the mechanism by which nucleation takes place can have a large impact on the product formed under operation and as such, different operating conditions could mean that there is a large change in batch-to-catch variance of products, effecting final product quality.

Industrial crystallisations are usually performed in the HEN region of crystallisation, with encrustation being a large negative outcome of large scale operation[7–9]. If it is known that a process could be run in the HON region, then these issues could be overcome.

C.9 Critical nucleus

Table C.2 displays the values of r^* and i^* calculated under the IbD methodology for all compositions studied. Initial Volume represents the initial solution volume present in the vial before antisolvent addition to make volume up to 1 ml.

Initial Volume (ml)	***S***	r^* **(nm)**	i^* **(molecules)**	**Initial Volume (ml)**	***S***	r^* **(nm)**	i^* **(molecules)**
0.3	3.68	0.53	3.70	**0.35**	3.16	0.56	4.42
0.3	3.36	0.56	4.50	**0.35**	2.90	0.60	5.45
0.3	3.07	0.60	5.58	**0.35**	2.66	0.65	6.88
0.3	2.80	0.65	7.07	**0.35**	2.44	0.71	8.91
0.3	2.55	0.71	9.18	**0.35**	2.24	0.78	11.89
0.4	2.72	0.52	3.61	**0.45**	2.36	0.50	3.25
0.4	2.51	0.57	4.57	**0.45**	2.18	0.55	4.25
0.4	2.31	0.62	5.93	**0.45**	2.01	0.61	5.75
0.4	2.12	0.68	7.94	**0.45**	1.86	0.68	8.09
0.4	1.96	0.76	11.05	**0.45**	1.72	0.78	11.97
0.5	2.06	0.51	3.31	**0.55**	1.82	0.46	2.40
0.5	1.91	0.56	4.53	**0.55**	1.69	0.52	3.48
0.5	1.77	0.63	6.46	**0.55**	1.57	0.60	5.35
0.5	1.64	0.73	9.73	**0.55**	1.46	0.71	8.92
0.5	1.52	0.85	15.77	**0.55**	1.36	0.87	16.66
0.6	1.51	0.54	4.04	**0.65**	1.37	0.55	4.11
0.6	1.41	0.65	6.93	**0.65**	1.28	0.69	8.33
0.6	1.32	0.81	13.49	**0.65**	1.20	0.95	21.37
0.6	1.23	1.08	32.25	**0.65**	1.12	1.51	86.91
0.7	1.25	0.84	15.20				
0.7	1.17	1.18	41.55				

0.7	1.10	1.98	195.46

C.10 References

1. Camacho Corzo, D. ., Ma, C. ., Ramachandran, V., Mahmud, T. & Roberts, K. . Crystallisation Route Map. in *Engineering Crystallography: From Molecule to Crystal to Functional Form. NATO Science for Peace and Security Series A: Chemistry and Biology* (eds. Roberts, K. ., Docherty, R. & Tamura, R.) 179–213 (Springer, 2017).
2. Kashchiev, D. *Nucleation*. (Butterworth-Heinemann, 2000).
3. Kashchiev, D., Borissova, A., Hammond, R. B. & Roberts, K. J. Dependence of the critical undercooling for crystallization on the cooling rate. *J. Phys. Chem. B* **114**, 5441–5446 (2010).
4. Kashchiev, D., Borissova, A., Hammond, R. B. & Roberts, K. J. Effect of cooling rate on the critical undercooling for crystallization. *J. Cryst. Growth* **312**, 698–704 (2010).
5. Mullin, J. W. *Crystallization*. (Butterworth-Heinemann, 2001).
6. Technobis. Crystal16. (2020). Available at: https://www.crystallizationsystems.com/crystal16.
7. Liang, K. *et al.* An examination into the effect of stirrer material and agitation rate on the nucleation of L-glutamic acid batch crystallized from supersaturated aqueous solutions. *Cryst. Growth Des.* **4**, 1039–1044 (2004).
8. Liang, K. *et al.* Examination of the Process Scale Dependence of l -Glutamic Acid Batch Crystallized from Supersaturated Aqueous Solutions in Relation to Reactor Hydrodynamics. *Ind. Eng. Chem. Res.* **43**, 1227–1234 (2004).
9. Al-Marri, M., Mahmud, T. & Roberts, K. J. A flexible heat transfer model for simulating the performance of batch cooling crystallization as a function of process scale size. in *Proceedings of the 17th International Symposium on Industrial Crystallization* (eds. Ulrich, J., Jansens, P. & Roelands, M.) 613–620 (Vol. 2, 2008).

Appendix D Supplementary Information: Influence of Solution Chemistry on the Solubility, Crystallisability and Nucleation Behaviour of Eicosane in Toluene/Acetone Mixed-Solvents

D.1 Abstract

This appendix contains supplementary information relating to Chapter 3. Average crystallisation and dissolution temperatures from 5 repeats of measurements are presented in Section D.2, over the full mixed solvent compositional range studied, as a function of heating cycle rate and solution concentration. The full range of data collected for the solubility and crystallisability of the solutions, calculated solution thermodynamic parameters and determined nucleation mechanisms are provided in Section D.3, D.4 and D.5, respectively. Atomic partial charges of eicosane, toluene and acetone used in grid-based molecular modelling studies are presented in section D.6. Predicted solvation sites of a single eicosane molecule solvated with single toluene and acetone molecules, at different energy cut-offs, are provided in Section D.7, alongside a description of the effect of calculating the intermolecular interactions of toluene with eicosane prior to acetone interactions with eicosane on the obtained results.

D.2 Crystallisation and Dissolution Temperatures

Average crystallisation (Tc) and dissolution (Tdiss) temperatures for eicosane in toluene/acetone mixed solvent solutions at each cooling/heating rate (q) and each solution concentration, as a function of mol fraction of acetone (y), are shown in Table D.1. The full compositional range from pure toluene to pure acetone are studied, with 11 compositions studied in total. The standard deviation (std) of the data is also displayed from 5 repeats of each crystallisation and dissolution experiment. The data provided for each solvent used highlights the influence that the solute composition, solute concentration and cooling rate has upon the crystallisation behaviour of eicosane in toluene/acetone mixed solvent solution.

Table D.1. Average crystallisation (Tc) and dissolution (Tdiss) temperatures at different heating cycle rates (q) as a function of solvent composition and solution concentration. The standard deviations (SD) from 5 repeats of Tc and Tdiss are presented.

q (°C min^{-1})	**Tc (°C)**	**SD**	**Tdiss (°C)**	**SD**	**Tc (°C)**	**SD**	**Tdiss (°C)**	**SD**	**Tc (°C)**	**SD**	**Tdiss (°C)**	**SD**	**Tc (°C)**	**SD**	**Tdiss (°C)**	**SD**
y = 0																
	250 g L^{-1}				**300 g L^{-1}**				**350 g L^{-1}**				**450 g L^{-1}**			
0.25	9.74	0.25	11.96	0.11	11.36	0.09	13.27	0.19	12.58	0.12	14.62	0.15	14.75	0.09	16.40	0.37
1	9.22	0.20	13.01	0.54	10.74	0.30	15.05	0.38	12.03	0.09	15.48	0.65	14.19	0.18	18.06	0.18
2	8.27	0.26	15.08	0.49	9.75	0.19	16.83	0.30	11.22	0.22	18.51	0.53	13.28	0.16	20.44	0.27
3.2	7.57	0.27	17.26	0.53	8.97	0.16	19.52	0.25	10.34	0.12	20.44	0.62	12.68	0.11		
	550 g L^{-1}				**650 g L^{-1}**				**750 g L^{-1}**				**850 g L^{-1}**			
0.25	16.45	0.16	18.13	0.34	17.52	0.11	18.90	0.29	18.48	0.16	20.54	0.11	19.54	0.19	21.18	0.28
1	15.66	0.23	20.52	0.38	16.81	0.19	22.55	0.15	17.77	0.18	22.26	0.23	18.77	0.18	23.92	0.32
2	15.08	0.16	23.39	0.57	15.90	0.30	24.91	0.15	16.85	0.17	25.73	0.08	18.22	0.12	26.74	0.15
3.2	14.04	0.24	25.96	0.05	15.70	0.17	26.80	0.28	16.14	0.16	29.34	0.15	17.12	0.18	30.47	0.08
y = 0.14																
	200 g L^{-1}				**300 g L^{-1}**				**400 g L^{-1}**				**500 g L^{-1}**			
0.25	10.38	0.15	12.42	0.09	13.50	0.09	14.78	0.17	15.49	0.05	16.90	0.25	16.28	0.26	18.25	0.24
1	9.66	0.06	12.92	0.43	12.64	0.24	16.38	0.38	14.60	0.15	18.61	0.23	16.20	0.13	20.37	0.49
2	8.68	0.16	14.24	0.20	12.02	0.10	18.14	0.49	14.24	0.17	20.13	0.28	15.70	0.13	21.73	0.25
3.2	8.37	0.15	16.17	0.28	11.51	0.12	20.13	0.57	13.52	0.08	22.72	0.56	14.84	0.16	24.91	0.20
	700 g L^{-1}				**800 g L^{-1}**											
0.25	18.85	0.13	20.74	0.44	20.08	0.12	21.59	0.18								
1	18.53	0.21	23.01	0.30	19.37	0.21	24.13	0.46								
2	17.89	0.21	26.29	0.08	18.53	0.11	28.01	0.33								
3.2	16.73	0.28	30.33	0.21	17.32	0.22	31.59	0.15								
y = 0.26																

	200 g L^{-1}				300 g L^{-1}				400 g L^{-1}				500 g L^{-1}			
0.25	12.69	0.24	14.70	0.08	15.35	0.14	16.99	0.28	17.17	0.13	18.46	0.16	18.62	0.11	19.75	0.20
1	11.98	0.21	16.31	0.38	14.72	0.12	18.75	0.54	16.28	0.15	21.11	0.48	17.85	0.18	21.84	0.40
2	11.21	0.13	18.02	0.38	13.97	0.19	20.30	0.48	15.80	0.17	22.33	0.17	17.18	0.15	24.28	0.59
3.2	10.42	0.20	18.39	0.14	13.32	0.09	22.10	0.56	15.04	0.16	25.41	0.35	16.40	0.15	27.29	0.21
y = 0.38																
	200 g L^{-1}				**300 g L^{-1}**				**400 g L^{-1}**				**500 g L^{-1}**			
0.25	15.07	0.07	16.96	0.05	17.50	0.05	18.92	0.19	18.75	0.16	20.29	0.22	20.14	0.09	21.47	0.28
1	14.19	0.27	18.22	0.57	16.85	0.21	20.43	0.15	18.24	0.28	22.33	0.27	19.37	0.19	23.99	0.44
2	13.54	0.10	19.84	0.54	16.11	0.15	22.55	0.13	17.55	0.08	25.00	0.47	18.78	0.11	26.66	0.43
3.2	12.99	0.09	21.97	0.48	15.39	0.07	25.12	0.34	16.93	0.14	27.81	0.11	18.04	0.08	29.94	0.23
y = 0.49																
	150 g L^{-1}				**250 g L^{-1}**				**350 g L^{-1}**				**450 g L^{-1}**			
0.25	15.24	0.13	17.77	0.07	18.69	0.09	20.14	0.23	20.20	0.08	21.49	0.15	21.30	0.13	22.84	0.25
1	14.89	0.10	17.93	0.00	17.93	0.10	21.16	0.28	19.56	0.15	23.80	0.00	20.40	0.11	25.66	0.55
2	13.46	0.17	20.61	0.25	17.05	0.25	24.69	0.36	18.90	0.14	26.02	0.40	19.74	0.19	28.12	0.31
3.2	13.18	0.20	21.79	0.11	16.68	0.11	25.26	0.17	18.33	0.13	28.14	0.13	19.07	0.22	30.52	0.23
y = 0.59																
	150 g L^{-1}				**250 g L^{-1}**				**350 g L^{-1}**				**450 g L^{-1}**			
0.25	18.40	0.11	20.24	0.09	20.78	0.08	22.26	0.18	22.05	0.05	23.61	0.31	22.96	0.13	24.85	0.15
1	17.38	0.23	21.37	0.42	19.65	0.18	24.68	0.23	21.04	0.11	26.38	0.41	22.15	0.18	27.26	0.29
2	16.77	0.19	22.92	0.38	19.27	0.22	25.65	0.30	20.79	0.24	27.73	0.49	21.73	0.15	29.22	0.35
3.2	16.03	0.22	24.63	0.33	18.74	0.05	27.40	0.11	20.23	0.05	29.84	0.19	21.01	0.09	31.79	0.13
y = 0.68																
	150 g L^{-1}				**250 g L^{-1}**				**350 g L^{-1}**				**450 g L^{-1}**			
0.25	20.72	0.11	22.72	0.09	22.55	0.05	24.35	0.32	23.81	0.09	25.85	0.08	24.54	0.13	26.68	0.11
1	20.00	0.18	23.99	0.20	21.96	0.26	26.42	0.43	22.98	0.26	28.36	0.05	23.82	0.08	29.53	0.15
2	19.27	0.14	25.53	0.12	21.57	0.11	27.91	0.09	22.59	0.13	30.25	0.20	22.88	0.11	32.18	0.08

3.2	18.59	0.20	27.13	0.13	20.83	0.13	30.06	0.13	21.88	0.15	32.36	0.25	22.43	0.14	34.87	0.13
y = 0.77																
	100 g L^{-1}				**200 g L^{-1}**				**300 g L^{-1}**				**400 g L^{-1}**			
0.25	21.35	0.19	23.53	0.08	24.11	0.13	26.22	0.09	25.23	0.16	27.41	0.10	25.72	0.28	28.34	0.09
1	20.88	0.27	24.78	0.20	23.60	0.12	28.04	0.15	24.68	0.14	29.63	0.18	25.42	0.19	31.14	0.30
2	20.15	0.08	25.49	0.09	23.01	0.14	29.26	0.19	24.17	0.07	31.15	0.19	24.83	0.08	33.31	0.33
3.2	19.18	0.21	27.61	0.15	22.11	0.08	32.00	0.08	23.05	0.15	34.60	0.25	23.72	0.21	35.66	0.09
y = 0.85																
	75 g L^{-1}				**175 g L^{-1}**				**275 g L^{-1}**				**375 g L^{-1}**			
0.25	23.07	0.12	25.08	0.04	26.24	0.19	28.18	0.12	27.36	0.11	29.25	0.12	27.86	0.09	30.02	0.10
1	22.49	0.15	26.30	0.18	25.66	0.20	29.77	0.10	26.38	0.13	32.17	0.25	27.14	0.18	33.00	0.14
2	21.77	0.13	26.80	0.08	24.97	0.21	31.09	0.15	26.14	0.13	33.06	0.19				
3.2	21.14	0.14	28.18	0.16	24.59	0.13	32.22	0.18	25.41	0.16	35.48	0.07	26.00	0.17	37.14	0.20
y = 0.93																
	20 g L^{-1}				**60 g L^{-1}**				**100 g L^{-1}**				**140 g L^{-1}**			
0.25	18.71	0.43	20.74	0.14	25.00	0.15	26.89	0.09	27.36	0.11	28.92	0.11	28.24	0.18	30.13	0.08
1	17.57	0.30	21.59	0.15	24.33	0.21	28.08	0.11	26.60	0.15	30.41	0.13	27.81	0.23	31.98	0.18
2	17.16	0.21	21.63	0.18	24.03	0.15	28.42	0.15	26.06	0.11	31.19	0.15	27.07	0.16	33.10	0.18
3.2	15.82	0.30	23.03	0.11	23.13	0.16	29.70	0.13	25.76	0.13	32.12	0.09	26.58	0.08	34.35	0.16
y = 1																
	5 g L^{-1}				**15 g L^{-1}**				**25 g L^{-1}**				**35 g L^{-1}**			
0.25	12.34	0.73	13.71	0.26	20.47	0.15	21.97	0.25	23.55	0.07	25.43	0.24	25.95	0.04	27.05	0.37
1	11.08	0.10	14.81	0.30	19.49	0.20	22.86	0.30	23.09	0.08	26.13	0.19	25.13	0.05	28.44	0.11
2	10.14	0.33	15.19	0.40	18.59	0.16	23.37	0.13	22.66	0.19	26.72	0.14	24.57	0.13	28.87	0.13
3.2	10.75	0.28	18.53	0.22	18.63	0.24	25.71	0.04	22.64	0.32	29.61	0.08	24.46	0.14	31.91	0.19

D.3 Solubility and Supersolubility Data

Table D.2. Solubility (T_e) and supersolubility ($T_{c,l}$) data of eicosane in toluene:acetone solvent mixture solutions, together with the calculated steady-state MSZW over a range of concentrations. Standard error (SE) values are also presented.

Conc. (g L^{-1})	$T_{c,l}$ (°C)	SE	T_e (°C)	SE	MSZW (°C)	SE	Conc. (g L^{-1})	$T_{c,l}$ (°C)	SE	T_e (°C)	SE	MSZW (°C)	SE
y = 0							**y = 0.14**						
250	9.92	0.10	11.37	0.15	1.46	0.18	**200**	10.39	0.26	11.85	0.27	1.46	0.37
300	11.54	0.10	12.81	0.14	1.27	0.17	**300**	13.47	0.20	14.46	0.14	0.98	0.24
350	12.78	0.02	13.90	0.44	1.13	0.44	**400**	15.47	0.19	16.48	0.19	1.01	0.27
450	14.88	0.12	15.79	0.06	0.91	0.14	**500**	16.57	0.17	17.82	0.38	1.26	0.42
550	16.58	0.11	17.72	0.33	1.14	0.34	**700**	19.16	0.16	19.83	0.09	0.67	0.19
650	17.49	0.28	18.47	0.91	0.97	0.95	**800**	20.32	0.05	20.80	0.26	0.47	0.26
750	18.60	0.13	19.56	0.26	0.97	0.29							
850	19.69	0.11	20.57	0.19	0.88	0.22							
y = 0.26							**y = 0.38**						
200	12.81	0.08	14.30	0.16	1.49	0.18	**200**	15.05	0.20	16.51	0.05	1.47	0.21
300	15.45	0.09	16.80	0.24	1.35	0.26	**300**	17.61	0.08	18.36	0.04	0.75	0.09
400	17.18	0.17	18.24	0.51	1.06	0.53	**400**	18.87	0.06	19.74	0.13	0.88	0.14
500	18.70	0.11	19.20	0.08	0.50	0.14	**500**	20.20	0.12	20.94	0.18	0.74	0.22
y = 0.49							**y = 0.59**						
150	15.42	0.33	17.09	0.56	1.67	0.65	**150**	18.39	0.21	19.88	0.04	1.49	0.22
250	18.69	0.24	19.76	0.86	1.07	0.89	**250**	20.64	0.31	22.37	0.54	1.73	0.63
350	20.26	0.11	21.28	0.37	1.02	0.39	**350**	21.94	0.27	23.67	0.58	1.74	0.64
450	21.31	0.18	22.67	0.50	1.36	0.53	**450**	22.97	0.15	24.58	0.32	1.61	0.35
y = 0.68							**y = 0.77**						
150	20.80	0.11	22.44	0.11	1.65	0.16	**100**	21.59	0.05	23.23	0.29	1.64	0.30
250	22.63	0.09	24.16	0.31	1.53	0.32	**200**	24.29	0.05	25.84	0.31	1.55	0.32
350	23.80	0.17	25.75	0.45	1.95	0.48	**300**	25.45	0.12	26.92	0.39	1.47	0.41
450	24.58	0.21	26.41	0.44	1.83	0.49	**400**	26.02	0.16	28.22	0.50	2.20	0.52
y = 0.85							**y = 0.93**						
75	23.17	0.09	25.00	0.25	1.82	0.26	**20**	18.80	0.25	20.60	0.32	1.81	0.40
175	26.27	0.16	28.16	0.33	1.89	0.37	**60**	25.09	0.14	26.85	0.28	1.77	0.31
275	27.29	0.24	29.34	0.67	2.05	0.71	**100**	27.29	0.22	29.00	0.35	1.71	0.41
375	27.90	0.17	29.98	0.82	2.09	0.84	**140**	28.36	0.06	30.18	0.49	1.83	0.49
y = 1													
5	11.92	0.69	13.08	0.71	1.16	0.99							
15	20.27	0.43	21.53	0.43	1.26	0.61							
25	23.48	0.19	24.76	0.60	1.28	0.63							
35	25.81	0.20	26.57	0.52	0.76	0.55							

D.4 Solution Thermodynamics Data

Table D.3. Thermodynamic parameters and activity coefficients (Υ) as a function of temperature calculated from van't Hoff analysis. SE is the calculated standard error in results. The linear correlation values (R^2) of the van't Hoff plots are also provided.

Acetone mol fraction (y)	Enthalpy of dissolution (kJ mol^{-1})	SE - Enthalpy of dissolution (kJ mol^{-1})	Entropy of dissolution (kJ mol^{-1} K^{-1})	SE - Entropy of dissolution (kJ mol^{-1} K^{-1})	R^2	Enthalpy of mixing (kJ mol^{-1})	SE - Enthalpy of mixing (kJ mol^{-1})	Entropy of mixing (kJ mol^{-1} K^{-1})	SE - Entropy of mixing (kJ mol^{-1} K^{-1})	Conc. Range (g L^{-1})	$ln\,\Upsilon = aT + c$
0	78.36	1.41	0.255	0.005	0.998	35.50	1.41	0.116	0.005	250 - 850	-0.05T + 1.60
0.14	93.99	0.98	0.307	0.003	1.000	51.13	0.98	0.169	0.003	200 - 800	-0.07T + 2.16
0.26	116.28	5.80	0.382	0.020	0.995	73.42	5.80	0.243	0.020	200 - 500	-0.11T + 3.01
0.38	132.89	4.05	0.436	0.014	0.998	90.02	4.05	0.297	0.014	200 - 500	-0.13T + 3.76
0.49	130.71	3.00	0.425	0.010	0.999	87.85	3.00	0.286	0.010	150 - 450	-0.12T + 4.12
0.59	155.35	7.04	0.504	0.024	0.996	112.48	7.04	0.365	0.024	150 - 450	-0.16T + 5.32
0.68	182.22	10.69	0.590	0.036	0.993	139.36	10.69	0.452	0.036	150 - 450	-0.19T + 6.64
0.77	198.03	10.30	0.638	0.034	0.995	155.17	10.30	0.500	0.034	100 - 400	-0.21T + 7.73
0.85	224.72	17.66	0.721	0.059	0.988	181.86	17.66	0.582	0.059	75 - 375	-0.24T + 9.38
0.93	144.45	10.02	0.448	0.033	0.990	101.58	10.02	0.309	0.033	20 - 140	-0.14T + 7.24
1	100.52	5.53	0.296	0.019	0.994	57.65	5.53	0.157	0.019	5 - 35	-0.08T + 6.41

D.5 Nucleation Mechanism Data

Representative examples of the polythermal data analysis of $\ln u_c$ vs. $\ln q$ plots of y = 0.38 and 0.68 solutions are given in Figure D.1, with the resultant nucleation mechanisms provided in Table D.4. Example plots of u_c vs. $\ln q$ for y = 0.68, for effective interfacial tension calculation, are given in Figure D.2.

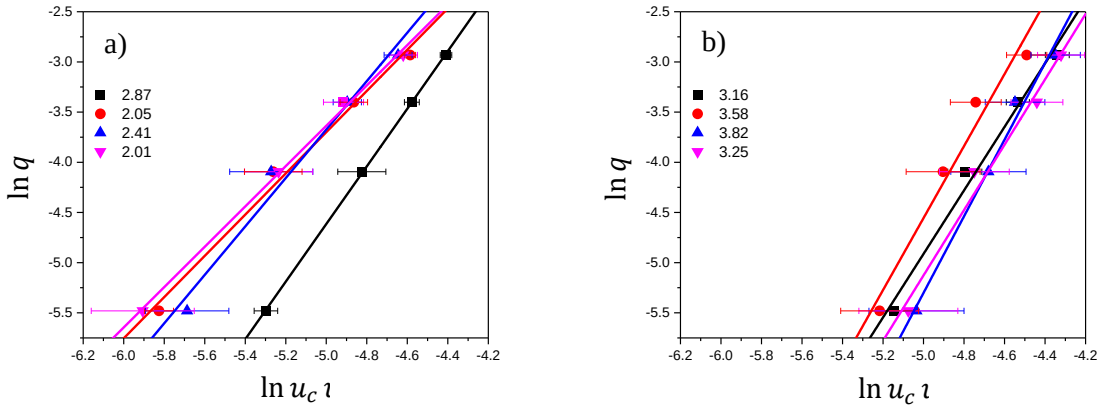


Figure D.1. $\ln u_c$ vs. $\ln q$ plots for (a) y = 0.38 (showing IN) at concentrations of 200 (black square), 300 (red circle), 400 (blue upwards pointing triangle) and 500 g L^{-1} (pink downwards pointing triangle) and (b) y = 0.68 (showing PN) 150 (black square), 250 (red circle), 350 (blue upwards pointing triangle) and 450 g L^{-1} (pink downwards pointing triangle). Legend on graph gives values of slope for linear regressions fitted, for each concentration.

Table D.4. Slopes of linear regressions of $\ln u_c$ vs. $\ln q$ plots for the range of solvent compositions studied, with the resultant nucleation mechanism determined from the "rule of three" KBHR analysis, alongside R^2 values of the fitted regressions and the standard errors (SE) of the slopes. The '' denotes a low correlation fitting and as such the analysis has a lower confidence value and may be a potentially unreliable result.*

Conc. (g L^{-1})	Slope of best-fit straight line of ln uc vs. ln q	SE	R^2, linear fitting	Nucleation mechanism	Conc. (g L^{-1})	Slope of best-fit straight line of ln uc vs. ln q	SE	R^2, linear fitting	Nucleation mechanism
y = 0					**y = 0.14**				
250	2.87	0.48	0.95	IN	**200**	2.80	0.27	0.98	IN
300	2.65	0.35	0.96	IN	**300**	2.26	0.04	0.99	IN
350	2.51	0.38	0.96	IN	**400**	2.37	0.18	0.99	IN
450	2.25	0.26	0.97	IN	**500**	3.15	1.32	0.74	PN*
550	2.45	0.25	0.98	IN	**700**	2.08	0.55	0.88	IN
650	2.24	0.21	0.98	IN	**800**	1.63	0.15	0.98	IN
750	2.18	0.18	0.98	IN					
850	2.16	0.23	0.98	IN					
y = 0.26					**y = 0.38**				
200	2.89	0.29	0.98	IN	**200**	2.87	0.02	0.99	IN
300	2.87	0.29	0.98	IN	**300**	2.05	0.14	0.99	IN
400	2.37	0.12	0.99	IN	**400**	2.41	0.27	0.97	IN
500	1.64	0.03	0.99	IN	**500**	2.01	0.07	0.99	IN
y = 0.49					**y = 0.59**				

150	2.82	0.75	0.88	IN	**150**	2.70	0.09	0.99	IN
250	2.32	0.14	0.99	IN	**250**	3.08	0.28	0.98	PN
350	2.53	0.15	0.99	IN	**350**	3.41	0.36	0.98	PN
450	2.67	0.06	0.99	IN	**450**	3.32	0.25	0.99	PN
y = 0.68					**y = 0.77**				
150	3.16	0.28	0.98	PN	**100**	3.18	0.67	0.92	PN
250	3.58	0.48	0.96	PN	**200**	3.27	0.61	0.93	PN
350	3.82	0.31	0.99	PN	**300**	3.04	0.63	0.92	PN
450	3.25	0.32	0.98	PN	**400**	3.91	1.30	0.82	PN
y = 0.85					**y = 0.93**				
75	3.61	0.45	0.97	PN	**20**	2.84	0.38	0.96	IN
175	4.00	0.38	0.98	PN	**60**	3.74	0.62	0.95	PN
275	3.84	0.41	0.97	PN	**100**	3.70	0.12	0.99	PN
375	4.04	0.41	0.99	PN	**140**	3.92	0.66	0.95	PN
y = 1									
5	1.68	0.49	0.85	IN					
15	2.28	0.33	0.96	IN					
25	4.16	0.48	0.97	PN					
35	1.95	0.24	0.97	IN					

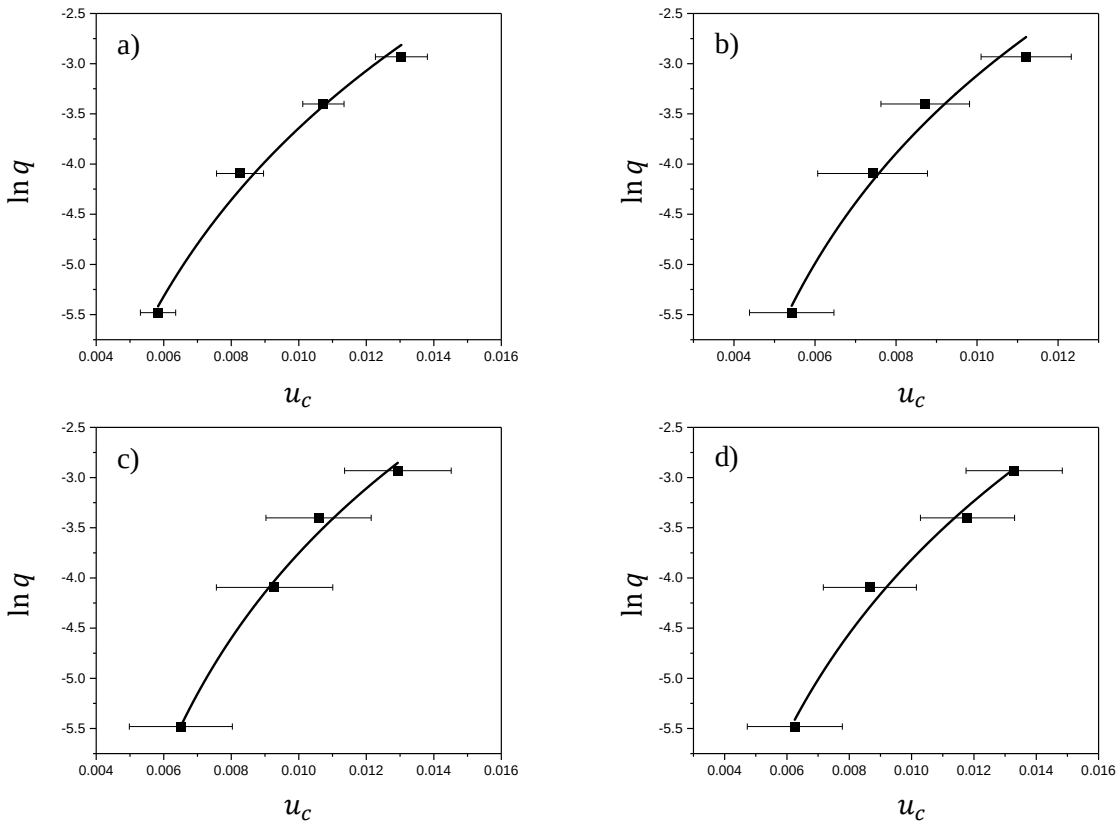


Figure D.2. u_c vs. ln q plots for y = 0.68; (a) 150 g L^{-1}; (b) 250 g L^{-1}; (c) 350 g g L^{-1}; (d) 450 g L^{-1}. Data fitted with KBHR equation, $ln\, q = ln\, q_0 + a_1\, ln\, u_c - \frac{a_2}{(1-u_c)u_c^2}$, to determine nucleation kinetic parameters (black line on plots).

D.6 Atomic Charges

The atomic partial charges calculated for eicosane, toluene and acetone are shown in Table S5, with the corresponding atomic labels represented in Figure D.3.

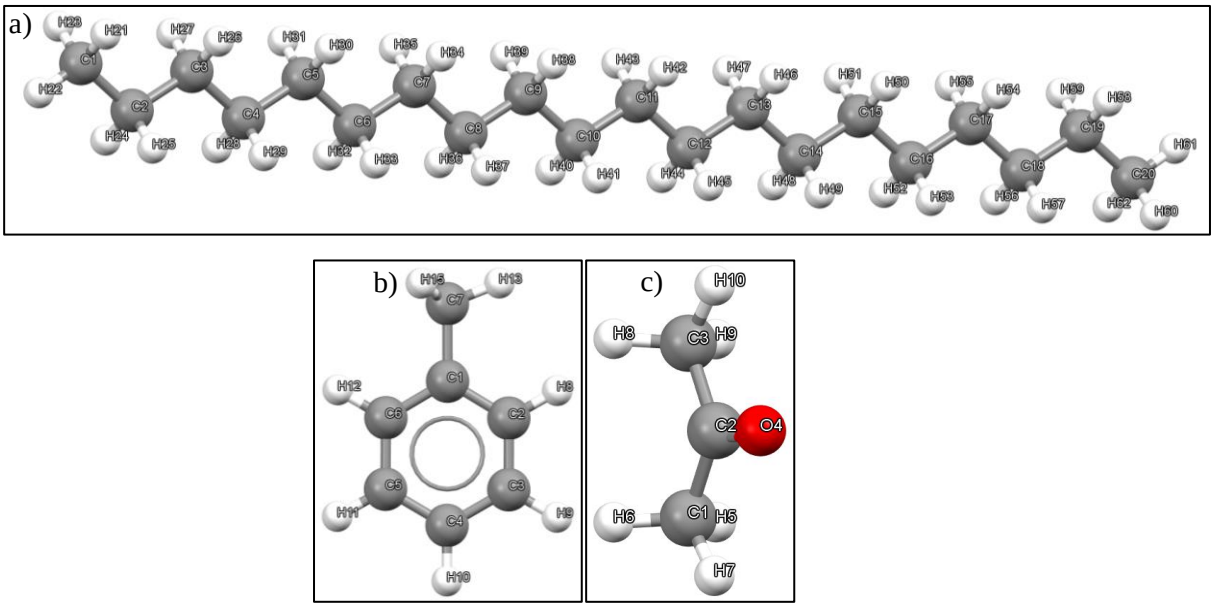


Figure D.3. Atomic labels for a) eicosane, b) toluene and c) acetone. C represents carbon atoms, H represents hydrogen atoms and O represents and oxygen atom.

Table D.5. Atomic partial charges and corresponding atomic labels calculated for eicosane, toluene and acetone molecules.

Eicosane Atomic Label	Eicosane Partial Charges	Toluene Atomic Label	Toluene Partial Charges	Acetone Atomic Label	Acetone Partial Charges
C1	-0.2170	C1	0.2056	C1	-0.3620
C2	0.1420	C2	-0.1970	C2	0.6768
C3	0.0171	C3	-0.0383	C3	-0.3623
C4	-0.0241	C4	-0.1522	O4	-0.5176
C5	0.0467	C5	-0.0248	H5	0.0889
C6	0.0096	C6	-0.2152	H6	0.0889
C7	0.0168	C7	-0.2530	H7	0.1046
C8	0.0396	H8	0.0992	H8	0.0891
C9	-0.0083	H9	0.0790	H9	0.0888
C10	0.0445	H10	0.0966	H10	0.1046

C11	0.0445	H11	0.0740
C12	-0.0083	H12	0.1111
C13	0.0396	H13	0.0737
C14	0.0168	H14	0.0707
C15	0.0096	H15	0.0706
C16	0.0467		
C17	-0.0240		
C18	0.0171		
C19	0.1420		
C20	-0.2170		
H21	0.0463		
H22	0.0510		
H23	0.0463		
H24	-0.0270		
H25	-0.0269		
H26	-0.0078		
H27	-0.0076		
H28	-0.0037		
H29	-0.0039		
H30	-0.0136		
H31	-0.0137		
H32	-0.0068		
H33	-0.0067		
H34	-0.0102		
H35	-0.0103		
H36	-0.0136		
H37	-0.0138		
H38	-0.0053		
H39	-0.0051		
H40	-0.0172		
H41	-0.0170		
H42	-0.0170		
H43	-0.0172		
H44	-0.0051		
H45	-0.0053		

H46	-0.0138		
H47	-0.0136		
H48	-0.0103		
H49	-0.0102		
H50	-0.0067		
H51	-0.0068		
H52	-0.0137		
H53	-0.0136		
H54	-0.0039		
H55	-0.0037		
H56	-0.0076		
H57	-0.0078		
H58	-0.0269		
H59	-0.0270		
H60	0.0463		
H61	0.0510		
H62	0.0463		

D.7 Grid-based Molecular Modelling

Figure D.4 summarises the full results of the calculated solvation sites for a single eicosane molecule solvated with toluene and acetone, using different low-pass energy cut-off filters.

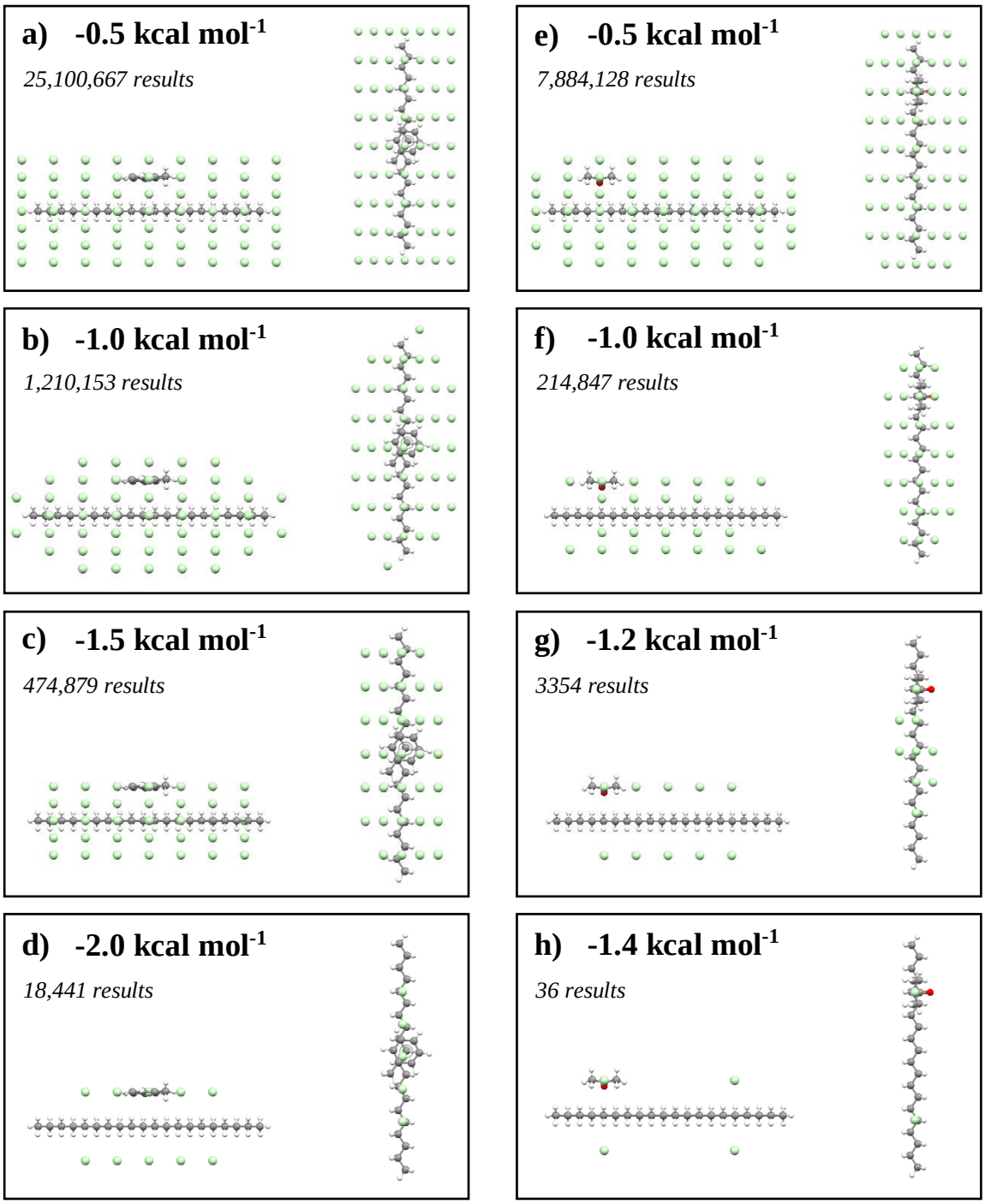


Figure D.4. Interaction energy fields of toluene (a, b, c and d) and acetone (e, f, g and h) probe molecules, with a central eicosane molecule. Toluene and acetone molecules show most negative interaction energy site. The green dots represent interaction locations of the probes, which passed the set energy filter cut-off, which is highlighted at the top left of images. A total of 331,986,600 points (location + rotation) were searched for each simulation, with the number of results found for each one shown below the high-energy cut-off values set. More negative energy filters highlight most favourable interaction sites with eicosane molecule.

Appendix E Supplementary Information: Understanding and Designing Tailor-Made Additives for Controlling Nucleation: Case Study of p-Aminobenzoic Acid Crystallising from Ethanolic Solutions

E.1 Abstract

This appendix contains supplementary information relating to Chapter 5. A brief background to the crystallisation science of pABA is presented (Section E.2), followed by the grid optimisation procedure for in silico grid search analysis (Section E.3). Next, the overall interaction energies calculated through the grid search analysis are presented and discussed (Section E.4), followed with the calculated intermolecular interaction contributions to the calculated total interaction energies from intermolecular grid search analysis (Section E.5). The determined most energetically favourable dimer geometries are presented for all pABA:pABA and pABA:TMA dimers (Section E.6), along with the calculated solvation energies (Section E.7) and the interaction energies of 5 pABA molecules with the dimers (Section E.8). A representation of amino-3-methoxybenzoic acid (AMBA3), 4-amino-2-methoxybenzoic acid (AMBA2) and 4-amino-3-nitrobenzoic acid (ANBA3) within the pABA crystal structure is provided, using spacefill visualisation (Section E.9). The results of the statistical t-test for analysis of crystallisation temperatures is provided (Section E.10), followed by metastable zone width (MSZW) analysis of p-aminobenzoic acid (pABA) crystallising from ethanol solution in the absence and presence of seven tailor-made additives (TMAs) (Section E.11), as well as optical micrographs of crystals collected from these experiments (Section E.12). Average crystallisation (T_c) and dissolution (T_{diss}) temperatures determined from pABA and pABA:ANBA3 crystallising from ethanol solutions over a range of solution concentrations are presented (Section E.13). Van't Hoff analysis results are also provided alongside data on the crystallisability of pABA and pABA:ANBA3 in ethanol solutions (Section E.14). Plots of u_c vs q in ln-ln coordinates for determination of nucleation mechanisms of pABA:ANBA3 in ethanol solutions as well as plots of u_c vs $\ln q$ for determination of nucleation kinetic parameters for pABA:ANBA3 are provided (Section E.15).

E.2 pABA Crystallisation Background

pABA has a number of polymorphic forms, but has two major polymorphs, α- and β-pABA, with α-pABA being the most commonly observed form. This paper concerns the α-polymorph, which is subsequently referred to simply as pABA. pABA crystallises in the monoclinic crystal system, with space group $P2_1/n$ and 2 molecules in the asymmetric unit cell. Intermolecular

interactions within the crystal structure are dominated by hydrogen bonding, through carboxylic acid group -O-H···O- dimers (synthon A) and -N-H···O- hydrogen bonding between carboxyl and nitro groups (synthon C), as well as head-to-head π-π stacking interactions of the phenyl rings (synthon B) (see Figure E.1).

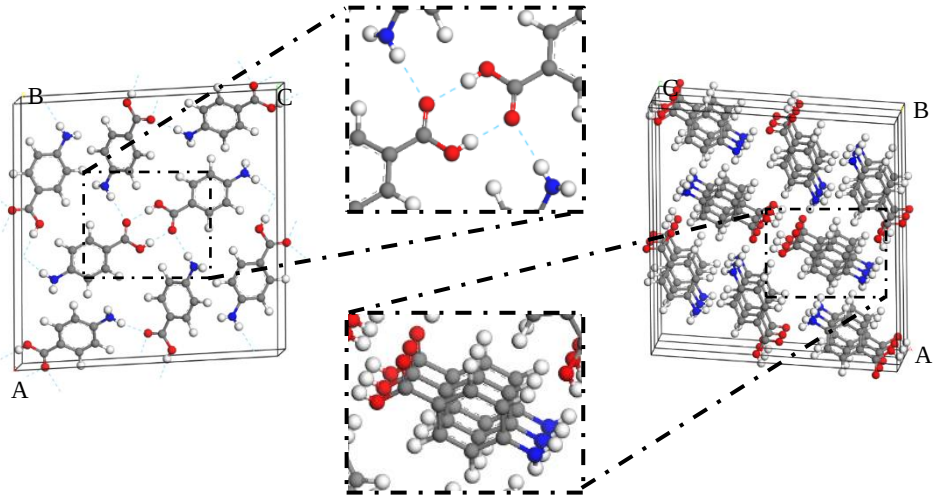


Figure E.1. pABA crystal structure. Left-hand side - pABA unit cell, showing carboxylic dimer -O-H···O- hydrogen bonding and -N-H···O- hydrogen bonding. Inset shows dominant hydrogen bonding tetramer intermolecular interactions. Blue dashed lines show intermolecular hydrogen bonding. Right-hand side - pABA structural packing in the c-axis, showing π-π stacking of the cyclic rings of pABA. Inset highlights π-π stacking. Taken from AMBNAC07 in CCDC[1].

There is an abundance of literature that focusses upon the self-assembly of pABA in the nucleation process. The important synthons were first studied intensively by Rosbottom et al.[2] which identified the three key synthons of pABA (A, B and C) in the solid-state. This work demonstrated that the synthon A interaction was stronger than synthons B and C. The importance of synthon B was further studied by Rosbottom et al.[3] with respect to the influence of nitromethane on the crystallisation of pABA. It was found that synthon B had a large influence on the growth process and morphology of pABA. Following this, Cruz-Cabeza et al.[4] suggested that the synthon B interaction is the key step in pABA nucleation, under the assumption that the clusters of pABA in solution have the same packing as the mature crystal. Black et al.[5], focussing on how tailor-made additives were able to interrupt important synthons of pABA, also suggested that the aromatic stacking step controlled pABA nucleation. However, Toroz et al.[6] found that the synthon A pABA dimers are more stable in ethanol solution than the synthon B dimers. This was also supported by SAXS experiments that suggested that, in ethanol solution, synthon A H-bonded dimers were present in solution prior to nucleation and contributed to the prenucleation clusters, whereas there was little evidence of the existence of

the synthon B π-π stacking dimers. Sullivan et al.[7] also studied the nucleation of pABA in a number of solvents and found that the rate determining step to nucleation is the desolvation of the carboxylic acid group, suggesting synthon A formation is the key step in the nucleation pathway of pABA. Turner et al.[8] also found that there is a higher undercooling required to nucleate pABA in ethanol solution than acetonitrile. Ethanol strongly solvates the carboxylic acid group of pABA[9], whereas acetonitrile only weakly solvates this group[7]. This corroborates the findings of Sullivan et al., suggesting that the synthon A interaction strongly controls the nucleation of pABA in ethanol solution. Furthermore, more recent work by Rosbottom et al.[10] demonstrated the dominance of the synthon A dimers in various solvents, including ethanol, with it calculated to be much more stable than other possible synthons, except in water, which was suggested to be why the β-pABA polymorph is obtained from crystallisation from water at certain conditions.

This is an interesting topic and currently an open question, however, from the evidence (shown both ways), on balance, the view of the literature is more suggestive of synthon A dominance in ethanol solution. Clearly more work needs to be done to confirm whether synthon A or synthon B dominates the nucleation pathway of pABA from solution.

Nucleation of pABA from ethanol solution has been found to proceed via a kinetically controlled instantaneous nucleation mechanism, whereby all pABA nuclei formed instantly and subsequently undertook crystal growth. Prior to this stage, a distribution of monomers and dimers of pABA have been suggested to exist in an undersaturated ethanol solution, forming larger, more structured, clusters with an increase in solution supersaturation[6].

E.3 Grid Optimisation

The optimised grid geometry used as part of the in silico TMA screening studies is displayed in Figure E.2, which used the software package Mercury[11] to visualise the grid. Prior to selection of this geometry a grid optimisation procedure was undertaken. This involved varying grid size by altering radius distance as well as the number of steps of grid points in each direction (radius, the polar angle and on the equator). The purpose of the grid optimisation was to set a grid that enabled the strongest pABA:pABA and pABA:TMA intermolecular interactions to be calculated as well as a large number of interactions to be calculated overall, to give an overview of interaction energy changes as a function of intermolecular interaction strength rankings. Furthermore, in order to visualise the grid in software that can read .mol file types (such as Mercury), the number of grid points had to be less than ≈ 950 points. After numerous iterations, a spherical grid with radius of 15 Å from the target molecule (pABA) with

10 steps of grid points on the radius, the polar angle and on the equator, provided a grid with total points of 936, which was defined for energy calculations.

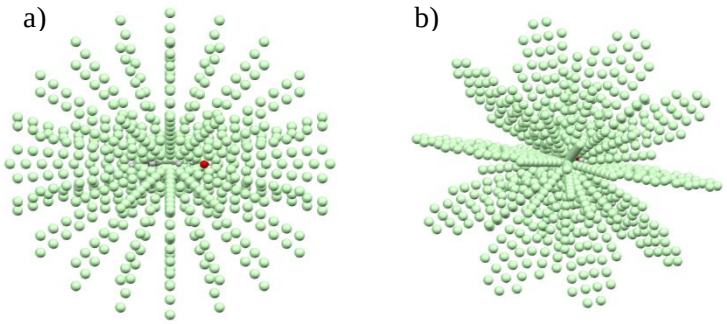


Figure E.2. Spatial grid defined around target pABA molecule for calculation of intermolecular interaction energy calculations. Grid points shown by green spheres.

E.4 Intermolecular Interaction Energies

Consideration of the full range of intermolecular interaction energies (Figure E.3) reveals minimal change in the overall trend in values of interaction energies for pABA:pABA and pABA:TMAs studied. Therefore, it can be assumed that the TMAs that have competitive binding capabilities to pABA (ANBA3, AMBA2 and AMBA3) are still likely to be the TMAs that have a more substantial effect on pABA nucleation inhibition from ethanol solution.

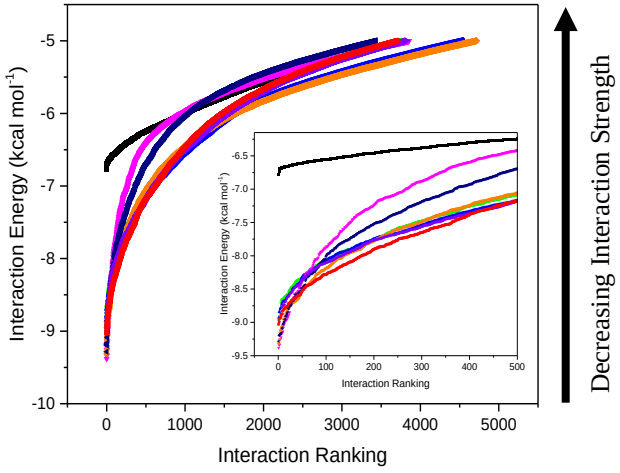


Figure E.3. Interaction energies for all pABA:pABA / pABA:TMA intermolecular interactions calculated to total -5 kcal mol^{-1} or lower. Inset shows top 500 interactions. pABA:pABA (red hexagon), pABA:mABA (green circle), pABA:ANBA2 (blue upward triangle), pABA:ANBA3 (magenta downward triangle), pABA:AMBA2 (orange diamond), pABA:AMBA3 (navy left triangle), pABA:pASA (violet right triangle) and pABA:pNP (black square).

Furthermore, this is also seen by plotting intermolecular interaction energies as histogram plots, Figure E.4. From these plots it is clear that ANBA3, AMBA2 and AMBA3 have the strongest interactions with a pABA molecule compared to all other TMAs and pABA itself.

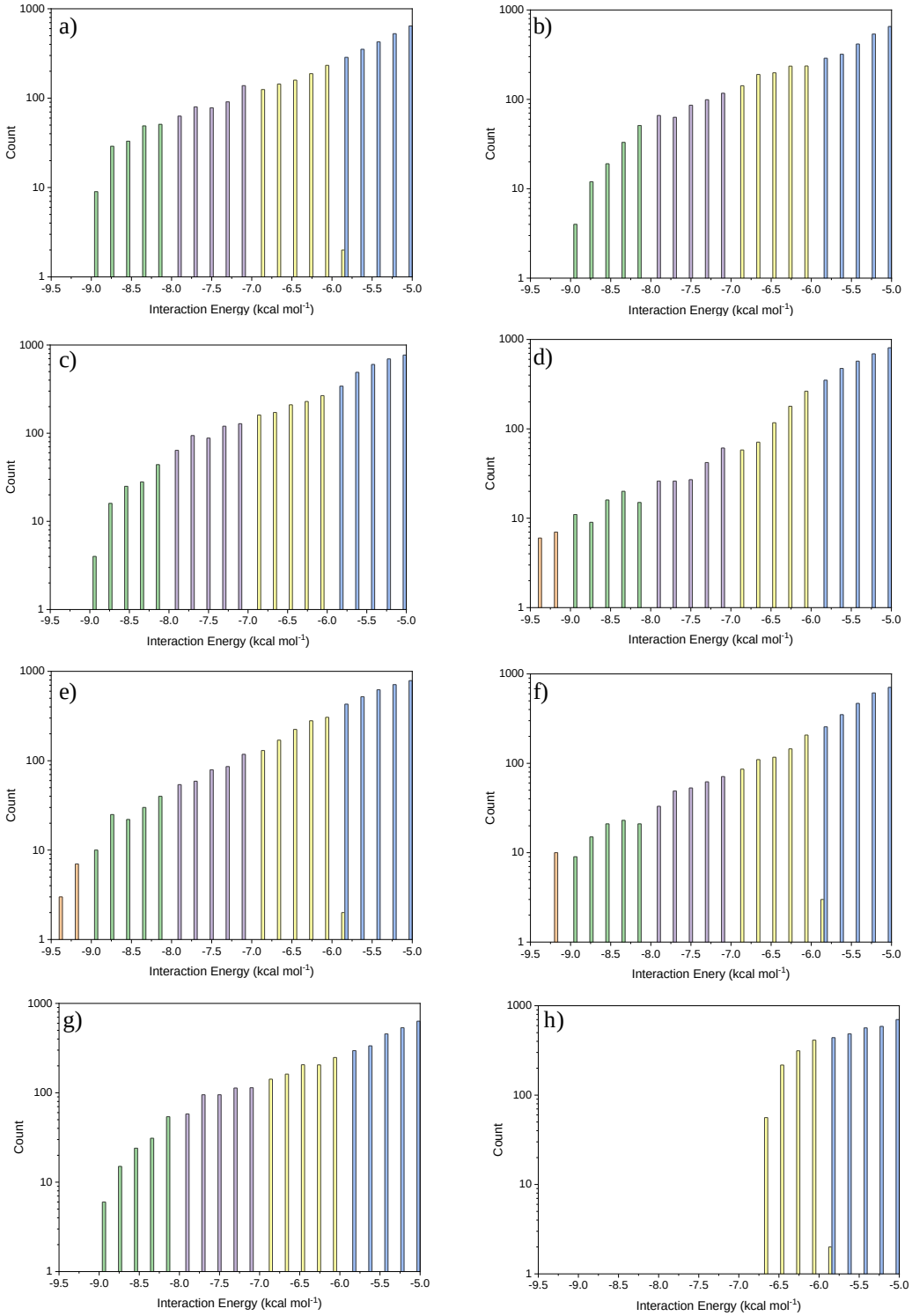
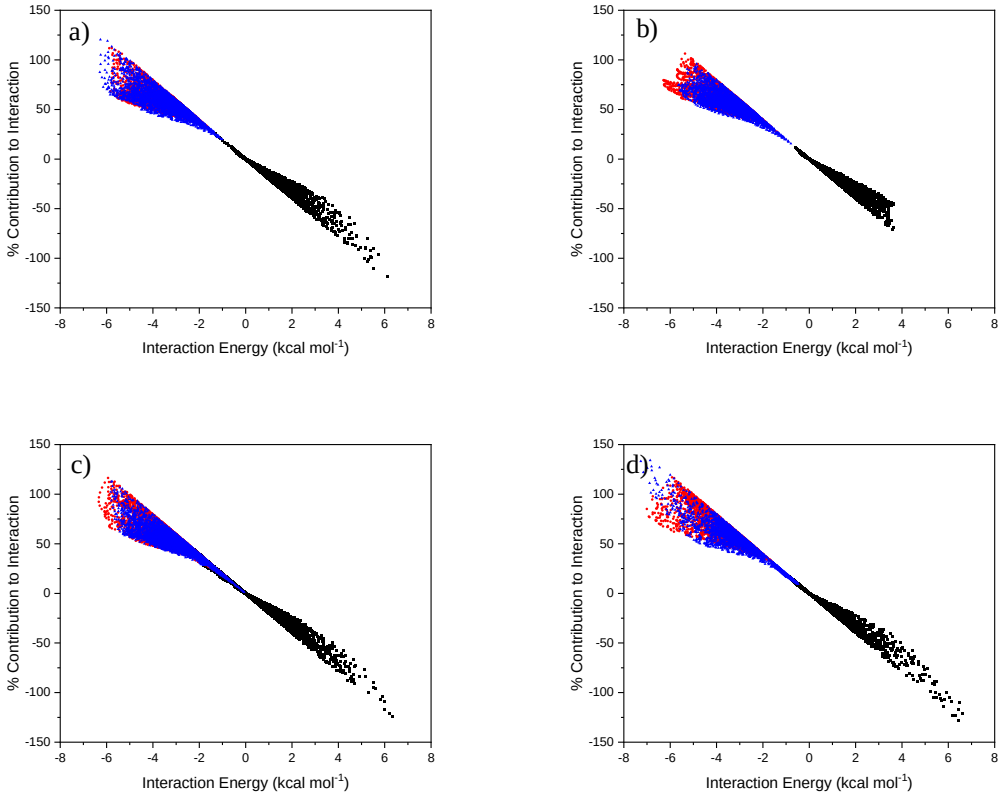


Figure E.4. Histogram plots of intermolecular interaction energies for pABA:pABA and all pABA:TMAs, for interactions calculated to total -5 kcal mol^{-1} or lower. a) pABA:pABA, b) pABA:mABA, c) pABA:ANBA2, d) pABA:ANBA3, e) pABA:AMBA2, f) pABA:AMBA3, g) pABA:pASA, h) pABA:pNP. Different colours represent calculated energies in different bands: orange is for -9.0 to -9.4 kcal mol^{-1}, green is for -8.0 to -9.0 kcal mol^{-1}, purple is for -7.0 to -8.0 kcal mol^{-1}, yellow is for -6.0 to -7.0 kcal mol^{-1} and blue is for -5.0 to -6.0 kcal mol^{-1}. Each bar represents counts for each 0.2 kcal mol^{-1} energy bin from -9.4 to -5.0 kcal mol^{-1}.

E.5 Intermolecular Interaction Contributions

A comparison of interaction type over a large range of calculated interactions demonstrated the dominant interaction types overall. Examples of interaction types for intermolecular interactions calculated to total -5 kcal mol^{-1} or lower for pABA:pABA and pABA:ANBA3 are displayed in Figure E.5. It is clear the hydrogen bonding and electrostatic interactions dominated the formation of the dimers, whereas van der Waals interactions mainly repelled this formation, but are much weaker on the whole than the other intermolecular interaction types.



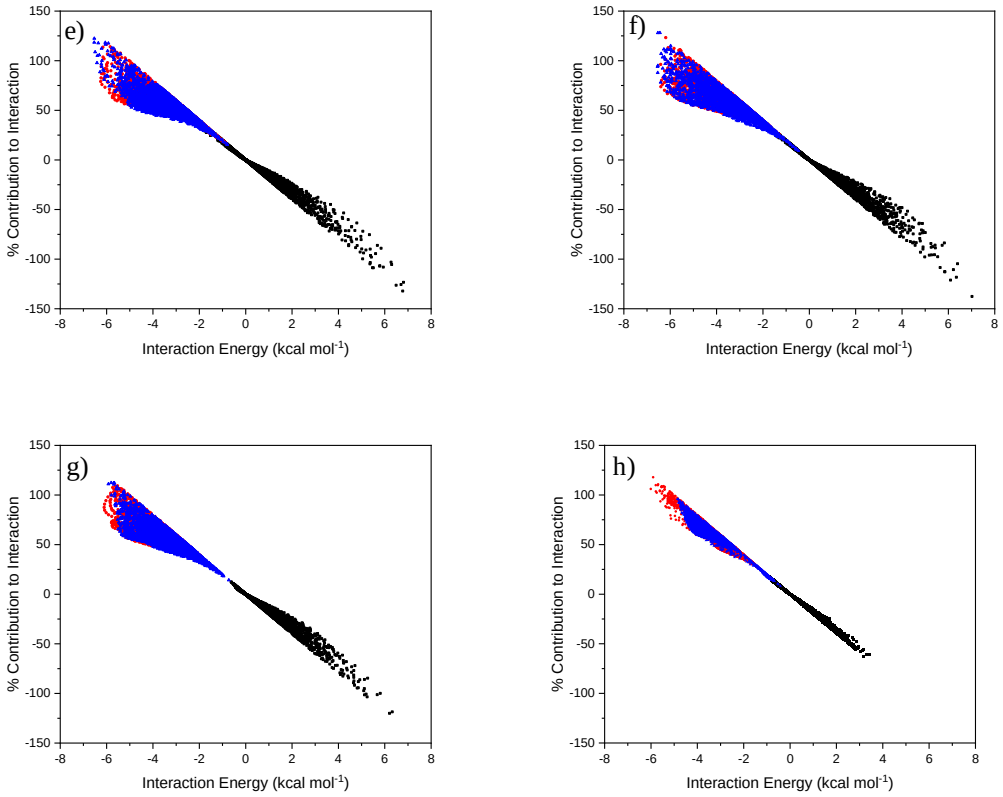


Figure E.5. % Contribution of hydrogen bonding (red circles), electrostatic (blue triangles) and Van der Waals (black squares) intermolecular interactions for all pABA:pABA / pABA:TMA interactions calculated to total -5 kcal mol^{-1} or lower. a) pABA:pABA, b) pABA:mABA, c) pABA:ANBA2, d) pABA:ANBA3, e) pABA:AMBA2, f) pABA:AMBA3, g) pABA:pASA, h) pABA:pNP.

E.6 Dimer Interaction Geometries

The intermolecular interaction geometries of the calculated most favourable interactions for all pABA:pABA and pABA:TMA dimers calculated from the initial in silico screening results is given in Figure E.6. All interactions except pABA:pNP are the synthon A interaction.

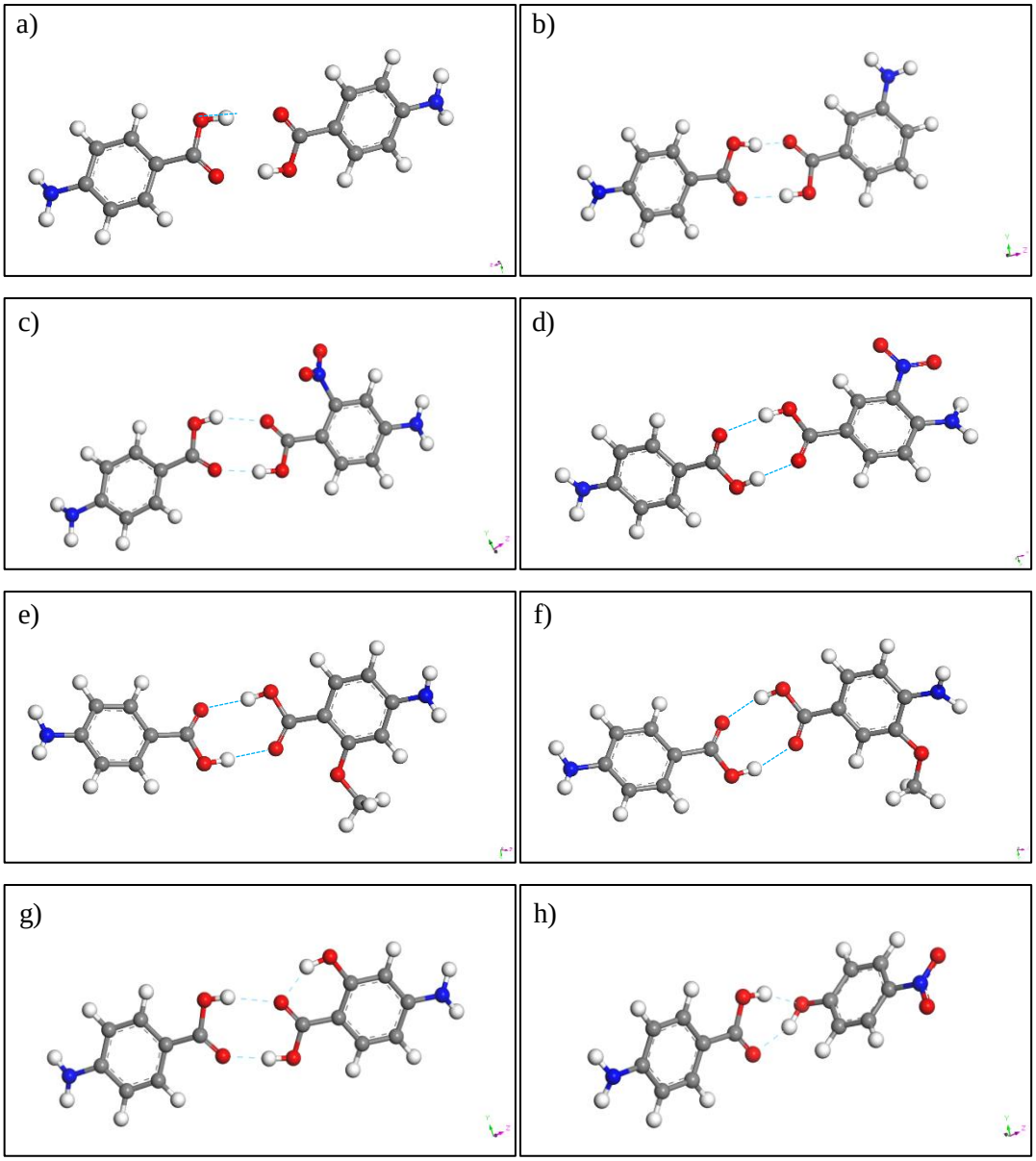


Figure E.6. Most favourable interactions of a) pABA:pABA, b) pABA:mABA, c) pABA:ANBA2, d) pABA:ANBA3, e) pABA:AMBA2, f) pABA:AMBA3, c) pABA:pASA and d) pABA:pNP, calculated from intermolecular grid search. Hydrogen bonding shown by blue dashed lines.

E.7 Dimer - Solvation Energies

The most favourable pABA:pABA and pABA:TMA dimers from the intermolecular grid search were used to determine solvation energies. The solvation energies of 20 ethanol molecules with each dimer were calculated using the intermolecular grid search method. The values of solvation energies for all dimers are displayed in Table E.1. The results indicate that the pABA:TMA dimers are more strongly solvated than the pABA:pABA dimer, suggesting that these dimers are more stable in solution and harder to desolvate.

Table E.1. Solvation energies of 20 ethanol molecules interacting with pABA:pABA and pABA:TMAs. Colour shading indicates solvation of pABA:pABA (yellow) and the more favourable interaction dimers compared to pABA:pABA (blue).

Molecule in dimer with pABA	pABA	mABA	ANBA2	ANBA3	AMBA2	AMBA3	pASA	pNP
Solvation Energy (kcal mol^{-1})	-58.71	-65.55	-77.77	-76.03	-60.43	-73.52	-65.05	-69.90

E.8 Dimer – pABA interaction energies

A comparison of the intermolecular interaction energies of 5 pABA molecules with pABA:pABA and pABA:TMA dimers is summarised in Table E.2. The intermolecular grid search software calculates the strongest interaction between pABA probes and the dimer in sequential order, however, the interaction number in Table E.2 demonstrates that the interaction strength does not decrease with interaction number (from 1 – 5). This is due to not only pABA interactions with the dimers being calculated, but also interactions with other pABA molecules present. The total interaction energy calculated for all pABA:TMAs is stronger than that of pABA:pABA. This indicates that once desolvation of dimers would occur in solution to enable subsequent pABA molecules to interact with the stable dimer structure, the favourable intermolecular interactions would mean more energy would be required to remove the TMA from the nucleation cluster, before pABA nucleation could take place, inhibiting the nucleation process further.

Table E.2. Intermolecular interaction energies of 5 pABA molecules interacting with pABA:pABA and pABA:TMAs. Colour shading indicates interactions with pABA:pABA (yellow) and the more favourable interaction dimers compared to pABA:pABA (blue).

	pABA	mABA	ANBA2	ANBA3	AMBA2	AMBA3	pASA	pNP
Interaction Number	Intermolecular Interaction Energy (kcal mol^{-1})							
1	-6.21	-6.45	-6.94	-6.53	-6.66	-6.42	-6.01	-6.30
2	-2.22	-2.25	-1.22	-3.70	-6.35	-2.55	-1.63	-1.44
3	-1.39	-1.15	-4.02	-1.36	-1.63	-4.54	-3.45	-4.42
4	-2.69	-2.89	-2.33	-1.22	-2.92	-5.01	-1.36	-1.36
5	-1.68	-5.71	-3.40	-4.25	-3.06	-1.26	-3.09	-1.62
Total	-14.19	-18.44	-17.91	-17.07	-20.62	-19.79	-15.54	-15.14

E.9 TMAs in pABA Crystal Structure

To conceptualisation how the TMAs could potentially inhibit formation of the pABA crystal structure, Figure E.7 displays visualisations of the strongest interactions of pABA:TMAs, determined from the in silico results, within the pABA crystal structure, in place of one pABA molecule.

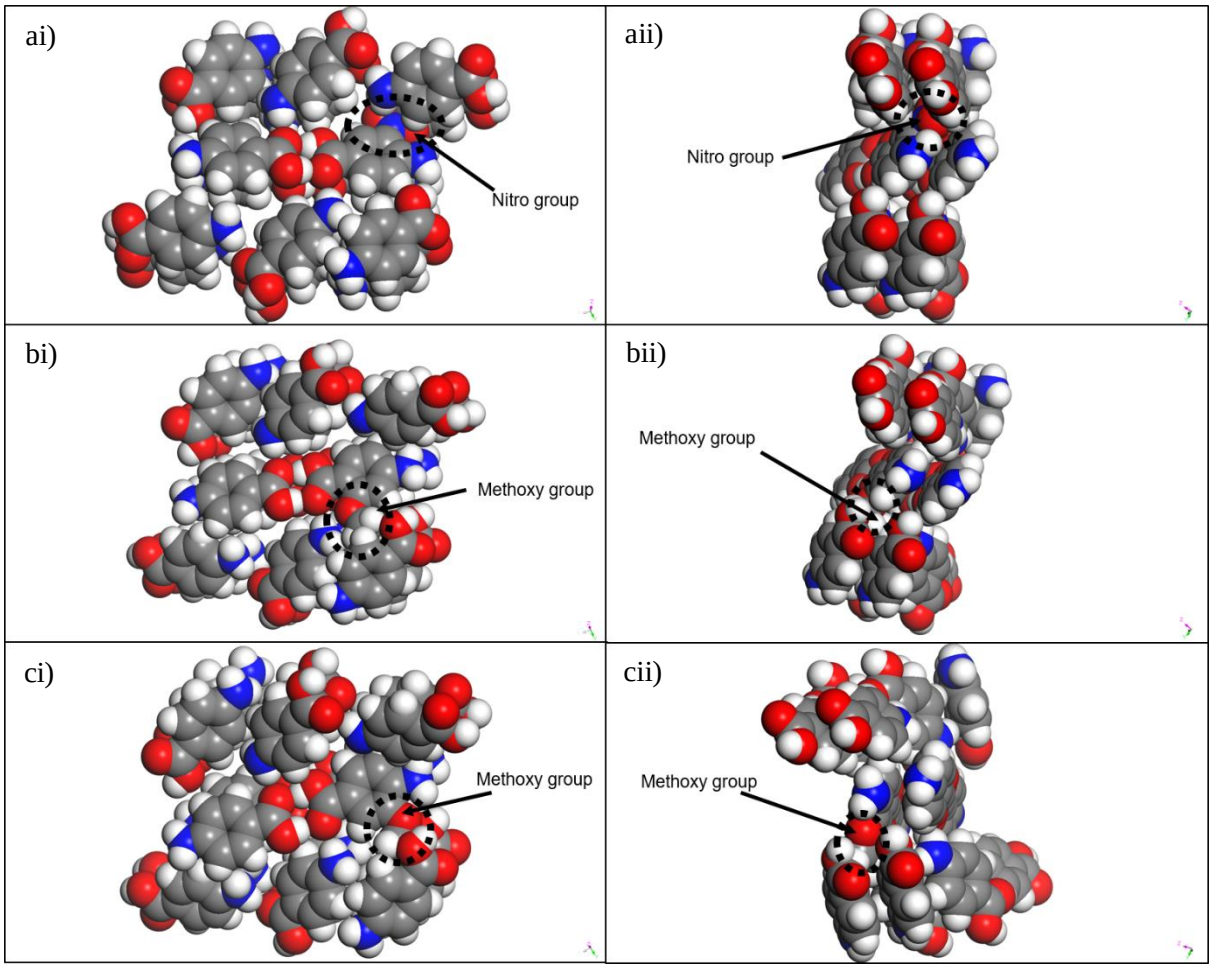


Figure E.7. Visualisation of a) ANBA3, b) AMBA2 and c) AMBA3 within the pABA unit cell, based on the calculated strongest interaction geometry. i) View along b axis, ii) view along c axis. Spacefill view of molecules used to visualise potential TMA disruption. Nitro and methoxy moieties would inhibit pABA molecules close to them from packing in the required pABA unit cell structure. Crystal structure taken from AMBNAC07 in CCDC[1].

E.10 Statistical T-test

A statistical T-test was performed on T_c values for the results of the experimental TMA screen. The inbuilt Data Analysis tool in Microsoft Excel was used to assess the data, using the T-test: Paired two samples for means with an alpha value of 0.05. Each pABA:TMA result was compared to results collected for pABA in ethanol solutions to assess whether the mean of T_c

showed statistical significance with respect to being different from that of pABA, with the null hypothesis being no statistical significant difference in the mean value. From a two-tailed analysis, it was found that only ANBA3, AMBA2 and AMBA3 showed statistical significance in being different to the T_c mean of pABA. The values of the probability that T (the calculated difference) ≤ the t-value is provided in Table E.3 for all pABA:TMA results. This value being lower than the alpha value (0.05) represents statistically significant difference in mean values.

Table E.3. Values calculated for probability T ≤ t-value calculated from statistical T-test analysis. Values less than 0.05 represent data that has statistical significant difference in mean values of T_c.

pABA:TMA	pABA:mABA	pABA:ANBA2	pABA:ANBA3	pABA:AMBA2
P(T≤t) two-tail	0.12	0.55	1.21E-06	2.83E-03
pABA:TMA	pABA:AMBA3	pABA:pNP	pABA:pASA	
P(T≤t) two-tail	1.85E-03	0.82	0.94	

E.11 TMA Screen MSZWs

Figure E.8 shows MSZW results obtained for each solution studied in the experimental TMA screen. The experimental results corroborate the findings from the intermolecular grid search screen, with little variation in MSZW observed for pABA:pABA, pABA:mABA, pABA:ANBA2, pABA:pNP and pABA:pASA, and the most effective TMAs being found to be ANBA3, AMBA2 and AMBA3, increasing the MSZW by an average of 22.4 °C, 10.6 °C and 5.5 °C, respectively.

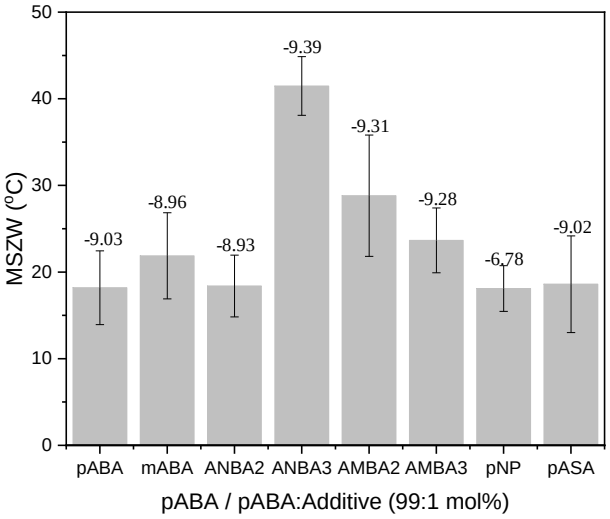


Figure E.8. MSZW at 0.5 °C min^{-1} heating cycle determined for pABA:pABA and pABA:TMAs (99:1 mol%) in ethanol solution. Error bars show standard deviations of results. Values above error bars are the strongest interaction energies for each dimer pair, calculated from the intermolecular grid search, in kcal mol^{-1}.

E.12 pABA Optical Micrographs

Crystals from the experimental TMA screening experiments were collected for morphological assessment. The crystals were collected through Buchner vacuum filtration of the crystallised solutions using filtration paper, before being placed in an oven at 50 °C until dry.

An Olympus BX51 microscope was used to study crystal morphology. Optical micrographs collected from the morphological study are displayed in Figure E.9.

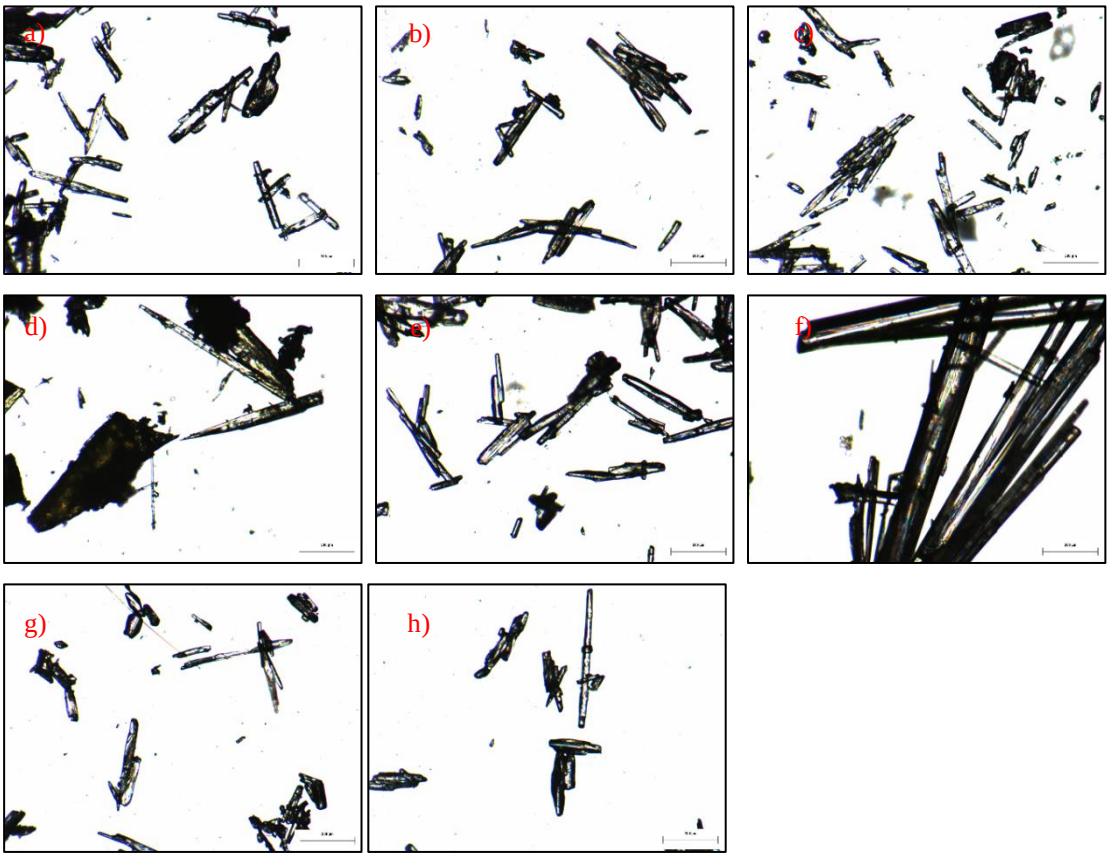


Figure E.9. Optical micrographs showing collected crystals from crystallisation experiments. a) pABA:pABA, b) pABA:mABA, c) pABA:ANBA2, d) pABA:ANBA3, e) pABA:AMBA2, f) pABA:AMBA3, g) pABA:pASA, h) pABA:pNP. All show alpha-pABA needle morphology.

E.13 Crystallisation and Dissolution Temperatures

Average T_c and T_{diss} values obtained from repeats of polythermal crystallisation cycles are displayed in Tables E.4 and E.5 for pABA in ethanol solutions and pABA:ANBA3 in ethanol solutions, respectively.

Table E.4. T_c and T_{diss} values from pABA in ethanol crystallisation studies, along with the standard deviation (std) of results, for all concentrations studied.

Cooling Rate	Tc	std	Tdiss	std	Tc	std	Tdiss	std
	0.14 g g^{-1}				**0.15 g g^{-1}**			
0.3	5.64	2.76	17.70	1.13	11.12	4.21	22.94	0.08
0.5	2.56	1.62	18.95	0.59	3.97	1.23	23.23	0.08
0.7	-2.21	1.14	20.22	0.10	1.77	3.11	23.60	0.04
0.9	-7.53	6.09	20.53	0.11	0.27	3.58	24.27	0.19
	0.16 g g^{-1}				**0.17 g g^{-1}**			
0.3	15.07	2.10	27.22	0.08	18.99	2.17	31.11	0.11
0.5	9.59	10.68	27.61	0.13	12.75	2.32	31.53	0.18
0.7	5.44	2.83	28.11	0.11	10.61	8.99	31.89	0.05
0.9	0.05	6.58	28.69	0.56	8.12	0.35	32.25	0.11

Table E.5. T_c and T_{diss} values from pABA:ANBA3 in ethanol crystallisation studies, along with the standard deviation (std) of results, for all concentrations studied. Empty table cells shows where data was not collected due to issues in large inconsistencies of repeats and/or problems assessing transmission data.

Cooling Rate	Tc	std	Tdiss	std	Tc	std	Tdiss	std
	0.18 g g^{-1}				**0.19 g g^{-1}**			
0.3	-0.07	5.36	34.27	0.42	5.76	1.58	37.33	0.53
0.4	-0.03	2.74	35.41	0.27	5.45	2.50	38.67	0.70
0.5	-2.11	3.87	35.45	0.42	3.62	2.58	38.02	0.63
0.6	-	-	-	-	-	-	38.50	1.26
0.7	-2.96	1.77	35.94	0.87	1.57	2.15	38.80	0.39
0.8	-2.92	4.59	-	-	1.61	3.23	-	-
0.9	-3.81	3.12	36.04	0.46	1.18	6.25	40.14	1.25
	0.20 g g^{-1}				**0.21 g g^{-1}**			
0.3	13.79	1.30	40.42	1.02	18.25	1.67	47.64	1.29
0.4	13.20	1.81	42.36	1.71	15.90	1.87	47.94	3.25
0.5	10.47	6.21	42.30	1.62	14.20	3.41	47.29	2.84
0.6	8.95	6.58	-	-	13.84	2.15	-	-
0.7	8.35	2.79	41.36	1.57	12.63	4.35	45.19	1.76
0.8	7.68	1.56	-	-	11.28	3.61	-	-
0.9	5.25	1.33	41.52	0.52	11.14	4.45	45.23	2.77

E.14 Crystallisability and van't Hoff Analysis

A van't Hoff analysis was undertaken to assess solution thermodynamics of the crystallising systems, Figure E.10. Negligible changes were found in the enthalpy and entropy of dissolution between both systems, with low activity coefficients, with a strong dependence on solution concentration determined for each system, Table E.6. The majority of solutions showed less than ideal behaviour, however, the two lowest pABA in ethanol solution concentrations were found to be more than ideal, demonstrating the changing solvent-solute interaction strengths with changing solution concentration.

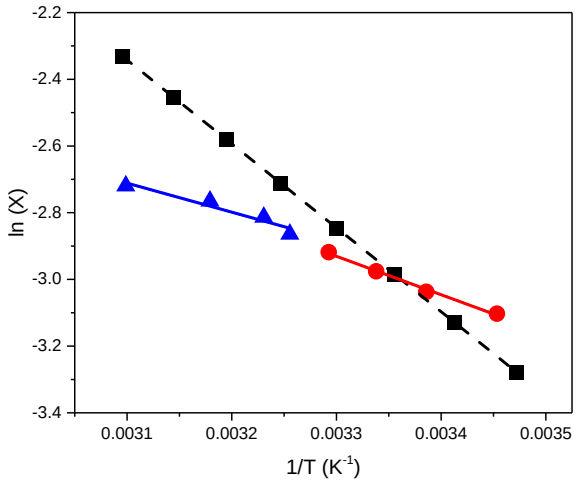


Figure E.10. van't Hoff plot for pABA and pABA:ANBA3 in ethanol solution. Dashed black line represents ideal solubility and solid lines represent experimental solubilities for the different systems. pABA in ethanol solution is shown by red circles. pABA:ANBA3 in ethanol is shown by blue triangles.

Table E.6. Thermodynamic parameters derived from van't Hoff analysis for pABA and pABA:ANBA3 in ethanol solutions.

Conc. (g g^{-1})	ΔH_{diss} (kJ mol^{-1})	ΔS_{diss} (kJ K^{-1} mol^{-1})	Activity Coefficient	Conc. (g g^{-1})	ΔH_{diss} (kJ mol^{-1})	ΔS_{diss} (kJ K^{-1} mol^{-1})	Activity Coefficient
pABA				**pABA:ANBA3**			
0.14	-9.58	7.0x10^{-3}	0.88 - 1.10	0.18	-7.23	1.1x10^{-4}	1.14 - 1.46
0.15				0.19			
0.16				0.20			
0.17				0.21			

E.15 Nucleation Kinetic Analysis

Plots of u_c vs q in ln-ln coordinates produced, with slopes of fitted linear regressions providing information as to the mechanism of nucleation, are displayed in Figure E.11 for all concentrations studied for pABA:ANBA3 in ethanol solutions. A slope <3 indicated an Instantaneous nucleation (IN) pathway, whereas a slope >3 signified a Progressive nucleation (PN) pathway. IN describes the process in which all nuclei form instantly and subsequently undergo crystal growth, whereas in PN nuclei continuously form in the presence of growing crystals. Plots of u_c vs ln q with slopes fitted with Equation A.58 for the determination of the KBHR parameters a_1, a_2 and q_0 are displayed in Figure E.12.

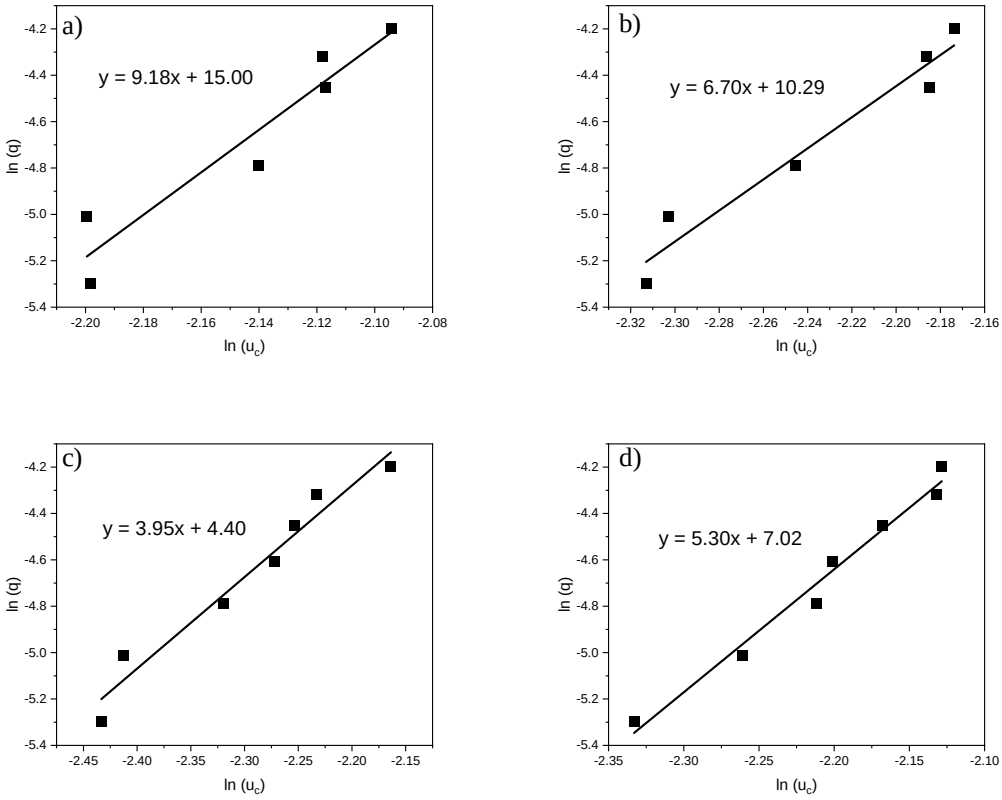


Figure E.11. u_c vs q in ln-ln coordinate plots for pABA:ANBA3 in ethanol solutions at different solution concentrations: a) 0.18 g g^{-1}, b) 0.19 g g^{-1}, c) 0.20 g g^{-1} and d) 0.21 g g^{-1}. Line shows linear regression of points, with equation of line displayed. The gradient provides information on nucleation mechanism.

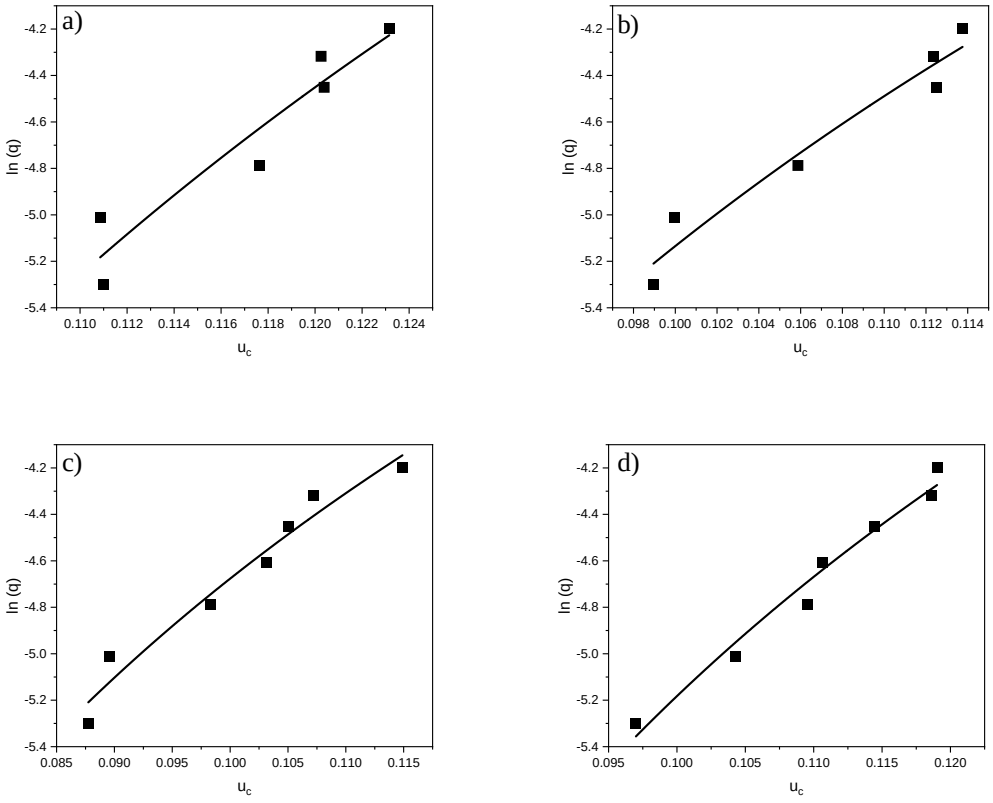


Figure E.12. u_c vs $\ln q$ plots for pABA:ANBA3 in ethanol solutions at different solution concentrations: a) 0.18 g g^{-1}, b) 0.19 g g^{-1}, c) 0.20 g g^{-1} and d) 0.21 g g^{-1}. Line shows fitted equation from KBHR analysis ($\ln q = \ln q_0 + a_1 \ln u_c - \frac{a_2}{(1-u_c)u_c^2}$).

E.16 References

1. Sullivan, R. A. & Davey, R. J. Concerning the crystal morphologies of the α and β polymorphs of p-aminobenzoic acid. *CrystEngComm* **17**, 1015–1023 (2015).
2. Rosbottom, I., Roberts, K. J. & Docherty, R. The solid state, surface and morphological properties of p-aminobenzoic acid in terms of the strength and directionality of its intermolecular synthons. *CrystEngComm* **17**, 5768–5788 (2015).
3. Rosbottom, I. *et al.* Influence of Solvent Composition on the Crystal Morphology and Structure of p-Aminobenzoic Acid Crystallized from Mixed Ethanol and Nitromethane Solutions. *Cryst. Growth Des.* **17**, 4151–4161 (2017).
4. Cruz-cabeza, A. J., Davey, R. J. & Sachithananthan, S. Aromatic stacking - a key step in nucleation. *Chem. Commun.* **53**, 7905–7908 (2017).
5. Black, J. F. B., Cruz-Cabeza, A. J., Davey, R. J., Willacy, R. D. & Yeoh, A. The Kinetic Story of Tailor-made Additives in Polymorphic Systems: New Data and Molecular Insights for p-Aminobenzoic Acid. *Cryst. Growth Des.* **18**, 7518–7525 (2018).

6. Toroz, D. *et al.* Towards an understanding of the nucleation of alpha-para amino benzoic acid from ethanolic solutions: a multi-scale approach. *Faraday Discuss.* **179**, 79–114 (2015).
7. Sullivan, R. A. *et al.* Revealing the roles of desolvation and molecular self-assembly in crystal nucleation from solution: Benzoic and p -aminobenzoic acids. *Cryst. Growth Des.* **14**, 2689–2696 (2014).
8. Turner, T. D. *et al.* The influence of solution environment on the nucleation kinetics and crystallisability of para-aminobenzoic acid. *Phys. Chem. Chem. Phys.* **18**, 27507–27520 (2016).
9. Rosbottom, I., Pickering, J., Hammond, R. B. & Roberts, K. J. A Digital Workflow Supporting the Selection of Solvents for Optimising the Crystallisability of Para Aminobenzoic Acid. *Org. Process Res. Dev.* **24**, 500–507 (2020).
10. Rosbottom, I., Toroz, D., Hammond, R. B. & Roberts, K. J. Conformational and structural stability of the single molecule and hydrogen bonded clusters of para aminobenzoic acid in the gas and solution phases. *CrystEngComm* **20**, 7543–7555 (2018).
11. The Cambridge Crystallographic Data Centre (CCDC). Mercury. (2020). Available at: https://www.ccdc.cam.ac.uk/solutions/csd-system/components/mercury/.

Appendix F Supplementary Information: Influence of a Polymeric Additive on the Crystallisability and Nucleation Mechanism for the Model Fuel System of Eicosane Crystallising from Supersaturated Toluene Solutions

F.1 Abstract

This appendix contains supplementary information relating to Chapter 6. Average crystallisation and dissolution temperatures from 5 repeats of measurements are presented in Section F.2, over the full range of solution concentrations and IA treat rates, as well as via both turbidity analysis route measurements (STR and RRT).

F.2 Crystallisation and Dissolution Temperatures

Average crystallisation (T_c) and dissolution (T_{diss}) temperatures for eicosane crystallising from toluene solutions in the absence and presence of the cold flow improver additive IA, at each cooling/heating rate (q) and each solution concentration, are shown in Table F1. A range of IA treat rates are studied from 0.1 to 10 wt% IA within solution. The standard deviation (std) of the data is also displayed from 5 repeats of each crystallisation and dissolution experiment.

Table F1. Average crystallisation (T_c) and dissolution (T_{diss}) temperatures for eicosane crystallising from toluene solutions in the absence and presence of the cold flow improver additive IA, at each a range of cooling/heating rates (q) and solution concentrations. The standard deviation (std) of the data is also displayed from 5 repeats of each crystallisation and dissolution experiment.

Cooling rate (°C min^{-1})	T_c (°C)	std	T_{diss} (°C)	std	T_c (°C)	std	T_{diss} (°C)	std	T_c (°C)	std	T_{diss} (°C)	std	T_c (°C)	std	T_{diss} (°C)	std
	0 wt% IA															
Conc. (g L^{-1})	250				350				450				550			
0.25	9.7	0.2	12.0	0.1	12.6	0.1	14.6	0.1	14.8	0.1	16.4	0.4	16.5	0.2	18.1	0.3
1	9.2	0.2	13.0	0.5	12.0	0.1	15.5	0.6	14.2	0.2	18.1	0.2	15.7	0.2	20.5	0.4
2	8.3	0.3	15.1	0.5	11.2	0.2	18.5	0.5	13.3	0.2	20.4	0.3	15.1	0.2	23.4	0.6
3.2	7.6	0.3	17.3	0.5	10.3	0.1	20.4	0.6	12.7	0.1	24.6	0.5	14.0	0.2	26.0	0.1
	0.1 wt% IA															
Conc. (g L^{-1})	200				300				400				500			
0.25	7.3	0.2	11.8	0.0	10.6	0.1	14.8	0.1	13.1	0.1	17.0	0.1	14.8	0.1	18.6	0.1
1	6.7	0.2	12.9	0.2	10.1	0.2	16.6	0.1	12.4	0.3	19.0	0.1	14.2	0.1	20.6	0.2
2	6.1	0.4	14.3	0.2	9.2	0.2	17.8	0.2	11.8	0.2	20.5	0.0	13.6	0.1	22.5	0.1
3.2	5.2	0.1	16.1	0.1	8.5	0.2	20.1	0.1	11.0	0.2	22.8	0.1	12.7	0.4	25.3	0.2
	0.5 wt% IA															
Conc. (g L^{-1})	250				350				450				550			
0.25	8.3	0.6	13.3	0.2	11.7	0.1	15.7	0.1	13.7	0.1	17.6	0.1	14.9	0.3	19.1	0.1
1	8.4	0.1	14.8	0.2	10.9	0.2	17.7	0.1	12.9	0.1	19.7	0.2	14.5	0.2	21.2	0.1
2	7.5	0.3	16.3	0.1	10.6	0.2	19.0	0.1	12.5	0.2	21.3	0.1	13.8	0.1	23.5	0.1
3.2	6.5	0.3	19.0	0.4	9.7	0.2	22.0	0.1	11.8	0.4	24.4	0.1	13.0	0.0	26.7	0.2
	2 wt% IA															
Conc. (g L^{-1})	250				350				450				550			
0.25	7.8	0.2	13.2	0.1	10.8	0.1	15.4	0.1	12.5	0.1	17.2	0.1	14.2	0.2	18.6	0.1
1	7.5	0.3	14.6	0.2	10.1	0.3	17.0	0.1	12.0	0.1	19.1	0.1	13.4	0.2	20.6	0.2

2	6.6	0.2	16.0	0.1	9.5	0.2	18.7	0.1	11.5	0.2	20.9	0.1	12.7	0.1	22.8	0.1
3.2	5.9	0.2	18.0	0.1	8.8	0.1	20.6	0.1	10.8	0.1	23.2	0.1	12.0	0.1	24.9	0.0
	3wt% IA															
Conc. (g L^{-1})	250				350				450				550			
0.25	7.5	0.1	13.3	0.1	10.3	0.1	15.5	0.1	12.1	0.1	17.2	0.0	13.7	0.1	18.5	0.0
1	6.9	0.2	14.6	0.2	9.7	0.1	17.0	0.2	11.6	0.1	19.0	0.2	13.0	0.2	20.3	0.1
2	5.9	0.3	16.2	0.1	9.1	0.1	18.5	0.0	10.9	0.1	20.7	0.1	12.3	0.2	22.4	0.1
3.2	5.3	0.2	18.2	0.1	8.3	0.1	20.6	0.1	10.4	0.1	23.2	0.0	11.6	0.1	25.0	0.1
	5 wt% IA															
Conc. (g L^{-1})	250				350				450				550			
0.25	6.5	0.2	13.2	0.1	9.2	0.1	15.4	0.1	11.2	0.1	17.1	0.1	12.5	0.1	18.5	0.1
1	6.1	0.1	14.4	0.1	8.6	0.1	17.0	0.1	10.5	0.1	18.7	0.1	9.2	1.4	21.7	0.5
2	5.3	0.2	15.9	0.2	8.2	0.1	18.5	0.1	10.2	0.1	20.8	0.1	9.1	0.9	23.9	0.2
3.2	5.0	0.1	18.6	0.2	7.7	0.1	21.4	0.2	9.6	0.3	23.4	0.1				
	10wt% IA															
Conc. (g L^{-1})	250				350				450				550			
0.25	4.3	0.1	12.8	0.1	7.1	0.1	15.1	0.1	8.9	0.1	16.7	0.1	10.5	0.1	18.1	0.1
1	3.7	0.2	14.2	0.1	6.6	0.2	16.8	0.1	8.4	0.1	18.3	0.1	9.6	0.1	19.7	0.1
2	3.2	0.2	15.0	0.1	6.4	0.1	17.9	0.1	8.0	0.1	20.3	0.1	9.2	0.2	22.6	0.3
3.2	2.1	0.1	18.2	0.2	5.6	0.1	20.3	0.2	7.5	0.1	22.2	0.5	8.6	0.1	24.4	0.1